BARRIER-ENERGY COULOMB EXCITATION WITH SEGA-JANUS

By

Daniel Milton Rhodes

A DISSERTATION

Submitted to
Michigan State University
in partial fulfillment of the requirements
for the degree of

Physics – Doctor of Philosophy

2021

ABSTRACT

BARRIER-ENERGY COULOMB EXCITATION WITH SEGA-JANUS

By

Daniel Milton Rhodes

Experimentally determined indicators of nuclear shape and collectivity are crucial benchmarks on the quest to understand the structure of exotic nuclei. In even-even nuclei, the electromagnetic $B(E2; 2^+_1 \to 0^+_1)$ transition strength is an excellent indicator of collectivity which is sensitive to nuclear deformation, shell-breaking effects, and nucleon-nucleon correlations. Describing the evolution of $B(E2)$ transition strengths with decreasing neutron number in the even-even $Z = 50$ $^{104-130}$Sn isotopes continues to be challenging for large-scale shell-model calculations due to the strong enhancement of collectivity approaching $N = 50$. This renders measures of quadrupole collectivity near $N = Z = 50$ ^{100}Sn particularly interesting.

The experimental technique of subbarrier Coulomb excitation can be used to probe shape and collectivity in nuclei by providing sensitivity to both $B(E2)$ transition strengths as well as spectroscopic quadrupole moments. In this work, the results of an inverse-kinematics Coulomb excitation experiment on $N = 58$, $Z = 48$ ^{106}Cd using the JANUS setup at the NSCL's ReA3 facility is presented. The current results further the systematic understanding of nuclear structure approaching $N = Z = 50$ ^{100}Sn, and they clarify discrepant results reported in the literature for ^{106}Cd.

Shell model calculations were performed in order to understand the structure of ^{106}Cd. An analysis of $E2$ rotational invariants allowed for a detailed comparison of experiment to theory which revealed a large degree of triaxiality in ^{106}Cd that is not captured by the calculations. High-j neutron configurations are shown to be crucial for describing the shape of the heavier Cd isotopes, but this affect cannot explain the current results for ^{106}Cd.

In the Appendix of this work, the analysis and preliminary results of a Coulomb excitation experiment on the unstable nucleus ^{80}Ge is presented. This experiment also used the JANUS

setup, and it was performed in order to provide one of the first indicators of nuclear shape in the neutron-rich Ge isotopes near $N = 50$.

Copyright by
DANIEL MILTON RHODES
2021

To my wife, Deanna.

ACKNOWLEDGEMENTS

During my graduate student career, I received support from a large community of people both at NSCL and MSU as well as from my personal friends and family. This list of acknowledgements is not exhaustive, and I am thankful that I was, and still am, part of such a broad, supportive community.

First, I wish to thank my advisor, Dr. Alexandra Gade, whose guidance and mentorship made this dissertation possible. Her support was always available, any time of any day. Her enthusiasm for research and desire to share knowledge were tremendously helpful during my graduate career. Dr. Gade's guidance made obtaining a PhD an engaging and academically stimulating experience.

I am grateful to Dr. Dirk Weisshaar, who was always eager to share his knowledge of γ-ray detectors. Without fail, I would learn some new piece of information whenever Dirk offered his insight into a particular topic. His attention to detail ensured any work I performed was always rigorously scrutinized.

To all the post-docs and graduate students of the gamma group I worked with during my time at NSCL, thank you. You all provided support, knowledge, and camaraderie which made my experience at NSCL enjoyable. To my fellow graduate students, thank you for helping ease the burden of the SeGA pager.

I also wish to acknowledge my parents, Chris and Alma Rhodes, who have provided me with every opportunity I could ask for in life. Without my parents, nothing I've done would have been possible.

I am deeply grateful to my wife, Deanna, who has been at my side for over seven years. Deanna has provided continuous support, care, and love during my graduate career. She would listen to me speak about my work, even though it was of no particular interest to her. Whenever the Lab would threaten to take too much of my time, Deanna would remind me not to forget the other aspects of life. To Deanna, thank you.

TABLE OF CONTENTS

LIST OF TABLES

LIST OF FIGURES

CHAPTER 1

INTRODUCTION

1.1 Atomic Nuclei

An atomic nucleus is a quantum many-body system made up of Z positively-charged protons and N electrically-neutral neutrons which form a total of $A = N + Z$ nucleons. A particular nucleus is typically denoted ${}^{A}X(Z)$, where $X(Z)$ is the chemical symbol of the element with Z protons. Nuclei with the same Z, N, or A are referred to as isotopes, isotones, and isobars, respectively. Typical nuclear radii are of order 10 fm (1 fm = 10^{-15} m), indicating the quantum nature of the system. Atomic radii are of order 10 nm (1 nm = 10^{-9} m), so the nucleus makes up very little of the atomic volume. However, the nucleus contains essentially all of the mass of an atom.

Protons and neutrons are both spin-1/2 fermions. Notably, protons as well as neutrons are (separately) indistinguishable, and thus they obey the Pauli exclusion principle and Fermi-Dirac statistics more generally. The Pauli exclusion principle prevents two identical fermions from occupying the same quantum state, and, as will be discussed in Section 1.2, this has a significant impact on nuclear properties.

Nucleons are not fundamental particles. They are hadrons, a family of composite particles made up of quarks. A proton consists of two up quarks and one down quark, while a neutron contains two down quarks and one up quark. The quarks are bound together by the strong force, which is mediated by the exchange of gluons as described by the theory of quantum chromodynamics [1].

Despite the Coulomb repulsion between protons, the nucleons are bound together by the nuclear force to form a nucleus. The nuclear force is a residual of the fundamental strong interaction between the constituent quarks of the individual nucleons. Thus the nuclear force is analogous to the Van der Waals force between neutral atoms and molecules, which is a residual of the fundamental Coulomb interaction.

In general, there is no simple analytical form for the nuclear potential. Since nucleons are

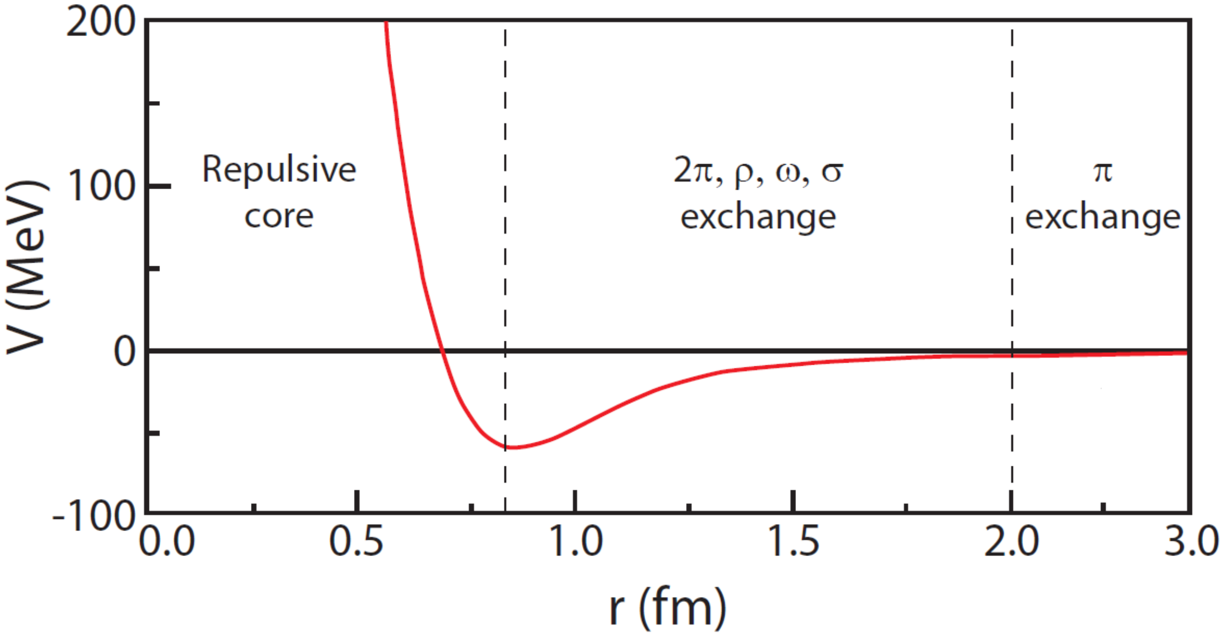

Figure 1.1: The central component of the NN interaction. Three main features are visible: a strongly repulsive core, a local minimum, and a tail with rapidly diminishing strength. The distances at which the potential can be modelled by the exchange of π, ρ, ω and σ mesons are indicated. Figure adapted from [5].

composite particles, there are many-body forces which enter the total potential. (For example, the interaction between two nucleons is affected by the presence of a third nucleon; this is a three-body force.) However, many broad features of the nuclear force can be understood by inspecting only the two-body nucleon-nucleon (NN) potential. There are many terms which contribute to the interaction between two nucleons, including a central scalar potential, a central vector (spin-orbit) term, and a non-central tensor component. Due to the availability of precise nucleon-nucleon scattering data, the free NN interaction is well constrained [2, 3], and it is observed to be approximately charge-independent [4]. The central part of the NN potential is shown in Fig. 1.1.

As indicated in Fig. 1.1, the central component of the nucleon-nucleon interaction can be divided into three regions. At the shortest distances, the interaction is strongly repulsive, which is refereed to as the "hard core." Over intermediate distances, the force is attractive, and at the longest distances there is only a rapidly diminishing attractive tail. At medium and long distances, the force can be modeled by the exchange of light mesons [6], which are particles formed by quark-antiquark

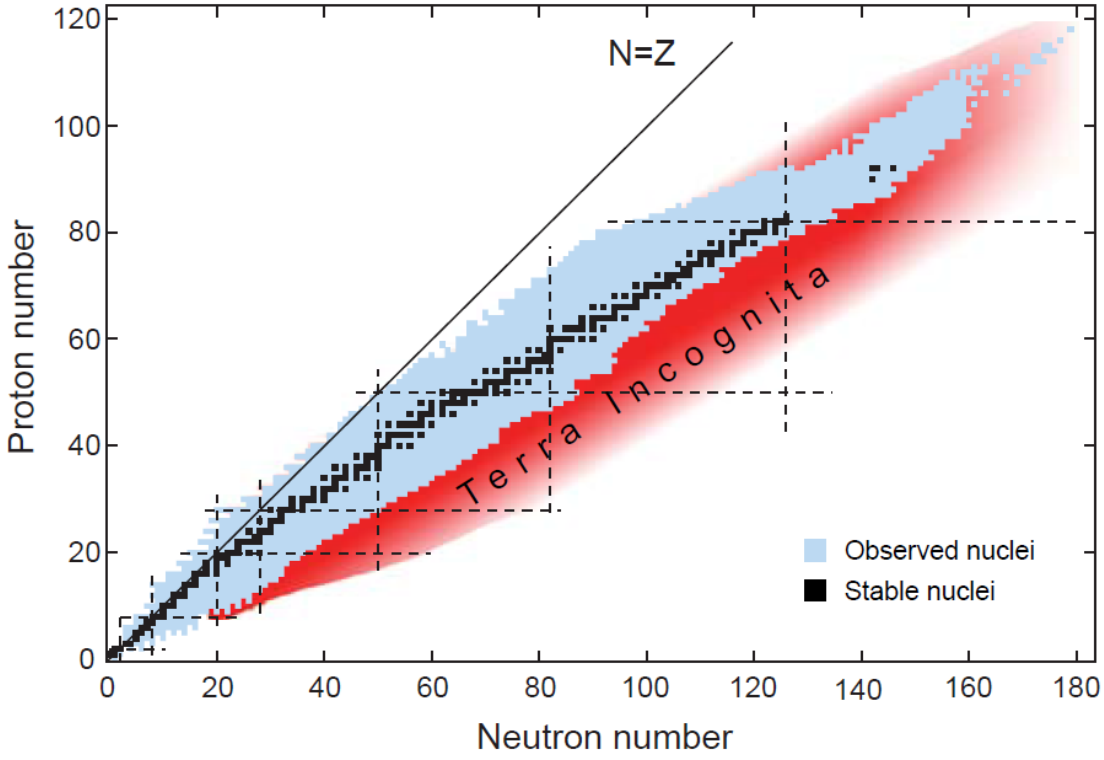

Figure 1.2: The Chart of Nuclides. The *y*-axis is the the proton number, the *x*-axis is the neutron number, and each square represents an individual nucleus. Figure from [7], originally adapted from [8].

pairs. At distances larger than approximately 2.5 fm, the Coulomb force dominates.

The competition between the attractive nuclear force and the repulsive Coulomb force has a very obvious impact on which nuclei form bound systems. As the mass number increases, the nuclei must become more neutron rich to overcome the increasing Coulomb repulsion. This effect can be seen clearly in the Chart of Nuclides, shown in Fig. 1.2. For increasing Z, the extant nuclei bend away from the $N = Z$ line and move toward the $N > Z$ region.

The Chart of Nuclides depicts the nuclear landscape. The black squares represent stable isotopes, of which there are less than 300 [8]. The path through the nuclear landscape formed by these stable isotopes is referred to as the Valley of Stability. The blue squares denote the roughly 3000 isotopes known to exist [9], and the red squares show the ~ 7000 nuclei predicted to exist [10] but which have not been observed. The dashed vertical and horizontal lines show the conventional magic numbers (see Section 1.2). Clearly, the vast majority of nuclei are unstable against radioactive decay or fission and thus, with few exceptions, do not exist naturally on Earth.

Another consequence of the nuclear force, particularly its hard core, is nuclear "saturation," which refers to the roughly constant density inside a nucleus. Considering also the short range of the nuclear force, a single nucleon will interact most strongly with its immediate neighbors, and as the number of nucleons increases, the single nucleon will will have a weaker interaction with the additional nucleons due to the increasing volume. At some point, the interaction energy per nucleon will reach a maximum, referred to as the saturation energy. While additional nucleons still contribute to the total energy, the saturation energy is the point past which increasing the nuclear mass is not energetically favorable.

The effect of nuclear saturation is clearly observed from an inspection of nuclear binding energies. The binding energy is the amount of energy required to break up a nucleus into its component nucleons, and it is a measure of the total interaction energy in a nucleus. Experimentally determined values for the binding energy are shown for many nuclei in Fig. 1.3; the effect of saturation is clear in the upper panel. The constant nuclear density also implies that the volume of a nucleus is proportional to the number of nucleons, $V \propto A$.

1.2 Nuclear Models

An overarching goal of nuclear physics is the creation of a theoretical model that can predict the proprieties of a nucleus based on its proton and neutron numbers. One of the earliest and simplest is the Liquid Drop Model [12], which treats a nucleus as an incompressible fluid in an attempt to calculate the binding energy. Like a liquid drop, a nucleus has a roughly constant density (the consequence of saturation) and short range interactions. Under this assumption, the binding energy can be calculated as

$$BE_{LD} = a_V A - a_S A^{2/3} - a_C \frac{Z^2}{A^{1/3}} - a_A \frac{(N-Z)^2}{A} + \delta(N,Z), \tag{1.1}$$

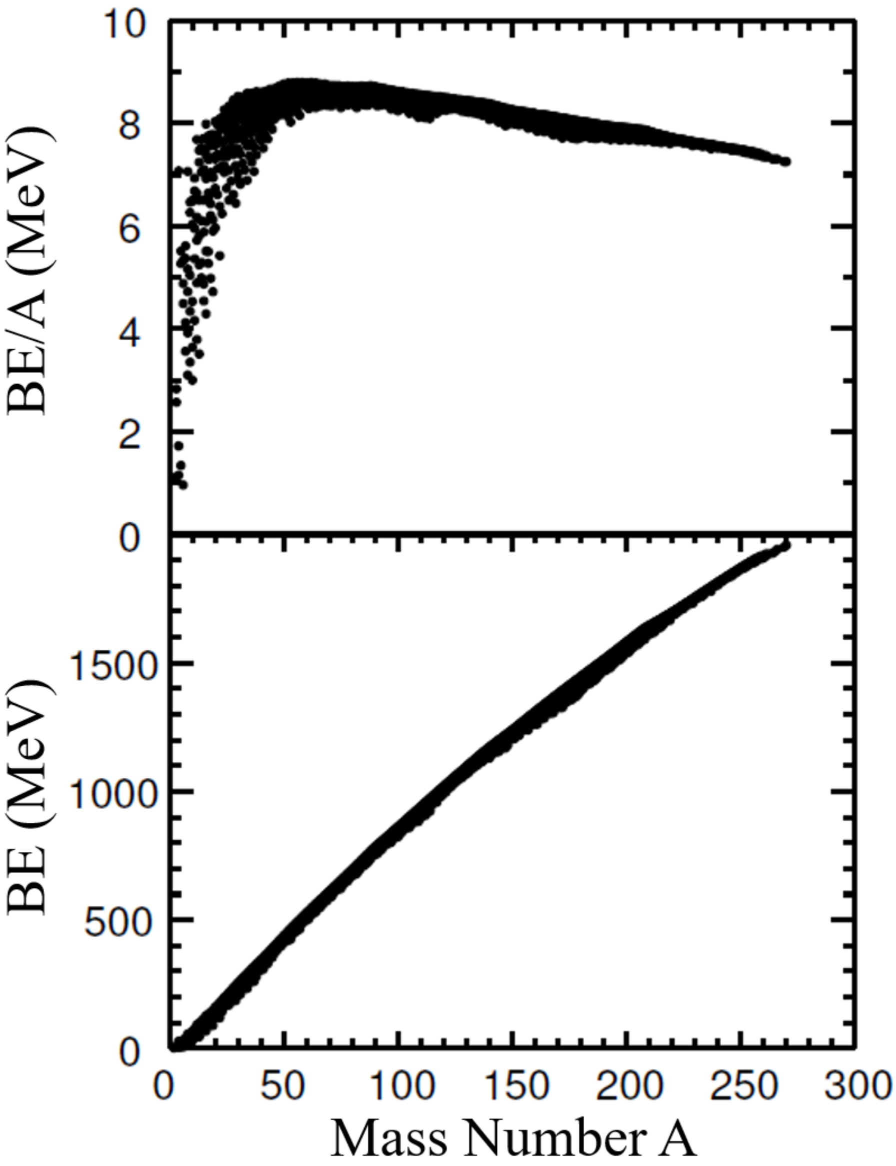

Figure 1.3: The total binding energy BE (lower) and binding energy per nucleon (upper) as a function of the mass number. The turning point near $A = 60$, caused by saturation, is clear in the upper panel. Stable nuclei tend to have a large BE/A [11]. Figure adapted from [11].

where

$$\delta(N,Z) = \begin{cases} -a_P A^{-1/2} & N \text{ and } Z \text{ odd} \\ a_P A^{-1/2} & N \text{ and } Z \text{ even} \\ 0 & A \text{ odd.} \end{cases} \tag{1.2}$$

In Eqs. 1.1 and 1.2, the dependence on Z, N, or A of each term has a clear physical motivation, and their strengths $a_X > 0$ can be found from fits to experimental data. The volume term a_V describes the linear increase in energy with increasing volume of the droplet, and is thus proportional to A. The surface term a_S corrects for the missing interaction energy of nucleons at the surface, which depends on the surface area, so it is proportional to $A^{2/3}$. The Coulomb term a_C arises from the electric repulsion between the protons and is proportional to $Z^2/R = Z^2/A^{1/3}$.

Because nucleons are spin-1/2 fermions which each obey the Pauli principle, the energy is minimized (and binding maximized) when there is an equal number of protons and neutrons for a given A. This gives rise to the anti-symmetry term a_A which penalizes proton-neutron asymmetry. The final term is motivated by the experimentally observed staggering in the binding energy for even and odd numbers of protons or neutrons (not visible in Fig. 1.3). To account for this, a pairing term a_P (contained in $\delta(N,Z)$) is added which is attractive for even Z, N and is repulsive for odd Z, N.

The difference between the experimentally determined binding energy and the liquid drop prediction is shown in Fig. 1.4. Two features are immediately apparent. First, the Liquid Drop Model is accurate to roughly 10 MeV for most nuclei, while the average binding energy per nucleon is about 8 MeV. Second, there are regular, systematic discrepancies between the data and the model prediction. Nuclei near $N = 28$, 50, 82, and 126 are significantly more bound than the Liquid Drop model predicts when compared to nuclei further away from these numbers. This suggests that nuclei have internal structure which is not captured by the simplified Liquid Drop Model.

The numbers 28, 50, 82, and 126, along with 2, 8, and 20 which are not clearly visible in Fig. 1.4, are referred to as the "magic" numbers. The same pattern in the binding energy is observed as a function of Z, so the magic numbers are the same for both protons and neutrons. A nucleus with

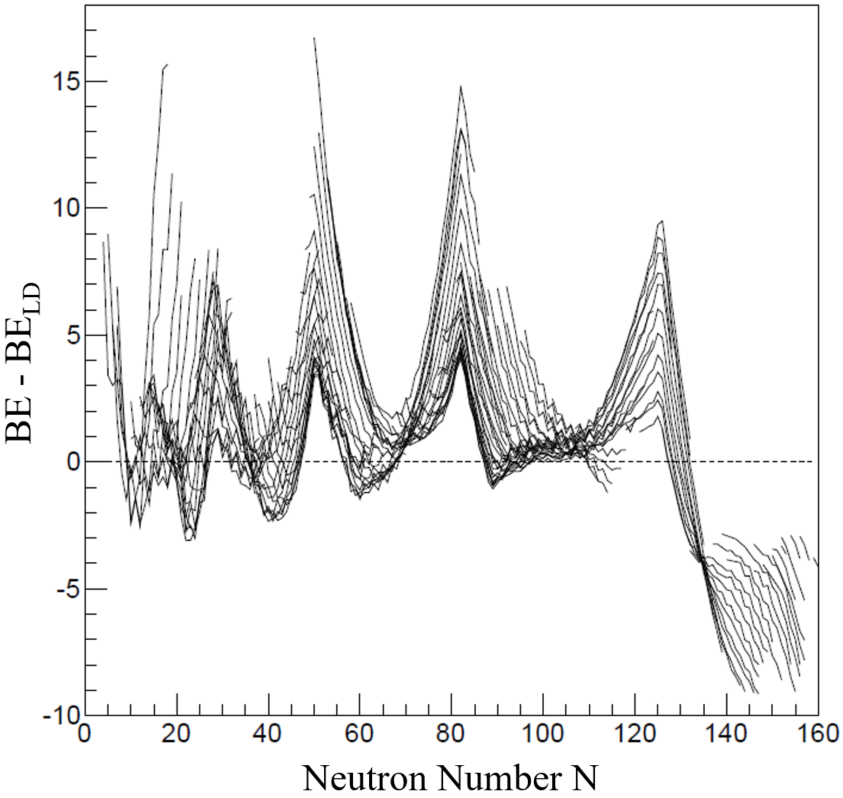

Figure 1.4: The difference between the experimentally determined binding energy and the liquid drop energy as a function of the neutron number for nuclei with $Z \geq 8$. The parameters used for this figure are [11, 13] $a_V = 15.54$, $a_S = 17.23$, $a_C = 0.697$, $a_A = 22.6$, and $a_P = 12.0$, all in MeV. Figure from [13] with data from [14].

either a magic N or Z is referred to as singly-magic, and a nucleus with both a magic N and Z is called doubly-magic. The observation of the magic numbers lead to the development of the nuclear shell model [15, 16].

1.2.1 The Shell Model

The nuclear shell model is a microscopic quantum description of the nucleons in a nucleus. Neglecting the Coulomb interaction and only considering two-body forces between the nucleons, the nuclear Hamiltonian for A nucleons is written as [11]

$$\hat{H} = \sum_{k=1}^{A} \frac{p_k^2}{2m_k} + \sum_{k<l}^{A} V_{kl}(\mathbf{r}_k - \mathbf{r}_l), \tag{1.3}$$

where $\mathbf{p}_k$, $\mathbf{r}_k$, and m_k are the momentum, position, and mass of the k-th nucleon, respectively. V_{kl} is the two-body interaction between the nucleons. Assuming the A nucleons do not interact strongly, one can consider a single-particle central potential $U(r)$ which is generated by all A nucleons. This allows Eq. 1.3 to be written as

$$\hat{H} = \left\{ \sum_{k=1}^{A} \left(\frac{p_k^2}{2m_k} + U(r_k) \right) \right\} + \left\{ \sum_{k<l}^{A} V_{kl}(\mathbf{r}_k - \mathbf{r}_l) - \sum_{k=1}^{A} U(r_k) \right\} \equiv \hat{H}_0 + \hat{V}_{res}. \tag{1.4}$$

In Eq. 1.4, $\hat{H}_0$ describes the independent motion of a particle in a mean field. The term $\hat{V}_{res}$ is the remaining interaction between nucleons beyond what is generated by the mean field, which is called the residual interaction. In the independent particle model [17, 18], one takes $\hat{V}_{res} = 0$ and a nucleus is approximated as A nucleons moving independently in the mean field.

1.2.1.1 The Independent Particle Model

A common first choice of the mean-field $U(r)$ is the harmonic oscillator (HO) potential

$$U_{\mathrm{HO}}(r) = \frac{1}{2} m\omega^2 r^2, \tag{1.5}$$

where m is the nucleon mass, ω is the adjustable oscillator frequency, and r is the distance the from the center of the nucleus. The harmonic oscillator potential has several advantageous properties, such as analytically expressible wave-functions and the ability to separate the many-body Hamiltonian into terms only dependent on intrinsic and center-of-mass degrees of freedom. The energy levels of the HO potential depend on the radial quantum number n and orbital angular momentum quantum number l, generally redefined into the single principle quantum number $N = 2n + l$. They are given by

$$E_N = (N + 3/2)\hbar\omega, \tag{1.6}$$

where $\hbar$ is the reduced Planck constant. It is noted that one method of specifying ω is by requiring the calculated root-mean-square charge radius matches the experimentally determined value [11].

As can be seen from the left column of Fig. 1.5, which shows the calculated energy levels for different mean-field potentials, the HO potential reproduces the first three magic numbers 2, 8, and

20, but it fails to produce the higer magic numbers. The HO potential increases to infinity with increasing r, which is markedly different than the short-range nuclear interaction (see Fig. 1.1). An improvement might be expected if a more realistic mean-field potential is chosen, such as the Woods-Saxon (WS) potential

$$U_{WS}(r) = V_o f_{ws}(r), \tag{1.7}$$

$$f_{ws}(r) = \frac{1}{1 + \exp\left(\frac{r-R_o}{a_o}\right)}. \tag{1.8}$$

In Eqs. 1.7 and Eq. 1.8 above, V_o is the potential depth, $R_o = r_o A^{1/3}$ is the nuclear radius, and a_o is the diffuseness. A typical [11, 19] set of parameters is $V_o \approx 50$ MeV, $r_o = 1.27$ fm, and $a_o = 0.67$ fm. In principle the strength V_o depends on whether one is considering protons or neutrons and is adjusted based on the proton-neutron asymmetry. Inspection of the middle column of Fig. 1.5 shows that the WS potential still fails to the predict magic numbers beyond N,$Z = 20$. This potential does, however, produce some new features, such as breaking the degeneracy of levels with the same principle quantum number N.

The crucial component of the mean-field potential is an additional strong coupling term between the intrinsic spin **s** and orbital angular momentum **l** of a nucleon. This is given by

$$U_{LS}(r, \mathbf{l}, \mathbf{s}) = V_{so} \frac{1}{r} \frac{df_{ws}(r)}{dr} (\mathbf{l} \cdot \mathbf{s}), \tag{1.9}$$

where V_{so} is the strength of the interaction. A typical value is $V_{so} = 22$ MeV. The radial dependence of U_{LS} is given by the derivative of $f_{ws}(r)$ to ensure it is surface-peaked. This is physically motivated as a nucleon in the interior of a nucleus is subjected to an equal amount of spin-up and spin-down nucleons, which leads to a cancellation of the LS interaction [11].

The third column of Fig. 1.5 shows that taking a mean-field potential of $U = U_{WS} + U_{LS}$ successfully predicts all observed magic numbers (at stability). The introduction of the LS coupling term additionally breaks the degeneracy of orbits with the same l value. As such, each orbit must be specified by the additional quantum number $j = l \pm 1/2$ which results from the LS coupling, i.e.

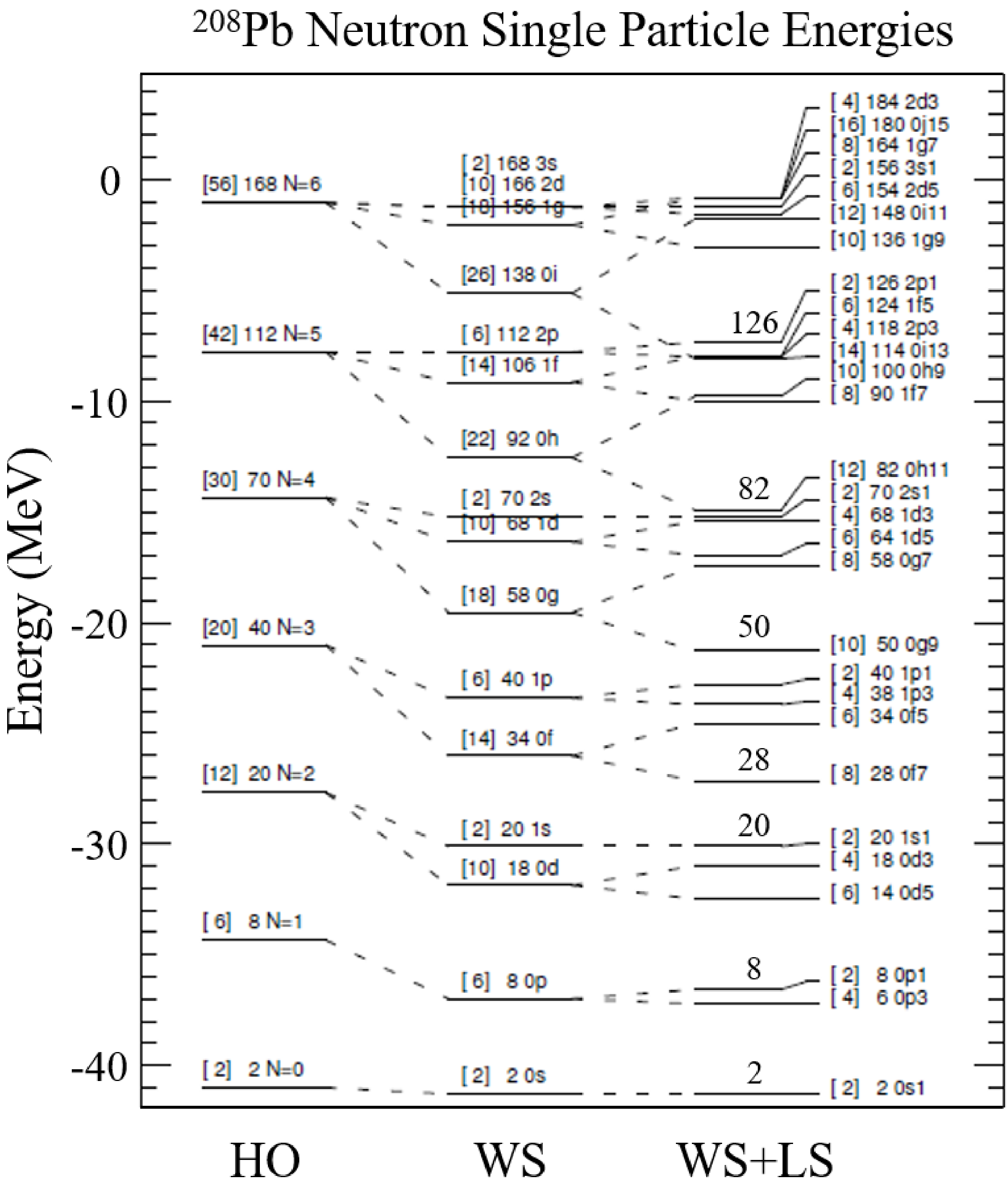

Figure 1.5: The neutron single-particle energies in ^{208}Pb for various mean field potentials. For each level, the number in brackets is the maximum number of nucleons allowed in that level by the Pauli principle, and the number next to the quantum numbers is a running sum of the maximum allowed nucleons. The magic numbers which result from the WS+LS potential are indicated. Figure adapted from [11].

$\mathbf{j} = \mathbf{l} + \mathbf{s}$. Note the single-particle orbit characterized by $j_> = l + 1/2$ is split to a lower energy than $j_< = l - 1/2$.

The single-particle orbits from the WS+LS potential are generally labeled using the spectroscopic notation nl_{2j}, which is employed in Fig. 1.5. The radial quantum number n = 0,1,2... specifies the number of nodes in the radial wave-function, and the orbital angular momentum number l is represented by s, p, d, f, g, h... for l = 0, 1, 2, 3, 4, 5... The LS coupling to total angular momentum $\mathbf{j}$ means each level nl_{2j} has $2j + 1$ projections m_j, with m_j running from $-j$ to j in integer steps. Considering the Pauli exclusion principle, this implies the maximum number of nucleons in each orbit is $2j + 1$.

An additional quantum number conserved by the nuclear Hamiltonian is the parity π. A parity transformation $\mathcal{P}$ is the inversion of all spatial coordinates $\mathbf{r} \rightarrow -\mathbf{r}$, i.e. $\mathcal{P} f(\mathbf{r}) = \pi f(-\mathbf{r})$. The parity quantum number of a single-particle orbit depends only on l, and it it given by $\pi_l = (-1)^l$. The parity of the entire nuclear configuration is determined by the product of the parity of all nucleons

$$\pi = \prod_i^A \pi_l^{(i)} = \prod_i^A (-1)^{l_i}. \tag{1.10}$$

It is easy to see that an even number of nucleons in any orbit will contribute positive parity. Similar to the total parity, the nuclear configuration will also form a total spin J which results from coupling all $\mathbf{j}_i$ of the nucleons, $\mathbf{J} = \sum_i^A \mathbf{j}_i$. This leads to the common notation J^π used to specify a nuclear state. Pairs of identical nucleons preferentially couple to $J = 0$ [20], and in fact all nuclei with an even Z and even N have a ground-state J^π of 0^+.

The independent particle shell model is particularly well-suited to predict ground-state J^π values for nuclei which are one nucleon away from being doubly-magic [20]. This is accomplished by placing the nucleons in the lowest lying energy level allowed by the Pauli exclusion principle. Note that since protons and neutrons are distinguishable, they each fill their own set of orbits[1]. Taking $Z = 82$, $N = 127$ ^{209}Pb as an example, we see that the protons form a closed shell, and

---

[1] The Coulomb interaction can be added to the mean field potential if desired, which will make a slight adjustment to the proton single-particle orbits.

there is one neutron outside the $N = 126$ closed shell which is placed in the $1g_9$ orbit. Thus, we can predict the ground state of ^{209}Pb to have $J^\pi = 9/2^+$.

In this model, excited-state configurations are also simple to construct. They are formed by promoting a nucleon from its ground-state orbit to one lying higher in energy. Taking again ^{209}Pb as an example, we can consider the simplest reconfiguration: promoting the last neutron from $1g_9$ to $0i_{11}$. This results in an excited state with quantum numbers $11/2^+$ at an energy given by the difference between the $0i_{11}$ and $1g_9$ single-particle energies. Indeed, the ground state and first excited state in ^{209}Pb are known experimentally to be $9/2^+$ and $11/2^+$, respectively, just as the independent particle model predicts. Nuclei with properties well-described by the independent-particle model are often called "single-particle-like" nuclei.

As discussed above, the independent particle model can predict ground-state and some excited-state properties in nuclei near the magic numbers. For quantitative predictions of more detailed nuclear structure properties, particularly in nuclei further away from the magic numbers, one must go beyond the independent particle model. This can be done by including the residual two-body interaction beyond the mean-field (see Eq. 1.4).

1.2.1.2 Configuration Interaction

Incorporating the residual interaction between nucleons prevents separating the nuclear system into A independent particles, where the total nuclear wavefunction is given by the anti-symmetric product of the single-particle wavefuntions of the individual nucleons (a Slater determinant [21]). The residual interaction introduces mixing between Slater determinants representing different configurations, hence the name configuration interaction.

In the configuration interaction shell model, the nuclear Hamiltonian is written in matrix form

$$H_{ij} = \langle \Phi_i | \hat{H}_0 + \hat{V}_{res} | \Phi_j \rangle, \tag{1.11}$$

where $|\Phi_i\rangle$ are the unperturbed many-body wavefunctions of the mean-field Hamiltonian $\hat{H}_0$. The total wavefunction is found by diagonalizing the Hamiltonian matrix with respect to the chosen basis. The mean-field Hamiltonian is often already diagonal in the chosen basis, and thus the one-body matrix elements $\langle i|\hat{H}_0|j\rangle$ define the single-particle energies discussed above. The residual interaction creates additional two-body matrix elements $\langle ij|\hat{V}_{res}|kl\rangle$ which define the nucleon-nucleon interactions.

Including the residual interaction between all nucleons for nuclei with $A \gtrsim 12$ will make the matrix dimension become intractably large for computation. In these cases it is necessary to define an inert core of A_{core} nucleons which are represented by a single Slater determinant and do not contribute to the excited state configurations; only the remaining $A - A_{\text{core}}$ active *valence* nucleons can be promoted out of the ground state configuration. Often, the the core is chosen to be a nearby doubly-magic nucleus. A further truncation is required to define what single-particle levels the valence nucleons can be promoted to, referred to as the valence space. The choice of an inert core and a valence space defines the model space for a shell model calculation.

The precise form of the residual interaction is not know. Accurate potentials have been derived from nucleon-nucleon scattering data [2, 3, 22]. However, directly using these potentials in the nuclear Hamiltonian will not produce accurate results if configurations from outside the model space contribute appreciably, which is often the case. There is another method of deriving the residual interaction which forgoes its connection to the individual nucleon degrees of freedom. Instead, the single-particle energies and two-body matrix elements are treated as free parameters in a fit of experimental binding energies and excited state energies [23, 24].

Effective interactions for nuclear Hamiltonians are fully defined by the fitted single-particle energies and two-body matrix elements. The interactions depend on the mass regime, and in general they can have different parameters depending on what experimental data is included in the fitting procedure. The accuracy and applicability of a particular effective interaction rapidly deteriorates if it is applied to a mass regime which is not constrained by the data used in the fit.

1.2.2 Collective Models

In many nuclei, particularly those away from magic numbers, a large number of nucleons can contribute coherently to the excited-state configurations. In these cases, macroscopic geometric models can be used which describe the collective motion of the nucleons. The most commonly considered forms of collective motion are vibrations and rotations.

1.2.2.1 Vibrational Nuclei

In a vibrational model of nuclei, a nucleus is treated as an incompressible fluid drop which oscillates about a spherical equilibrium. That is to say, a nucleus is considered to have a spherical ground state and excited-state configurations are generated by phonons, the elementary excitation in a quantum treatment of vibrations. Only considering quadrupole vibrations, the first excited state will have $J^\pi = 2^+$ and be located at the energy of a single phonon.

Higher-lying excited states are generated by multiple phonons. Due to the different possible couplings of the phonon spins, multi-phonon configurations will produce multiple excited states with different J but which are degenerate in energy. The multi-phonon state energies are simply multiples of the one-phonon energy, i.e. [20]

$$E_{\text{vib}}(N_p) = N_p E_{\text{vib}}(N_p = 1), \tag{1.12}$$

where N_p is the number of phonons. The allowed J^π values for a two-phonon configuration are 0^+, 2^+, and 4^+, while for three phonons they are 0^+, 2^+, 3^+, 4^+, and 6^+ [20].

In reality, no nucleus is a perfect quadrupole vibrator. However, vibrational-like behaviour can still be indicated by closely-spaced states of the correct J^π located roughly at multiples of the first excited state energy. This is most common in nuclei just outside of closed shells where the ground state is still dominated by spherical configurations but even the lowest-lying excited states will involve a reconfiguration of multiple nucleons.

1.2.2.2 Rotational Nuclei

In addition to vibrations, one can consider rotations as a form of collective motion. Quantum mechanically, an object cannot rotate about an axis-of-symmetry, so a spherically symmetric quantum object cannot rotate at all. Thus, for a nucleus to rotate, it must be deformed. Assuming only quadrupole deformation, the radial shape of the deformed object is given by [25]

$$R(\theta, \phi) = R_o \left[1 + \sum_{\mu} (-1)^u \alpha_{2\mu} Y_{2\mu}(\theta, \phi) \right], \tag{1.13}$$

where $Y_{2\mu}$ are the rank-2 spherical harmonics.

The five coordinates $\alpha_{2\mu}$ specify both the quadrupole (ellipsoidal) deformation of the nucleus as well as its orientation in space in any reference frame. It is most convenient to use the instantaneous body-fixed frame (the intrinsic frame), where the coordinate axes are aligned with the principle axes of the ellipsoid. The five coordinates can then be specified by a rotation to the intrinsic frame (three Euler angles) and two parameters which define the shape. In this reference frame the radial shape is still given by Eq. 1.13, but the $\alpha_{2\mu}$ can be parametrized as

$$\alpha_{20} = \beta_2 \cos\gamma \tag{1.14}$$

$$\alpha_{2\pm 1} = 0 \tag{1.15}$$

$$\alpha_{2\pm 2} = \frac{1}{\sqrt{2}} \beta_2 \sin\gamma \tag{1.16}$$

In Eqs. 1.14 to 1.16, β_2 and γ are the Bohr parameters [25, 26] used to specify the radial shape of a quadrupole deformed object. It is easy to see that (by definition)

$$\beta_2 = \sqrt{\sum_{\mu} |\alpha_{2\mu}|^2} \tag{1.17}$$

and as such is a measure of the overall quadrupole deformation. The parameter γ specifies the deviation from axial symmetry, and its affect can be seen by evaluating the deviation of each principle axis of the ellipsoid from the average radius R_o. This is given by [20, 25]

$$\delta R_n \equiv R_n - R_o = \sqrt{\frac{5}{4\pi}} \beta_2 R_o \cos\left(\gamma - \frac{2\pi}{3} n \right) \quad n = 1, 2, 3. \tag{1.18}$$

From Eq. 1.18 it is seen that for $\gamma = 0$, $\delta R_3 > 0$ and $\delta R_1 = \delta R_2 < 0$. For $\gamma = \pi/3$, $\delta R_2 < 0$ and $\delta R_3 = \delta R_1 > 0$.

The crucial detail from the above simple relations is that both $\gamma = 0$ and $\gamma = \pi/3$ imply axial symmetry, i.e. two of the radial deviations δR_n are equal. However for $\gamma = 0$, the ellipsoid is compressed in two dimensions and elongated in the third, while for $\gamma = \pi/3$ it is elongated in two dimensions and compressed in the third. This is the distinction between axially symmetric prolate ($\gamma = 0$) and oblate ($\gamma = \pi/3$) shapes; these shapes are shown in Fig. 1.6. The region $0 < \gamma < \pi/3$ describes a triaxial shape, with maximal triaxiality at $\gamma = \pi/6$. It can also be seen from Eq. 1.18 that all unique shapes are contained in the region $0 \leq \gamma \leq \pi/3$; all other γ values are equivalent to a redefition of the axes.

For rigidly deformed axially-symmetric nuclei (prolate or oblate), the excited state energies are those of a quantum-mechanical symmetric top [20, 28]

$$E_{\mathrm{rot}}(J) = \frac{\hbar^2}{2\mathcal{I}} J(J+1), \tag{1.19}$$

where $\mathcal{I}$ is the moment of inertia. While the excited state energies Eq. 1.19 are simple for axially symmetric rotors, they will have a more complicated form, with an additional dependence on γ, when axially-asymmetric shapes are allowed. The evolution of the excited state energies for a triaxial rigid rotor [29] are shown in Fig. 1.7. The presence of rotational behaviour is most common far away from the magic numbers where the number of nucleons outside of closed shells can create deformation even in the ground state.

The nuclear models discussed above are powerful tools for understanding the properties of nuclei. In particular, the energy systematics predicted by the collective models provide an exceptionally clear signature of collective vs single-particle-like behavior. A commonly used signature is the ratio of the first 4^+ energy to the first 2^+ energy, denoted $R_{4/2}$. For a spherical vibrator $R_{4/2} = 2.0$, for a maximally-asymmetric rigid rotor $R_{4/2} = 2.5$, and for a symmetric rigid rotor $R_{4/2} = 3.33$ [20]. The ratio $R_{4/2}$ is shown for even-even nuclei in Fig. 1.8.

The effect of nuclear shell structure and collectivity is clear in Fig. 1.8. Close to the magic numbers, nuclei display vibrational-like behavior. Moving further away from the magic numbers,

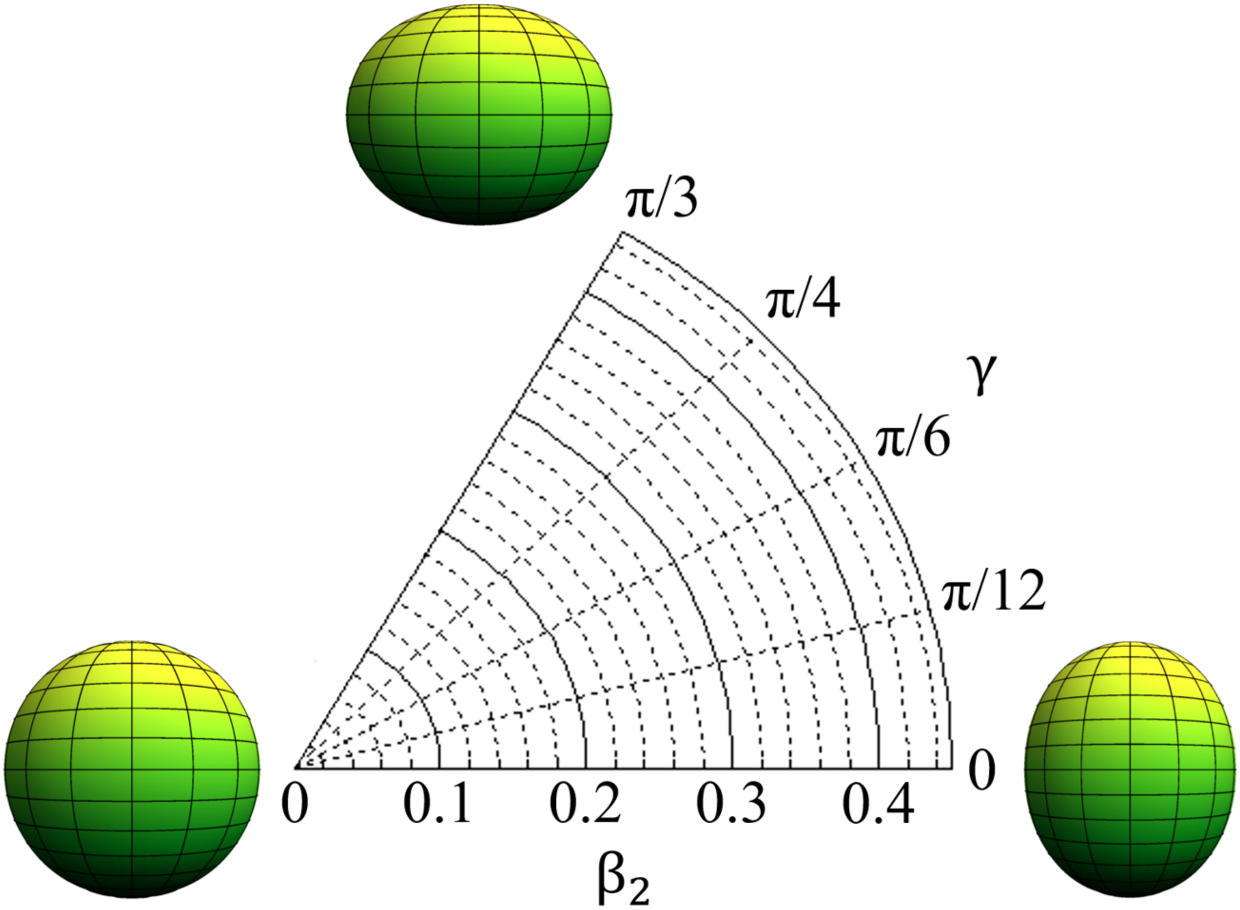

Figure 1.6: Spherical, prolate, and oblate quadrupole deformations. The contours show axially-symmetric shapes, and the region $0 < \gamma < \pi/3$ corresponds to axial asymmetry. Contours from [27].

nuclei rapidly transition to asymmetric rotors and then to almost pure symmetric rigid-rotors at mid-shell. While these signatures help isolate the dominant nature of the collectivity, there is a strong connection between rotations and vibrations (i.e. a deformed rotor can also vibrate). The coupling of these two modes can be described using the more general Bohr Hamiltonian [25, 26].

The collective models are most naturally applied to even-A nuclei. However, they can be extended to odd-A nuclei in two related ways [20]: by considering a nucleon moving in a deformed mean-field, or by considering the coupling of valence nucleons to the collective motion of the core. The former method is often called the deformed shell model [31] or Nilsson model [32], and the latter is a particle-plus-rotor model [33]. Both are extensions of the independent-particle shell

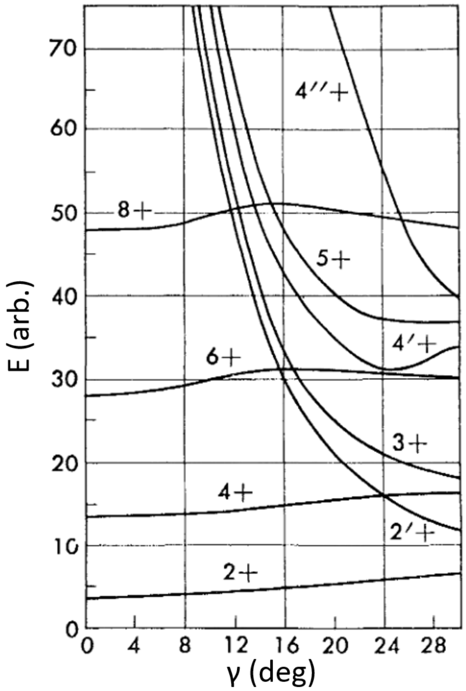

Figure 1.7: Relative energies of the excited states in a triaxial rotor model as a function of γ. The primes are used to differentiate states with the same J^{π}. Figure adapted from [20].

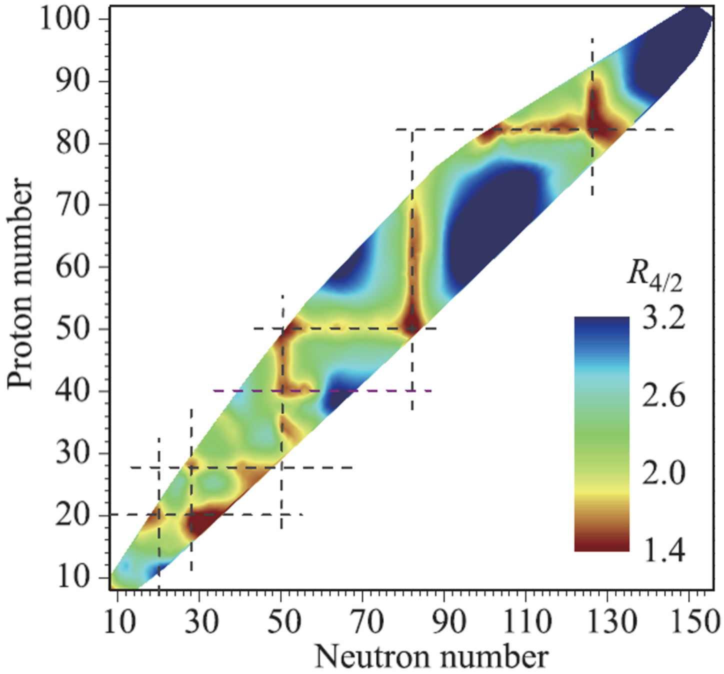

Figure 1.8: The ratio $R_{4/2}$ for even-even nuclei across the nuclear chart. Dashed lines indicate the magic numbers (excluding 2 and 8). Figure adapted from [30].

model which explicitly incorporate collective effects.

1.3 Electromagnetic Transitions

While the energies of excited states, emphasized in the previous section, provide a first hint at the underlying nuclear structure, additional information is gained by studying their decay properties. Low-lying excited states bound to particle emission will decay primarily by emitting electromagnetic radiation (photons), commonly called γ rays. Other electromagnetic decays, such the as emission of conversion electron or internal pair production, are also possible. Neglecting the small recoil energy of the nucleus, the γ-ray energy is equal to the difference in energy between the initial and final nuclear states.

A γ-ray transition is classified by its multipolarity λ and character C, which can be either electric ($C = E$) or magnetic ($C = M$). A particular γ-ray transition is denoted $C\lambda$. Electric and magnetic γ-ray transitions carry opposite parity, which affects the possible initial and final states they can connect. For an initial state of parity π_i and a final state of π_f, this restriction is given by

$$\pi_i \pi_f = \pi_C (-1)^{\lambda}, \tag{1.20}$$

where $\pi_E = 1$ and $\pi_M = -1$. This means the allowed γ-ray transitions between states with $\pi_i = \pi_f$ are $M1$, $E2$, $M3$, $E4$..., and states with $\pi_i = -\pi_f$ can be connected by $E1$, $M2$, $E3$, $M4$... γ-ray transitions.

Along with parity, γ-ray transitions are subject to angular momentum selection rules as well. For an initial state with spin I_i and final state with I_f, the γ-ray transition must obey

$$\left|I_i - I_f\right| \leq \lambda \leq \left|I_i + I_f\right|. \tag{1.21}$$

Note that since γ rays are spin-1 bosons, an $E0$ γ-ray transition is forbidden since the γ ray must carry at least one unit of angular momentum. $E0$ transitions do occur, but they must proceed via another decay mode such electron conversion or internal pair production. There are no $M0$ transitions since magnetic monopoles do not exist.

The electromagnetic operator, which is responsible for γ-ray decay, depends on the character of the transition. For electric transitions, the operator is given by [11]

$$O(E\lambda)_\mu = \sum_k e_k r_k^\lambda Y_{\lambda\mu}(\theta_k, \phi_k), \tag{1.22}$$

where the sum is over all A nucleons, e_k is the charge and (r_k, θ_k, ϕ_k) are the coordinates of the kth nucleon, respectively. The $Y_{\lambda\mu}$ are standard spherical harmonics. The magnetic transition operator is given by

$$O(M\lambda)_\mu = \sum_k \left(g_k^{(s)} \mathbf{s}_k + \frac{2g_k^{(l)}}{\lambda + 1} \mathbf{l}_k \right) \cdot \nabla \left[r_k^\lambda Y_{\lambda\mu}(\theta_k, \phi_k) \right] \mu_N, \tag{1.23}$$

where $\mu_N = \frac{e\hbar}{2m_p c} \approx 0.105$ e $\cdot$ fm is the nuclear magneton [11] and e is the fundamental charge. The terms $\mathbf{s}_k$, $g_k^{(s)}$, $\mathbf{l}_k$ and $g_k^{(l)}$ are the spin, spin gyromagnetic ratio (g-factor), orbital angular momentum, and orbital g-factor, respectively. See Sect. 2.3.2 for the origin of these operators.

In Eqs. 1.22 and 1.23, the nucleon charges and g-factors have typical "free-space" values. For neutrons, these are $e_n = 0$, $g_n^{(s)} = -3.826$, and $g_n^{(l)} = 0$, while for protons they are $e_p = 1$, $g_p^{(s)} = 5.586$, and $g_p^{(l)} = 1$ [11]. However, increased effective values can be used which account for model space truncations in a shell model calculation; the particular effective values will depend on the mass region and the severity of the truncation [11].

The transition rate from an initial state $|I_i M_i\rangle$ to a final state$|I_f M_f\rangle$ is given by a sum over all allowed transitions between those two states [34, 11]

$$W_{M_i M_f \mu} = \sum_{C\lambda} \frac{8\pi(\lambda + 1)}{\lambda[(2\lambda + 1)!!]^2 \hbar} \left(\frac{E_\gamma}{\hbar c} \right)^{2\lambda+1} \left| \langle I_f M_f | O(C\lambda)_\mu | I_i M_i \rangle \right|^2, \tag{1.24}$$

where E_γ is the γ-ray energy and c is the speed of light. Usually, M_i, M_f, and μ cannot be observed in experiments. Thus it is useful to average over the initial magnetic substates M_i and sum the contributions of all projections μ to all final substates M_f [11]. This yields

$$W_{if} = \frac{1}{2I_i + 1} \sum_{M_i M_f \mu} W_{M_i M_f \mu} \tag{1.25}$$

$$= \sum_{C\lambda} \frac{8\pi(\lambda + 1)}{\lambda[(2\lambda + 1)!!]^2 \hbar} \left(\frac{E_\gamma}{\hbar c} \right)^{2\lambda+1} \frac{\left| \langle I_f || O(C\lambda) || I_i \rangle \right|^2}{2I_i + 1}, \tag{1.26}$$

where the double-bar notation implies the matrix element has been "reduced" via the Wigner-Eckhart theorem:

$$\langle I_f M_f | \mathcal{O}(C\lambda)_\mu | I_i M_i \rangle = (-1)^{I_f - M_f} \begin{pmatrix} I_f & \lambda & I_i \\ -M_f & \mu & M_i \end{pmatrix} \langle I_f || \mathcal{O}(C\lambda) || I_i \rangle. \tag{1.27}$$

Above, the term in parentheses indicates a Wigner $3j$-symbol. The Wigner-Eckhart theorem separates the M_f, M_i, and μ dependence of the matrix element, and, notably, it implies the total transition rate W_{if} is independent of M_i, M_f, and μ. This is due to the orthogonality relation

$$\sum_{M_i M_f \mu} (-1)^{I_f - M_f} \begin{pmatrix} I_f & \lambda & I_i \\ -M_f & \mu & M_i \end{pmatrix} = 1. \tag{1.28}$$

Eq. 1.26 implies that the lowest allowed multipolarity decay will be dominant. For the same character of decay and a typical γ-ray energy, the lowest allowed multipolarity λ will have a decay rate roughly seven orders of magnitude larger than the next allowed multipolarity $\lambda + 2$. When an initial state can decay to a final state via both transition characters (a mixed transition), it is observed that the lowest multipolarity of each character can have comparable decay rates. Thus it is useful to define a mixing ratio given by [11]

$$\delta^2 \left(\frac{C\lambda + 1}{C'\lambda} \right) = \frac{W_{if}(C\lambda + 1)}{W_{if}(C'\lambda)}, \tag{1.29}$$

where by convention the higher multipolarity is in the numerator.

The total transition rate also determines the lifetime τ of the excited state $|I_i\rangle$, which is related to the sum of total transition rates to all possible final states

$$\frac{1}{\tau} = W_i = \sum_f W_{if}. \tag{1.30}$$

For each possible decay, one can define a partial lifetime $\tau_p = \tau / b$, where b is the branching fraction of the decay.

1.3.1 Reduced Transition Probabilities

The last factor in Eq. 1.26 is defined as the "reduced transition probability" $B(C\lambda; I_i \to I_f)$,

$$B(C\lambda; i \to f) \equiv \frac{\left| \langle I_f || \mathcal{O}(C\lambda) || I_i \rangle \right|^2}{2I_i + 1}. \tag{1.31}$$

As seen, they depend on "off-diagnonal" matrix elements $\langle I_f||O(C\lambda)||I_i\rangle$ and thus describe how strongly two states are connected by a particular transition $C\lambda$ (hence the name). Using Eqs. 1.26 and 1.30, the reduced transition probabilities $B(C\lambda)$ can be related to the partial lifetime of the decay [11].

$$B(E1) = \frac{0.629}{E_\gamma^3 \tau_p}\ e^2\mathrm{fm}^2\mathrm{MeV}^3\mathrm{fs} \tag{1.32}$$

$$B(E2) = \frac{816}{E_\gamma^5 \tau_p}\ e^2\mathrm{fm}^4\mathrm{MeV}^5\mathrm{ps} \tag{1.33}$$

$$B(E3) = \frac{1760}{E_\gamma^7 \tau_p}\ e^2\mathrm{fm}^6\mathrm{MeV}^7\mu\mathrm{s} \tag{1.34}$$

$$B(M1) = \frac{56.8}{E_\gamma^3 \tau_p}\ \mu_N^2\mathrm{MeV}^3\mathrm{fs} \tag{1.35}$$

$$B(M2) = \frac{74.1}{E_\gamma^5 \tau_p}\ \mu_N^2\mathrm{fm}^2\mathrm{MeV}^5\mathrm{ns} \tag{1.36}$$

It is common to express the $B(C\lambda)$ transition strengths in "Weisskopf" units instead of the absolute units given in Eqs. 1.32 to 1.36. Weisskopf units are defined by [11]

$$B_W(E\lambda) = \frac{1}{4\pi}\left(\frac{3}{3+\lambda}\right)^2 \left(1.2A^{1/3}\right)^{2\lambda}\ e^2\mathrm{fm}^{2\lambda}, \tag{1.37}$$

$$B_W(M\lambda) = \frac{10}{\pi}\left(\frac{3}{3+\lambda}\right)^2 \left(1.2A^{1/3}\right)^{2\lambda-2}\ \mu_N^2\mathrm{fm}^{2\lambda-2}. \tag{1.38}$$

Weisskopf units represent an estimate of the transition strength for a single nucleon, and they correct somewhat for the natural dependence of the $B(C\lambda)$ on the mass number.

Reduced transition strengths are excellent indicators of collective vs. single-particle-like behavior. Recalling from section 1.2.2 the emphasis collective models place on *quadrupole* collectivity (quadrupole vibrations, quadrupole deformation), it can perhaps be anticipated that large electric quadruple transition strengths $B(E2)$ provide the most direct indication of collective behavior. The right panel of Fig. 1.9 shows the evolution of $B(E2; 0_1^+ \rightarrow 2_1^+)$ excitation strengths, which are related to transition strengths via

$$B(C\lambda; i \rightarrow f) = \frac{2I_f+1}{2I_i+1} B(C\lambda; f \rightarrow i). \tag{1.39}$$

Thus, $B(E2; 0_1^+ \rightarrow 2_1^+) = 5B(E2; 2_1^+ \rightarrow 0_1^+)$.

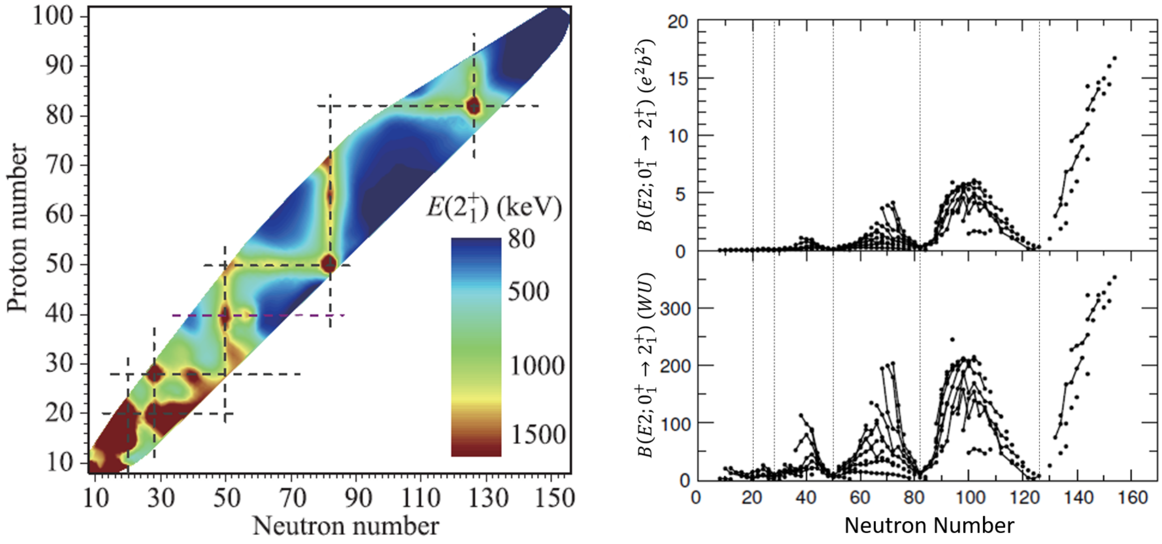

Figure 1.9: The first 2^+ excited state energy for even-even nuclei across the nuclear chart (left), and the $B(E2;0_1^+ \to 2_1^+)$ excitation strength as a function of N for various isotopic chains (right). Dashed lines indicate the magic numbers (excluding 2 and 8). The top right panel gives the $B(E2)$ in absolute units e^2b^2, while the bottom panel uses Weisskopf units. Figures adapted from [30] (left) and [11] (right).

Fig. 1.9, right, shows clearly that the $B(E2)$ are minimized at the magic numbers and maximized far away from them. This indicates again the dominantly collective behavior of non-magic nuclei and the single-particle-like behavior of magic nuclei. The left panel of Fig. 1.9 shows a related signature: the energy of the first 2^+ excited state. Nuclei near closed shells tend to have a high $E(2_1^+)$, while those further away from magic numbers have a low $E(2_1^+)$. The strong correspondence of *high* $E(2_1^+) \leftrightarrow$ *low* $B(E2)$ can be understood qualitatively from Eq. 1.33, which states $B(E2) \propto E_\gamma^{-5}$.

As seen from Figs. 1.8 and 1.9, both rotational-like behavior and $B(E2)$ strengths tend to increase when moving further from the magic numbers. There is a corresponding relation in the rotational model between the quadrupole deformation parameter β_2 and the expected $B(E2)$ value. Assuming both a rigid deformation and that the protons are uniformly distributed over the nuclear volume, this is given by [35]

$$\beta_2 = \frac{4\pi}{3ZeR_o^2}\sqrt{B(E2;0_1^+ \to 2_1^+)}. \tag{1.40}$$

Eq. 1.40 states that $B(E2)$ values are sensitive to the magnitude of deformation. However, transition strengths alone are not sensitive to whether the excited state has prolate, oblate, or triaxial deformation, which is determined by the γ degree of freedom in the rotational model. The quadrupole moment of an excited state, which is proportional to the diagonal $E2$ matrix element $Q_s(I_f) \propto \langle I_f || \mathcal{O}(E2) || I_f \rangle$, determines its specific shape. See Section 2.2.1 for more details on quadrupole moments.

In the triaxial rigid rotor model, Q_s depends on both β_2 and γ. For the first two 2^+ states, this model predicts [29]

$$Q_s(2_1^+) = -\frac{18}{7}\frac{ZeR_o^2}{\sqrt{5\pi}}\frac{\beta_2\cos(3\gamma)}{\sqrt{9-8\sin^2(3\gamma)}} = -Q_s(2_2^+). \tag{1.41}$$

Eq. 1.41 implies that for axially-symmetric rotors ($\gamma = 0, \pi/3$), the magnitude of Q_s is maximized. This leads to the more common relation, by combing Eqs. 1.40 and 1.41, for an axially-symmetric rigid rotor:

$$\left|Q_s(2_1^+)\right| = \frac{2}{7}\sqrt{\frac{16\pi}{5}B(E2;0_1^+ \to 2_1^+)} \quad \text{for } \gamma = 0, \pi/3. \tag{1.42}$$

While $\left|Q_s(2_1^+)\right|$ is maximized for axial symmetry, $Q_s(2_1^+) = 0$ for maximal asymmetry $\gamma = \pi/6$. However, $Q_s(2_1^+) = 0$ also for $\beta_2 = 0$ independent of γ. Because of this, small quadrupole moments can be indicative of either triaxial deformation ($\gamma \approx \pi/6$) or the absence of collective behavior ($\beta_2 \approx 0$).

The preceding sections focused on the properties of excited nuclear states and gave some simple descriptions of the underlying nuclear physics. Nothing has yet been said about any mechanism which actually causes the nucleus to become excited. Spontaneous decay processes, such as α [36] and β [37] decay, often leave the daughter nucleus in an excited state. There are also a myriad number of reactions which can cause a nuclear excitation. The reaction mechanisms can broadly be separated by whether the excitation is caused by a nuclear reaction [38], such as in nucleon knockout [39], or by an electromagnetic interaction, such as in nuclear resonance fluorescence [40] or Coulomb excitation [41]. The various reaction mechanisms carry sensitivity to different nuclear properties; this work is focused on probing collective properties using Coulomb excitation.

CHAPTER 2

COULOMB EXCITATION

The excitation of one nucleus in the electromagnetic field of another nucleus is referred to as Coulomb excitation. Since the interaction is electromagnetic, the excitation depends on the very same set of matrix elements which determine the γ-ray transition rates W introduced in Ch. 1. To first order, the cross section for magnetic excitations are reduced by a factor of β^2 compared to electric excitations, so they are heavily suppressed at the low beam energies discussed in this work [41]. Thus matrix elements of the magnetic operator $O(M\lambda)$ are not needed to describe the excitation process. Magnetic matrix elements do influence the γ-ray decay process, so they are still important for any experimental measurement.

In Coulomb excitation measurements, the experimental conditions are typically chosen such that the electric quadrupole ($E2$) interaction is the dominant excitation mode. In these experiments, the $E2$ operator will primarily mediate the excitation cross section of low-lying positive parity states in the yrast and yrare sequences [41]. Because of this, Coulomb excitation experiments are most commonly used to determine the quadrupole collective properties of nuclei, such as $B(E2)$ transition strengths and spectroscopic quadrupole moments Q_s. Though less common, electric dipole ($E1$) [42] and octupole ($E3$) [43, 44] excitation modes can also be observed in Coulomb excitation.

As an experimental technique, Coulomb excitation is several decades old. The first Coulomb excitation measurements employed a "normal" kinematics reaction scheme, where the nucleus of interest is made into a target which is bombarded by a projectile (the probe). These experiments were performed with beam energies below the Coulomb barrier (Section 2.2), and they were restricted to the study of stable nuclei since unstable nuclei cannot easily be made into targets.

With the advent of rare-isotope beam (RIB) facilities such as RIKEN and NSCL [45], unstable nuclei became available for experimental study. However, the normal kinematics reaction scheme had to be replaced by "inverse" kinematics, a scheme where the projectile is the nucleus of interest.

The most exotic nuclei are created by projectile fragmentation and in-flight separation [46] with energies often exceeding 100 MeV/u, which is always well above the Coulomb barrier. Using Coulomb excitation with such high-energy beams necessitated the more recent development of intermediate-energy Coulomb excitation (Section 2.1).

Irrespective of the beam energy regime, the most basic assumption in Coulomb excitation is that the interaction is purely electromagnetic. This assumption is true if the two colliding nuclei maintain a separation greater than the range of the nuclear force, which ensures the excitation cross section will not have any contribution from the nuclear potential [41]. This enables an interpretation of experimental data that is independent of any model of the nuclear force as the excitation process can be described purely in terms of the well-known electromagnetic interaction.

Systematic experimental studies of Coulomb-nuclear interference effects [47, 48, 49] have shown a conservative estimate of the minimum separation which ensures there is no interaction in the nuclear potential is given by [41]

$$R_{min} = \left[1.25\left(A_P^{1/3} + A_T^{1/3}\right) + 5\right] \text{ fm}, \tag{2.1}$$

where R_{min} is the distance between the centers of the two colliding nuclei and the subscripts P and T refer to the projectile and target, respectively. The expression $1.25A^{1/3}$ is an approximation for the radius of a nucleus; thus the condition given in Eq. 2.1 states that the surfaces of the two nuclei remain at least 5 fm apart. In practice, there are two primary methods for ensuring Eq. 2.1 is satisfied when performing Coulomb excitation experiments.

2.1 Intermediate-Energy Coulomb Excitation

One method to ensure the colliding maintain the minimum separation of Eq. 2.1 is to restrict the scattering angle of the projectile, which is related to the impact parameter b of the reaction via

$$b = \frac{a}{\gamma}\cot\left(\frac{\theta_{CM}}{2}\right), \tag{2.2}$$

$$a = \frac{Z_P Z_T e^2}{m_o c^2 \beta^2}. \tag{2.3}$$

In Eqs. 2.2 and 2.3, a is the half-distance of closest approach, $\gamma = \sqrt{\frac{1}{1-\beta^2}}$ is the Lorentz factor, $\beta = \frac{v}{c}$ is the velocity of the projectile relative to the speed of light, θ_{CM} is the scattering angle in the center-of-mass frame, and m_o is the reduced mass of the system.

Using Eq. 2.2, one can ensure the nuclei maintain the minimum safe separation by restricting θ_{CM}. This is the basis of intermediate-energy Coulomb excitation [50], so-named because the energy of the incoming beam is well above the Coulomb barrier of the projectile-target combination as mentioned earlier. This technique has been used extensively to assess collectivity in a wide array of nuclei [51, 52, 53, 54, 55, 56, 57, 58, 59, 60] at beam energies of several tens to hundreds of MeV/u.

Intermediate-energy Coulomb excitation has many advantages as an experimental technique. The high beam energy increases the Coulomb excitation cross section, and use of thick, high-Z targets can further increase the luminosity; this allows experiments to be performed with very low beam rates, down to a few particles per second. The high beam energy also affects which final states can be populated. Since the interaction time is small, multi-step processes are strongly suppressed, and thus only states which can be reached in a single step from the initial[1] nuclear state will be observed. The data collected from these experiments can be interpreted using the semi-classical theory of relativistic Coulomb excitation developed by Alder and Winther [62], which uses a perturbative treatment of the interaction to relate the observed cross-sections to $B(E2)$ transition strengths.

2.2 Barrier-Energy Coulomb Excitation

Another method to ensure that Eq. 2.1 is satisfied is by limiting the kinetic energy of the projectile E_P such that the minimum safe distance corresponds to the classical turning point of the projectile's trajectory for a head-on collision. This energy, referred to as the "Coulomb barrier" for

---

[1] Usually, the initial state is the nuclear ground state, though it is also possible to induce Coulomb excitation from excited isomeric states [53, 61].

a projectile-target combination, is given by [41]

$$\begin{aligned} E_{CB} &= \frac{e^2}{4\pi\epsilon_0}\frac{A_P + A_T}{A_T}\frac{Z_P Z_T}{R_{min}}, \\ \frac{e^2}{4\pi\epsilon_0} &\approx 1.440\ \text{MeV}\cdot\text{fm}. \end{aligned} \tag{2.4}$$

Experiments which satisfy $E_P \leq E_{CB}$ are referred to as barrier-energy or sub-barrier-energy Coulomb excitation [41]. In these experiments, there is no need to restrict the scattering angle θ_{CM} as is done in intermediate-energy Coulomb excitation.

As mentioned previously, Barrier-energy Coulomb excitation is a traditional experimental method which has long been used to study collectivity in nuclei. Originally, these experiments were performed in normal kinematics. However, the extension of barrier-energy Coulomb excitation to inverse kinematics was enabled by RIB facilities that provide beams at a few MeV/u. The application of inverse-kinematics barrier-energy Coulomb excitation to unstable nuclei greatly increases the experimental understanding possible for these nuclei by both expanding the number excited which can be populated as well as providing sensitivity to quadrupole moments.

Several techniques exist for producing low-energy RIBs. Isotope separation online (ISOL) facilities, such as TRIUMF-ISAC [63] and REX-ISOLDE [64], use a high-intensity proton beam to fragment a heavy production target. The fragmentation products then diffuse out of the target and are ionized and accelerated; this process generally creates a strong chemistry dependence of the available beams. The NSCL utilizes a novel and unique scheme to produce low-energy RIBS by projectile fragmentation followed by in-flight separation, thermalization of the RIB in a gas-cell, and then ionization and re-acceleration. This process is essentially chemistry-independent, and in principle any RIB can be studied if it is produced with sufficient intensity ($\gtrsim 10^3$ pps).

The earliest barrier-energy experiments [65, 66, 67], dating to the 1950's, studied stable nuclei in normal kinematics, and the probes used were light ions such as protons and ^{4}He nuclei. Due to the low-Z of probes, only single-step Coulomb excitation was observed and thus an interpretation based on first-order perturbation theory was adequate [41] to extract the $B(E2)$ transition strengths. Once heavier ions, such as ^{16}O, became available as probes, observation of "multiple" Coulomb

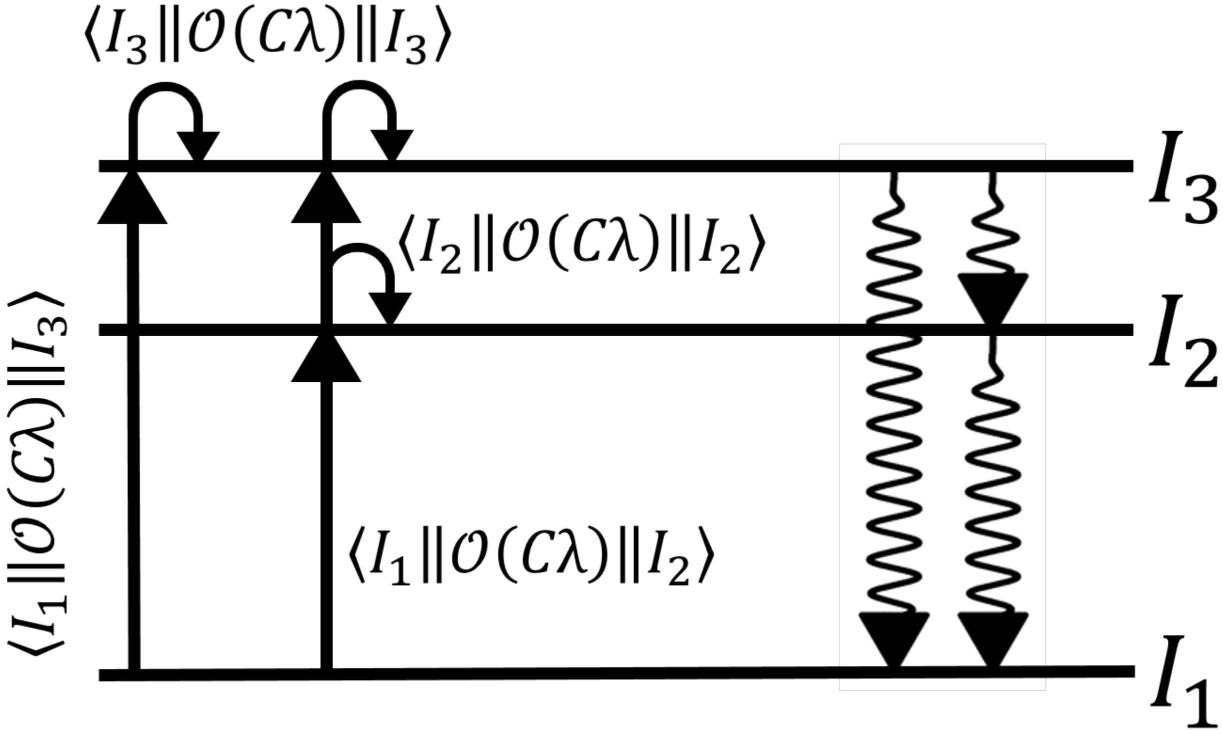

Figure 2.1: A depiction of the multiple excitation paths (left) and decay paths (right) possible in multiple Coulomb excitation experiments. The nuclear matrix elements responsible for a particular excitation are indicated; these same matrix elements determine the γ-ray decay properties.

excitation [68] became possible due to the increased strength of the electromagnetic interaction.

When high-Z probes are used, the lower bombarding energy in barrier-energy Coulomb excitation, which implies a longer interaction time, allows multi-step processes to occur. Multiple Coulomb excitation enables the study of excited nuclear states beyond those which can be reached in a single step from the initial state, and it allows a particular final state to be populated via more than one excitation pathway. This situation is shown schematically in Fig. 2.1.

With the use of the highest-Z probes available, such as ^{208}Pb, states with spins up to $30\hbar$ have been populated via multiple Coulomb excitation in highly deformed nuclei [41]. The excitation of such a large number of excited states provides experimental sensitivity to very many matrix elements; in some cases a complete set of $E2$ matrix elements can be extracted from the low-lying level scheme. Much like intermediate-energy Coulomb excitation, multi-step barrier-energy

Coulomb excitation has been extensively used to determine collective properties in a wide range of nuclei [69, 70, 71, 72, 73, 74, 75, 76, 77, 78, 79].

The presence of multiple Coulomb excitation also complicates somewhat the interpretation of experimental data, as the number of higher-order processes and the large strength of the interaction make a perturbative treatment not viable [80]. Instead, the semi-classical approximation [41, 81, 80, 82] is used to formulate the Schrödinger equation as a set of coupled differential equations (see Section 2.3), and computer codes [83, 84, 85] are used to solve these equations directly via numerical integration.

2.2.1 The Reorientation Effect

One particularly interesting example of multi-step Coulomb excitation is known as the nuclear reorientation effect. As the projectile impinges on the target, both nuclei are subjected to a time-dependent "orientation" energy. This is due to the interaction of their excited-state spectroscopic quadrupole moments $Q_s(I)$ with the strong electric field generated by the collision partner [86]. The orientation energy $E(t)$ is given by

$$E(t) = \frac{ZeQ_s(I)}{r^3(t)} \frac{3M^2 - I(I+1)}{4I(2I-1)}, \tag{2.5}$$

where Q_s, I, and M describe the excited nucleus, Z describes the nucleus in the ground state, and $r(t)$ is the distance between the two nuclei. The spectroscopic quadrupole moment of an excited state is directly related to the diagonal $E2$ matrix element, and it is given by

$$Q_s(I) = \sqrt{\frac{16\pi}{5}} \begin{pmatrix} I & 2 & I \\ -I & 0 & I \end{pmatrix} \langle I||O(E2)||I\rangle. \tag{2.6}$$

While the $B(C\lambda; I_i \to I_f)$, which depend on off-diagonal matrix elements, characterize transitions between two nuclear states I_1 and I_2, quadrupole moments describe transitions between the magnetic substates of a particular excited state I. Thus the reorientation effect is a two-step process in which the intermediate and final states are the same; this is represented by the curved arrows in Fig. 2.1. Spectroscopic quadrupole moments determine the character of the (LAB-frame)

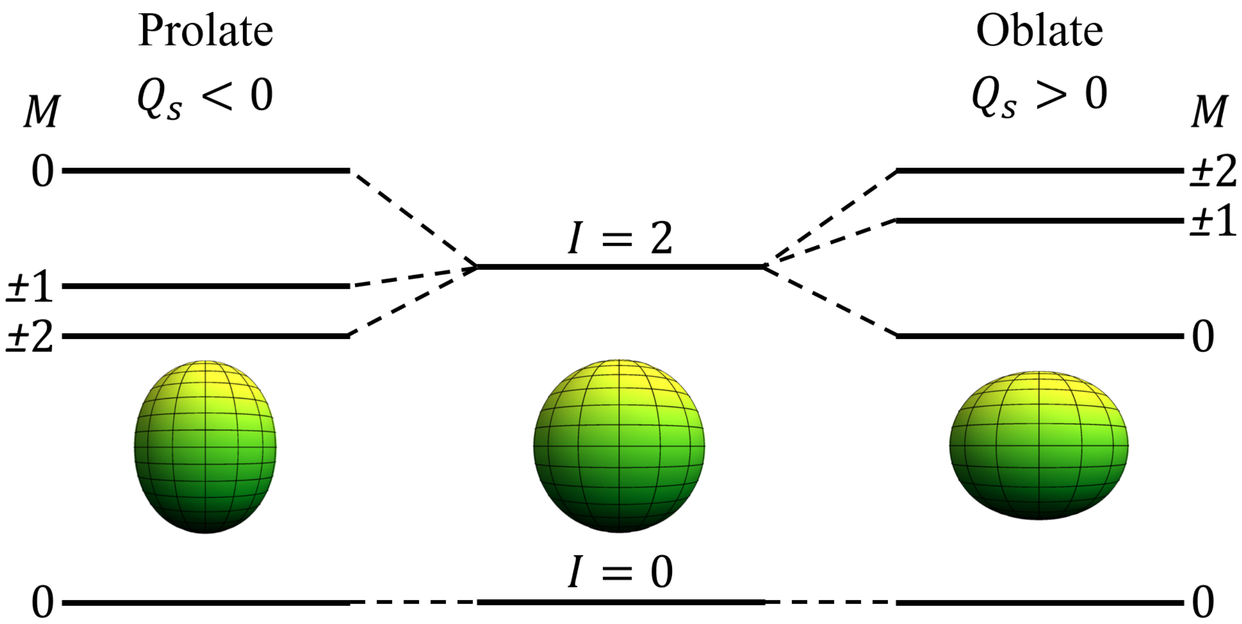

Figure 2.2: The M substate splitting of an $I = 2$ excited state assuming a prolate (left) and oblate (right) shape. The substates are split in opposite directions due to the different sign of Q_s. Contours from [27]

quadrupole deformation of a nuclear state: $Q_s < 0$ implies a prolate deformation, $Q_s > 0$ implies an oblate deformation, and a spherical configuration is indicated by $Q_s = 0$. (This can also be seen from Eq. 1.41 via the γ dependence of Q_s in a rigid-rotor model.)

Critically, the energy given by Eq. 2.5 depends on the spin-projection M of the excited state. This implies the degenerate magnetic substates are split by the presence of an electric field gradient [86]. As can also be seen from Eq. 2.5, the splitting of the M substates depends on both the magnitude and sign of the quadrupole moment. Thus the substates of a prolate excited state will have opposite splitting compared to an oblate state. This is shown in Fig. 2.2.

The probability of Coulomb excitation has a strong dependence on the energy of the excited state. Considering the dominance of the $\Delta M = 0$ excitation path, the substate splitting will also result in a change of the Coulomb excitation cross section. Assuming an $I = 0$ initial state, prolate excited states will have a smaller excitation cross section relative to the spherical case, as the $M = 0$ substate will be raised. Oblate excited states will have an increased cross section, as the $M = 0$ substate is lowered.

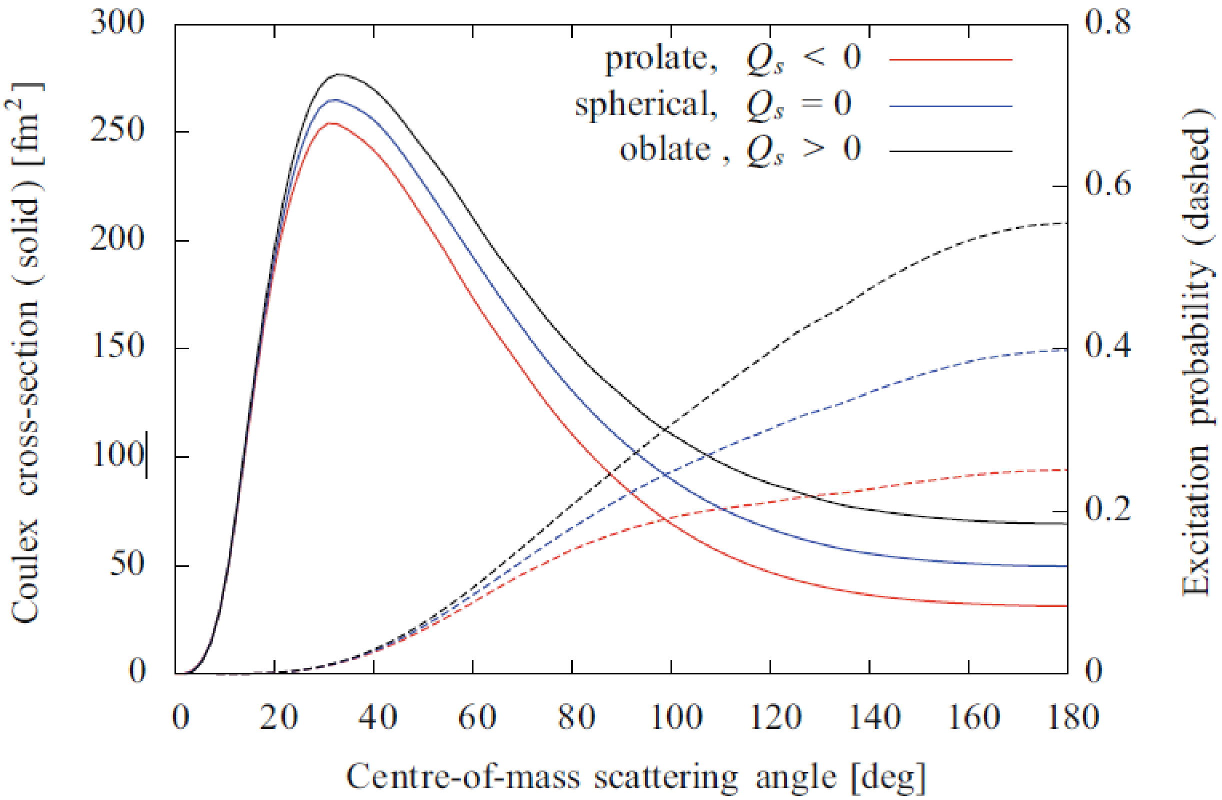

Figure 2.3: Coulomb excitation cross section (solid) and excitation probability (dashed) of an excited 2^+_1 state, as a function of the scattering angle, for different excited state quadrupole moments. The reorientation effect is clear. Note the excitation cross section is given by the product of the excitation probability (dashed lines) with the Rutherford cross section (not shown). Figure taken from [87]; see [87] for details of the calculations.

Further, the size of the splitting depends strongly of the distance between the nuclei through the $1/r^3$ term in Eq. 2.5. The distance bewteen the nuclei is minimized, and thus the splitting is maximized, for large scattering angles (see Eq 2.2). Conversely, the splitting is minimized for small scattering angles. This creates a second-order angular dependence of the excitation cross section due to the quadrupole moment, shown in Fig. 2.3. This is the most prominent experimental signature of the reorientation effect in barrier-energy Coulomb excitation. It can be exploited by measuring the Coulomb excitation cross sections at different scattering angles, which will provide direct sensitivity to the excited state quadrupole moment.

Another experimental signature of the reorientation effect, for example, is a change in the angular distribution of the decay γ rays. This arises because the nuclear alignment induced by

Coulomb excitation depends of population pattern of the M substates, which is changed by the different substate splitting (see Section 2.4.1); this is the basis of the "reorientation-precession" technique for measuring quadrupole moments [86, 88].

2.2.2 Rotational Invariants

As mentioned above, the large number of multi-step processes which can occur in barrier energy Coulomb excitation, including the reorientation effect, provide sensitivity to a very large set of nuclear matrix elements. Quadrupole collectivity produces correlations among these matrix elements, and thus there are generally fewer significant collective degrees of freedom than there are individual matrix elements [41]. It is useful to project the collective degrees of freedom, from both data and theory calculations, to gain further insight over an inspection of the individual matrix elements. This can be accomplished by exploiting the properties of the electromagnetic operators (Eqs. 1.22 and 1.23) [41].

The electromagnetic operators are spherical tensors and as such zero-coupled products can be formed which are invariant under rotations [41, 89]. The electric quadrupole operator $O(E2)_\mu$ can be parametrized in the intrinsic frame as [41]

$$E(2,0) = Q\cos\delta, \tag{2.7}$$

$$E(2,\pm1) = 0, \tag{2.8}$$

$$E(2,\pm2) = \frac{1}{\sqrt{2}}Q\sin\delta. \tag{2.9}$$

The parameters (Q,δ) are analogous to the Bohr parameters (β_2,γ) which describe the radial shape of a quadrupole deformed object as discussed in Section 1.2.2. The geometric interpretation of (Q,δ) is the same as the Bohr parameters, except (Q,δ) describe the quadrupole deformation only of the charge distribution.

Using the general tensor product [11]

$$\left[T^{\lambda_1}\otimes U^{\lambda_2}\right]_{\lambda\mu} = \sum_{\mu_1\mu_2}\langle\lambda_1\mu_1\lambda_2\mu_2|\lambda\mu\rangle T_{\lambda_1\mu_1}U_{\lambda_2\mu_2}, \tag{2.10}$$

the two lowest-order zero-coupled products can be evaluated from Eqs. 2.7 to 2.8 as [90, 41]

$$[E2 \otimes E2]^0 = \frac{1}{\sqrt{5}} Q^2, \tag{2.11}$$

$$\left\{[E2 \otimes E2]^2 \otimes E2\right\}^0 = \frac{\sqrt{2}}{\sqrt{35}} Q^3 \cos(3\delta). \tag{2.12}$$

The expectation value of these invariant products for a state $|s\rangle$ can be evaluated in the LAB-frame using an intermediate state expansion, yielding [90]

$$\langle Q^2 \rangle = \sqrt{5} \frac{(-1)^{2I_s}}{\sqrt{2I_s + 1}} \sum_r M_{sr} M_{rs} \begin{Bmatrix} 2 & 2 & 0 \\ I_s & I_s & I_r \end{Bmatrix}, \tag{2.13}$$

$$\langle Q^3 \cos(3\delta) \rangle = \frac{\sqrt{35}}{\sqrt{2}} \frac{(-1)^{2I_s+1}}{2I_s + 1} \sum_{tu} M_{su} M_{ut} M_{ts} \begin{Bmatrix} 2 & 2 & 2 \\ I_s & I_t & I_u \end{Bmatrix}. \tag{2.14}$$

Above, the shorthand notation $M_{sr} = \langle s || \mathcal{O}(E2) || r \rangle$ has been employed, and the curly brackets denote a Wigner $6j$-symbol. Only these two lowest-order products will be presented here. See, for example, Refs [41, 89, 90, 91] for expressions of higher-order invariant products.

The invariant sums given above are completely model-independent results which assume only the spherical tensor nature of the $E2$ operator. They provide sensitivity to the intrinsic quadrupole deformation of a nuclear state from a set of measured $E2$ matrix elements and provide model-independent evidence for intrinsic prolate, oblate, or triaxial shapes. Higher-order invariants can be formed which relate to the statistical dispersion of the centroids given by Eqs. 2.13 and 2.14; these determine whether the deformation is of a rigid or soft nature (see, for example, Refs. [72, 92]). Note that the triaxial rotor model, for instance, assumes a rigid deformation [29].

The number of matrix elements necessary for an accurate evaluation of the of summations increases rapidly with the complexity of the invariant product [41, 91]. In well deformed nuclei, the ground-state deformation is generally dominated by the $\langle 0^+_1 || \mathcal{O}(E2) || 2^+_1 \rangle$ matrix element, and thus the centroids of ground-state deformation parameters can often be extracted from moderate-statistics Coulomb excitation experiments [74]. However, the affects of truncation should generally be investigated when evaluating the invariant sums from experimental data. See Ref. [91] for a general discussion of convergence of the quadrupole sums for nuclei in the $20 \le A \le 52$ mass range.

2.3 Semi-Classical Theory

In the semi-classical description of sub-barrier Coulomb excitation, the relative motion of the colliding nuclei, which is governed by the monopole-monopole part of the Coulomb potential, is assumed to follow a classical hyperbolic trajectory [81]. This is well justified if the parameter η, defined as the ratio of the half-distance of closest approach a to the wavelength of relative motion $\lambdabar$, is much larger than unity, i.e [82]

$$\eta \equiv \frac{a}{\lambdabar} = \frac{Z_P Z_T e^2}{\hbar c \beta} \gg 1. \tag{2.15}$$

Note the condition $\eta \gg 1$ is closely related to the requirement of a sub-barrier beam energy $E_P \leq E_{CB}$. For sub-barrier Coulomb excitation of heavy-ions ($Z > 10$), $10 < \eta < 1000$ and thus $\eta \gg 1$ is easily fulfilled.

For the assumption of classical hyperbolic orbit to be valid, any nuclear excitations which occur during the reaction must not distort the orbit. This is true if [82]

$$\Delta E_n / E_P \ll 1, \tag{2.16}$$

where ΔE_n is the energy difference between the excited nuclear state $|n\rangle$ and the initial state. In typical heavy-ion Coulomb excitation, E_P is a few hundred MeV, while the excited states populated are typically located no higher than a few MeV in excitation energy.

Under the above assumptions of Eqs. 2.15 and 2.16, the differential cross-section for the Coulomb excitation of state $|n\rangle$ takes an especially simple form [82]:

$$\left(\frac{d\sigma}{d\Omega}\right)_n = P_n \left(\frac{d\sigma}{d\Omega}\right)_R \tag{2.17}$$

$$\left(\frac{d\sigma}{d\Omega}\right)_R = \frac{a^2}{4 \sin^4 (\theta_{CM}/2)}, \tag{2.18}$$

where P_n is the probability of exciting the state $|n\rangle$ and $\left(\frac{d\sigma}{d\Omega}\right)_R$ is the Rutherford scattering cross-section.

2.3.1 Coupled Differential Equations

Using the semi-classical approximation, the time-dependent Schrödinger equation can be written in the following form [82]

$$i\hbar\frac{\partial}{\partial t}|\psi(t)\rangle = [H_0 + V(t)]\,|\psi(t)\rangle, \tag{2.19}$$

where $|\psi(t)\rangle$ is the wave-function of the excited nucleus (target or projectile), H_0 is the free intrinsic nuclear Hamiltonian, and $V(t)$ is the interaction between the monopole (unexcited) and multipole (excited) moments of the colliding nuclei. Thus excitations in the target and projectile can be considered independently, each governed by Eq. 2.19. There is in principle a mulitpole-multipole interaction which does not allow such a separation; this interaction is negligibly small and can be ignored [82]. Note the monopole-monopole interaction, which cannot cause a nuclear excitation, is accounted for when determining the classical trajectory of the reaction described in Sect. 2.3.3.

Expanding the time-dependent wave-function in terms of the eigenstates of H_0,

$$\begin{aligned} |\psi(t)\rangle &= \sum_n a_n(t)|n\rangle \\ H_0|n\rangle &= E_n|n\rangle \\ a_n(t) &= \langle n|\psi\rangle \exp\left[iE_nt/\hbar\right], \end{aligned} \tag{2.20}$$

one can exploit the orthonormality of the eigenstates, $\langle n|k\rangle = \delta_{nk}$, and write the Schrödinger equation as a set of coupled differential equations

$$i\hbar\frac{d}{dt}a_n(t) = \sum_m \langle n|V(t)|m\rangle \exp\left[i\left(E_n - E_m\right)t/\hbar\right] a_m(t). \tag{2.21}$$

The coupled differential equations in Eq 2.21 define the expansion coefficients (or excitation amplitudes) $a_n(t)$, and they can be solved assuming the nucleus is in a particular initial state $|k\rangle$ before the collision, i.e $a_n(-\infty) = \delta_{kn}$. The amplitudes after the collision determine the probability P_n of exciting the state $|n\rangle$ via [82]

$$\begin{aligned} P_n &= a_n a_n^* \\ a_n &\equiv a_n(\infty). \end{aligned} \tag{2.22}$$

2.3.2 The Electromagnetic Interaction

To solve the differential equations 2.21, the electromagnetic interaction is written as an expansion of multipole moments [82]:

$$V(t) = \sum_{\lambda=1}^{\infty} \sum_{\mu=-\lambda}^{\lambda} \frac{4\pi Ze}{2\lambda+1} (-1)^{\mu} S_{C\lambda\mu}(t) \mathcal{M}(C\lambda, -\mu), \tag{2.23}$$

where Z is the proton number of the unexcited nucleus. The functions $S_{C\lambda\mu}(t)$ depend on the character of the excitation. For electric excitations,

$$S_{E\lambda\mu}(t) = \frac{Y_{\lambda\mu}\left(\theta_P(t), \phi_P(t)\right)}{\left[r_P(t)\right]^{\lambda+1}}, \tag{2.24}$$

and for magnetic excitations,

$$S_{M\lambda\mu}(t) = \frac{1}{c\lambda} \frac{d\mathbf{r}_P(t)}{dt} \frac{\left(\mathbf{r}_P(t) \times \nabla\right)}{\left[r_P(t)\right]^{\lambda+1}} Y_{\lambda\mu}\left(\theta_P(t), \phi_P(t)\right). \tag{2.25}$$

In Eqs. 2.24 and 2.25, the coordinates $\mathbf{r}_P(t) = (r_P(t), \theta_P(t), \phi_P(t))$ are the time-dependent spherical coordinates of the projectile in any frame of reference with the origin at the center-of-mass of the target.

In Eq. 2.23, $\mathcal{M}(C\lambda, \mu)$ is an electromagnetic multipole moment of the excited nucleus. For electric moments,

$$\mathcal{M}(E\lambda, \mu) = \int \rho(\mathbf{r}) r^{\lambda} Y_{\lambda\mu}(\mathbf{r}) d\tau, \tag{2.26}$$

while for magnetic moments,

$$\mathcal{M}(M\lambda, \mu) = \frac{1}{c(\lambda+1)} \int \mathbf{j}(\mathbf{r}) r^{\lambda} \left(\mathbf{r} \times \nabla\right) Y_{\lambda\mu}(\mathbf{r}) d\tau. \tag{2.27}$$

The quantities $\rho(\mathbf{r})$ and $\mathbf{j}(\mathbf{r})$ are the nuclear charge and current densities, respectively, and the integration is performed over the coordinates $\mathbf{r}$ measured with respect to the center-of-mass of the excited nucleus.

Assuming the nucleus can be described as point-charge nucleons which generate a convection current plus a magnetization current due to the dipole moments of individual nucleons [81], the charge and current densities can be written as

$$\rho(\mathbf{r}) = \sum_k e_k \delta(\mathbf{r} - \mathbf{r}_k) \tag{2.28}$$

$$\mathbf{j}(\mathbf{r}) = \sum_k e_k \left[\mathbf{v}_k \delta(\mathbf{r} - \mathbf{r}_k)\right]_{\mathrm{sym}} + c g_k^{(s)} \left(\nabla \times \mathbf{s}_k\right) \delta(\mathbf{r} - \mathbf{r}_k) \mu_N. \tag{2.29}$$

Here, $\mathbf{v}_k$ is the velocity, and the subscript "sym" denotes symmetrization of the factors in the brackets [81]. Using the forms of $\rho(\mathbf{r})$ and $\mathbf{j}(\mathbf{r})$ given above, the multipole moments of Eqs. 2.26 and 2.27 can be evaluated [81], and one finds

$$\mathcal{M}(C\lambda, \mu) = \mathcal{O}(C\lambda)_\mu. \tag{2.30}$$

Thus, Eqs. 2.26 to 2.29 are the origin of the electromagnetic transition operators $\mathcal{O}(C\lambda)_\mu$ introduced in Ch. 1.

2.3.3 Orbital Motion

The functions $S_{C\lambda\mu}(t)$ depend on time implicitly through the coordinates $\mathbf{r}_P(t)$ of the projectile, which is assumed to following the classical hyperbolic orbit. This orbit, along with a convenient coordinate system for evaluation of the $S_{C\lambda\mu}(t)$, is shown in Fig. 2.4. The hyperbolic orbit can described by the dimensionless parameters ϵ and ω, defined by

$$\begin{aligned} \epsilon &= \frac{1}{\sin(\vartheta/2)} \\ t &= \frac{a}{v}\left[\epsilon \sinh(\omega) + \omega\right], \end{aligned} \tag{2.31}$$

where v is the initial velocity of the projectile. The parameter ϵ is the orbit eccentricity, and ω is a dimensionless time.

With this parametrization, the Cartesian and spherical coordinates are given explicitly by

$$\begin{aligned} x &= 0, & r &= a\left[\epsilon \cosh(\omega) + 1\right], \\ y &= a\sqrt{\epsilon^2 - 1}\sinh(\omega), & \sin\theta &= \frac{\sqrt{\epsilon^2 - 1}\sinh(\omega)}{\epsilon \cosh(\omega) + 1}, \\ z &= a\left[\cosh(\omega) + \epsilon\right], & \phi &= \pi/2, \end{aligned} \tag{2.32}$$

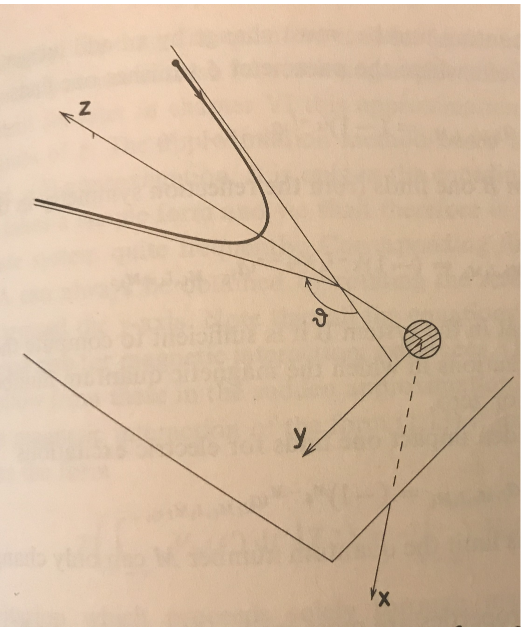

Figure 2.4: Coordinate system "B" from [82] used to evaluate the excitation amplitudes. The positive z-axis bisects the asymptotic velocities of the projectile, the x-axis is perpendicular to the plane of orbit, and the y-axis is chosen such that the y-component of the projectile's velocity is positive. The scattering angle ϑ is indicated. Figure from [82].

and the functions $S_{C\lambda\mu}(t)$ are now replaced by dimensionless "collision" functions $Q_{C\lambda\mu}(\epsilon,\omega)$ [82, 90] given by

$$Q_{C\lambda\mu}(\epsilon,\omega) = a^{\lambda}\frac{(2\lambda-1)!!}{(\lambda-1)!}\sqrt{\frac{\pi}{2\lambda+1}}\frac{r(\omega)}{f_C}S_{C\lambda\mu}(t(\omega)) \tag{2.33}$$

where $f_M = \beta$ and $f_E = 1$.

Labeling the nuclear states by both their spin I and spin-projection M, i.e. $|k\rangle = |I_kM_k\rangle$, the coupled differential equations 2.21 can now be written explicitly as

$$\frac{d}{d\omega}a_{I_nM_n}(\omega) = -4i\sqrt{\pi}\frac{Ze}{\hbar v}\sum_{\substack{C\lambda\mu\\ I_mM_m}} f_C Q_{C\lambda\mu}(\epsilon,\omega)\frac{\sqrt{2\lambda+1}(\lambda-1)!}{a^{\lambda}(2\lambda+1)!!}\exp\left\{i\xi_{nm}\left[\epsilon\sinh(\omega)+\omega\right]\right\}$$

$$(-1)^{I_m-M_m}\begin{pmatrix} I_m & \lambda & I_n\\ -M_m & \mu & M_n\end{pmatrix}\langle I_m||\mathcal{O}(C\lambda)||I_n\rangle a_{I_mM_m}(\omega), \tag{2.34}$$

where $\xi_{nm} = \frac{a}{\hbar v}\left(E_n - E_m\right)$ is measure of the adiabacity of the reaction. It can be seen here clearly why magnetic excitations are negligible. The factor f_C introduces a factor of β to the differential amplitudes of magnetic excitation which is not present for electric excitation. To first order, this reduces the magnetic excitation probability by a factor of β^2, and in sub-barrier Coulomb excitation $\beta^2 \lesssim 0.003$, typically.

2.4 Gamma Decay

The rate of γ-ray decay of a nuclear state is given in Ch. 1 by Eq. 1.30. Excited states which only decay via an electromagnetic transition typically have lifetimes approximately 10^8 times longer than the Coulomb excitation process [90]. This enables a treatment of the γ-ray decay process which is independent of the Coulomb excitation process [82].

2.4.1 Nuclear Alignment

Coulomb excitation introduces a preferential alignment of the excited nuclear state [82]. This alignment can be expressed in terms of the statistical tensor $\rho_{k\kappa}$ [93, 82] as

$$\rho_{k\kappa}(I) = \frac{\sqrt{2I+1}}{2I_o+1} \sum_{M_o M M'} (-1)^{I-M'} \begin{pmatrix} I & k & I \\ -M' & \kappa & M \end{pmatrix} a^*_{IM'}(I_o M_o) a_{IM}(I_o M_o), \tag{2.35}$$

where I_o is the spin of the initial state. It is noted that Eq. 2.35 is written in very general form; it is valid irrespective of how the excitation amplitudes a are evaluated (via numerical integration, perturbation theory, etc.).

The nuclear alignment implies that the angular distribution of decay γ rays will not be isotropic. Assuming a state I_1 decays to state I_2 via transitions of multipolarities λ and λ', the probability $P(\mathbf{k})$ of γ-ray emission in the direction $\mathbf{k}$ is given by [82]

$$P(\mathbf{k}) = \frac{d\Omega}{4\pi W_1} \sum_{\substack{k \text{ even} \\ \kappa\lambda\lambda'}} \sqrt{2k+1}\,\delta_{C\lambda}\delta^*_{C\lambda'} F_k(\lambda\lambda' I_2 I_1) \frac{\rho_{k\kappa}(I_1)}{\rho_{00}(I_1)} D^{k*}_{\kappa 0}(\mathbf{z} \to \mathbf{k}), \tag{2.36}$$

where W_1 is given by Eq. 1.30 and the $D^k_{\kappa\kappa'}(\mathbf{z} \to \mathbf{k})$ are Wigner rotation functions which describe a rotation of the *LAB* system such that its z-axis points along the direction $\mathbf{k}$. The "transition amplitude" $\delta_{C\lambda}$ is given by

$$\delta_{C\lambda} = i^{s(C\lambda)} \sqrt{\frac{8\pi(\lambda+1)}{\lambda[(2\lambda+1)!!]^2\hbar} \left(\frac{E_\gamma}{\hbar c}\right)^{2\lambda+1}} \frac{\langle I_f || O(C\lambda) || I_i \rangle}{\sqrt{2I_i+1}}, \tag{2.37}$$

where $s(E\lambda) = \lambda$ and $s(M\lambda) = \lambda + 1$. It is noted an equivalent definition of the transition rate (Eq. 1.26) is given by

$$W_{if} = \sum_{C\lambda} (-1)^{s(C\lambda)+1} |\delta_{C\lambda}|^2. \tag{2.38}$$

The angular correlation functions $F_k(\lambda\lambda' I_2 I_1)$ are given by [94, 82]

$$F_k(\lambda\lambda' I_2 I_1) = (-1)^{I_1+I_2-1}\sqrt{(2k+1)(2I_1+1)(2\lambda+1)(2\lambda'+1)} \begin{pmatrix} \lambda & \lambda' & k \\ 1 & -1 & 0 \end{pmatrix} \begin{Bmatrix} \lambda & \lambda' & k \\ I_1 & I_1 & I_2 \end{Bmatrix}. \tag{2.39}$$

The F_k functions are typically called γ-γ correlation functions, though here they are used to describe the angular distribution of only a single γ ray. This is because the alignment induced by the Coulomb excitation process is quite similar to the alignment induced by γ-ray decay [81]. It is noted that an isotropic distribution can be generated by setting $\rho_{k\kappa} = \delta_{k0}\delta_{\kappa 0}$.

If one chooses to evaluate the excitation amplitudes such that they can be expressed in a closed form, for example with perturbation theory, the statistical tensor (Eq 2.35) and angular distribution (Eq. 2.36) can be written as explicit functions. This allows the total γ-ray angular distribution $W(\theta_\gamma)$, integrated over the particle scattering angle, to be written in the more familiar form:

$$W(\theta_\gamma) = \sum_k a_k P_k(\cos(\theta_\gamma)), \tag{2.40}$$

where the P_k are Legendre polynomials. The coefficients a_k have been evaluated via perturbation theory to first and second order, as well as by a quantum-mechanical treatment, in Ref. [81].

The nuclear alignment induced by Coulomb excitation can be significantly attenuated by experimental effects. In many Coulomb excitation experiments, both the scattered projectile and recoiling target will be left in highly ionized, highly-excited atomic configurations after the collision [95]. If the ions emerge from the target into a vacuum, these excited electronic configurations will relax to the atomic ground state on a timescale similar to the lifetime of the excited nuclear states; this process produces rapidly fluctuating hyperfine magnetic fields which will be felt by the nucleus prior to γ-ray decay.

The magnetic dipole moment of the excited state will couple to the hyperfine magnetic fields, which are of order 10^4 Tesla. This interaction attenuates the nuclear alignment and is thus referred to as the "deorientation" effect. Do to the complexity of the fluctuating hyperfine fields, a simplified two-state model is often used to account for this effect [95, 96] by introducing attenuation coefficients G_k which modify the statistical tensor:

$$\rho_{k\kappa} \to G_k \rho_{k\kappa}. \tag{2.41}$$

The two-state model has several adjustable parameters, and default values have been obtained from fits to deorientation effect data from a range of nuclei [90, 97] which account for this affect quite well [41].

2.4.2 Angular Correlations

The statistical tensor $\rho_{k\kappa}$ also provides a natural framework for describing the typical angular correlations observed in a γ-ray cascade. After the decay of state I_1, described by $\rho_{k_1\kappa_1}$, to the state I_2, the alignment of state I_2 is given by [82]

$$\rho_{k_2\kappa_2}(I_2)\frac{d\Omega}{4\pi W_1} = \sum_{\substack{k \text{ even} \\ \kappa\lambda\lambda' k_1\kappa_1}} (-1)^{k_1+\kappa_1}\sqrt{\frac{(2k+1)(2k_1+1)}{2k_2+1}} \begin{pmatrix} k_1 & k & k_2 \\ -\kappa_1 & \kappa & \kappa_2 \end{pmatrix}$$
$$\delta_{C\lambda}\delta^*_{C\lambda'} F_k^{k_2 k_1}(\lambda\lambda' I_2 I_1)\frac{\rho_{k_1\kappa_1}(I_1)}{\rho_{00}(I_1)} D^{k*}_{\kappa 0}(\mathbf{z} \to \mathbf{k}). \tag{2.42}$$

The triple correlation coefficient $F_k^{k_2 k_1}$ is given by [82].

$$F_k^{k_2 k_1}(\lambda\lambda' I_2 I_1) = (-1)^{\lambda'+k_2+k_1+1}\sqrt{(2I_1+1)(2I_2+1)}$$
$$\sqrt{(2\lambda+1)(2\lambda'+1)(2k+1)(2k_1+1)(2k_2+1)} \begin{pmatrix} \lambda & \lambda' & k \\ 1 & -1 & 0 \end{pmatrix} \begin{Bmatrix} I_2 & \lambda & I_1 \\ I_2 & \lambda' & I_1 \\ k_2 & k & k_1 \end{Bmatrix}, \tag{2.43}$$

where the factor in curly brackets is a Wigner $9j$-symbol.

If the initial alignment is known, Eqs. 2.36 and 2.42 enable the calculation of both the initial γ-ray angular distribution and the subsequent γ-γ angular correlations for an arbitrarily long γ-ray cascade. The initial angular distribution is given by Eq. 2.36, the statistical tensor is then "updated" by Eq. 2.42, and the subsequent angular distribution can be generated again from Eq. 2.36 using the updated statistical tensor.

2.5 The GOSIA Code

In principle, the network of coupled differential equations (Eq. 2.34) should include all excited states, and determining the final excitation amplitudes would involve an integration of all channels over the full range of the classical hyperbolic orbit, i.e. over $-\infty < \omega < \infty$. In practice, only a subset of excited states can be considered, and the integration is performed only over a finite range of ω which can be determined by the desired accuracy [90]. Multiple computer codes have been developed for this task [84, 83, 85]; they allow, for a given set of matrix elements, a quantitative calculation of multi-step Coulomb excitation probabilities for specified experimental conditions, such as the bombarding energy and projectile scattering angle. The most commonly used code is GOSIA [90, 83].

GOSIA was designed in 1980 to facilitate the extraction of electromagnetic matrix elements from data collected during barrier-energy multi-step Coulomb excitation experiments. Typically, the primary observables from these experiments are γ-ray yields as a function of scattering angle. Because of this, evaluation of the excitation probabilities is not the only functionality of GOSIA; it subsequently calculates the γ-ray decays which will result from the excited state population distribution. The γ-ray yield calculations in GOSIA account for several effects, such as [90, 87]: γ-ray angular distributions including the effects of deorientation, γ-γ angular correlations, a relativistic transformation to a common reference frame, and integration over the γ-ray detector geometry.

The yield calculations are performed for a specific bombarding energy and scattering angle, while experimental data is collected over a range of energy and angle. GOSIA accounts for this by performing the "point" calculations at user-defined energy and angle mesh points, and then the resulting surface is integrated to obtain final yields. These integrated yields can be compared

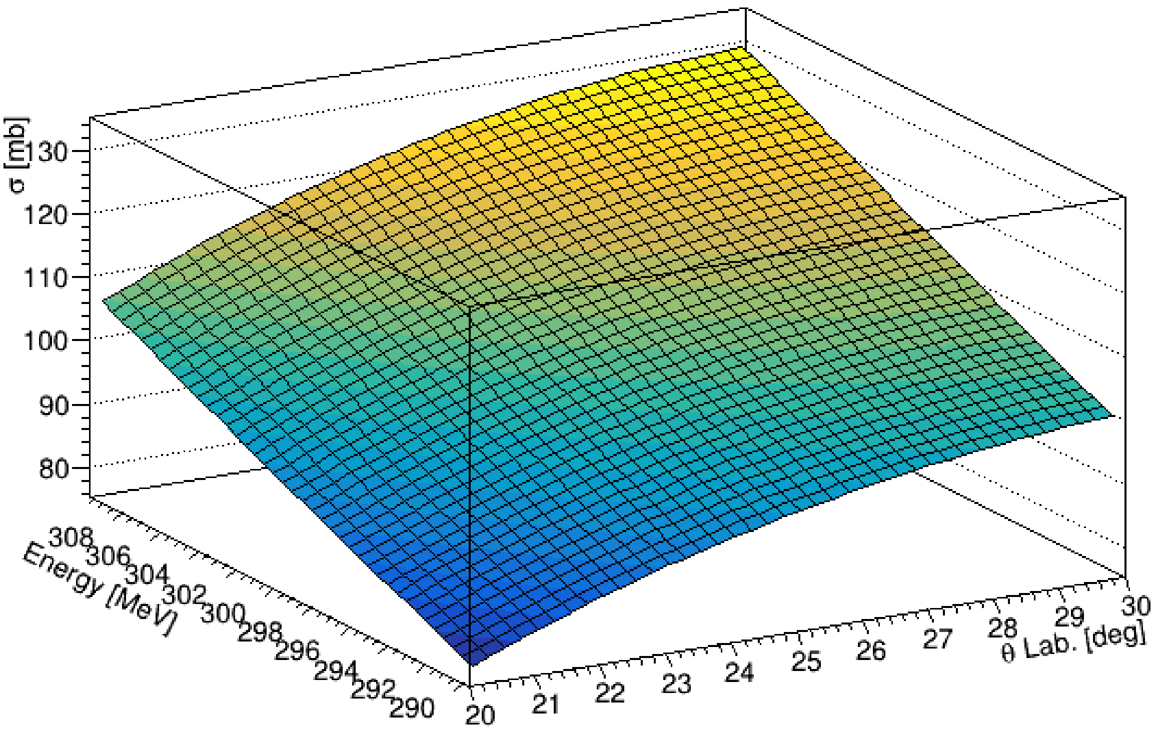

Figure 2.5: Dependence of the Coulomb excitation cross section on the bombarding energy and scattering angle for an excited 2_1^+ state. GOSIA integrates this surface to obtain γ-ray yields which can be compared directly to experimental data. Figure from Ref. [85].

directly to experimental data. An example of the energy and angle dependence of Coulomb excitation is shown in Fig. 2.5

The comparison of calculated and experimental yields provides sensitivity to the nuclear matrix elements, which govern both the excitation and decay processes. This comparison is the primary functionality of GOSIA. Using the nuclear matrix elements as parameters, GOSIA employs a least-squares search routine to find the set of matrix elements which best describe the data. A χ^2-like statistic is constructed (partially) from the agreement of calculated and experimental yields at each point in the multi-dimensional parameter space, driving the minimization.

GOSIA can consider up to 999 electric ($\lambda \leq 6$) and magnetic ($\lambda \leq 2$) matrix elements which connect up to 99 nuclear states and has been optimized to perform such high-dimensional χ^2 searches [90]. Many fast, analytical approximations are used during the search routine to make the large number of Coulomb excitation calculations feasible. To help constrain the search, GOSIA can incorporate previous experimental results, including uncertainties, for lifetimes, branching ratios, mixing ratios, and the matrix elements themselves. Agreement with these constraints is incorporated directly into the χ^2 statistic and thus they are treated on an equivalent footing as the γ-ray yields.

After convergence of the minimization, a final GOSIA calculation can be run to estimate the statistical uncertainties for the extracted matrix elements. This cannot be accomplished in the typical manner by requesting a $\chi_{\text{min}} + 1$ increase [90]. Instead, GOSIA defines a differential probability function dP for each parameter, and then it determines the integration range for which the integrated probability is 68.3% of the integral over the entire parameter range. This can be expresssed as

$$\frac{\int_{x_o}^{x_o+\delta x} \frac{dP(x)}{dx} dx}{\int_{x_o}^{x_{\text{max}}} \frac{dP(x)}{dx} dx} = 0.683, \tag{2.44}$$

where x is the investigated parameter with a best-fit value of x_o, δx is the diagonal upper error bar, and x_{max} is the user-defined upper limit. GOSIA performs this search independently in each direction, which in general will result in asymmetric error bars.

The error estimation procedure is divided into two steps, both of which use a 68.3% integrated probability requirement [90, 87]. First, the parameters are sampled individually while all others are kept fixed. This results in the "diagonal" uncertainty δx. In the second step, correlations with the other parameters are accounted for. This done with a very similar integration procedure, except in this step all parameters are varied along an estimated path of maximum correlation. This correlation path is approximated as a straight line in the parameter space, and it is found by performing a one-step minimization of all *other* parameters while the investigated parameter is fixed at $x_o + \delta x$ [90].

The outcome of a GOSIA analysis is a set of reduced matrix elements of the electromagnetic operators that best describe the experimental data, i.e. the measured γ-ray yields as a function of scattering angle. The sensitivity to the $E\lambda$ matrix elements arises from both the Coulomb excitation and γ-ray decay processes, while sensitivity to $M\lambda$ matrix elements can be gained through the γ-ray decay process, particularly if decay branching ratios or mixing ratios are known.

The estimated uncertainties, which include correlations among the matrix elements, represent the statistical precision of the measurement. Thus it is generally necessary to consider systematic uncertainties in addition to the statistical uncertainties estimated by GOSIA.

CHAPTER 3

EXPERIMENTAL SETUP

In typical Coulomb excitation experiments, a beam of nuclei is accelerated to a desired energy and impinged upon a stationary reaction target, which is surround by radiation detectors. During the collision, either the projectile or the target can be Coulomb excited; if the projectile is the nucleus-of-interest, the experiment is in inverse kinematics. After Coulomb excitation, the nucleus will be in an excited state which promptly decays via γ-ray emission[1]. Detection of the de-excitation γ rays enables the determination of which excited states were populated[2], and detection of either the scattered projectile or the recoiling target can determine the reaction kinematics.

The Joint Array for Nuclear Structure (JANUS) [100] was designed specifically for inverse-kinematics sub-barrier Coulomb excitation experiments performed at the ReAccelerator facility (ReA3) [101] at the National Superconducting Cyclotron Laboratory (NSCL) [45]. The commissioning experiment was performed in January 2017 [100], and several more experiments have been performed successfully since [102, 74, 103], including the first Coulomb excitation experiment of a rare isotope at ReA3 [102].

JANUS is comprised of two primary components. It combines the Segmented Germanium Array (SeGA) [104] for γ-ray detection with two highly segmented silicon semiconductor detectors for detection of the heavy charged particles (scattered projectiles and recoiling target). The simultaneous detection of γ-rays and charged particles, enabled by these two detection systems, allows for a complete characterization of the Coulomb excitation process. A cartoon schematic of JANUS is shown in Fig. 3.1.

---

[1] There are other decays modes, such as the emission of a conversion electron, which must be accounted for when interpreting Coulomb excitation data.

[2] In experiments with light ions, it is possible to discriminate excited states using particle spectroscopy [98, 99]

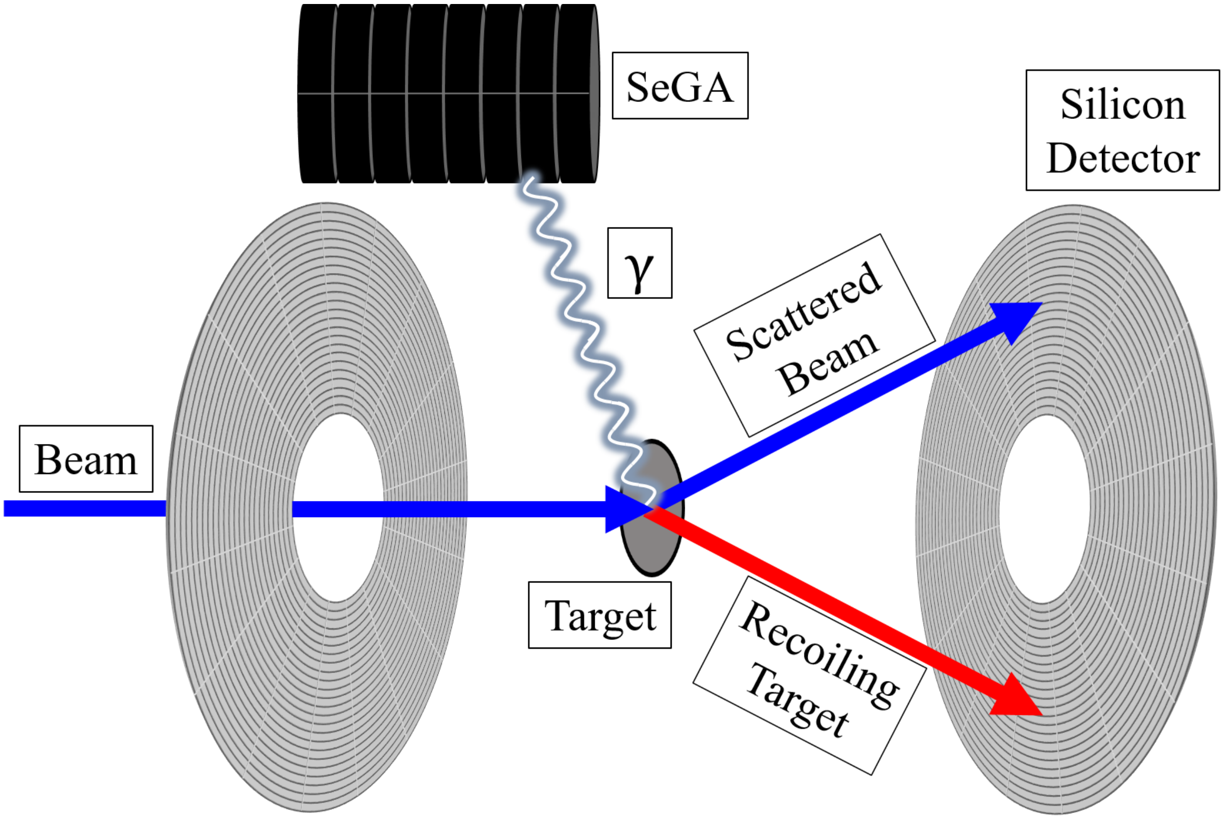

Figure 3.1: A cartoon schematic showing the layout of JANUS. Figure adapted from [105].

3.1 Charged Particle Detection

3.1.1 Detection Principles

As a heavy charged particle moves through matter, it will undergo inelastic collisions with atomic electrons[3] in the material [106]. These collisions transfer energy to the electrons from the heavy particle, slowing it down. Depending on the amount of energy transferred, atoms in the material can either be excited, where the electron is promoted to a higher orbit but is still bound to the atom, or ionized, where the electron is removed from the atom.

The cross section for the atomic collisions are quite high, so very many collisions will occur over a short distance, and each collision removes only a small portion of the heavy particle's energy. This

---

[3] It is also possible for the particle to interact with nuclei in the material; this is rare and not generally relevant for detection of charged particles.

makes it unnecessary to consider the collisions individually. Instead, they are treated as a single, continuous process which is characterized by the "stopping power" of the material [106, 107]. This is given by the Bethe-Bloch formula as

$$\frac{dE}{dx} = -2\pi N_A r_e^2 m_e c^2 \rho \frac{zZ^2}{A\beta^2} \ln\left(\frac{2m_e \gamma^2 v^2 W_{\max}}{I^2} - 2\beta^2\right), \tag{3.1}$$

where N_A is Avagadro's number, r_e is the classical electron radius, m_e is the electron mass, ρ, z, and A are the density, proton number, and mass number of the material, respectively, Z and v are the proton number and velocity of the incident heavy particle, and $\beta = v/c$. $W_{\max}$ is the maximum energy transfer to an electron, and I is the mean excitation potential of the material, which is generally found experimentally.

The important feature of Eq. 3.1 is its dependence on z, Z^2, and $1/\beta^2$. First, an incident particle will lose more energy per unit length for an increasing proton number of the absorption material, which of course impacts what materials are used for particle detection. For a given detection material, a slower incident particle will lose energy more rapidly than a faster one due to the factor $1/\beta^2$, and a higher-Z incident particle will have more rapid energy loss due to the Z^2 dependence. The strong Z dependence in Eq. 3.1 is the foundation of most particle identification techniques in experiments where multiple different species of nuclei may be detected.

There are several methods for detecting heavy charged particles [106]. In the JANUS setup, silicon semiconductor detectors are employed. In such detectors, a bias voltage is applied across the detector which ensures the entire detector volume is depleted [106]. Ionizing radiation incident anywhere in a fully-depleted material will create free charge carriers (electron-hole pairs) that will be collected at their respective electrical contacts.

The total charge collected at the electrical contacts can be measured with e.g. charge-sensitive pre-amplifiers, and the amplitude of the signal is directly proportional to energy deposited by the incident particle. The band-gap of silicon is large enough ($\approx$ 1.1 eV [106]) for these detectors to be operated at room temperature. Even at room temperature, random thermal fluctuations will not provide enough energy to create electron-hole pairs (due to the large band gap), and thus there are

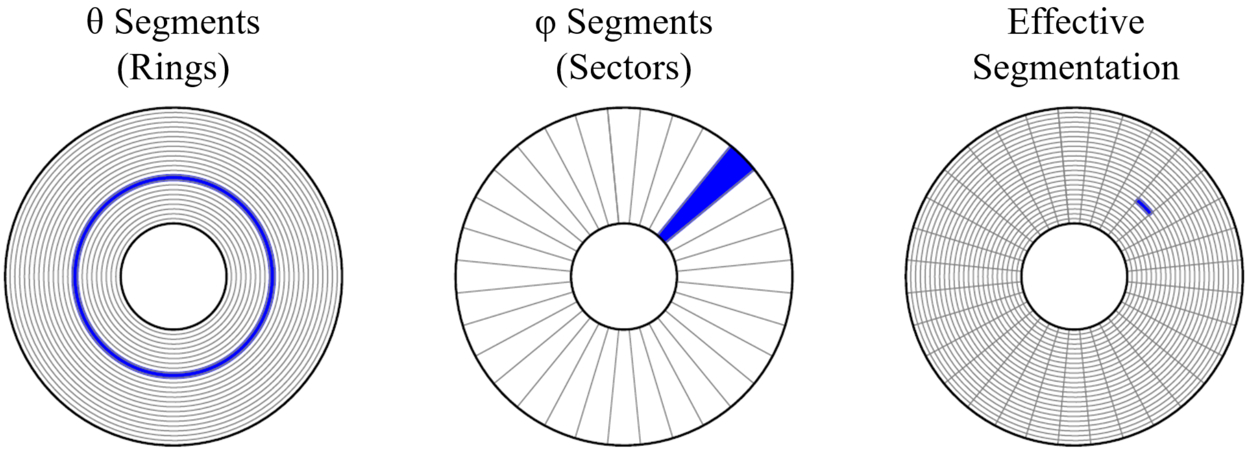

Figure 3.2: Segmentation of the JANUS silicon detectors. Figure adapted from [108].

no thermal excitations which could contribute "noise" to charge carriers created by actual incident radiation.

3.1.2 The JANUS Silicon Detectors

The two silicon detectors used in JANUS are highly-segmented, annular doubled-sided S3-type detectors manufactured by Micron Technology, Inc. Each detector has an inner radius of 1.1 cm and an outer radius of 3.5 cm, and they are approximately 300 μm think. For experiments with JANUS, the heavy charged particles have an estimated range of $\lesssim$ 30 μm in silicon, so they will easily be stopped by the detectors, depositing all of their energy. The detectors are operated at a 40 V bias, at which point they are fully depleted.

The electrical contacts on the two surfaces of each detector have unique segmentation. On one side, there is 24-fold segmentation along the radial direction, forming rings; on the other, there is 32-fold segmentation in the azimuthal direction, forming sectors. The combination of rings and sectors forms an effective segmentation of $24 \times 32 = 768$ pixels which provide the position resolution of the detectors. This segmentation is shown in Fig. 3.2.

As shown in Fig. 3.1, the silicon detectors are placed on either side of the target and perpendicular to the incoming beam. The detectors can be mounted such that either side (rings or sectors) is facing the target. However, it was found that the radially-segmented side has a significantly thicker

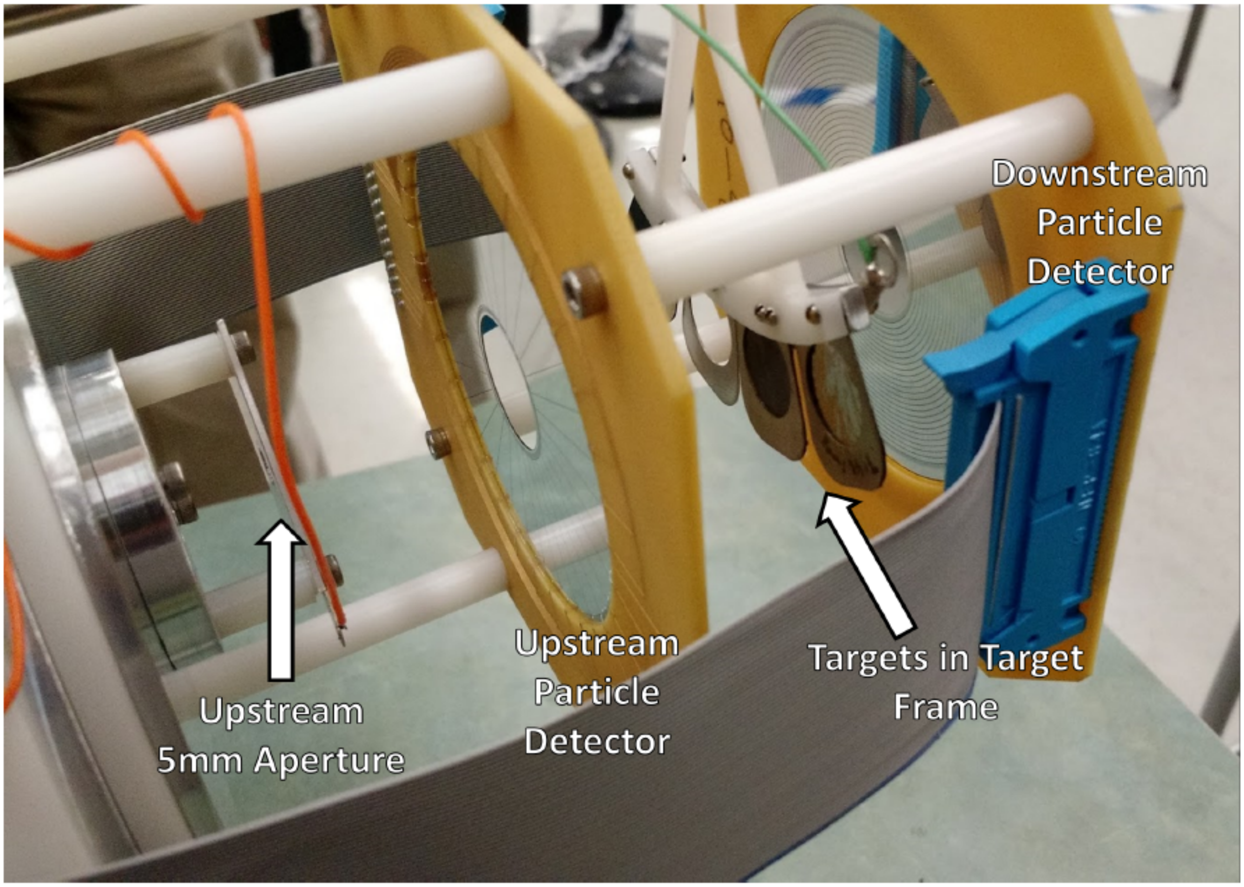

Figure 3.3: The two JANUS silicon detectors and the target wheel together in the mounting assembly. Note this figure shows shows the ring ring side of the silicon detectors facing the target, which is incorrect (see text). Also visible are two wires which enable a current reading from the beam-tuning apertures. Figure from [108].

dead layer than the azimuthally-segmented side. Thus the detectors are always mounted with the sectors facing the target.

In the typical configuration of JANUS, the downstream detector is separated from the target by 2.6 cm, and the upstream detector is separated by 3.4 cm. With this geometry, the downstream detector covers LAB frame scattering angles $22.9° < \theta_{LAB} < 53.4°$, and the upstream detector covers $134° < \theta_{LAB} < 162°$, providing 16.2% and 12.7% of 4π, respectively (both detectors have full 360° converge in ϕ_{LAB}). The segmentation provides a localization of roughly 1.3° in θ_{LAB} and 11.25° in ϕ_{LAB}, which also depends on the target-detector separation. The mounting apparatus for the detectors and target is shown in Fig. 3.3.

The target wheel can hold several targets at one time, each of which can be rotated into and out of the beam path using a rod system (not shown). This allows multiple targets be used in one experiment without needing to deconstruct any part of the setup, an important feature for Coulomb excitation experiments. A positive voltage can be applied to the target frame in order to suppress secondary δ-electrons, which are created by the passage of the heavy particle through the target, from hitting the silicon detectors. The δ-electrons would otherwise constitute a source of low energy background. Also shown in Fig. 3.3 are two apertures that are used for beam tuning.

3.1.3 Reaction Kinematics

Beyond the basic principles of charged particle detection, the techniques employed with the JANUS silicon detectors rely entirely on the well-known two-body reaction kinematics of Coulomb scattering. The most natural description of a two-body reaction occurs in the center-of-mass (CM) frame of reference,[4] and the distribution of the CM frame scattering angle is governed by the Rutherford differential cross section (Eq. 2.18). The LAB frame angles θ_P and θ_T of each particle can be calculated for a given CM angle via [90, 109, 110]

$$\tan\theta_P = \frac{\sin\theta_{CM}}{\cos\theta_{CM} + \tau}, \tag{3.2}$$

$$\tan\theta_T = \frac{\sin(\pi - \theta_{CM})}{\cos(\pi - \theta_{CM}) + \tilde{\tau}}, \tag{3.3}$$

where

$$\tau = \frac{m_P}{m_T}\tilde{\tau}, \tag{3.4}$$

$$\tilde{\tau} = \sqrt{\frac{E_P}{\tilde{E}}}, \tag{3.5}$$

$$\tilde{E} = E_P - \Delta E\left(1 + \frac{m_P}{m_T}\right). \tag{3.6}$$

---

[4] The Coulomb excitation process is also most naturally described in a CM frame, making extraction of CM frame parameters crucial for these experiments.

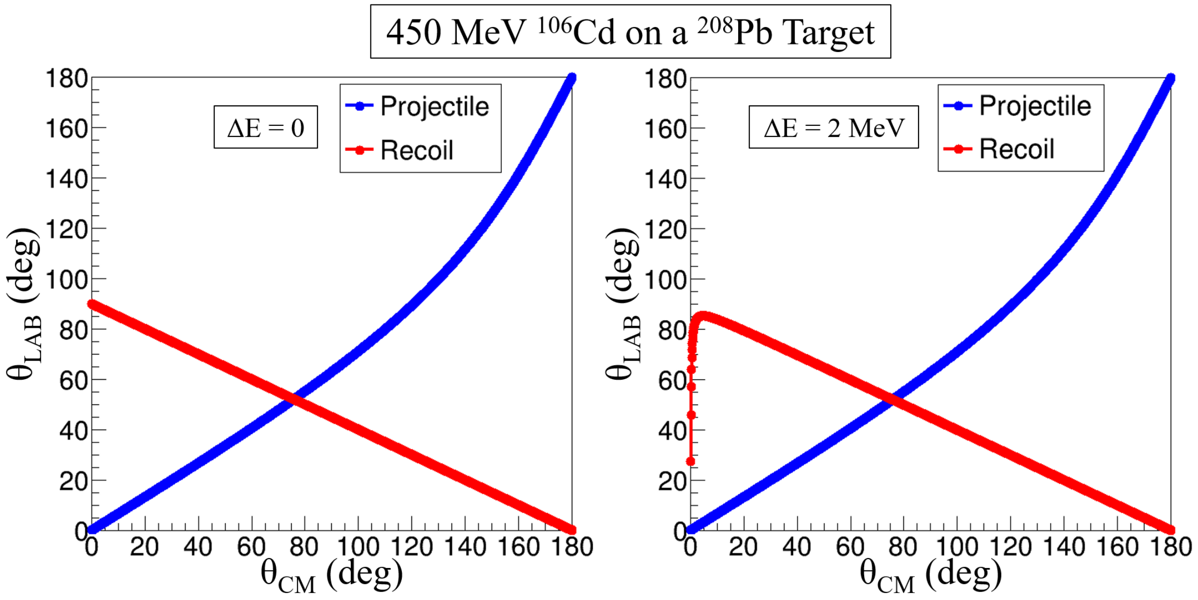

Figure 3.4: *LAB* frame angles as a function of the *CM* angle for the indicated two-body scattering reaction. The left panel shows elastic scattering ($\Delta E = 0$), and the right shows inelastic scattering ($\Delta E = 2$ MeV).

In Eqs. 3.4 to 3.6, m_P and m_T are the masses the projectile and target, respectively, E_P is the initial kinetic energy of the projectile in the *LAB* frame, and ΔE is the energy transferred to a nuclear excitation. The *LAB* frame scattering angles are shown as a function of the *CM* angle in Fig. 3.4.

The dependence of the *LAB* frame scattering angles on τ and $\tilde{\tau}$ has an important consequence: there can be a maximum allowed scattering angle for each particle, given by

$$\sin\theta_P^{\max} = 1/\tau \qquad \text{for } \tau \geq 1, \tag{3.7}$$

$$\sin\theta_T^{\max} = 1/\tilde{\tau}. \tag{3.8}$$

Note $\tilde{\tau} \geq 1$ always, so the maximum recoil angle always obeys $\theta_T^{\max} \leq 90°$. Typically, $\tau > 1$ only when $m_P > m_T$. However, $\tau > 1$ is possible when $m_P \leq m_T$ for inelastic scattering. For $\tau < 1$ there is no bound on θ_P. An example of the angle transformations for $m_P > m_T$ is shown in Fig. 3.5.

In experiments, the angles (and all other observables) will be measured in the *LAB* frame, which means Eqs. 3.2 and 3.3 must be inverted. The *CM* angle can be related to the *LAB* frame

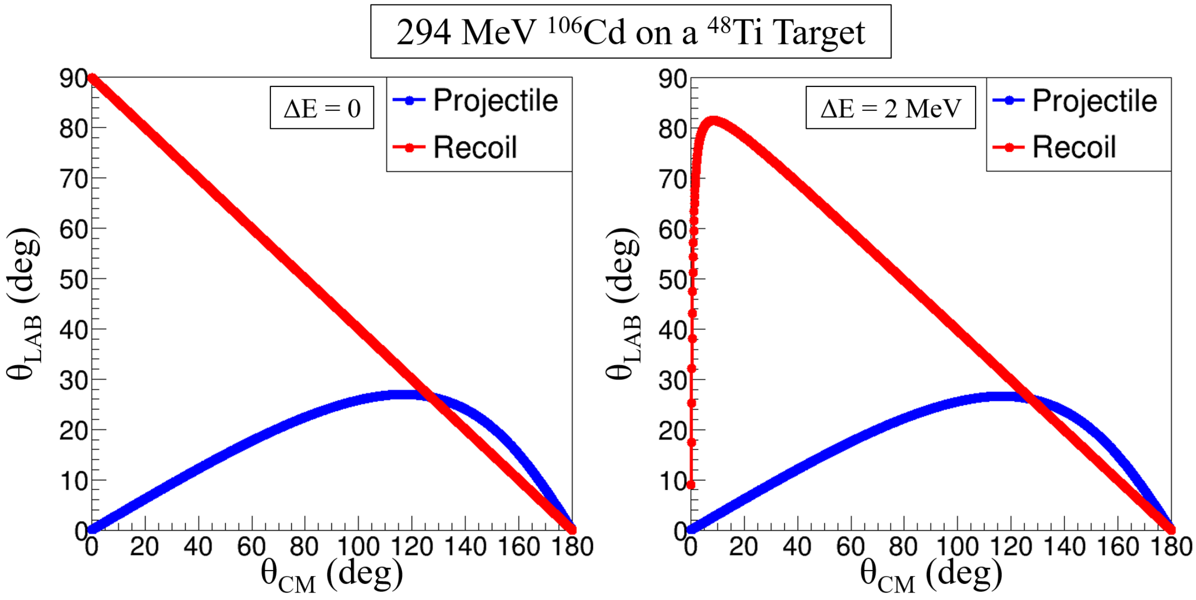

Figure 3.5: *LAB* frame angles as a function of the *CM* angle for the indicated two-body scattering reaction. Because $m_P > m_T$, the maximum projectile scattering angle is $\theta_P^{\max} = 26.9°$. The left panel shows elastic scattering ($\Delta E = 0$), and the right shows inelastic scattering ($\Delta E = 2$ MeV).

angles via [90, 109]:

$$\theta_{CM} = \arcsin\left(\tau \sin\theta_P\right) + \theta_P \tag{3.9}$$

$$= \pi - \arcsin\left(\tilde{\tau} \sin\theta_T\right) - \theta_T. \tag{3.10}$$

The τ and $\tilde{\tau}$ dependence of the scattering angles is now more problematic, as $\theta_{CM}(\theta_{P,T})$ can become a double-valued function. This implies that, despite the two-body nature of the reaction, an observation of only one scattering angle may not be sufficient to determine uniquely the *CM* angle. It is also clear from Fig. 3.5 that, for projectile scattering angles near $\theta_P^{\max}$, observation of the recoil angle θ_T will allow the most precise determination of θ_{CM} even when the two kinematic solutions can be discriminated.

In the considerations given above, it was assumed that the *LAB* frame angles were known to correspond to a particular reaction product (scattered projectile or recoiling target). In general, however, observation of the scattering angles alone is not sufficient to discriminate between the two nuclei. Beyond the *LAB* frame angles, each particle will also be characterized by a unique "kinematic curve," i.e. the dependence of the particle's energy on the scattering angle. As a function

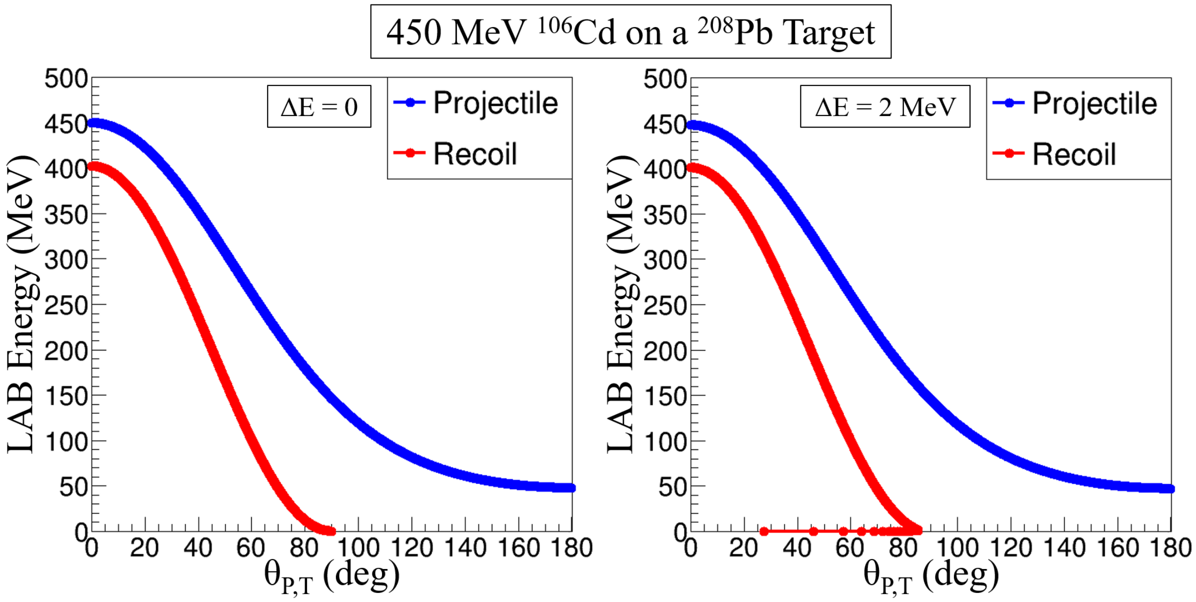

Figure 3.6: Kinematic curves which result from the indicated two-body scattering reaction. The left panel shows elastic scattering ($\Delta E = 0$), and the right shows inelastic scattering ($\Delta E = 2$ MeV).

of the CM angle, the LAB frame energies E_P' and E_T' after the reaction are given by [90, 109]

$$E_P' = \left(\frac{m_T}{m_P + m_T}\right)^2 \left(1 + \tau^2 + 2\tau \cos\theta_{CM}\right) \tilde{E}, \tag{3.11}$$

$$E_T' = \frac{m_P m_T}{(m_P + m_T)^2} \left(1 + \tilde{\tau}^2 + 2\tilde{\tau}\cos(\pi - \theta_{CM})\right) \tilde{E}. \tag{3.12}$$

The dependence of the energies after the reaction on the LAB frame angles is shown in Fig. 3.6 ($m_P < m_T$) and Fig. 3.7 ($m_P > m_T$).

In can be seen in Figs. 3.4 to 3.7 that, for inelastic scattering, the recoiling target also has a double valued kinematic curve, where the low-energy solution corresponds to low CM angles. For several reasons, these kinematic solutions are never of practical interest: the low CM angles $\theta_{CM} \lesssim 8°$ have the least sensitivity to Coulomb excitation, the low energy of the recoil $E_T' \lesssim 5$ MeV imply they usually will be stopped in the target, and, if they do exit the target, their low energy makes them very difficult to detect.

In JANUS, particle identification is accomplished by observing the kinematic curves. Both the energy and angle of the reaction products are recorded with the silicon detectors; the angle

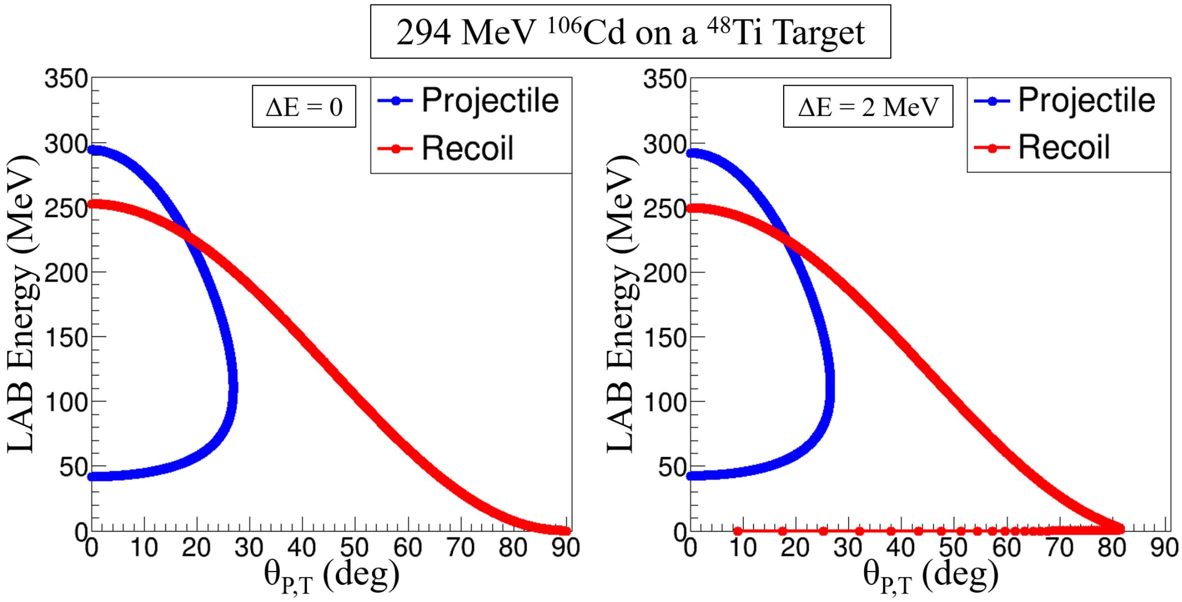

Figure 3.7: Kinematic curves which result from the indicated two-body scattering reaction. The double-valued kinematic solution, which arises because $m_P > m_T$, is clear. The left panel shows elastic scattering ($\Delta E = 0$), and the right shows inelastic scattering ($\Delta E = 2$ MeV).

information is obtained from the segmentation. The combined information is sufficient to uniquely characterize a particular scattering event, i.e. to determine θ_{CM}. This enables a crucial feature of particle detection with JANUS. The detection of one reaction product is sufficient to reconstruct the trajectory of the other.

The effective coverage for both reaction products is increased by kinematic reconstruction. However, experiments with JANUS are performed in inverse kinematics, so it is more useful to consider the additional coverage of the projectile scattering angle which is gained through target detection rather than vice-versa. The relationship between the two *LAB* frame angles and the increase in coverage for the projectile are shown in Figs. 3.8 ($m_P < m_T$) and 3.9 ($m_P > m_T$).

As is clear from Fig. 3.8, kinematic reconstruction can provide a significant increase in coverage, particularly for experiments with $m_P < m_T$. For the typical case shown in Fig. 3.8 ($m_P/m_T = 0.51$), the angles $54° \leq \theta_P \leq 104°$ are gained, which is an additional 41% of 4π. From Fig. 3.9, however, it is clear that kinematic reconstruction can also provide a negligible increase in coverage, particularly when $m_P > m_T$. For the case shown in Fig. 3.9 ($m_P/m_T = 2.2$), kinematic reconstruction is

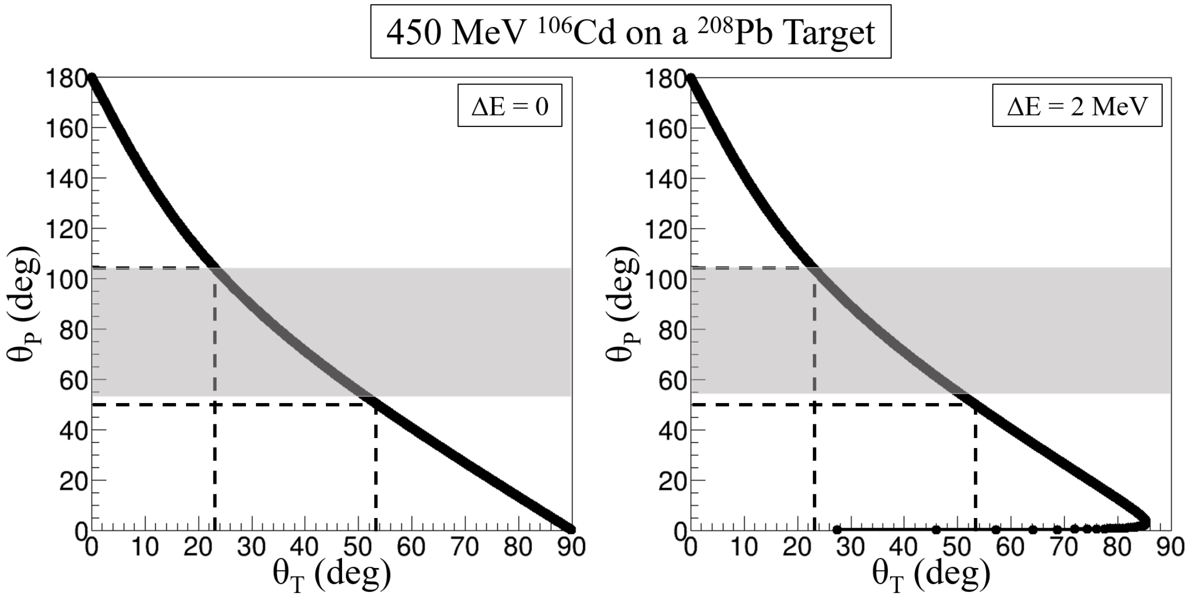

Figure 3.8: The projectile scattering angle as a function of the recoil angle for the indicated two-body scattering reaction. The vertical dashed lines show the physical coverage of the downstream detector, and the horizontal shaded grey region indicates the effective coverage for the projectile gained via kinematic reconstruction. The left panel shows elastic scattering ($\Delta E = 0$), and the right shows inelastic scattering ($\Delta E = 2$ MeV).

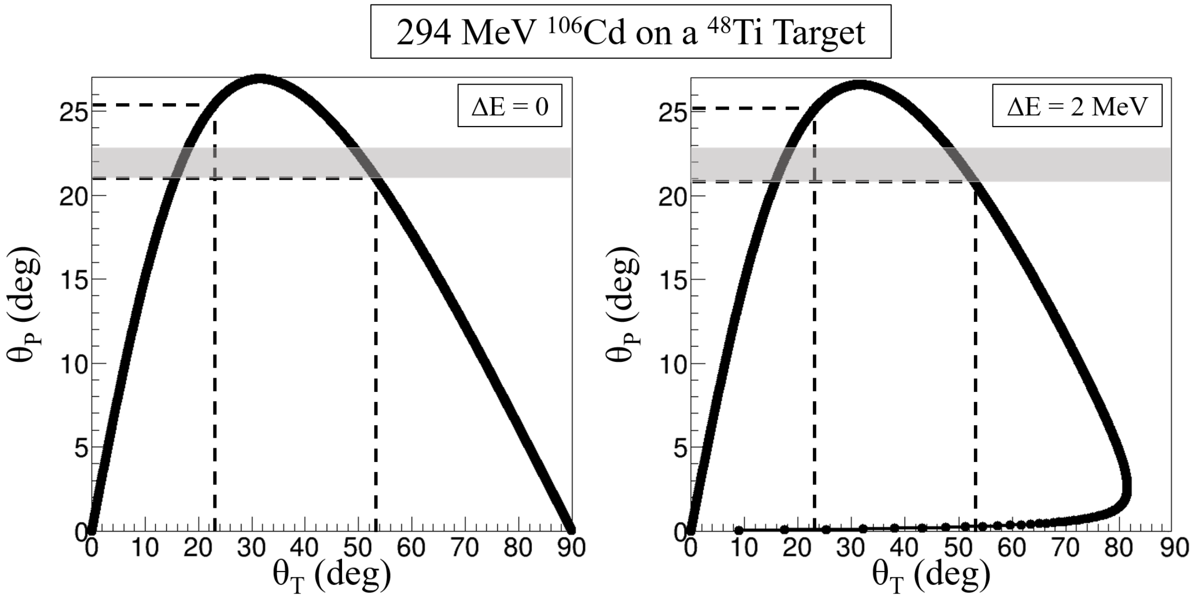

Figure 3.9: The projectile scattering angle as a function of the recoil angle for the indicated two-body scattering reaction. The vertical dashed lines show the physical coverage of the downstream detector, and the horizontal shaded grey region indicates the effective coverage for the projectile gained via kinematic reconstruction. The left panel shows elastic scattering ($\Delta E = 0$), and the right shows inelastic scattering ($\Delta E = 2$ MeV).

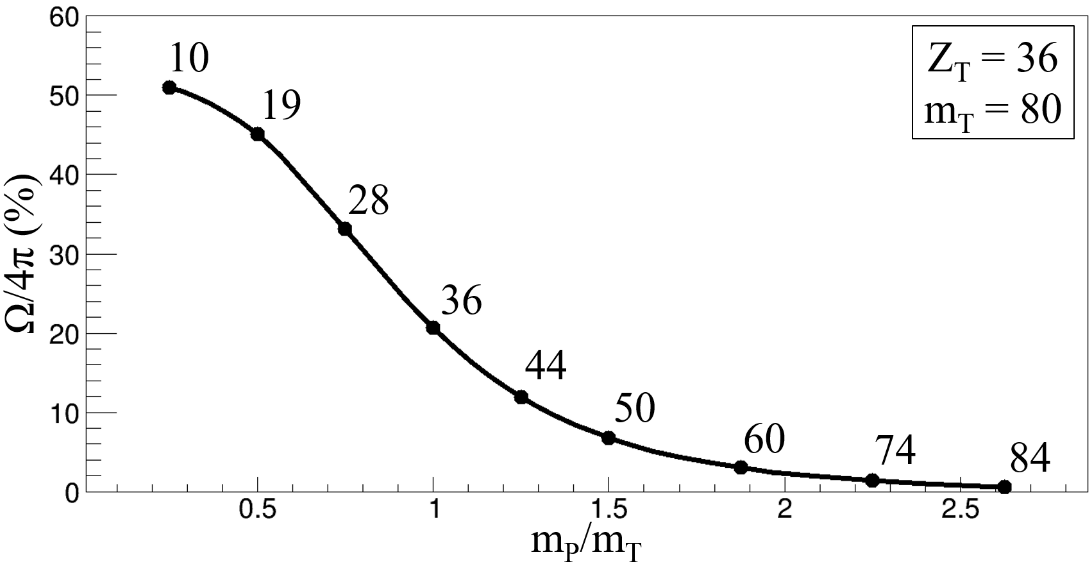

Figure 3.10: The solid angle coverage gained by kinematic reconstruction of the projectile as a function of m_P/m_T. The number by each point is the corresponding Z_P, and $E_P = E_{CB}$ for all points. This figure does not consider if the reconstructed angular range overlaps with the physical coverage of the detector.

irrelevant as only $\approx 2^\circ$ of converge is gained beyond the physical coverage of the detector.

The precise angular coverage gained through kinematic reconstruction depends on both the target-detector separation and the scattering system. In particular, it depends quite sensitively on the ratio m_P/m_T; this dependence is shown in 3.10. Note this figure does not consider if the reconstructed angular range overlaps with the physical coverage of the detector, as is done in Figs. 3.8 and 3.9. Taking this into account makes the reconstructed coverage drop much more rapidly with m_P/m_T, often to zero.

3.2 Gamma-Ray Detection

Similar to heavy charged particles, a γ ray can be detected when it interacts in a material, depositing some or all of its energy. However, much unlike charged particles, the energy depositions of a γ ray moving through a material cannot reasonably be treated as a single, continuous process. This is primarily due to two characteristics of γ-ray interactions: the cross sections are relatively low, allowing γ rays to have a large mean free path, and the individual interactions tend to alter

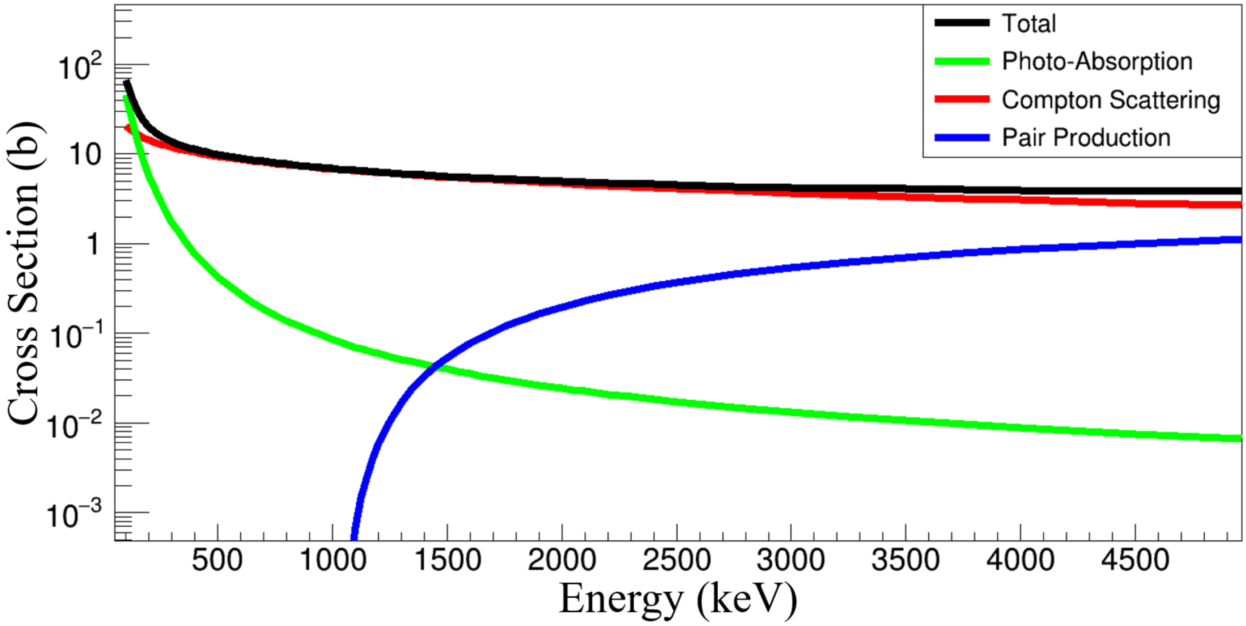

Figure 3.11: The cross sections of the three γ-ray interactions in bulk germanium, plus their sum. The data is from [111].

significantly the γ-ray momentum (both energy and direction). Because of this, γ-ray interactions in a material are considered individually.

3.2.1 Gamma-Ray Interactions in Matter

There are three ways in which a γ ray can interact in matter: photo-absorption, Compton scattering, and pair-production. The cross-sections for these interactions in germanium is shown as a function of the γ-ray energy in Fig. 3.11, and an idealized spectrum which displays the result of these interactions for a mono-energetic γ-ray is shown in Fig. 3.12

Photo-absorption is the process in which a γ-ray deposits all of its energy E_γ into a material by transferring it to an atomic electron, which is then ejected from the atom. The energy E_{e^-} of the electron is given by

$$E_{e^-} = E_\gamma - E_b, \tag{3.13}$$

where E_b is the atomic binding energy which is very small (a few eV) compared to the γ-ray energy (10s of keV of more). This process results in a count in the "Full Energy Peak" component of

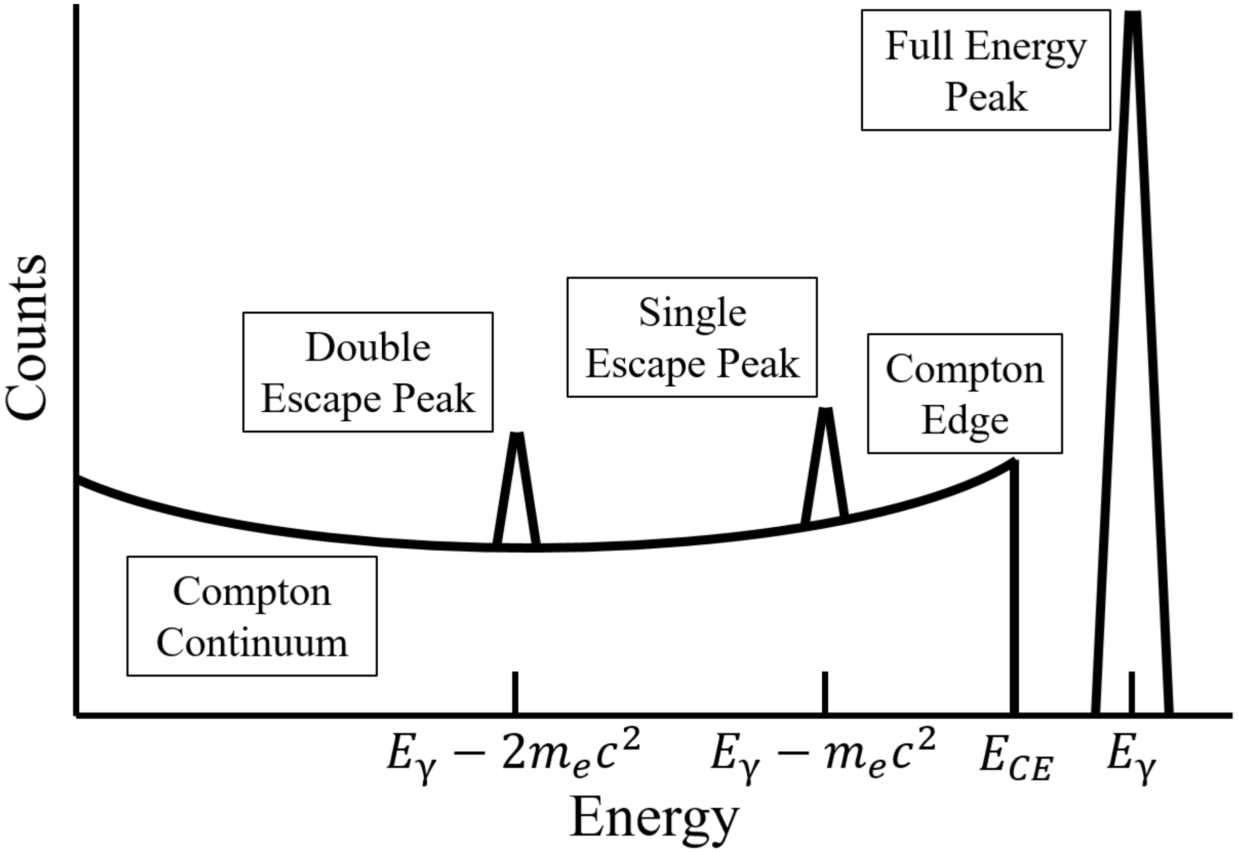

Figure 3.12: An idealized spectrum emphasizing the components which result from the interactions of a mono-energetic γ-ray with $E_\gamma > 2m_ec^2$. The origins of the individual components are discussed in the text.

the spectrum shown in Fig. 3.12. Photo-absorption is the dominant interaction for γ-ray energies below approximately 100 keV.

The inelastic scattering of a γ-ray off an electron is referred to as Compton scattering. During this process, a portion of the γ-ray's energy is transferred to the electron; the remaining γ-ray energy E'_γ is given by

$$E'_\gamma = \frac{E_\gamma}{1 + \left(\frac{E_\gamma}{m_ec^2}\right)(1 - \cos\theta)}, \tag{3.14}$$

where θ is the angle between the initial and final γ-ray momentum. Compton scattering is the dominant process for the energy regime most relevant for nuclear physics, from approximately a few hundred keV to a few MeV.

The energy transferred to the electron during Compton scattering depends on the angle θ; the minimum energy occurs for small angles $\theta \longrightarrow 0°$, while the maximum occurs for $\theta = 180°$. This maximum results in a sharp cutoff of the energies observed from Compton scattering, which is referred to as the "Compton Edge", shown in Fig. 3.12. The energy E_{CE} of the Compton Edge is given by

$$E_{CE} = \frac{2E_\gamma^2}{m_e c^2 + 2E_\gamma}. \tag{3.15}$$

The angle-dependence in Eq. 3.14 results in smooth distribution of deposited energy due to the Compton scattering of γ rays, labeled "Compton Continuum" in Fig. 3.12. Note this continuum is not flat as the distribution of the scattering angle is not isotropic. The differential cross section for Compton scattering is given by the Klein-Nishina formula [112]

$$\frac{d\sigma}{d\Omega} = \frac{r_e^2}{2} \frac{E_\gamma'^2}{E_\gamma^2} \left(\frac{E_\gamma'}{E_\gamma} + \frac{E_\gamma}{E_\gamma'} - \sin^2\theta \right), \tag{3.16}$$

where $r_e \approx 2.82$ fm is the classical electron radius, and E_γ' is also a function of θ given by Eq. 3.14.

Lastly, a γ ray can undergo pair-production. This is a process in which a γ ray interacts in the electric field of a nucleus and is converted into an electron-positron pair. Due to energy conservation, this process is only possible for γ-rays with $E_\gamma > 2m_e c^2 \approx 1022$ keV. The remaining γ-ray energy beyond $2m_e c^2$ is shared between the electron and positron as kinetic energy, i.e.,

$$E_{e^-} + E_{e^+} = E_\gamma - 2m_e c^2, \tag{3.17}$$

where E_{e^+} is the energy of the positron. This kinetic energy is absorbed by the detection material.

A very short time after pair-production, the positron will encounter an electron within the material, and the pair will annihilate. This creates two annihilation γ rays each with energy $E_\gamma^{\mathrm{annil}} = m_e c^2 \approx 511$ keV. If both of these annihilation γ rays are fully absorbed by the detector, the full energy of the initial γ ray is recovered. If one the annihilation γ rays escapes the detector, this results in the "Single-Escape Peak" at an energy of $E_\gamma - m_e c^2$ shown in Fig. 3.12. If both of the annihilation γ rays escape, this results in the "Double-Escape Peak" at $E_\gamma - 2m_e c^2$.

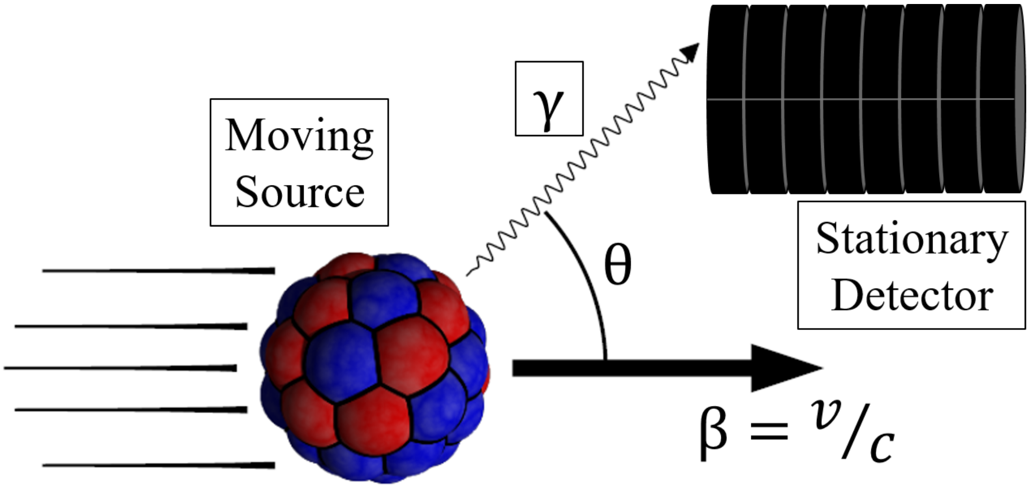

Figure 3.13: A schematic depiction of the Doppler Effect. Figure adapted from [108].

3.2.2 The Doppler Effect

When a γ ray is emitted from a moving source, the energy of the γ ray in the LAB frame is shifted with respect to its energy in the $REST$ frame of the emitter. This is known as the Doppler Effect, and it is shown schematically in Fig. 3.13. The energy E_γ^{LAB} of the γ ray in the LAB frame is given by

$$E_\gamma^{LAB} = \frac{E_\gamma^{REST}}{\gamma(1-\beta\cos\theta)}, \tag{3.18}$$

where E_γ^{REST} is the energy of the γ-ray in the $REST$ frame of the emitter, β is the velocity of the emitter relative to the speed of light, and θ is the angle between the emitter's momentum and the and γ ray's momentum.

When correcting for the Doppler Effect to recover the γ-ray energy E_γ, in addition to the intrinsic energy uncertainty ΔE_{intr} of the detector, the uncertainties $\Delta\beta$ on β and $\Delta\theta$ on θ also contribute to the overall uncertainty ΔE_γ. The contribution from each of these terms can be derived from Eq. 3.18 via the finite-differences derivative method; they are given by [50]

$$\left(\frac{\Delta E_\gamma}{E_\gamma}\right)^2 = \left(\frac{\beta\sin\theta}{1-\beta\cos\theta}\right)^2(\Delta\theta)^2 + \left(\frac{\cos\theta-\beta}{(1-\beta^2)(1-\beta\cos\theta)}\right)^2(\Delta\beta)^2 + \left(\frac{\Delta E_{\text{intr}}}{E_\gamma}\right)^2. \tag{3.19}$$

These contributions are shown as a function of θ in Fig. 3.14. The Doppler effect is the primary reason such a high level of segmentation is required for both particle and γ-ray detection in Coulomb

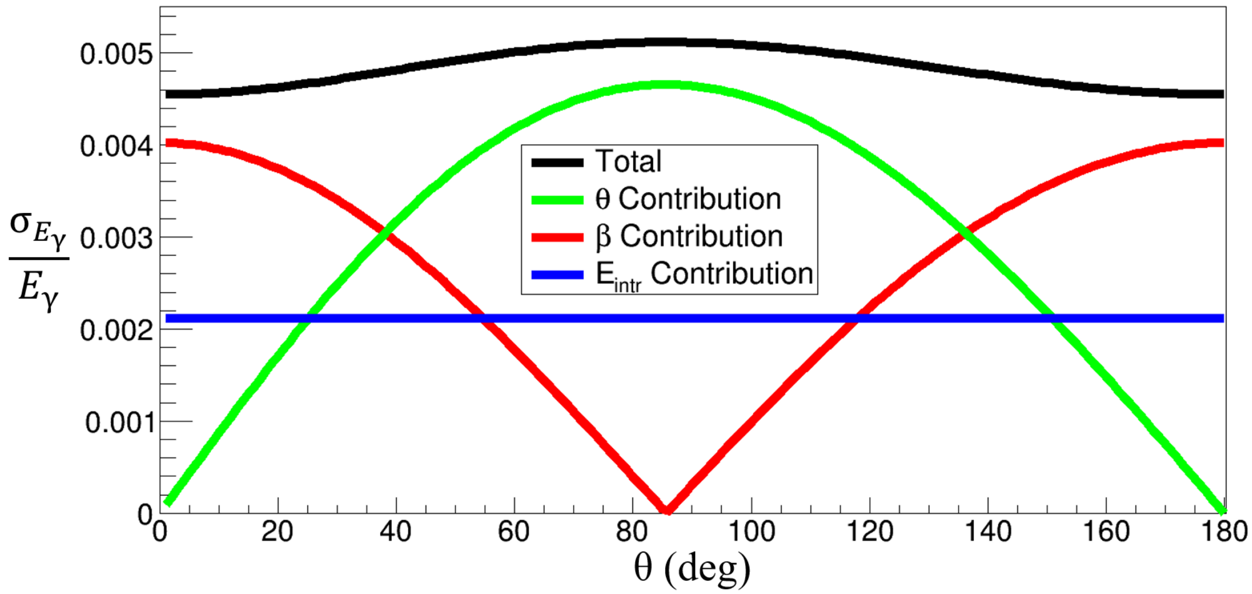

Figure 3.14: Contributions to the uncertainty on E_γ from the Doppler Effect and the intrinsic resolution of a detector. For this figure the uncertainties are assumed to be Gaussian, and standard deviations are used. The parameters used to make this figure are $E_\gamma = 659$ keV, $\sigma_{E_{\text{intr}}} = 1.4$ keV, $\sigma_\theta = 3.5°$, $\beta = v/c = 0.076$, and $\sigma_\beta = 0.004$.

excitation experiments with JANUS.

3.2.3 The Segmented Germanium Array

SeGA [104] is comprised of up to 18 individual γ-ray detectors which can be arranged in various configurations depending on the needs of a particular experiment. Each individual SeGA detector is comprised of three primary components: an active n-type High-Purity Germanium (HPGe) crystal, pre-amplifier electronics, and a liquid-nitrogen dewar. A single SeGA detector is shown in Fig. 3.15.

The HPGe crystal in each SeGA detector is a coaxial cylinder with 32-fold segmentation. The crystal is electronically segmented into eight "slices" along its axis of symmetry, and each slice is further segmented into four quadrants. A single electrical contact is placed along the inner radius of the crystal; only the electrical contacts at the outer radius are segmented. This geometry is shown in Fig 3.16.

The inner "central" contact of each detector is sensitive to charge deposited anywhere in the

Figure 3.15: A single SeGA detector. The large green cylinder is the liquid-nitrogen dewar. The germanium crystal is located in the aluminum housing at the bottom of the photo. Figure from [108].

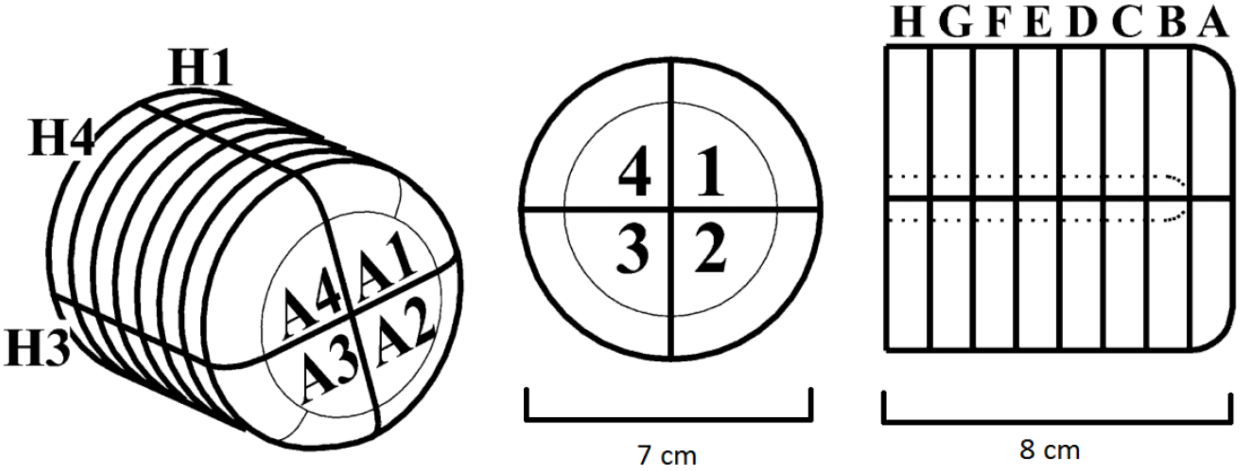

Figure 3.16: Segmentation of an individual SeGA detector. Figure from [108], originally adapted from [104].

crystal volume, while the segmented electrical contacts at the outer radius are only sensitive to charge deposited in a particular segment. Thus signals from the central contact provide the total energy deposited by a γ-ray, while the segment contacts provide energy and position information for individual γ-ray interactions.

For Coulomb excitation experiments with JANUS, 16 SeGA detectors are arranged in the compact "barrel" configuration, with the detector crystals concentrically surrounding the target position. This configuration, shown in Fig. 3.17, maximizes the solid angle subtended by the detectors. See, for example, Refs [5, 113] for a description of the SeGA configuration used in fast beam experiments.

Because the SeGA detectors are made of High-Purity Germanium, they must be kept at liquid-nitrogen temperatures during operation,[5] roughly 100 K. This suppresses random thermal excitations which would otherwise create a significant leakage current due to the small band-gap of germanium, approximately 0.7 eV [106]. Each detector is operated at bias voltage of roughly 4000 V, which is significantly higher than the 40 V applied to the silicon detectors. The higher bias is needed to deplete fully the much larger germanium crystals.

3.3 Data Acquisition System

For the commissioning experiment with JANUS [108, 100], a hybrid data acquisition system (DAQ) was used. The silicon detectors were read-out with an analog system, while SeGA was instrumented with a digital DAQ. For all subsequent JANUS experiments, a sufficient amount of digital electronics was available to employ an entirely digital DAQ, which is a significantly simpler system to setup and operate. A digitizing module can replace several independent components of a traditional analog DAQ, such as shaping modules, discriminators, and analog-to-digital and time-to-digital converters.

A digital DAQ offers several advantages. A timestamp is included in the data structure written for every processed signal, so correlation of all signals from all detectors can be accomplished offline

---

[5] The SeGA detectors are always kept at LN_2 temperatures, not just during operation, as repeated cooling down and warming up deteriorates their vacuum properties.

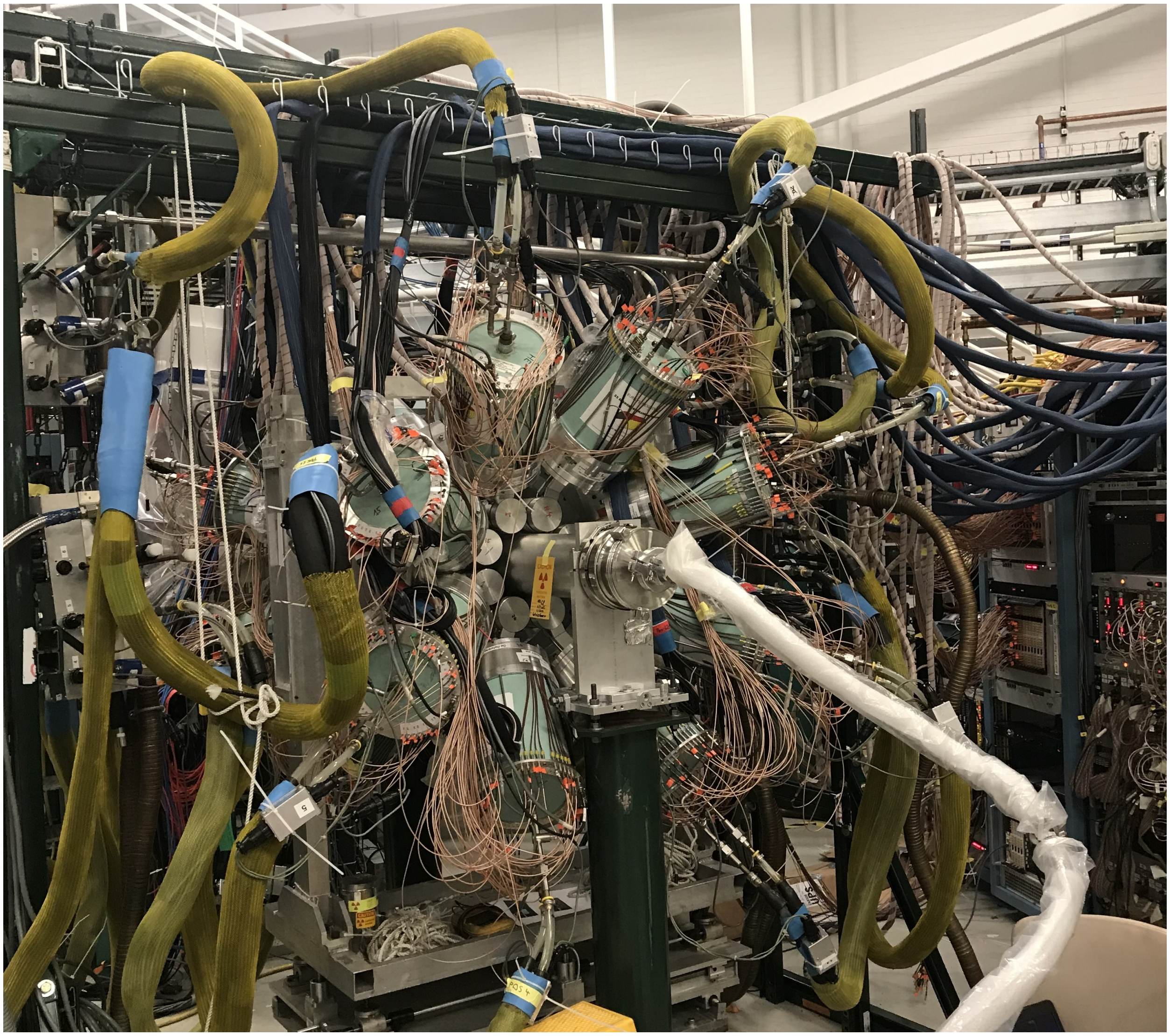

Figure 3.17: SeGA arranged in the barrel configuration at ReA3. Only six detector end-caps are visible arrayed around the beam pipe. The silicon detectors and target are inside the beam pipe.

simply by comparing their timestamps. The bandwidth provided by the digital DAQ, combined with the low rate of JANUS experiments, allows operation of the DAQ in a "free-running" mode. This means every channel triggers independently, and all signals are recorded and processed offline. This is a simple and safe way of recording experimental data as there is no need to construct more complicated "event" triggers (coincidence trigger, validation signals, etc.), which can possibly be misconfigured. Such mistakes could take a significant amount of time to notice due to the low rates in JANUS experiments. Due to the free-running DAQ, the acquired data mostly consists of γ-ray background. This is actually useful for tracking the energy calibration of the SeGA detectors over the course of the experiment.

The digital DAQ used with JANUS also enables the recording of signal waveforms, which have applications both for particle and γ-ray spectroscopy. For the SeGA detectors, signal waveforms can be processed in order to achieve a position resolution better than what is enabled by the physical segmentation of the detector; this is similar to the techniques employed in γ-ray tracking arrays like GRETINA [114, 115]. This level of resolution is not necessary for JANUS experiments, so signal waveforms were not recorded for this work. See Ref. [13] for details of the waveform processing algorithms used for sub-segment position resolution in SeGA.

A standard implementation of the digital DAQ commonly employed [116] at NSCL is used for JANUS experiments. This system employs 16-channel digitizing FPGA modules, called Pixie-16 modules, manufactured by the company XIA. The Pixie-16 modules used to instrument the SeGA detectors had a 100 MHz sampling frequency and 16-bit precision, while the silicon detectors were read-out with 250 MHz 16-bit digitizing modules. Considering the bandwidth of both SeGA and the silicon detectors with their corresponding preamplifiers (roughly 10 HMz for SeGA, somewhat faster for the silicon detectors), the 100 MHz modules are sufficient for both detection systems. The higher-frequency modules were used for the silicon detectors simply because there were not enough 100 MHz modules available.

The Pixie-16 modules must be configured for the specific detectors used in the experiment. For JANUS experiments, the most important settings are the parameters of the trapezoidal energy filter used to determine amplitudes of the digitized signals. In particular, the filter's gap length must be set according to the signal rise times, which depends on the detection system (700 ns for SeGA, ~10 ns for the silicon detectors). The filter's integration window was set by considering the signal rise time and the leakage current from the detectors. While the Pixie-16 modules can also employ a CFD algorithm to determine timestamps, this was not used and the timestamps were determined by the leading-edge trigger. Leading-edge triggers can cause a significant "walk" of the timing response for low-energy signals from the large-volume germanium detectors, but this is easily accounted for during offline analysis.

All Pixie-16 modules must be housed in a dedicated mainframe also manufactured by XIA, called crates here. The XIA crates also hold a computer which controls the Pixie-16 modules. As multiple crates are required for the JANUS DAQ, all crates must receive a synchronized time signal to ensure proper time correlation of the collected signals. This is accomplished by linking the crates together with timing cables and configuring the system so that a single "director" module is used to distribute a global time signal to all other "recipient" modules [117].

Each crate in the JANUS DAQ produces its own independent data stream, meaning it writes its data to a unique destination not shared by the other crates. These data streams were managed by the NSCLDAQ framework [118]. NSCLDAQ provides a unified framework for accepting data from multiple sources, merging all data streams into a single output, and writing the data to disk. NSCLDAQ also sends the start and stop signals to all XIA crates, which enables them to begin and end taking data synchronously.

The SeGA detectors output 33 signals each (32 segments plus one central contact), yielding 528 signals from all 16 detectors. Each silicon detector provides $32 + 24 = 56$ signals, which brings the total to 640 channels for the entire array. For this setup, 33 Pixie-16 modules are required to process all signals from SeGA, and an additional eight are used to read-out the silicon detectors. Strictly, only seven modules are needed for the silicon detectors, but using eight prevents any module from processing signals from both detectors, which is of practical convenience. Four crates are required to house all 41 modules. The JANUS digital DAQ is shown in Fig. 3.18. While slightly messy due

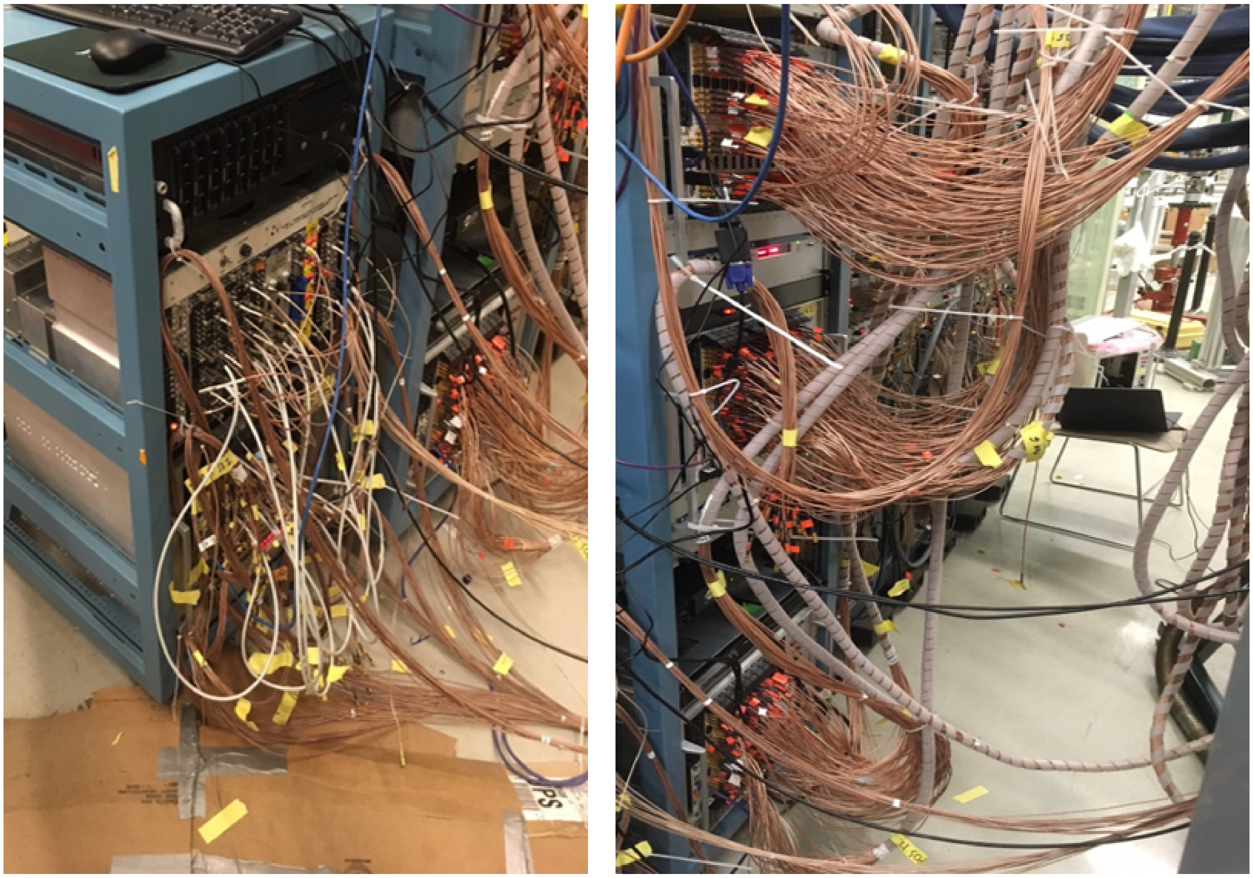

Figure 3.18: The JANUS digital DAQ. The left panel shows the crate and modules which processed the silicon detector signals, and the right shows the three crates necessary for SeGA.

to the high density of channels, the system is quite compact.

CHAPTER 4

COULOMB EXCITATION OF CADMIUM-106

The first multi-experiment campaign with JANUS at ReA3 took place from March to April 2018, during which time three separate experiments were performed successfully. These included a Coulomb excitation experiment of ^{72,76}Se [102, 74], and a fusion reactions study of ^{46}Ca [119], the first non-Coulomb excitation experiment performed with JANUS. The last experiment during this campaign was a Coulomb excitation measurement of ^{106}Cd [103], the topic of this work.

4.1 Motivation

As discussed in Chapter 1, the electromagnetic $B(E2; 2_1^+ \rightarrow 0_1^+)$ transition strength is a clear and widely-used measure of quadrupole collectivity in even-even nuclei. $B(E2)$ values are sensitive nuclear deformation, shell-breaking effects, and nucleon-nucleon correlations. Studies of collective properties in nuclei near $N = Z = 50$ ^{100}Sn, the heaviest self-conjugate doubly-magic nucleus known to exist, have revealed one of the most persistent puzzles in rare-isotope science. In the Sn isotopes, this transition strength has been reported from ^{104}Sn [120, 121] to ^{132}Sn [122], spanning a chain of 15 even-even Sn isotopes. The trend is asymmetric about mid-shell with enhanced collectivity towards ^{100}Sn. This evolution is shown is Fig. 4.1.

Evidence has been mounting [127, 120, 142] that the asymmetric evolution and enhancement with decreasing N of the Sn $B(E2)$ values are due to proton excitations out of the magic $Z = 50$ core. Only recent large-scale shell model calculations have been able to reproduce the experimentally observed trend across the entire isotopic chain in a consistent manner [142], meaning without varying the effective charges. As even-more neutron deficient nuclei become available for study at facilities such as FRIB, there is a need for reliable measurements in order to benchmark theoretical calculations and to track the evolution of collectivity in this important region of the nuclear chart.

The $Z = 48$ Cd isotopes, located just two protons below Sn, are prime candidates for displaying the underlying nuclear physics in this region. Perhaps surprisingly, there is no evidence for proton

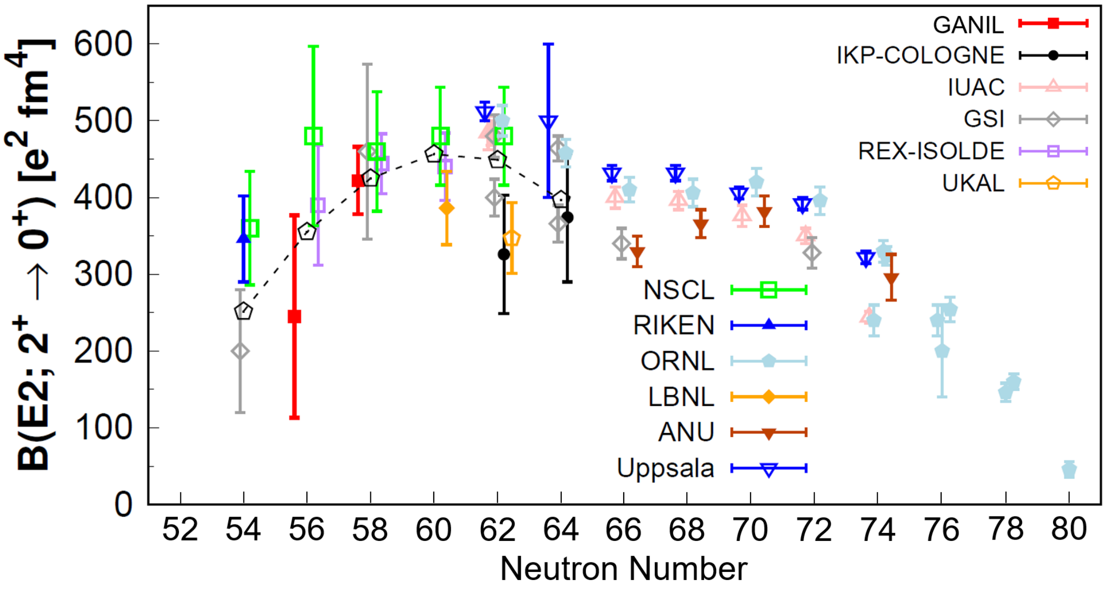

Figure 4.1: Evolution of $B(E2)$ values in the even-N $^{104-130}$Sn isotopes. The pentagons connected by dotted lines are shell model calculations from [123]. Figure adapted from [123] with data from [124, 125, 126, 127, 128, 129, 57, 130, 131, 132, 133, 134, 135, 120, 136, 137, 138, 139, 140, 141].

excitations across the $Z = 50$ shell gap in the Cd isotopic chain. Instead, the $B(E2)$ values decrease smoothly from mid shell ($A \approx 116$) out to the closed neutron shells at $A = 98$ and $A = 130$. The evolution of $B(E2)$ values of the Cd isotopes is shown in Fig 4.2.

While there is a slight asymmetry about mid shell in the Cd $B(E2)$ values, there is no sign of the strongly enhanced collectivity in the low-mass isotopes as there is for the Sn isotopic chain. The evolution of collectivity in Cd nuclei is generally well-described by conventional shell model calculations [147]; more recent calculations have attempted to capture the small asymmetry by considering the interplay of quadrupole and paring correlations [151].

Prior to this work, the known information on the lowest-lying levels in ^{106}Cd primarily stemmed from two Coulomb excitation measurements, one performed in the 1960s by Milner *et. al.* [149] and another from the 1970s by Esat *et. al.* [98]. In 2016, an excited-state g-factor measurement of ^{106}Cd by Benczer-Koller *et. al* [145] allowed for the extraction of lifetimes via the Doppler-shift-attenuation method from the observed, prominent γ-ray line shapes. The lifetime reported for the

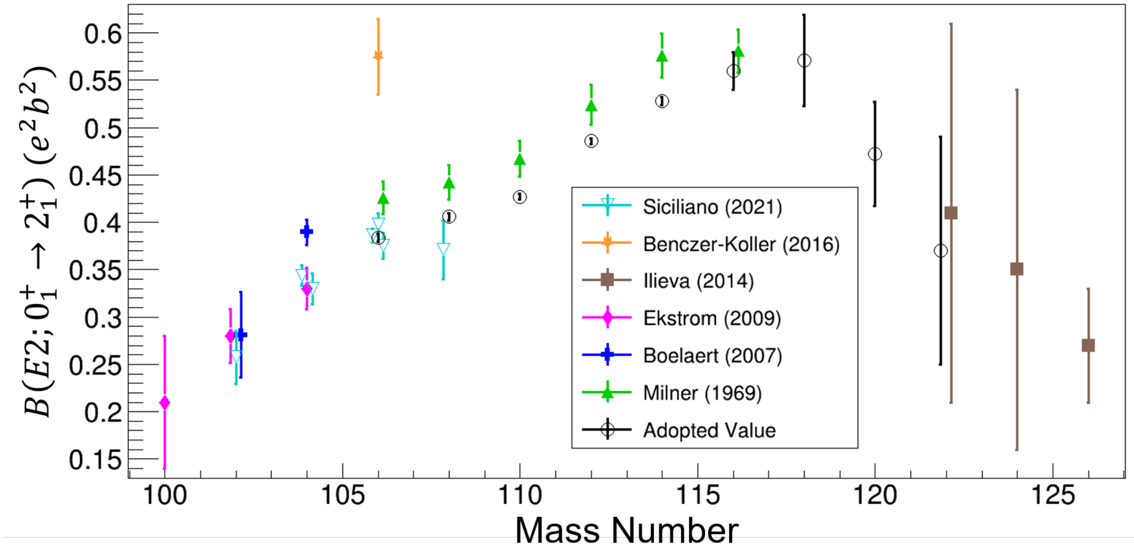

Figure 4.2: Evolution of $B(E2)$ values in the even-A $^{100-126}$Cd isotopes. Data from Siciliano [143, 144], Benczer-Koller [145], Ilieva [146], Ekstrom [147], Boelaert [148], Milner [149], and Adopted [150]. These data come from a mix of lifetimes measurements and Coulomb excitation.

2_1^+ exited state of ^{106}Cd from Ref. [145] was 33% below the previous literature value. As can be clearly seen from Fig 4.2, this implies a significant increase of the ^{106}Cd $B(E2)$ value.

The results from Ref. [145] not only disagree with the prior results for ^{106}Cd, they are also a major deviation from the systematics observed for the Cd isotopic chain. This is at odds with shell model predictions which have had success in describing the Cd $B(E2)$ values, as mentioned. Beyond the 2_1^+ excited state, several lifetimes for other excited states were reported in [145] which also disagree with the adopted values; resolving these discrepancies was also a goal of this work.

To extend the existing information on collectivity and shape to states previously out of reach, and to address the discrepancies that appeared with the most recent[1] measurement, an inverse-kinematics sub-barrier-energy Coulomb excitation experiment on ^{106}Cd was performed. This work is the first Coulomb excitation measurement of ^{106}Cd which employs modern accelerator facilities and particle and γ-ray detection arrays, and it uses the highest-Z probe yet.

---

[1] The results for ^{106}Cd from Ref. [145] were the most recent at the time the experiment discussed in this work was performed; two other experiments have been performed since [152, 144].

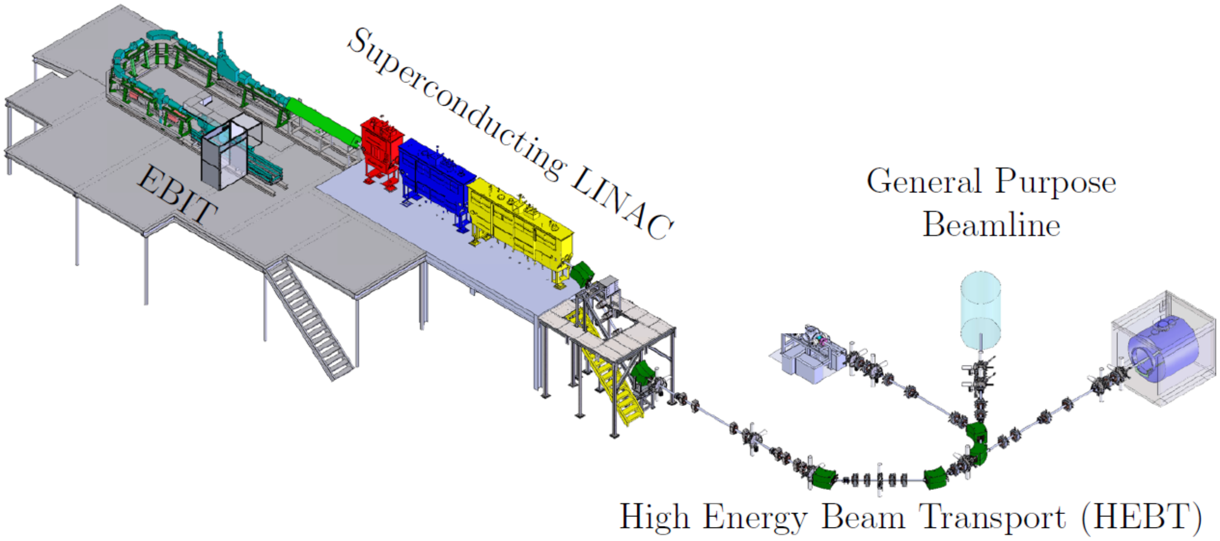

Figure 4.3: Layout of the ReA3 facility.

4.2 Experimental Details

The experiment was performed at the ReA3 [101] facility at NSCL [45]. As ^{106}Cd is a stable nucleus, the NSCL's coupled cyclotrons and A1900 fragment separator [153] were not needed to produce the ^{106}Cd beam. Instead, stable ^{106}Cd nuclei were vaporized and injected into the NSCL's electron-beam ion trap (EBIT) [154] where they were charge bred to 37+. An EBIT facility uses an electron beam to generate an electric field which confines the trapped ions radially; an external electric field is applied which axially confines the ions. While trapped, the ions will collide with the electron beam, which removes electrons from the ions thus increasing their charge state. Once the desired charged state is reached, the axial confinement is removed and the ions can leave the trap.

After charge-breeding, the 37+ charge state was selected using a magnetic separation system and the ions were injected into the ReA3 linear accelerator (LINAC). For acceleration, ReA3 uses a room-temperature radio-frequency quadrupole followed by the superconducting LINAC. The ionized ^{106}Cd atoms were accelerated to the desired energies and delivered to the JANUS setup located at the ReA3 general purpose beamline. An overview of the ReA3 facility is shown in Fig. 4.3.

The experiment consisted of three separate settings. Two settings used a 0.92 mg/cm^2 ^{208}Pb target, while the third employed a 0.98 mg/cm^2 ^{48}Ti target. For the two settings on the ^{208}Pb target, the ^{106}Cd nuclei were accelerated to 4.36 and 4.03 MeV/u; these energies are 99% and 91%, respectively, of the Coulomb barrier for ^{106}Cd impinged on ^{208}Pb. For the ^{48}Ti target, the ^{106}Cd beam was accelerated to 3.0 MeV/u, which is the Coulomb barrier of ^{106}Cd on ^{48}Ti.

The use of a ^{208}Pb target has several advantages. Its high Z increases the Coulomb excitation cross section for the impinging ^{106}Cd due to the strong electric field. Further, ^{208}Pb is doubly-magic, and as such it is very difficult to excite. In fact, no γ-ray transitions from excited states in ^{208}Pb were seen in this work. This provides an essentially background-free spectrum of γ-ray transitions from ^{106}Cd, which simplifies the data analysis. The use of two beam energies on the ^{208}Pb target enhances the sensitivity to the nuclear matrix elements due to the strong dependence of the Coulomb excitation cross section on the bombarding energy. The higher energy enhances the population of excited states beyond the 2_1^+ because the nuclei come closer together, increasing the electromagnetic field strength. The lower bombarding energy increases the sensitivity to the reorientation effect since the interaction time is increased.

The ^{48}Ti target provides its own, separate set of advantages. ^{48}Ti is not a magic nucleus, so it will be appreciably Coulomb excited by the impinging ^{106}Cd beam. As the spectroscopic data of the low-lying states ^{48}Ti are very well known [150], the observed target excitations can be used to define an absolute normalization for the measurement. The matrix elements of ^{106}Cd can be determined relative to this normalization without knowledge of the absolute beam rate or detection efficiencies, which significantly reduces systematic uncertainties. This analysis technique is described in more detail later in Section 4.5.

The target thicknesses were confirmed by measuring the energy loss of ^{4}He nuclei (α particles) which passed through them. The α particles where emitted from a radioactive ^{241}Am source, and their energies were measured both directly after emission and with the target placed in front of the ^{241}Am source. The energy loss measurements were performed at various locations on the targets' surfaces to confirm their uniformity, and SRIM [155] calculations were performed to

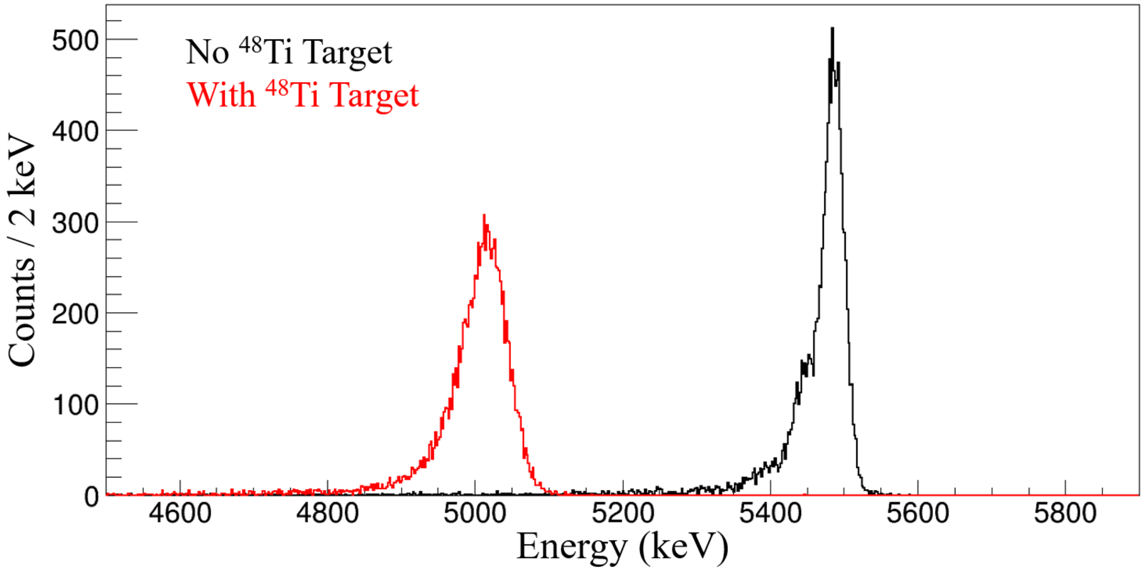

Figure 4.4: The observed energy of α particles emitted from a ^{241}Am source. The measurement was performed both with (red) and without (black) the target in front of the source. The energy difference between the two the measurements is the energy lost in the ^{48}Ti target and allows for a determination of the target thickness. Note the red spectrum is broader due to energy straggling.

extract the thickness from the measured energy loss. The spectra which resulted from an energy loss measurement with the ^{48}Ti target are shown in Fig. 4.4.

4.3 Data Analysis

As mentioned in Chapter 3, the JANUS DAQ is free-running, and all recorded signals are correlated offline based on a comparison of timestamps. For this analysis, a correlation window of 10 μs was used; signals with timestamps less than 10 μs apart are grouped together to define a single event. The free-running JANUS DAQ has another significant consequence: the vast majority of data collected is room-background γ-rays recorded in SeGA. Thus, the time-correlated events were filtered such that only events which contain a signal from the Si detectors were considered.

Since the Si silicon detectors are double-sided, a single particle entering one of the detectors will create two signals: one signal from the sector side and one from the ring side. In order to utilize the segmentation of JANUS, a ring and a sector must be paired together for each incident particle. The correlation of rings to sectors was done based on the energy deposited in either segment. First, all signals were ordered by their energies. Then, starting with the highest energy segments, a ring and sector were paired together if the ring energy was within ±10% of the energy deposited in the sector.

Due the geometry of the setup and particular kinematics of ^{106}Cd scattered by ^{208}Pb, it is possible for both the scattered ^{106}Cd and recoiling ^{208}Pb to enter the same ring for some scattering events. When this happens, the energy they deposit will be summed by the ring's electrical contact. As the particles must emerge back-to-back in the LAB frame to conserve momentum, they will enter opposite sectors. To account for this, an additional condition was used to correlate rings to sectors. If the sum of two sector energies was found to be within ±10% of a ring energy, each sector was paired to the ring. This process recovered both the ^{106}Cd and ^{208}Pb.

4.3.1 High-Energy Setting

With the above data processing applied, the kinematic curve from the downstream silicon detector during the higher-energy setting on the ^{208}Pb target is shown in Fig 4.5. Specifically, this figure shows the energy recorded by the sector plotted against the number of its correlated ring. As can be clearly seen, the scattered ^{106}Cd nuclei are well-separated from the recoiling ^{208}Pb, and the kinematic curves follow the expected shapes. A small amount of recoiling ^{12}C nuclei are also visible; these come from a thin carbon backing used to support the target.

The observed kinematic curves enable unambiguous event-by-event particle identification and characterization of the scattering process. As discussed in Chapter 3, knowledge of the scattering angle for either reaction product is sufficient to determine the CM scattering angle and thus uniquely determine the kinematics. The energy of the particle is only used to discriminate between the two reaction products. As such, no energy calibration of the silicon detectors was necessary and the energy axis in Fig. 4.5 corresponds to the raw ADC value recorded by the digitizing modules. This is true of all PID plots shown in this work. Note particle discrimination is only necessary in the forward silicon detector as the target nuclei cannot recoil backwards.

As mentioned previously, both the ^{106}Cd and the ^{208}Pb can enter the same ring for some

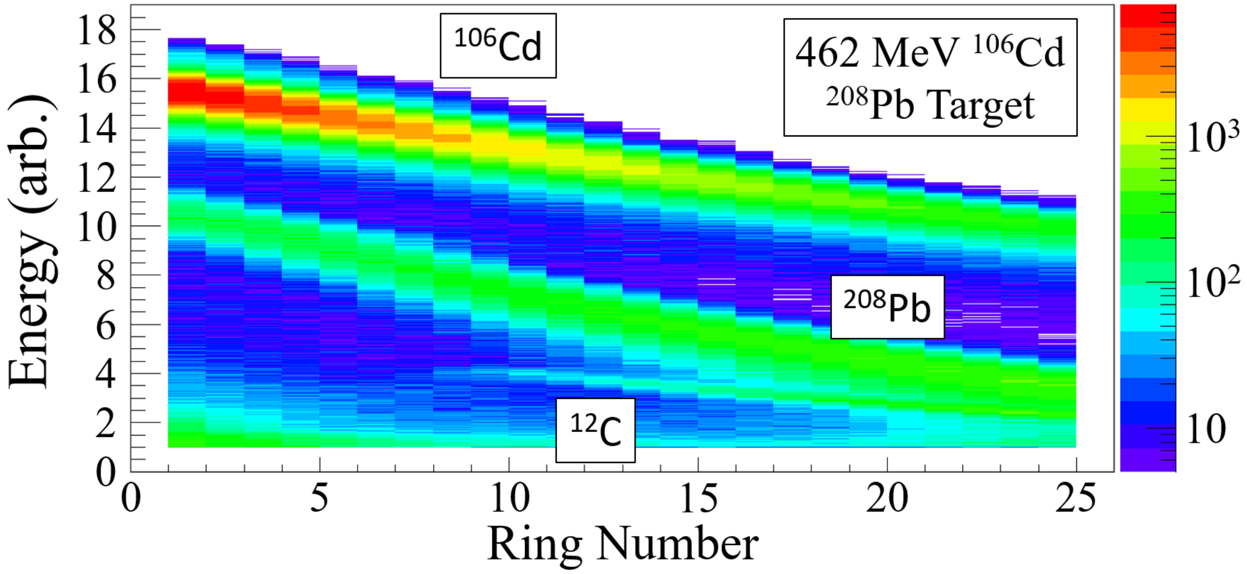

Figure 4.5: The observed kinematic curve for the higher-energy setting on the ^{208}Pb target. The energy recorded by the sector side is used. The ^{106}Cd and ^{208}Pb nuclei are clearly visible and distinguishable, as are ^{12}C nuclei from the target backing. Note that, for clarity, bins with less than five counts are excluded from this figure and a low-energy threshold has been applied. Figure adapted from [103].

scattering events. Since they always enter opposite sectors, this affect is not visible in Fig. 4.5. The same kinematic curve is shown in Fig. 4.6, except in this figure the ring energies are used; the energy summing is clear in the outer rings, centered on ring 22. The combined information from the ring and sector is still sufficient to discriminate the two nuclei, so this does not hinder the data analysis.

4.3.1.1 Particle-Gamma Coincidences

Using the kinematic curves shown in Fig. 4.5, either the ^{106}Cd or ^{208}Pb nuclei can be selected, and one can observe the γ-rays recorded in coincidence by SeGA. While all signals must occur within 10 μs to be correlated into an event, this window is significantly larger than the timing resolution achievable for coincidences between SeGA and the silicon detectors. A further reduction of background γ rays can be accomplished by applying a time gate to the coincident γ rays; this gate is shown in Fig. 4.7.

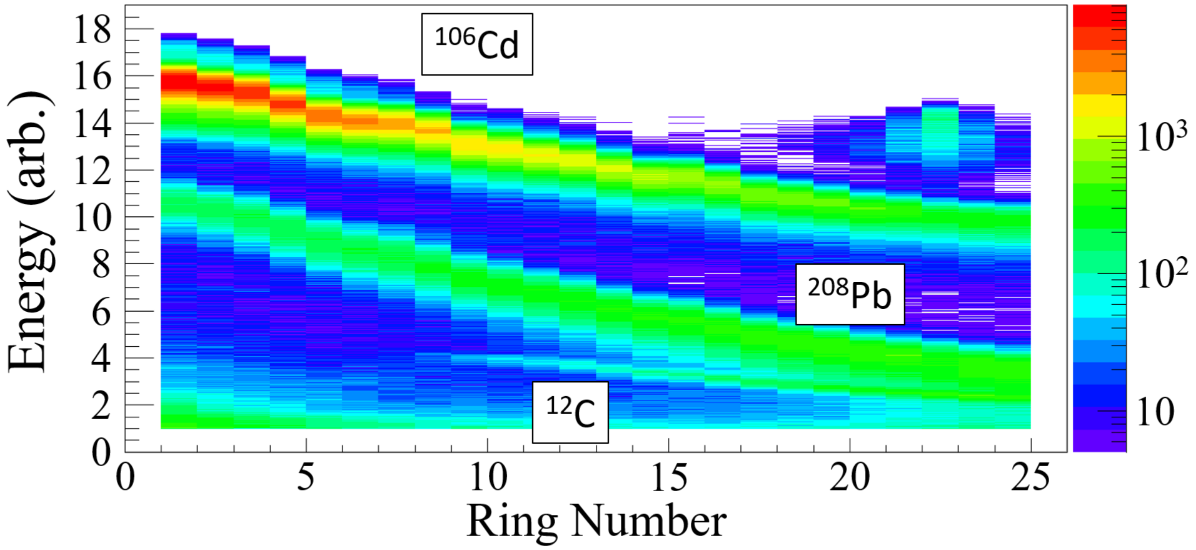

Figure 4.6: Identical to Fig. 4.5, except the energy recorded by the ring is used. The energy summing due to both the ^{106}Cd and ^{208}Pb entering the same ring is clear in the outer rings.

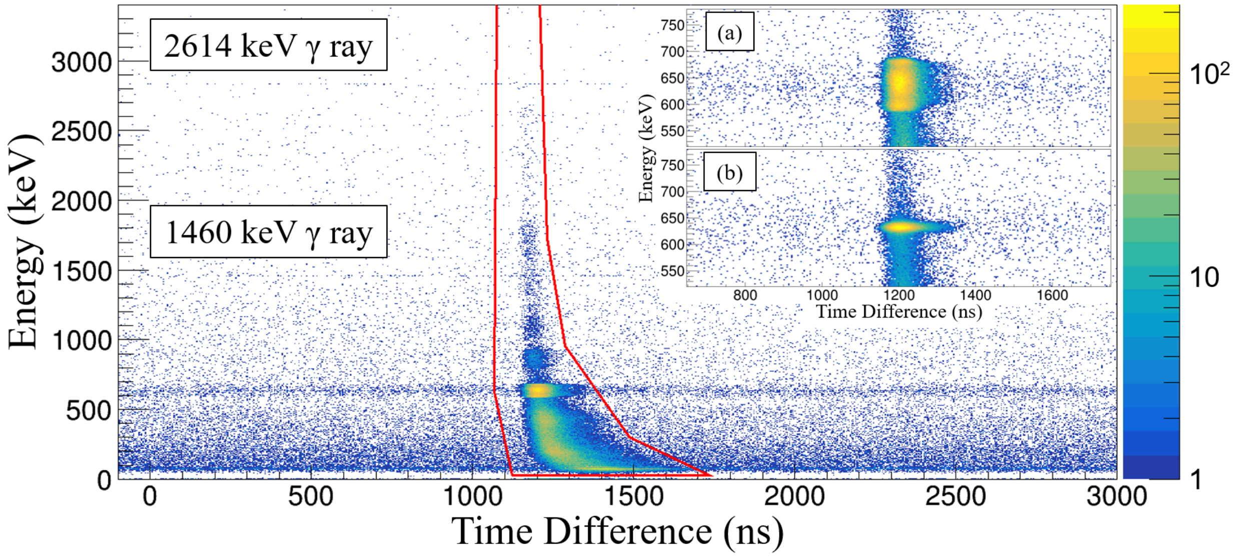

Figure 4.7: The γ-ray energy plotted against the time difference between the particle and γ ray. The gate used to select prompt γ rays is shown in red. No Doppler corrected is applied to the figure in the main panel, so room background γ rays are visible. The time walk seen at low γ-ray energy necessitates the use of a two-dimensional gate. The insets show a zoom of the region around the ^{106}Cd $2_1^+ \rightarrow 0_1^+$ transition without (a) and with (b) Doppler correction (see text).

As can be seen in Fig. 4.7, there is a γ-ray background which is uniformly distributed in time. No Doppler correction has been applied for the main figure, so two background γ-rays can be seen. These are a 1460 keV γ ray, which originates from the decay of ^{40}K into the 2^+_1 state of ^{40}Ar, and a 2614 keV γ ray, which comes from the decay of ^{208}Tl into the 3^-_1 state of ^{208}Pb. The large number of counts centered on a time difference of roughly 1250 ns are the "prompt" γ-rays. These γ rays are in true coincidence with the detected particle, as opposed to the time-random coincidences seen to either side of the prompt response. The gate drawn in red significantly reduces the time-random background in the γ-ray spectra.

In Fig. 4.7, there is a wide structure at roughly 630 keV which is also uniformly distributed in time. These are γ-rays, detected in SeGA, from the $2^+_1 \rightarrow 0^+_1$ transition in ^{106}Cd nuclei which were not detected in the silicon detectors. This is possible, for example, if a ^{106}Cd scatters with an angle less than 23°, passing through the inner radius of the silicon detector, but is still excited by the reaction. Because these γ-rays are uniform in time, some will also be present in the prompt γ-ray gate. Though these background γ-rays are very apparent in Fig. 4.7, they do not contribute appreciably to the prompt γ-ray spectrum. By applying the same gate to a region away from the prompt response, it was determined that less than 3% of the total statistics collected in prompt γ-ray spectra was due to time-random coincidences.

When Doppler-correction is applied to the prompt γ-ray spectrum (see Sect. 4.3.1.2), γ rays in true coincidence with detected ^{106}Cd nuclei will form a sharp peak. The time-random γ-rays from undetected ^{106}Cd will be broadened as the Doppler-correction is based on a particle which did not emit that γ-ray. This is shown in the insets of Fig. 4.7. Inset (a) is a zoom of the region around the ^{106}Cd $2^+_1 \rightarrow 0^+_1$ transition without Doppler-correction applied; inset (b) shows the same region with Doppler-correction applied. Clearly, only the true prompt γ-rays are corrected, while the time-random γ-rays are broadened. With Doppler-correction applied, much less than 1% of the statistics in the region directly around a Doppler corrected peak is due to time-random γ rays. This negligible contribution is easily accounted for when determining the background from the prompt γ-rays.

The time-random γ rays seen in Fig. 4.7 make a time gate necessary. Without this gate, the time-random contribution to the γ-ray spectra would increase roughly 20-fold and no longer be negligible. Also seen in Fig. 4.7 is a significant "walk" of the time difference for low-energy prompt γ rays. This is caused by the use of a simple leading-edge trigger for timestamp determination combined with the longer rise time of low-energy signals in large-volume germanium detectors. This walk necessitates the use of a two-dimensional gate instead of simply restricting the particle-γ time difference.

4.3.1.2 Doppler Correction

As discussed in Chapter 3, γ rays emitted from a moving source will be Doppler shifted. For the higher-energy setting on the ^{208}Pb target, the velocity of the ^{106}Cd nuclei is in the range $0.03 < \beta < 0.09$ depending on the scattering angle, which implies a significant Doppler shift. The Doppler effect can be seen clearly by correlating the γ-ray energy with two different angles, shown in Fig. 4.8 for γ-rays in coincidence with forward-scattered ^{106}Cd.

The top left panel of Fig. 4.8 shows the correlation of the LAB-frame γ-ray energy with the angle θ_{Dop} between the ^{106}Cd momentum and the γ-ray momentum; this is exactly the angle in the Doppler formula Eq. 3.18 and the angle indicated in Fig. 3.13. As can be seen, γ-rays emitted with $\theta_{\text{Dop}} > 90^\circ$ are shifted to lower energies, and γ-rays emitted at $\theta_{\text{Dop}} < 90^\circ$ are shifted to higher energy. The bottom panel shows the correlation with the difference between the azimuthal coordinates of the particle and γ-ray momentum vectors, that is $\phi = \phi_p - \phi_\gamma$. γ rays emitted with $\phi \approx \pi$ are shifted to low energy, and γ rays emitted with $\phi \approx 0, 2\pi$ are shifted to high energy.

Correcting for the Doppler effect is possible with JANUS due to the high segmentation of both SeGA and the silicon detectors. The detected particle's momentum direction is determined by the combined ring and sector information from the silicon detectors. The scattering angle, determined by the ring, is used to deduce the particle's velocity via Eqs. 3.10 to 3.12. For this analysis, an event-by-event β determination was used, and a small correction was applied to account for the energy loss of the particle in the target. Since the segment centers were used for the position

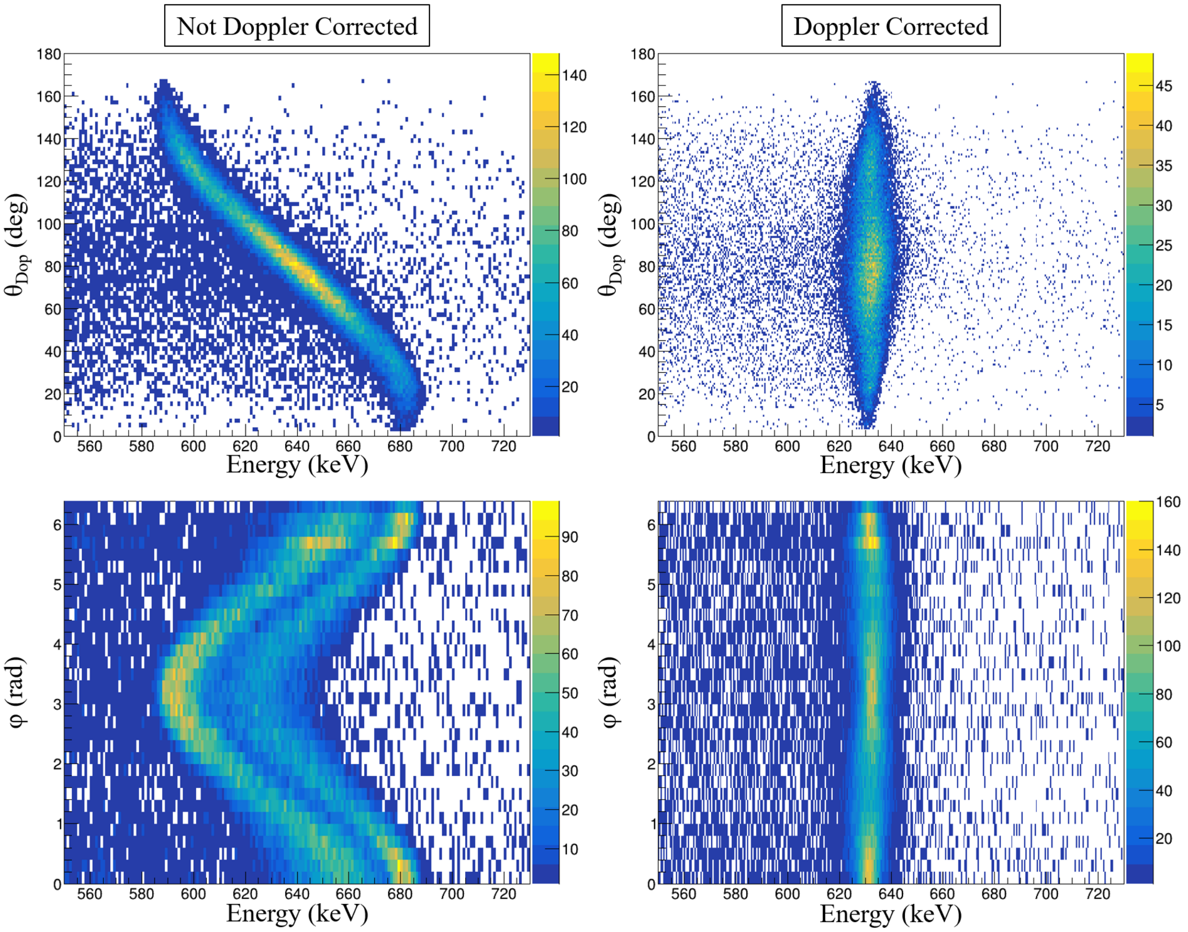

Figure 4.8: Observed γ-ray correlations for the 632 keV $2_1^+ \rightarrow 0_1^+$ transition in ^{106}Cd. The left panels are not Doppler corrected, the right panels are. The top two panels show the correlation of the γ-ray energy with the angle between the particle and γ ray. The bottom panels show the correlation with the ϕ angle explained in the text.

determination, each ring corresponds to specific β. As such, 72 different β values were used: 24 for forward-scattered ^{106}Cd, 24 for the ^{208}Pb recoils, and 24 for back-scattered ^{106}Cd.

The γ-ray momentum direction is determined by the segmentation of SeGA. Just as with the silicon detectors, the center of the segment was used to define the γ-ray position in SeGA. Due to the nature of γ-ray interactions discussed in Chapter 3, it is possible for multiple segments in a SeGA detector to record an energy deposition from the same γ ray. When this situation occurs, the segment which recorded the largest energy deposition is chosen to define the position. Note that the total γ-ray energy is always determined by the central contact; segment energies are only used to choose which segment is used for the position determination. See, for example, Ref. [115] for

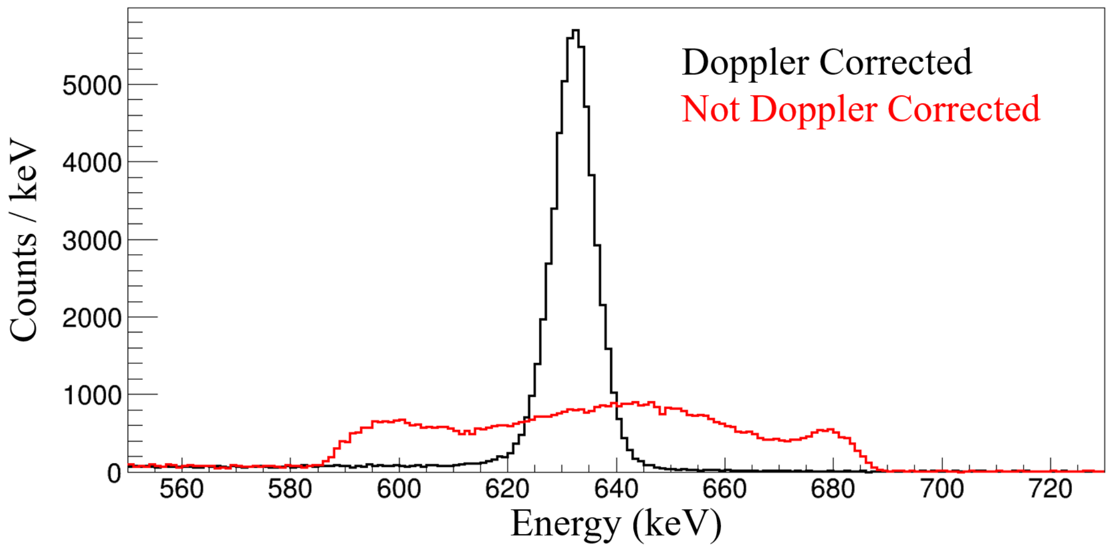

Figure 4.9: Doppler corrected γ-ray spectrum compared to the uncorrected spectrum for forward-scattered ^{106}Cd from the higher-energy setting on the ^{208}Pb target. The resolution of the Doppler-corrected peak is 1.5% FWHM.

a description of a tracking algorithm which can be used to determine the first γ-ray interaction in segmented germanium detectors.

After determining the particle velocity and the direction of both the particle and γ-ray with the above techniques, correcting for the Doppler effect simply entails adjusting the γ-ray energies recorded in SeGA by using Eq. 3.18. The right panels of Fig. 4.8 show the angle correlations for the Doppler-corrected γ-ray energies. As is clear, the angle-dependence of the γ-ray energy is removed by the Doppler correction, and a vertical line is visible at 632 keV, which the energy of the $2_1^+ \rightarrow 0_1^+$ transition in ^{106}Cd.

Fig. 4.9 shows the Doppler-corrected peak for the $2_1^+ \rightarrow 0_1^+$ transition in ^{106}Cd compared to the non-Doppler-corrected spectrum for forward-scattered ^{106}Cd. The energy resolution achieved in this work for the Doppler-corrected $2_1^+ \rightarrow 0_1^+$ transition is 1.5% FWHM. For back-scattered ^{106}Cd, this resolution improves to roughly 0.8% due to the smaller velocity of the back-scattered projectiles. Marginally better resolution was achieved for the lower-energy setting on the ^{208}Pb target, and a resolution of 1.0% was attained during the ^{48}Ti target setting. This is again due to the velocity.

As discussed in Chapter 2, the Coulomb excitation cross section has a strong dependence on the scattering angle. As such, the sensitivity of the measurement can be increased by subdividing the data into ranges based on the particle scattering angle. For the higher-energy setting on ^{208}Pb, the forward-scattered ^{106}Cd projectiles were divided into four angular ranges: ^{106}Cd detected in rings 1 to 6, 7 to 12, 13 to 18, and 19 to 24. The data from recoiling ^{208}Pb detection were divided into two ranges: rings 1 to 12 and 13 to 24. Back-scattered ^{106}Cd nuclei were considered as a whole. The Doppler-corrected γ-ray spectra collected in coincidence with each of these angle ranges is shown in Fig. 4.10.

From a close inspection of Fig. 4.10, the angular-dependence of Coulomb excitation can be observed. As the scattering angles increases, there is an increase in the number of γ-rays detected from transitions depopulating states beyond the 2_1^+ state, relative to the number of $2_1^+ \rightarrow 0_1^+$ transition γ rays. For example, the $6_1^+ \rightarrow 4_1^+$ transition is not observed in panels (a) and (b); it is just barely visible in panels (c) and (d), and it is plainly visible in panels (e) to (g). This is a clear indication of the enhancement of multi-step Coulomb excitation due to the increased electric field strength and interaction times which occur for large scattering angles.

The Doppler-corrected peaks in panel (f) of Fig. 4.10 have noticeably worse resolution than in all other angle ranges. Panel (f) corresponds to detection of the recoiling ^{208}Pb in rings 1 to 12 of the forward silicon detector. In this region, the ^{106}Cd nuclei have scattering angles near 90°, which means they scatter essentially straight into the target material. These ^{106}Cd nuclei will lose energy and come to a stop in the target material. Depending on the precise scattering angle, which determines the precise distance the ^{106}Cd nuclei travel while still in the target material, the ^{106}Cd can lose very different amounts of energy. This results in a large range of ^{106}Cd velocities at the time of decay, including fully-stopped ^{106}Cd. This worsens the Doppler correction for this angular range.

The affect of the ^{106}Cd nuclei stopping in the target is shown in Fig. 4.11. In the non-Doppler-corrected correlation (left panel), the γ rays emitted from in-flight ^{106}Cd form a curve similar to the curve shown in Fig. 4.8, while γ rays emitted from ^{106}Cd at rest form a sharp line at 632 keV.

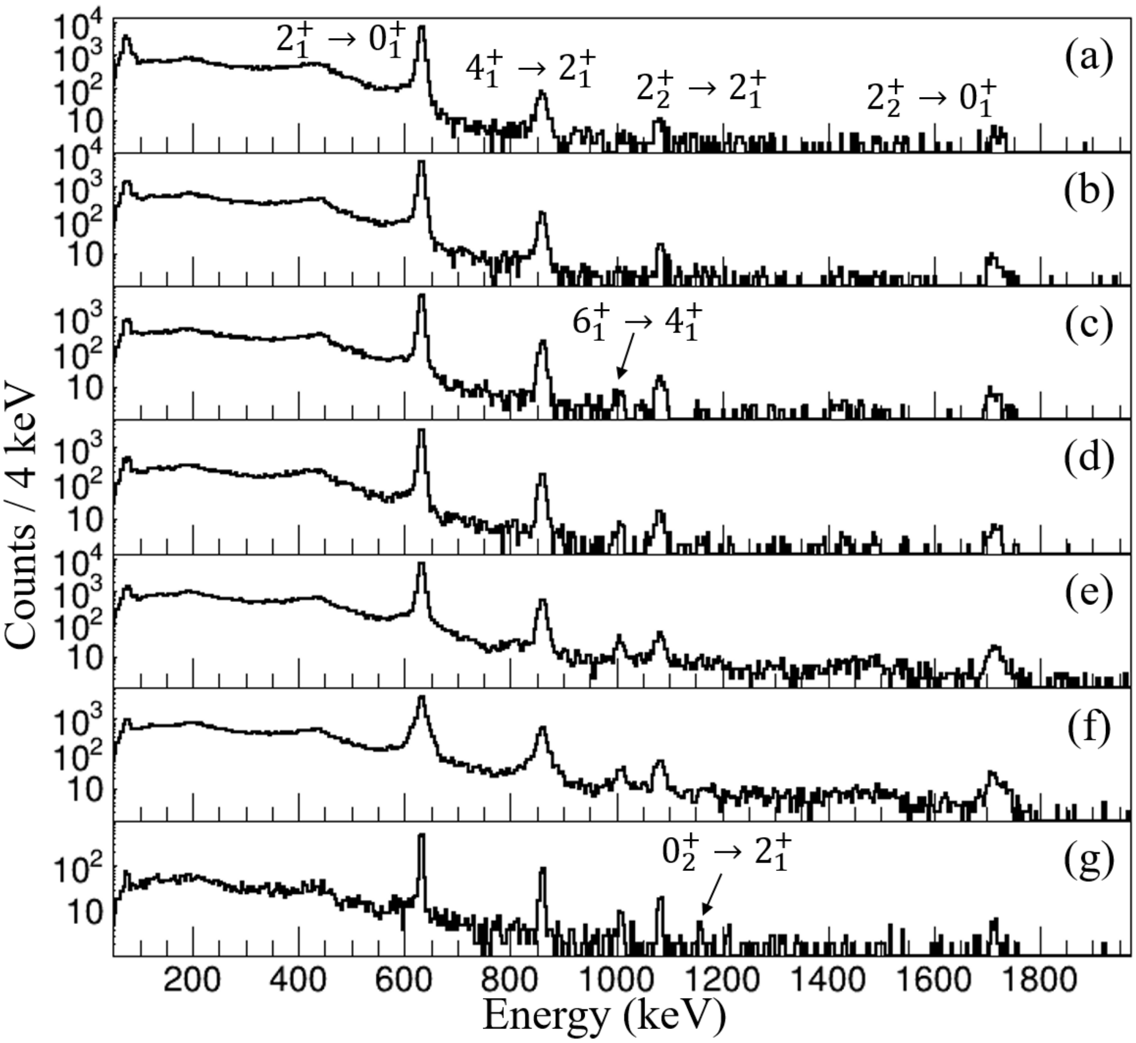

Figure 4.10: Total Doppler-corrected γ-ray spectra collected during the high-energy setting on the ^{208}Pb target. Observed γ-ray transitions are indicated. Each panel corresponds to a particular angle range as described in the text, and the panels are in order of increasing CM scattering angle.

The blurring between the stopped and in-flight components is due to the very strong dependence of the ^{106}Cd velocity on the scattering angle, as mentioned. When Doppler-correction is applied to this angular range (right panel), the stopped component is incorrectly broadened.

4.3.2 Low-Energy Setting

The kinematic curve observed during the lower-energy setting (4.03 MeV/u ^{106}Cd) on the ^{208}Pb target is shown in Fig. 4.12. It is very similar to the PID from the high-energy setting except for

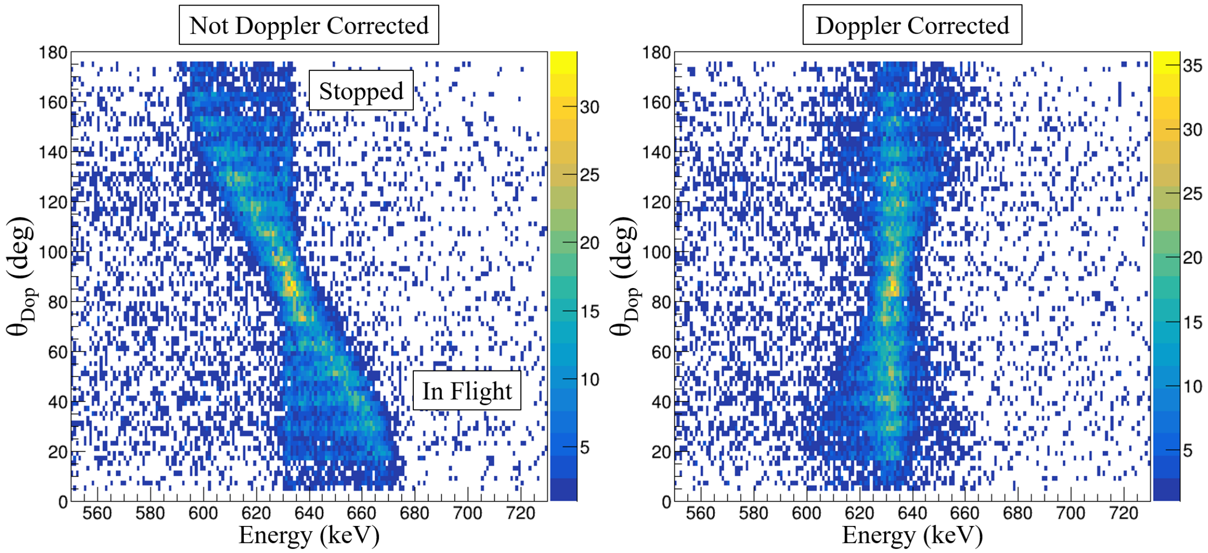

Figure 4.11: Correlation of E_γ with θ_{Dop} for ^{208}Pb recoils detected in rings 1 to 12 from the higher-energy setting. The left panel is not Doppler corrected, the right panel is. The effect of ^{106}Cd slowing down in the target is clear.

a small shift to lower energies. This data was also subdivided into scattering angle ranges. The forward-scattered ^{106}Cd were divided into three angular ranges: rings 1 to 8, 9 to 16, and 17 to 24. The data from target detection and back-scattered ^{106}Cd was divided identically as in the high-energy setting. The γ-rays detected in coincidence with this data is shown in Fig. 4.13.

The details of the data analysis, kinematics, and Doppler-correction for the lower-energy setting are essentially identical to the higher energy setting, so they won't be repeated. The dependence of the Coulomb-excitation cross section on the bombarding energy can roughly be seen by comparing Figs. 4.10 and 4.13. In the lower-energy setting, the $6_1^+ \rightarrow 4_1^+$ transition is not visible for forward-scattered ^{106}Cd (panels (a) to (c) in Fig. 4.13), which is unlike in the high-energy setting. While the Coulomb-excitation cross section to all excited states is reduced by the lower beam energy, multi-step processes, which are necessary to populate the 6_1^+ state in ^{106}Cd, are more severely hindered.

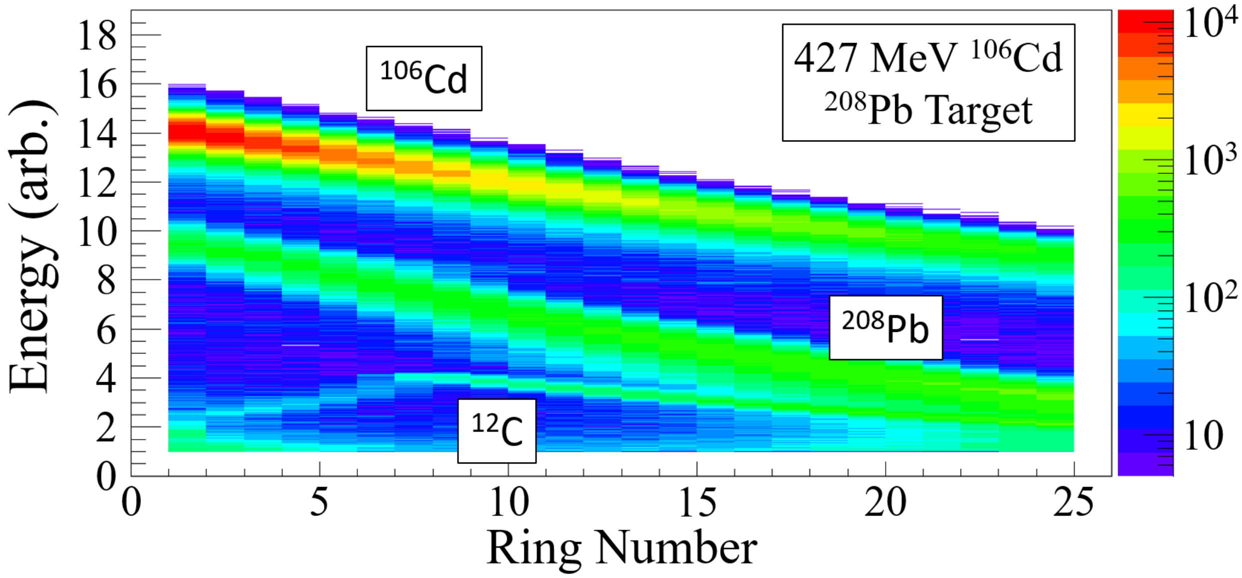

Figure 4.12: Kinematic curve for the low-energy setting on the ^{208}Pb target. The energy recorded by the sector is used. The ^{106}Cd and ^{208}Pb nuclei are clearly visible and distinguishable, as are ^{12}C nuclei from the target backing. Note that, for clarity, bins with less than five counts are excluded from this figure and a low-energy threshold has been applied.

4.3.3 Titanium Target Setting

The final setting of the experiment impinged 3.0 MeV/u ^{106}Cd on a ^{48}Ti target. As discussed in Chapter 3, the ^{106}Cd projectiles have a double-valued kinematic curve for this setting since they are heavier than the ^{48}Ti target nuclei. The kinematic curve observed during this setting is shown in Fig. 4.14.

As is seen from Fig. 4.14, the PID from the ^{48}Ti setting is more complicated than the previous two settings. First, the expected kinematic curves of ^{106}Cd impinged on a ^{48}Ti target can be seen. The double-valued solution for the scattered projectiles forms a rough semi-circle in the first few rings. The recoiling ^{48}Ti nuclei form the high-statistics "normal" kinematic curve.

During the experiment, by observing the PID, it was discovered that the ^{48}Ti target contained a contaminant. By inspecting the γ-rays which came in coincidence with the contaminant kinematic curves, the contamination was identified as ^{182,184,186}W, which are the most commonly occurring isotopes of tungsten. With this knowledge, the kinematic curve above the expected ^{48}Ti recoils is identified ^{106}Cd nuclei which scattered off the $^{\text{nat}}$W. The curve at low energies in the outer rings

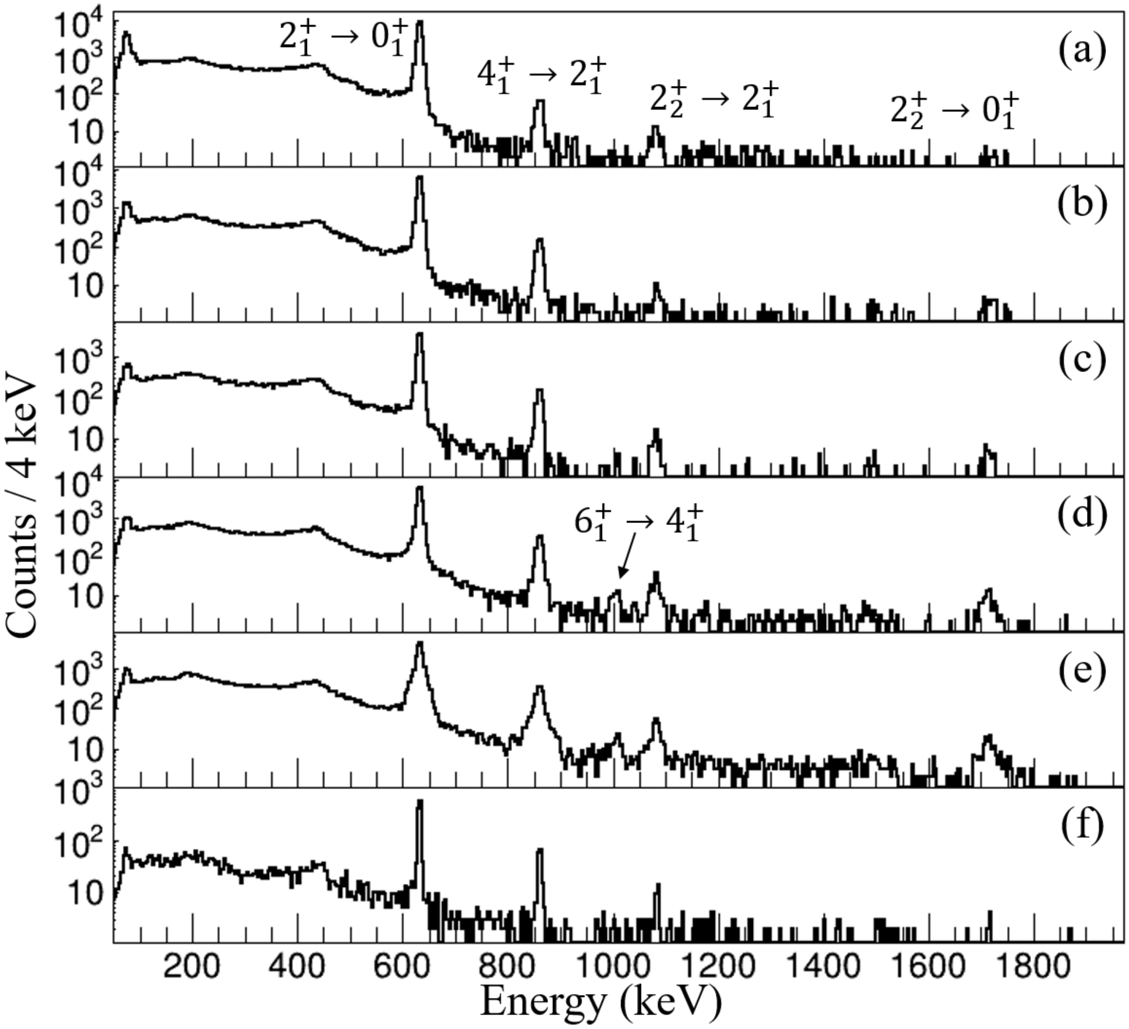

Figure 4.13: Total Doppler-corrected γ-ray spectra collected during the low-energy setting on the ^{208}Pb target. Observed γ-ray transitions are indicated. Each panel corresponds to a particular angle range as described in the text, and the panels are in order of increasing CM scattering angle.

is from the recoiling tungsten nuclei.

Several different methods were used to estimate the amount of tungsten present in the target. With knowledge of the beam rate, the number of $^{\text{nat}}$W in the target can be inferred from the number of ^{106}Cd nuclei scattered by the contamination, since this is determined by the well-know Rutherford cross section. As the low-lying states of the naturally-occurring tungsten isotopes have firmly-established lifetimes and transition rates, the number of γ-rays in coincidence with the contamination was also used to estimate the amount of tungsten present. Both a simplified estimate and a full GOSIA calculation were performed. All three of these estimates resulted in a $^{\text{nat}}$W

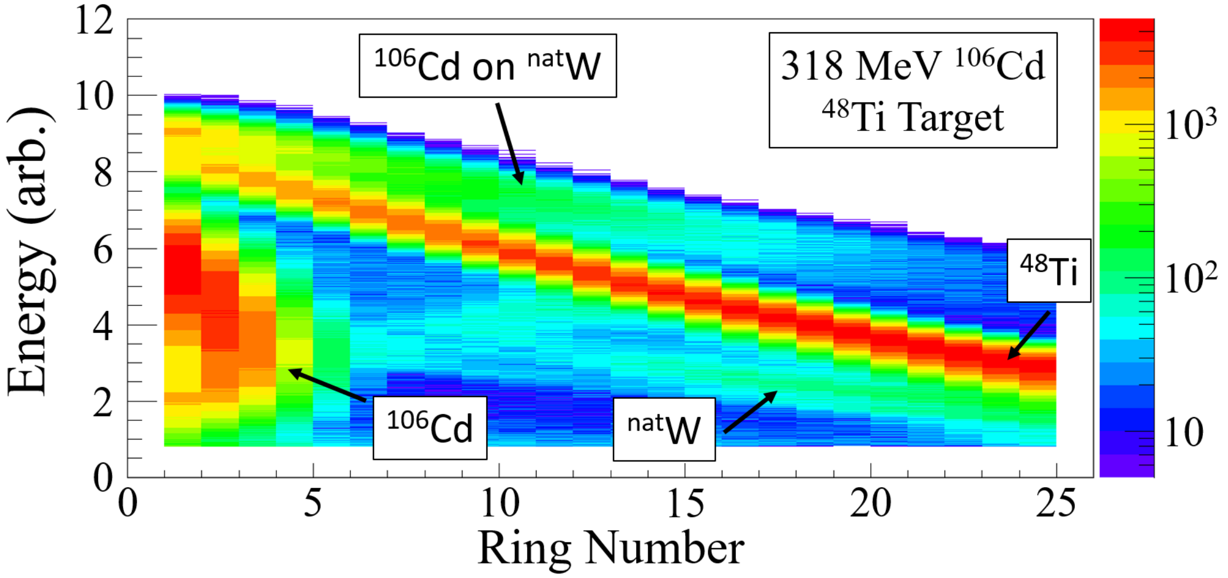

Figure 4.14: Kinematic curve for the ^{48}Ti target setting. The energy recorded by the sector side is used. Both the double-valued ^{106}Cd kinematic curve and the recoiling ^{48}Ti nuclei are clearly visible. Also visible are ^{106}Cd nuclei which were scattered by the ^{nat}W contamination; the recoiling ^{nat}W are also observed. Note that, for clarity, bins with less than five counts are excluded from this figure and a low-energy threshold has been applied.

contamination of 2-3% by mass.

Beyond the estimates from the experimental data, a precise chemical analysis of the ^{48}Ti target was performed by G. Severin and H. K. Clause. This determined that the target is composed of 3.1% tungsten by mass. This agrees well with the estimates from the experimental data and gives confidence that contamination is well understood. The contamination can largely be removed by gating on the PID plot, and the Coulomb excitation cross-section of ^{106}Cd scattered by the tungsten contamination is strongly suppressed as the bombarding energy is well below the Coulomb barrier. As such the contamination did not significantly impact the analysis.

Due to the kinematics of ^{106}Cd scattered by ^{48}Ti, both nuclei entered the forward silicon detector for nearly all recorded scattering events. As such, detection of either the scattered ^{106}Cd projectiles or the ^{48}Ti recoils corresponds to essentially the same CM angle range. For this data set, only γ-rays in coincidence with the target recoils were used for analysis, as the ^{48}Ti kinematic curve can be more easily divided into angular ranges. This data was divided into five ranges: ^{48}Ti

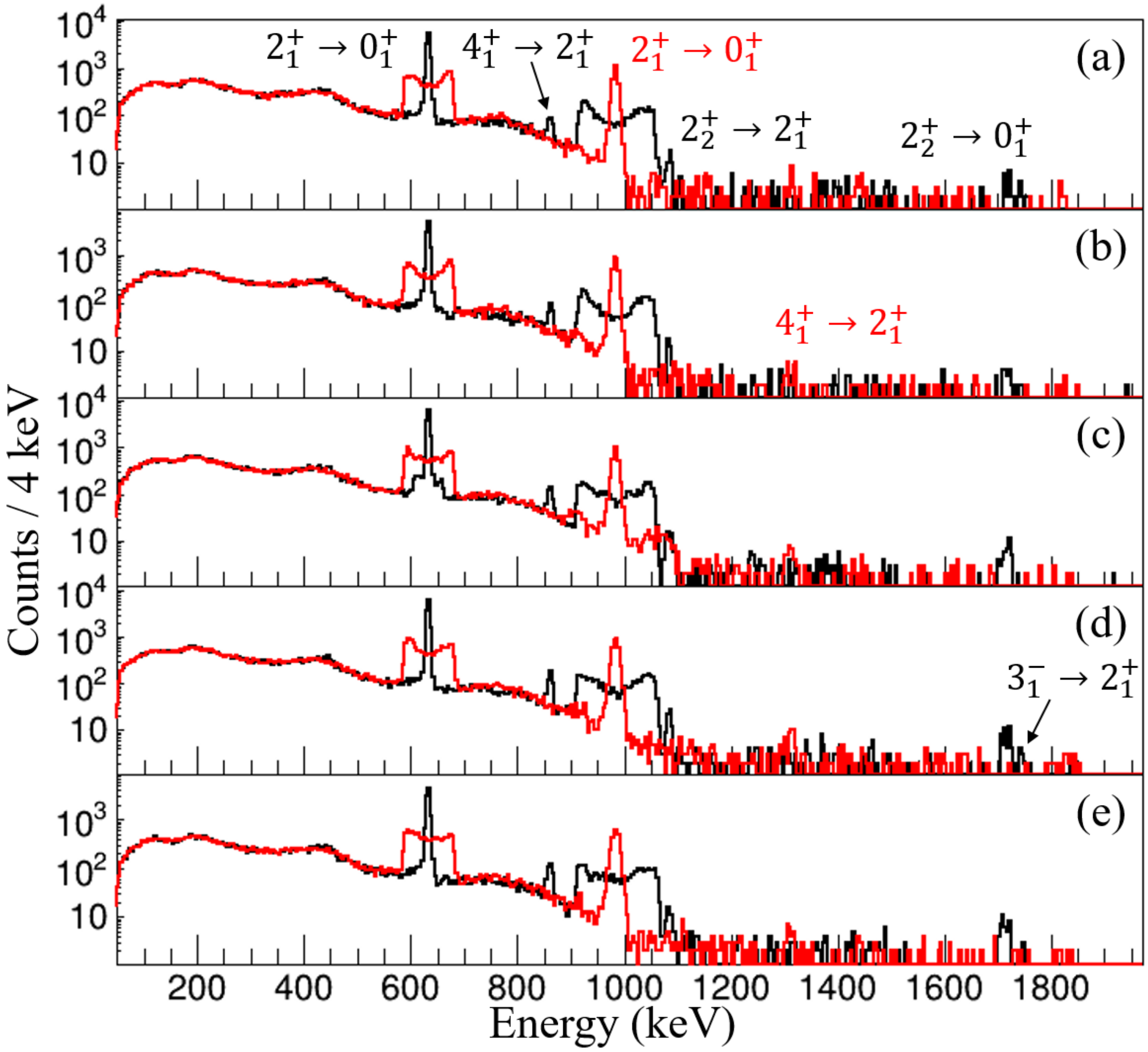

Figure 4.15: Total γ-ray spectra collected for target detection during the ^{48}Ti target setting. The black spectra are Doppler corrected for ^{106}Cd, and the red spectra are Doppler-corrected for ^{48}Ti. Observed γ-ray transitions are indicated in black for ^{106}Cd a red for ^{48}Ti. Each panel corresponds to a particular angle range as described in the text, and the panels are in order of increasing CM scattering angle.

detected in rings 1 to 5, 6 to 10, 11 to 15, 16 to 19, and 20 to 24. The γ-rays collected in coincidence with these angular ranges are shown in Fig. 4.15.

As can bee seen in Fig. 4.15, both the ^{106}Cd and ^{48}Ti nuclei were excited by the reaction. As discussed in Chapter 3, detection of one reaction product is sufficient to reconstruct the trajectory of the other, so Doppler correction can be applied to both nuclei. The Doppler-corrected peaks in panel (c) of Fig. 4.15 have two distinct components: a sharp peak, which is the expected shape, sitting on top of a broad base. This effect is not caused by the ^{106}Cd nuclei scattering into the target, which worsened the γ-ray resolution for target detection in the ^{208}Pb target settings. Because $m_P > m_T$ for the ^{48}Ti target setting, $\theta_P^{\max} = 26.9^\circ$ meaning the ^{106}Cd projectiles actually never scatter into the target.

The wide base beneath the Doppler-corrected peaks is caused by a particular feature of the reaction kinematics during this setting. As mentioned, for the large majority of recorded scattering events, both the ^{48}Ti and ^{106}Cd enter the silicon detector. For the angle range shown in panel (c), which corresponds to ^{48}Ti detected in rings 11 to 15, both particles enter the detector, but they also have roughly the same kinetic energy. For some scattering events in this region, the energy deposited in the detector by each reaction product will be essentially identical, so correlating a ring to its corresponding sector becomes ambiguous.

For these particular events, it is possible that the silicon ring the ^{106}Cd scattered into will be improperly correlated with the sector from the ^{48}Ti implant (and vice-versa). When this happens the positions determined for the nuclei are incorrect and the Doppler correction fails; this causes the broad base in panel (c) of Fig. 4.15. Note this improper correlation does not impact the observed kinematic curves, so this effect is not visible in Fig. 4.14.

In the *LAB* frame, the reaction products emerge back-to-back, which means the scattered ^{106}Cd and recoiling ^{48}Ti will always enter "opposite" sectors, i.e. sectors which are separated by 180°. Thus the improper correlation of rings to sectors corresponds exactly to a 180° rotation of the azimuthal coordinate ϕ_p of the particles' trajectories. The γ rays in coincidence with these events are seen clearly in Fig. 4.16, which shows the γ-ray energy plotted against the ϕ coordinate discussed earlier (see Fig. 4.8). The improperly correlated events can be successfully Doppler corrected by making the substitution $\phi_p \longrightarrow \phi_p + \pi$; this is shown in the right panel of Fig. 4.16. Both the simple γ-ray energy spectrum in Fig. 4.15 as well as the ϕ correlation of Fig. 4.16 can be used to extract how many γ rays are incorrectly broadened in the angle range, so this affect was successfully accounted for.

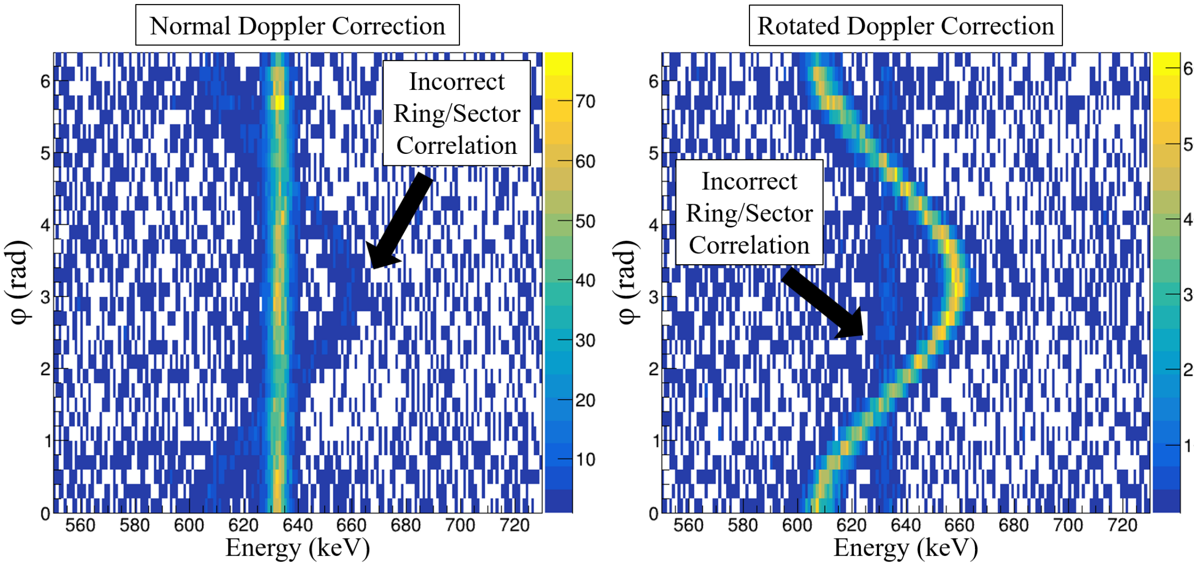

Figure 4.16: Correlation of E_γ with ϕ for ^{48}Ti nuclei detected in rings 11 to 15. The γ rays in coincidence with improperly correlated silicon events are obvious. The left panel shows the normal Doppler correction, and the right panel shows the Doppler correction with $\phi_p \longrightarrow \phi_p + \pi$.

4.4 Gamma-Ray Yields

For all angle ranges, the peak areas of all observed transitions were extracted from the γ-ray spectra shown in Figs. 4.10, 4.13, and 4.15. In order to transform the measured peak areas into actual γ-ray yields, the detection efficiency of SeGA must be known. An efficiency calibration of SeGA was performed using three γ-ray sources: ^{152}Eu, ^{226}Ra, and ^{133}Ba. As the activity of the ^{152}Eu source was the most precisely known, only this source was used for the absolute efficiency calibration. The other two sources were used for a relative efficiency calibration to extend the range of γ-ray energies beyond what is provided by the ^{152}Eu source. The efficiency data collected from all three sources, as well as the fitted efficiency curve, are shown in Fig. 4.17.

The detection efficiency of SeGA is well constrained for the γ-ray energies observed in this work, 600 keV $< E_\gamma <$ 1800 keV. At 1000 keV, SeGA provided an absolute γ-ray detection efficiency of 6.7% during this experiment. Note that, as mentioned, only the relative energy dependence of the detection efficiency is important; the absolute efficiency in not strictly necessary for the analysis presented in this work.

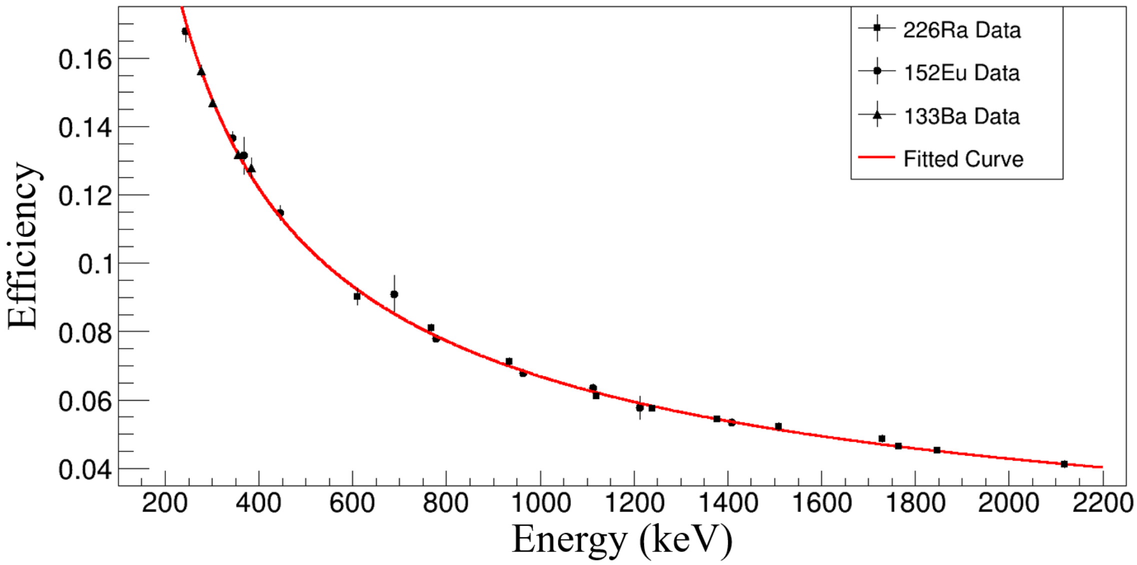

Figure 4.17: The γ-ray detection efficiency cure determined during this work for SeGA. Only the ^{152}Eu source was used for an absolute efficiency; the data from the other two sources were scaled to the ^{152}Eu data.

4.5 GOSIA Analysis

The γ-ray yield data was analyzed with a joint use of the GOSIA and GOSIA2 codes [90, 87]; a high-level description of GOSIA was given in Chapter 2. Along with the γ-ray yields as a function of scattering angle, GOSIA takes essentially all experimental conditions as input. These include the angular coverage of the particle and γ-ray detectors, the energy loss of the projectile traversing the target, the projectile's incident energy, and conversion-electron coefficients for the γ-ray decays.

The nuclear level schemes must also be provided as input. In analyses with GOSIA, excited states beyond the highest observed in experiment must be included in the calculations. These so-called buffer states can account for any unobserved feeding due to weak population of higher-lying states. Further, truncation of the network of coupled differential equations which govern the Coulomb excitation process results in an over-prediction of the population to the highest levels [90]; including buffer states makes this spurious numerical effect negligible. The level schemes for both ^{106}Cd and ^{48}Ti used during the GOSIA analysis are shown in Fig. 4.18.

Initially, the data collected on the ^{48}Ti target was analyzed independently using the Coulomb excitation code GOSIA2, which was developed specifically for a *simultaneous* analysis of projectile

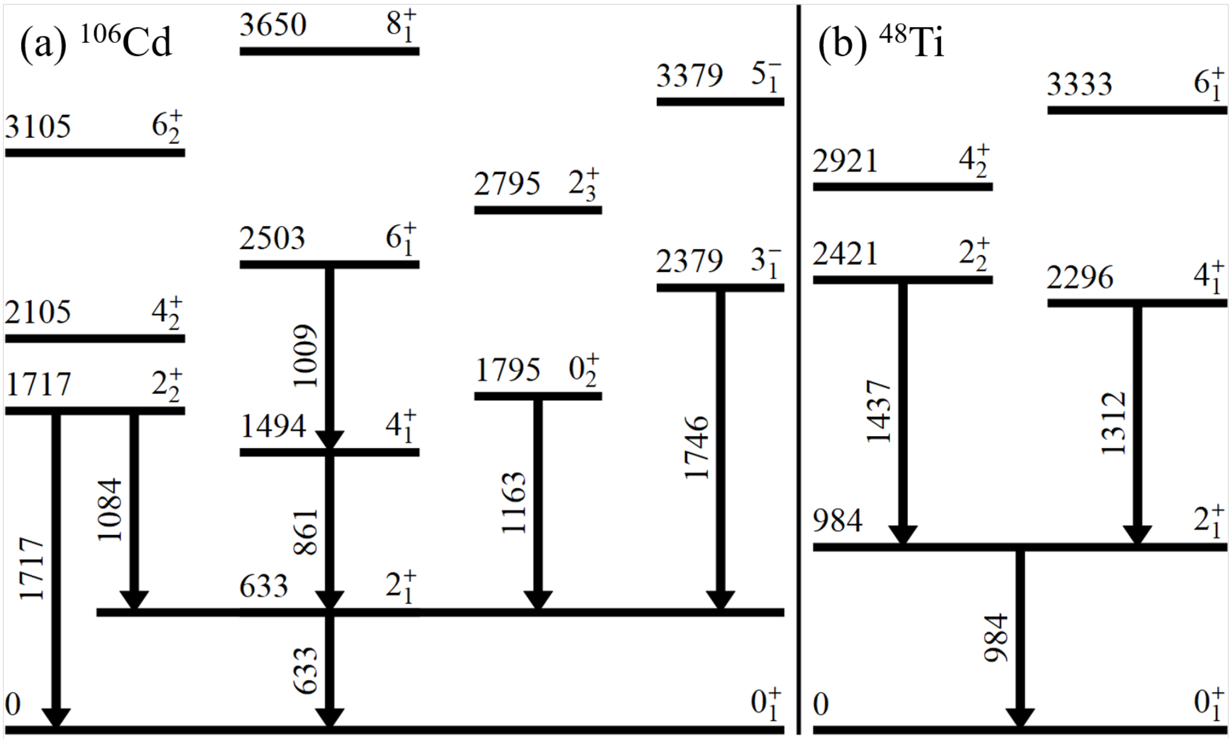

Figure 4.18: The levels schemes used during the GOSIA analysis for ^{106}Cd (left) and ^{48}Ti (right). Only γ-ray transitions observed during the experiment are indicated. States without a depopulating transition are buffer states. Energies are in keV.

and target excitations. Most commonly, GOSIA2 is used to solve the common problem of defining the absolute normalization which is needed to convert the γ-ray yields into a Coulomb excitation cross section. There are many effects which will introduce an overall scaling factor to the γ-ray yield data, such as absolute detection efficiency, the beam rate, how long data was collected, etc. Instead of requiring the absolute normalization, GOSIA introduces scaling factors to the yield calculations which account for these effects. Each angular subdivision of the three data sets, individually called "experiments" in GOSIA, is given its own[2] scaling factor which is applied to every calculated yield in that experiment. In a typical GOSIA analysis, the scaling factors are also fitted during the minimization routine and as such are additional free parameters beyond the nuclear matrix elements.

---

[2] GOSIA actually defines a unique scaling factor for every γ-ray detector in each experiment. As SeGA is always treated as "one" detector, only one normalization constant is used per GOSIA experiment.

Table 4.1: Literature data for ^{48}Ti employed during the GOSIA2 analysis. Data taken from NNDC/ENSDF [150].

State	Lifetime τ (ps)	Quantity	Value
2_1^+	5.83(14)	$2_2^+ \rightarrow 2_1^+$ Mixing Ratio	0.18(3)
4_1^+	1.10(10)	$2_2^+ \rightarrow 0_1^+/2_2^+ \rightarrow 2_1^+$ Branching Ratio	0.0514(22)
2_2^+	0.039(4)	$\langle 2_1^+ \Vert E2 \Vert 2_1^+ \rangle$	-0.234(11) eb

GOSIA2 is used to constrain strictly the scaling factors which are introduced to the γ-ray yield calculations. This is accomplished by providing the measured γ-ray yields from the ^{48}Ti target excitations along with the well-known spectroscopic data of the low-lying states in ^{48}Ti to the GOSIA2 code. This combined information is sufficient to determine the normalization. All observed transitions from ^{48}Ti were provided as input, though only the $2_1^+ \rightarrow 0_1^+$ transition is relevant as its yield is two orders of magnitude larger than the next strongest transition. The known lifetime of the 2_1^+ state in ^{48}Ti defines the average absolute scale, and its quadrupole moment constrains the relative scaling of the angular ranges. The spectroscopic data used in this analysis for ^{48}Ti is given in Table 4.1

The matrix elements of ^{106}Cd can be determined using the normalization constants defined by the ^{48}Ti target excitations. For the GOSIA2 analysis in this work, the ^{106}Cd $\langle 0_1^+ \Vert E2 \Vert 2_1^+ \rangle$ and $\langle 2_1^+ \Vert E2 \Vert 2_1^+ \rangle$ matrix elements were manually scanned while all other matrix elements in ^{106}Cd were fixed. At each point in the scan, the GOSIA2 code was used to calculate the expected ^{106}Cd yields and compare them to the measured values. The least-squares search routine was not employed for ^{106}Cd matrix elements during the GOSIA2 analysis. This process results in a two-dimensional χ^2 surface, with the best-fit matrix elements given at the minimum χ^2 value and the 1σ uncertainties given by a $\chi^2 < \chi^2_{\text{min}} + 1$ cut. No literature constraints for ^{106}Cd were used in this step of the analysis. The constrained matrix elements of ^{48}Ti were allowed to vary at each point in the scan; all stayed well within the literature uncertainties give in Table 4.1.

The second step of the joint GOSIA-GOSIA2 analysis uses the original GOSIA code. The best-fit $\langle 0_1^+ \Vert E2 \Vert 2_1^+ \rangle$ matrix element and its uncertainty extracted from the χ^2 surface are provided

Table 4.2: Literature data for ^{106}Cd employed during the GOSIA analysis. Data taken from NNDC/ENSDF [150].

Transition	Mixing Ratio	Transitions	Branching Ratio
$2_2^+ \to 2_1^+$	-1.44(11)	$4_2^+ \to 2_1^+/4_2^+ \to 4_1^+$	0.611(15)
$4_2^+ \to 4_1^+$	-0.314(22)	$4_2^+ \to 2_2^+/4_2^+ \to 4_1^+$	0.065(17)

as a constraint to this full GOSIA minimization. The three experimental settings were analyzed independently to ensure consistency and then combined into a single GOSIA calculation in order to maximally constrain the matrix elements. This was also a convenient way of creating the extensive GOSIA inputs.

During the full GOISA step of the analysis, the absolute normalization for the γ-ray yields was constrained by the GOSIA2 result for the $\langle 0_1^+||E2||2_1^+\rangle$ matrix element; in terms of defining the normalization constants, this is equivalent to the common practice of including the lifetime of the 2_1^+ excited state. However, the GOSIA2 result is an independent measurement of the ^{106}Cd $B(E2;0_1^+ \to 2_1^+)$. As such this analysis does not depend on previous lifetime measurements for ^{106}Cd at all. Considering a major motivation for this work is to resolve discrepant lifetime measurements, this is a crucial feature of the experimental scheme and data analysis procedure.

Beyond the constraint on the $\langle 0_1^+||E2||2_1^+\rangle$ matrix element, the full GOSIA calculation was constrained by the literature data for ^{106}Cd given in Table 4.2. These constraints primary affect the 4_2^+ state which was not observed during this experiment; it was included due to its close proximity to the 2_2^+ state. Additionally, the result from Ref. [156] for the mixing ratio of the $2_2^+ \to 2_1^+$ transition was included to constrain the $M1$ component of the mixed γ-ray decay.

During the full GOSIA minimization, the $\langle 0_1^+||E2||2_1^+\rangle$ matrix element is constrained but not fixed. This is because, during the GOSIA2 analysis, the matrix elements which couple to states beyond the 2_1^+ were not correct as they had not yet been determined. These incorrect couplings have an effect on the best-fit $\langle 0_1^+||E2||2_1^+\rangle$ matrix element extracted from GOSIA2, and thus this matrix element should be allowed to vary during the full GOSIA minimization in order to find a solution which best balances the GOSIA2 constraint with all three data sets.

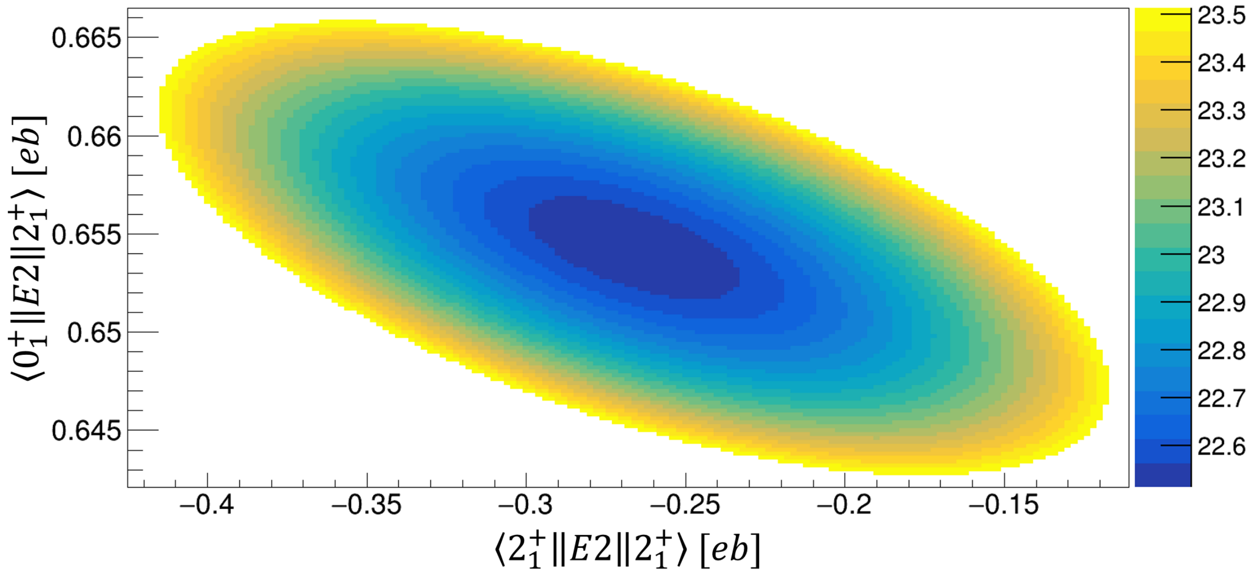

Figure 4.19: The final χ^2 surface from the GOSIA2 analysis with a $\chi^2 \leq \chi^2_{\text{min}} + 1$ restriction applied. This figure has smoothing applied to remove artifacts of the GOSIA minimization.

After convergence of the full GOSIA fit, the χ^2 surface is recreated; the matrix elements which couple to higher-lying states are now fixed at the values determined by the previous full GOSIA fit. The (more accurate) $\langle 0_1^+ || E2 || 2_1^+ \rangle$ matrix element from this new surface is then provided once again to a full GOSIA minimization, and this process is iterated until the results have converged [87]. The final χ^2 surface, after convergence of all matrix elements and with a $\chi^2 \leq \chi^2_{\text{min}} + 1$ restriction applied, is shown in Fig. 4.19. As is typical in the Coulomb excitation of even-even nuclei, there is a clear correlation between the $\langle 0_1^+ || E2 || 2_1^+ \rangle$ and $\langle 2_1^+ || E2 || 2_1^+ \rangle$ matrix elements when reproducing the γ-ray yield data (which is why a χ^2 surface analysis is used). The use of a moderately low-Z ^{48}Ti target helps reduce this effect.

Since the result from the χ^2 surface are used only to constrain the full GOSIA minimization, the matrix elements at the minimum χ^2 value in Fig. 4.19 are not precisely the final values quoted in Chapter 5. As mentioned previously, the full GOSIA minimization considers the ^{106}Cd γ-ray yields from all three settings. As such, 18 experiments were defined in the GOSIA calculations, and a total of 86 γ-ray yields were fitted using 24 matrix elements with 12 normalization constants as parameters. Note that many of these matrix elements, particularly those that couple to the buffer states, had a very small impact on the γ-ray yield calculations.

In order to reduce the number of parameters included during the minimization, GOSIA provides the ability to "link" different experiments together with relative normalization constants. These can be determined from the number of particles scattered into that angular range via [87]

$$N_i = \frac{N_p^{(i)}}{\Delta\theta_i \Delta\phi_i}, \tag{4.1}$$

where N_i is the relative normalization, $N_p^{(i)}$ is number of scattered nuclei, $\Delta\theta_i$ is the range of LAB frame scattering angles covered, and $\Delta\phi_i$ is the azimuthal coverage for experiment i. The number of detected nuclei can be determined most precisely when the ^{106}Cd scatter into the forward silicon detector, so the seven GOSIA experiments corresponding to forward-scattered ^{106}Cd were coupled together with the relative normalization constants given by Eq. 4.1. This reduces the number of fitted normalization constants from 18 to 12, increasing the sensitivity to the matrix elements. In particular, this increases the experimental sensitivity to quadrupole moments through the reorientation effect, as this is determined by the angular distribution of the γ-ray yields.

The reproduction of the measured γ-ray yields after convergence of the matrix elements from the iterative GOSIA-GOSIA2 analysis is shown in Figs. 4.20 to 4.25. In these figures, the x-axis is labelled "Experiment Number," which refers to a particular angle range within a specific setting; the vertical lines separate three settings. In all figures, the high-energy setting corresponds to experiment numbers 1 to 7, the low-energy setting corresponds to numbers 8 to 13, and the ^{48}Ti setting corresponds to 14 to 18. Experiments within a setting are in order of increasing CM scattering angle, i.e. they are in the same order as the γ-ray spectra shown in Figs. 4.10, 4.13, and 4.15.

The Z-score of a yield, shown in the bottom panel of Figs. 4.20 to 4.25, is simply the difference between experimental and calculated yield divided by the experimental uncertainty. Systematic uncertainties were included when extracting the γ-ray yields, so the error bars are not purely statistical. However, the Z-score can still be interpreted roughly as the number of standard deviations separating the measured and calculated yields. As can been seen, almost all yields are reproduced within 2σ, which is to be expected for the number of fitted yields. The horizontal dashed lines

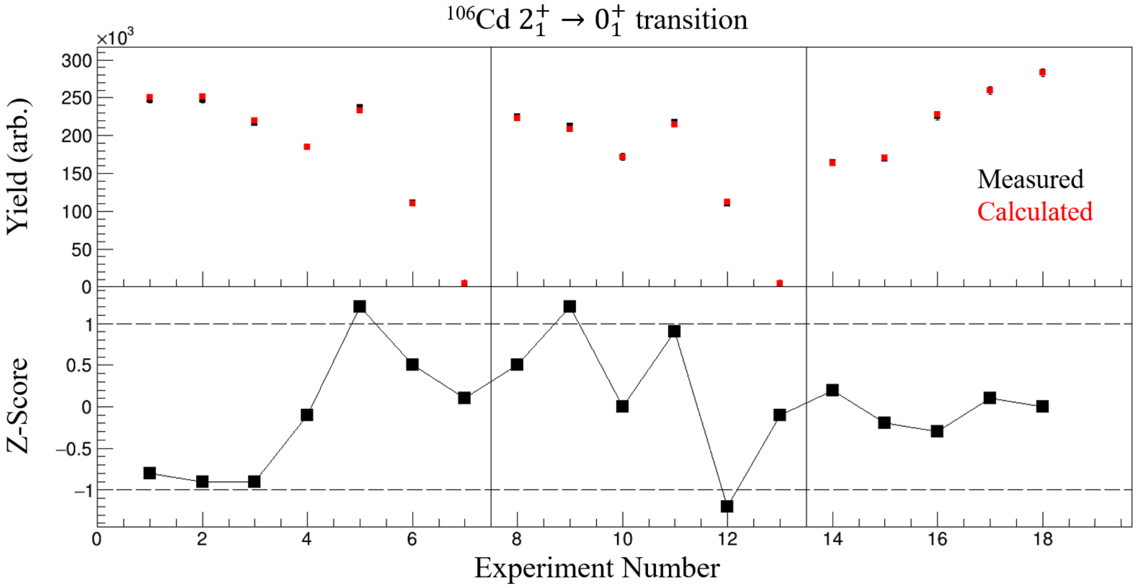

Figure 4.20: The reproduction of the 632 keV γ-ray yield from GOSIA. The top panel shows the direct comparison of calculated (red) and measured (black) yields. The bottom panel shows the discrepancy normalized to the experimental uncertainty. Vertical lines separate the three settings.

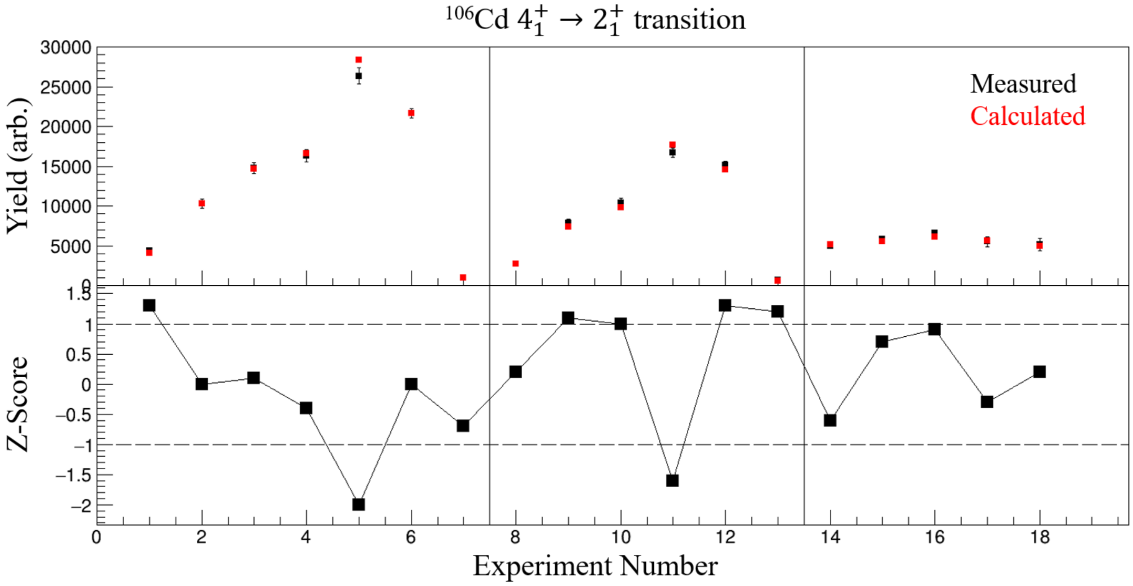

Figure 4.21: The reproduction of the 861 keV γ-ray yield from GOSIA. The top panel shows the direct comparison of calculated (red) and measured (black) yields. The bottom panel shows the discrepancy normalized to the experimental uncertainty. Vertical lines separate the three settings.

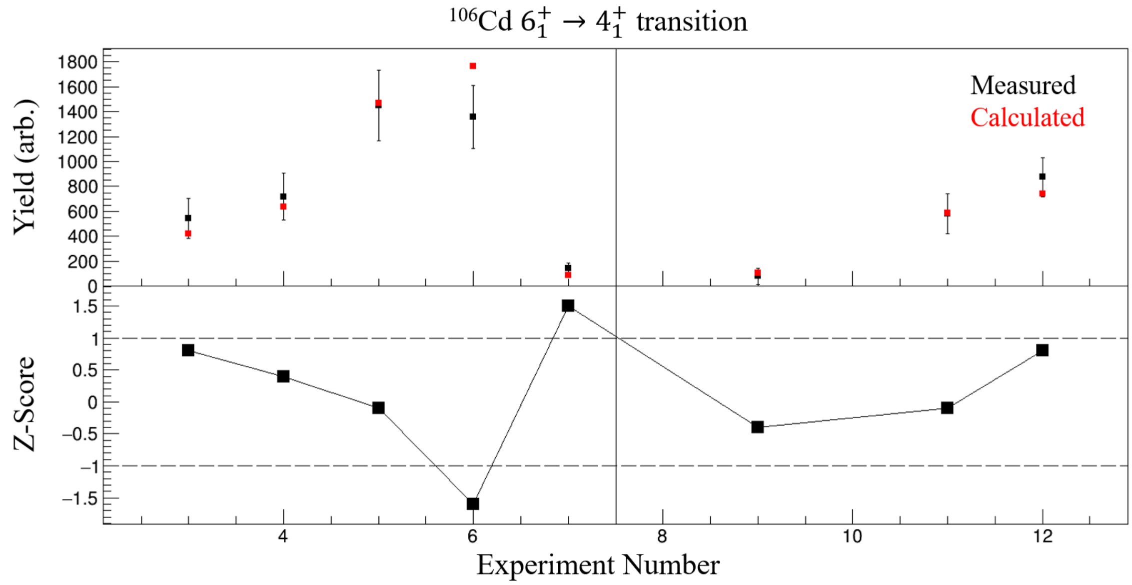

Figure 4.22: The reproduction of the 1009 keV γ-ray yield from GOSIA. The top panel shows the direct comparison of calculated (red) and measured (black) yields. The bottom panel shows the discrepancy normalized to the experimental uncertainty. Vertical lines separate the three settings.

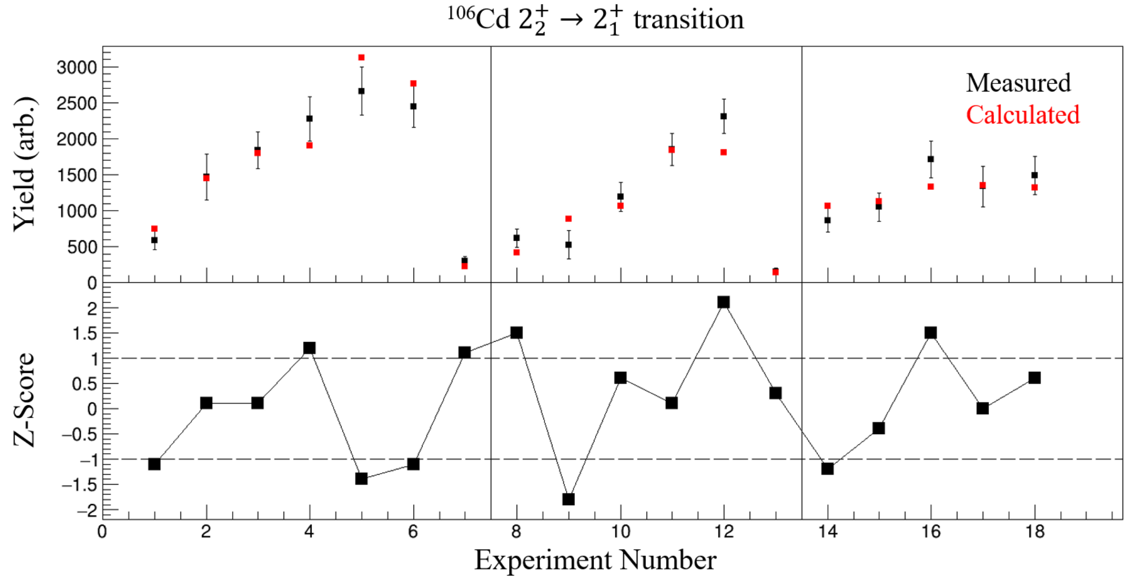

Figure 4.23: The reproduction of the 1084 keV γ-ray yield from GOSIA. The top panel shows the direct comparison of calculated (red) and measured (black) yields. The bottom panel shows the discrepancy normalized to the experimental uncertainty. Vertical lines separate the three settings.

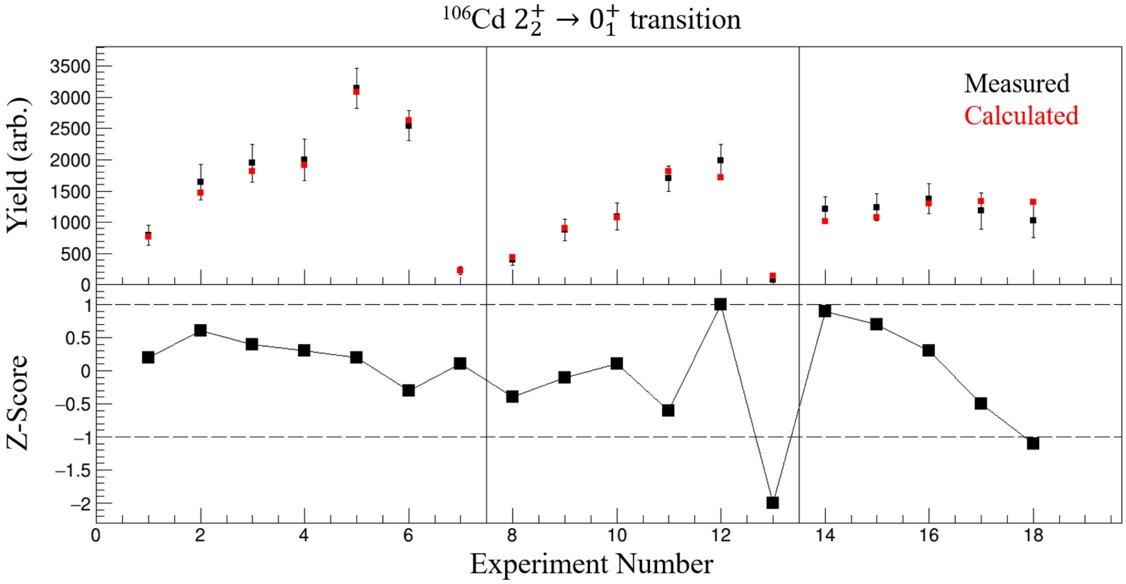

Figure 4.24: The reproduction of the 1716 keV γ-ray yield from GOSIA. The top panel shows the direct comparison of calculated (red) and measured (black) yields. The bottom panel shows the discrepancy normalized to the experimental uncertainty. Vertical lines separate the three settings.

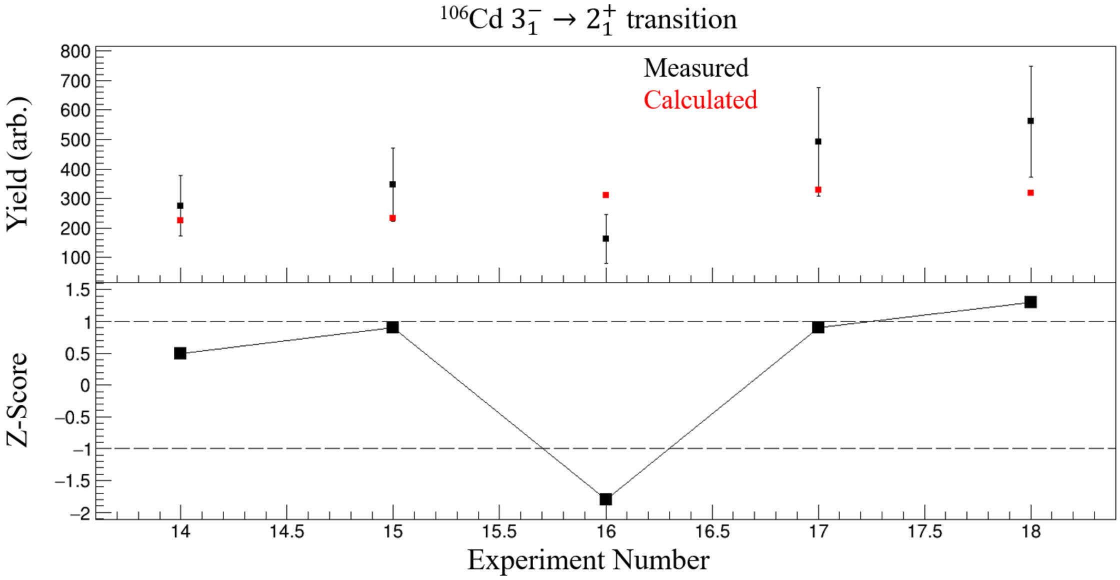

Figure 4.25: The reproduction of the 1746 keV γ-ray yield from GOSIA. The top panel shows the direct comparison of calculated (red) and measured (black) yields. The bottom panel shows the discrepancy normalized to the experimental uncertainty. Note this transition was only observed in the ^{48}Ti target setting.

denote the $\pm 1\sigma$ band. Using the typical rule-of-thumb for Gaussian uncertainties, about 68% of the yields should fall in this range. Note not all transitions were seen in all GOSIA experiments.

CHAPTER 5

RESULTS AND DISCUSSION

5.1 Experimental Results

As shown in the previous chapter, a GOSIA analysis was performed which successfully reproduced the measured γ-ray yields. The final matrix elements extracted from this analysis are given in Table 5.1, and the corresponding exited state lifetimes are shown in Table 5.2. Only matrix elements and lifetimes which were well constrained by the γ-ray yields collected during the experiment are given. The quoted uncertainties have been symmetrized and are the result of combining statistical and systematic effects. The dominant systematic error arises from the 1 mm ($\approx 3-4\%$) uncertainty on the separation between the reaction target and the silicon detectors.

As is apparent from Tables 5.1 and 5.2, the present work agrees well with the original Coulomb excitation data [149, 98] for all states observed, strongly supporting the adopted values over the discrepant results reported in [145]. The systematics of the $B(E2;0_1^+ \rightarrow 2_1^+)$ excitation strength along the Cd isotopic chain is shown again in Fig. 5.1, but this time with the present result indicated in red. Again, the agreement with original Coulomb excitation data [149, 98] is clear.

Also seen in Fig. 5.1 is satisfactory agreement with the results from Siciliano *et. al.* [143, 144], which is a recent lifetime measurement of excited states in ^{106}Cd using the recoil-distance Doppler-shift technique [159]. Siciliano *et. al.* measured several of the same lifetimes determined in this work, and a comparison of the results is given in Table 5.3. Refs. [143, 144] used two analysis techniques: the "Decay-Curve Method" (DCM) and the "Differential Decay-Curve Method" (DDCM), which are quoted separately. Further, Siciliano *et. al.* quotes two results from each method for the 2_2^+ state; these correspond to the two γ-ray decays from that state ($2_2^+ \rightarrow 0_1^+$ and $2_2^+ \rightarrow 2_1^+$).

Table 5.1: Matrix elements extracted from the present analysis compared to literature values.

$\langle J_i^\pi || E2 || J_f^\pi \rangle$ (eb)

J_i^π	J_f^π	This Work	Ref [145]	Ref [149]	Ref [98]	Ref [157]
0_1^+	2_1^+	0.652(11)	0.76(3)	0.653(13)	0.620(3)	-
2_1^+	2_1^+	-0.25(5)	-	-	-0.37(11)	-
2_1^+	4_1^+	1.044(25)	0.79(2)	1.11(7)	-	-
4_1^+	4_1^+	-0.52(24)	-	-	-	-
4_1^+	6_1^+	1.37(10)	-	-	-	-
6_1^+	6_1^+	-1.3(8)	-	-	-	-
0_1^+	2_2^+	0.169(4)	-	0.190(13)	-	-
2_1^+	2_2^+	0.415(15)	-	0.49(4)	-	0.32(5)
2_2^+	2_2^+	1.33(6)	-	-	-	-

$\langle J_i^\pi || M1 || J_f^\pi \rangle$ (μ_N)

J_i^π	J_f^π	This Work	Ref [149]	Ref [157]
2_1^+	2_2^+	-0.263(17)	-0.39	-0.35(5)

$\langle J_i^\pi || E3 || J_f^\pi \rangle$ $(eb^{\frac{3}{2}})$

J_i^π	J_f^π	This Work	Ref [158]
0_1^+	3_1^-	0.28(14)	0.40(5)

Table 5.2: Excited state lifetimes extracted from the present analysis compared to literature values. Since no literature lifetimes were used to constrain the GOSIA minimization, these results are independent of previous measurements.

Lifetime τ (ps)

State	This Work	Ref [145]	Ref [149]	Ref [98]	Ref [152]
2_1^+	9.5(3)	7.0(3)	9.4(4)	10.49(12)	9.9(12)
4_1^+	1.42(7)	2.5(2)	1.26(16)	-	-
6_1^+	0.54(8)	-	-	-	-
2_2^+	0.50(3)	0.28(2)	0.45(7)	-	-

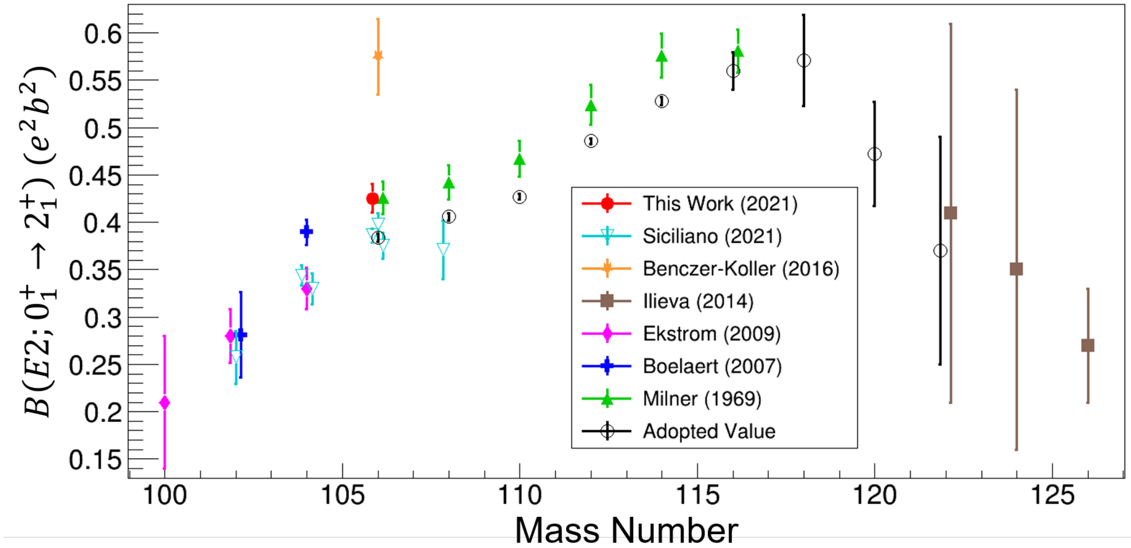

Figure 5.1: Evolution of $B(E2)$ values in the even-A $^{100-126}$Cd isotopes with the present result indicated in red.

Table 5.3: Excited state lifetimes extracted from the present analysis compared to the recent results from [143, 144].

Lifetime τ (ps)					
State	This Work	Ref [143] DDCM	Ref [143] DCM	Ref [144] DDCM	Ref [144] DCM
2_1^+	9.5(3)	10.4(2)	10.7(4)	-	10.1(3)
4_1^+	1.42(7)	-	-	1.4(2)	-
6_1^+	0.54(8)	-	-	1.3(6)	1.21(15)
2_2^+	0.50(3)	-	-	0.46(10), 0.41(4)	0.51(2), 0.55(3)

5.2 Shell Model Calculations

Large-scale shell-model calculations were performed to understand both the shape and collectivity of ^{106}Cd. A model space and Hamiltonian of a form similar to [147] was employed; this is based on an ^{88}Sr core with the valence ($1p_{1/2}$, $0g_{9/2}$) orbitals for protons and the ($0g_{7/2}$, $1d_{5/2}$, $1d_{3/2}$, $2s_{1/2}$, $0h_{11/2}$) orbitals for neutrons. Effective charges of $e_p = 1.6$ and $e_n = 1.0$ were used. This will be referred to as the Sr88 shell model calculation.

The calculations were carried out with the shell-model code NuShellX [160], and they reproduce well the recently calculated $B(E2; 2_1^+ \to 0_1^+)$ values from Table VI in Ref. [147] for ^{102,104}Cd. In order to run the ^{106}Cd calculation, a truncation of the neutron configurations was made allowing at most two neutrons in the $0h_{11/2}$ orbital. The resulting energies are within 50 keV of those in [147], and the $B(E2; 2_1^+ \to 0_1^+)$ also agrees. For all three nuclei, the quadrupole moments Q_s from our shell-model calculations are larger by a factor of roughly 2.2 over those in [147] due to an incorrect normalization applied in [147].

Calculated transition strengths and quadrupole moments are compared to the experimentally determined values in Table 5.4. Two shell-model calculations are presented; the calculation labelled $jj45$ will be explained later in this section. The Sr88 shell-model calculation reproduces the transition strengths in the ground-state band rather well. Additionally, the experimental transitions strengths of the 2_2^+ state are moderately well described. Note, however, that the shell model calculations place the calculated 2_2^+ and 2_3^+ states quite close in energy. The calculated 2_3^+ state has a lifetime, quadrupole moment, and decay pattern which are most similar to the experimental 2_2^+ state. As such, both states are included when comparing experimental and theoretical results, and the calculated 2_3^+ state should be associated with the experimental 2_2^+ state.

While the experimental $B(E2)$ transition strengths are well described by the shell model, it is also clear from Table 5.4 that the calculations do not reproduce the experimental quadrupole moments. Most significantly, the calculated $Q_s(2_1^+)$ is larger than the experimental value by roughly a factor of three. The experimentally determined quadrupole moments for all other states show a similar level of disagreement with the calculations.

Table 5.4: Transition strengths and spectroscopic quadrupole moments determined from this work compared to shell-model predictions.

$B(E2;J_i^\pi \to J_f^\pi)$ (e^2b^2)				
J_i^π	J_f^π	Experiment	jj45	Sr88
2_1^+	0_1^+	0.085(3)	0.0933	0.0774
4_1^+	2_1^+	0.121(6)	0.134	0.111
6_1^+	4_1^+	0.145(21)	0.104	0.0906
2_2^+	0_1^+	$5.7(3) \times 10^{-3}$	8.65×10^{-6}	4.72×10^{-4}
2_2^+	2_1^+	0.0345(25)	7.63×10^{-6}	7.27×10^{-4}
2_3^+	0_1^+	-	3.46×10^{-3}	2.76×10^{-3}
2_3^+	2_1^+	-	0.0103	7.82×10^{-3}

Spectroscopic Quadrupole Moment Q_s (eb)			
State	Experiment	jj45	Sr88
2_1^+	-0.19(4)	-0.603	-0.550
4_1^+	-0.39(18)	-0.760	-0.687
6_1^+	-0.8(5)	-0.563	-0.549
2_2^+	1.01(5)	-0.345	-0.205
2_3^+	-	0.611	0.4055

Due to the number of well-determined matrix elements extracted from this work, a comparison of the $E2$ rotational invariants $\langle Q^2 \rangle$ and $\langle Q^3 \cos(3\delta) \rangle$ [89, 41], which were described in Chapter 2, can be made to further explore the discrepancies between experiment and theory presented in Table 5.4. Only these two lowest-order rotational invariants for the ^{106}Cd ground state could be reliably extracted from the experimental data. To determine the quadrupole asymmetry parameter, we use the common [92, 75, 74] assumption that

$$\langle \cos(3\delta) \rangle \approx \frac{\langle Q^3 \cos(3\delta) \rangle}{\langle Q^2 \rangle^{3/2}}. \tag{5.1}$$

In this work, special attention is paid to the "normalized” quadrupole moment q_s, which is

Table 5.5: The ^{106}Cd ground state rotational invariants and normalized quadrupole moments determined from this work compared to shell-model calculations. The quoted uncertainties are purely experimental (see Table 5.1).

Ground State Rotational Invariants			
Invariant	Experiment	jj45	Sr88
$\langle Q^2 \rangle$ (e^2b^2)	0.454(14)	0.484	0.403
$\langle Q^3 \cos(3\delta) \rangle$ (e^3b^3)	-0.02(2)	0.265	0.198
$\langle \cos(3\delta) \rangle$	-0.06(6)	0.79	0.78

Normalized Quadrupole Moment q_s			
Experiment	jj45	Sr88	Ref [161]
-0.32(6)	-0.975	-0.976	-0.72

closely related to an approximation of the quadrupole asymmetry invariant $\langle \cos(3\delta) \rangle$ via

$$q_s = -\langle \cos(3\delta) \rangle_{2_1^+} = \frac{Q_s(2_1^+)}{\frac{2}{7}\sqrt{\frac{16\pi}{5} B(E2; 0_1^+ \to 2_1^+)}}. \tag{5.2}$$

Specifically, $\langle \cos(3\delta) \rangle_{2_1^+}$ is the quadrupole asymmetry when only the 2_1^+ excited state is considered in the calculation of the ground-state rotational invariants (see Eqs. 2.13 and 2.14). Recalling the rigid-rotor model of nuclei described in Chapter 1, q_s can be recognized as the ratio of the experimental quadrupole moment to the value predicted for an axially-symmetric rigid rotor. As such, the values $q_s = -1, 1$ indicate prolate and oblate deformations, respectively, while all intermediate values $-1 < q_s < 1$ imply triaxiality.

Loosely speaking, the quantity q_s is the first-order contribution to $\langle \cos(3\delta) \rangle$. In the same manner, the "leading-order" contribution to $\langle Q^2 \rangle$ is also quite simple:

$$\langle Q^2 \rangle_{2_1^+} = B(E2; 0_1^+ \to 2_1^+). \tag{5.3}$$

Clearly, $\langle Q^2 \rangle_{2_1^+}$ can be related to the quadrupole deformation β_2 predicted by a rigid-rotor nuclear model (see Eq. 1.40). A comparison of the experimental and theoretical rotational invariants, as well as the particularly important contribution q_s, is shown in Table 5.5.

Table 5.6: Contribution of individual matrix element products, or "loops," to the rotational invariants.

Contributions to $\langle Q^2 \rangle$ (e^2b^2)			
Component	Exp	jj45	Sr88
$\langle 0_1^+ \| E2 \| 2_1^+ \rangle \langle 2_1^+ \| E2 \| 0_1^+ \rangle$	0.425	0.467	0.387
$\langle 0_1^+ \| E2 \| 2_2^+ \rangle \langle 2_2^+ \| E2 \| 0_1^+ \rangle$	0.0286	4.32e-5	2.36e-3
$\langle 0_1^+ \| E2 \| 2_3^+ \rangle \langle 2_3^+ \| E2 \| 0_1^+ \rangle$	-	0.0173	0.0138
Sum:	0.454	0.484	0.403

Contributions to $\langle Q^3 \cos(3\delta) \rangle$ (e^3b^3)			
Component	Exp	jj45	Sr88
$\langle 0_1^+ \| E2 \| 2_1^+ \rangle \langle 2_1^+ \| E2 \| 2_1^+ \rangle \langle 2_1^+ \| E2 \| 0_1^+ \rangle$	-0.106	-0.371	-0.281
$\langle 0_1^+ \| E2 \| 2_1^+ \rangle \langle 2_1^+ \| E2 \| 2_2^+ \rangle \langle 2_2^+ \| E2 \| 0_1^+ \rangle$	0.091	5.5e-5	3.6e-3
$\langle 0_1^+ \| E2 \| 2_1^+ \rangle \langle 2_1^+ \| E2 \| 2_3^+ \rangle \langle 2_3^+ \| E2 \| 0_1^+ \rangle$	-	0.041	0.029
$\langle 0_1^+ \| E2 \| 2_2^+ \rangle \langle 2_2^+ \| E2 \| 2_2^+ \rangle \langle 2_2^+ \| E2 \| 0_1^+ \rangle$	0.038	-2.0e-5	-6.4e-4
$\langle 0_1^+ \| E2 \| 2_2^+ \rangle \langle 2_2^+ \| E2 \| 2_3^+ \rangle \langle 2_3^+ \| E2 \| 0_1^+ \rangle$	-	1.7e-4	4.4e-3
$\langle 0_1^+ \| E2 \| 2_3^+ \rangle \langle 2_3^+ \| E2 \| 2_3^+ \rangle \langle 2_3^+ \| E2 \| 0_1^+ \rangle$	-	0.014	7.4e-3
Sum:	0.023	-0.316	-0.237

As discussed in Chapter 2, the converge of the invariant sums should be investigated when they are calculated from experimental data. This can be accomplished by inspecting the contribution from individual terms in the sum. The decomposition of the invariant sums, for both experiment and theory, is presented in Table 5.6. As can be seen, the $\langle Q^2 \rangle$ invariant is almost entirely determined by the $\langle 0_1^+ || E2 || 2_1^+ \rangle$ matrix element, with only a small ($\approx$ 7%) contribution coming from the 2_2^+ state. The shell model calculations indicate that contributions from higher-lying 2^+ states are negligible. (Again, the calculated 2_3^+ state should be compared to the experimental 2_2^+ state.)

From Table 5.6, the $\langle Q^3 \cos(3\delta) \rangle$ invariant is clearly more sensitive to matrix elements other than $\langle 0_1^+ || E2 || 2_1^+ \rangle$. In fact, all experimentally determined values contribute appreciably to the sum. This again indicates the rapid increase in experimental data necessary to evaluate the higher-order invariant products. However, the shell model calculations indicate that the contribution to

$\langle Q^3 \cos(3\delta)\rangle$ from the experimental 2^+_3 state is small, which justifies extracting this invariant. Note the sum of the $\langle Q^3 \cos(3\delta)\rangle$ contributions must be multiplied by $-\sqrt{35/2}\begin{Bmatrix} 2 & 2 & 2 \\ 0 & 2 & 2 \end{Bmatrix} \approx -0.837$ to determine the actual value, while the prefactor for the $\langle Q^2\rangle$ invariant is simply $\sqrt{5}\begin{Bmatrix} 2 & 2 & 0 \\ 0 & 0 & 2 \end{Bmatrix} = 1$.

The very good reproduction of the $\langle Q^2\rangle$ invariant by the shell model implies that the magnitude of the deformation is well described. However, the disagreement in both $\langle \cos(3\delta)\rangle$ and q_s indicates that the type of deformation (or shape) is less well characterized; both measures imply a significant degree of triaxiality for ^{106}Cd which appears not to emerge from the shell-model calculations. Calculated values of q_s for Cd isotopes and the $N = 58$ isotones, compared to experimental values, are presented in Fig. 5.2. The data for ^{102,104}Cd were taken from Table V of Ref [147], while all other literature data are taken from NNDC/ENSDF [150]. Note the "leading-order" contributions β_2 and q_s are used for systematic comparisons because the actual quadrupole invariants cannot be calculated reliably from the existing data for many of the nuclei.

The discrepancy with experiment shown in Fig. 5.2 and Table 5.5 for the ^{106}Cd q_s cannot be accounted for within the Sr88 model space. Repeating the calculations in the expanded jj45 model space, which includes the $(0f_{5/2}, 1p_{3/2}, 1p_{1/2}, 0g_{9/2})$ proton orbitals, we find q_s is still close to -1 (see Table 5.5). Unlike the overall deformation parameter β_2, q_s is insensitive to the effective charges since these factors mostly cancel in the ratio of Eq. 5.2 (see Fig. 5.2); thus the discrepancy in q_s cannot be improved by adjusting the effective charges.

The total effective charge is $e_p = 1 + \delta e_p(\text{high}) + \delta e_p(\text{low})$ and $e_n = \delta e_n(\text{high}) + \delta e_n(\text{low})$. The $\delta e(\text{high})$ take into account the core-polarization from $2\hbar\omega$ $1p - 1h$ admixtures that are connected to the giant quadrupole resonance. Typical empirical values in the sd [162] and fp [163] model spaces are close to $\delta e_p(\text{high}) = \delta e_n(\text{high}) = 0.5$. The additional $\delta e(\text{low})$ are introduced to compensate for the truncation within the $0\hbar\omega$ shell, in particular the lack of proton excitations from $0g_{9/2}$ to $(0g_{7/2}, 1d_{5/2}, 1d_{3/2}, 2s_{1/2})$. In our case, we used $\delta e_p(\text{low}) = 0.1$ and $\delta e_n(\text{low}) = 0.5$.

It is interesting to compare the results for $Z = 48$ Cd isotopes, located two protons below the $Z = 50$ magic number, to the same results for the $Z = 26$ Fe isoptes, which lie two protons below the $Z = 28$ magic number. This comparison is shown in Fig. 5.3. Results for Fe are obtained

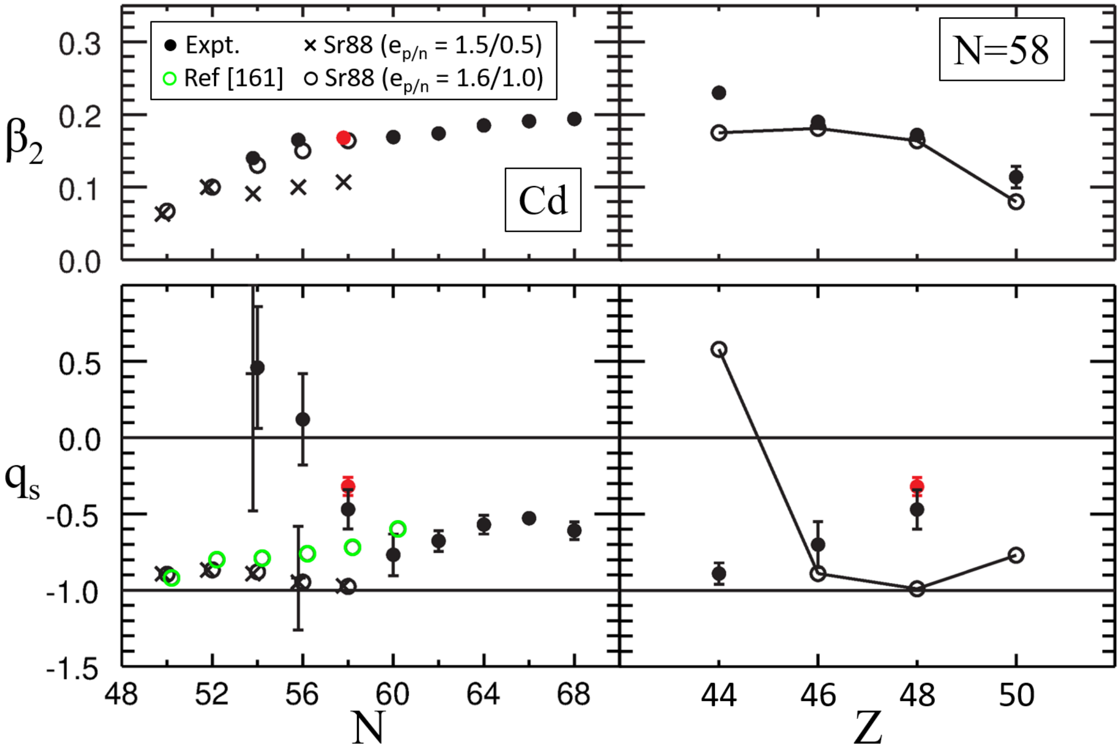

Figure 5.2: Calculated values of q_s (bottom) and quadrupole deformation β_2 (top) compared to experimental values for Cd isotopes (left) and $N = 58$ isotones (right). The experimentally determined value from this work is in red. The green circles are shell-model calculations from Ref [161] (see text). Figure adapted from [103].

with the $f7j4$ model space which consists of $0f_{7/2}$ for protons and ($0f_{5/2}$, $1p_{3/2}$, $1p_{1/2}$, $0g_{9/2}$) for neutrons. This is analogous to the Sr88 model space for Cd. As can be seen again, effective charges larger than e(high) are required to reproduce the experimental deformation.

Calculations for the light Fe isotopes were also performed in fp model space [163] which includes the ($0f_{7/2}$, $0f_{5/2}$, $1p_{3/2}$, $1p_{1/2}$) orbits for protons and neutrons. Importantly, calculations with the fp model space do not make a truncation within a major oscillator shell. As seen from Fig. 5.3, both the fp model space with only e(high) and the $f7j4$ model space with $e(\text{high})+e(\text{low})$ give $q_s \approx -1$ from $N = 28-34$. And for $N = 30, 32$ this agrees with experiment. This demonstrates that the affect of truncation within the major oscillator shell ($0\hbar\omega$) is accounted for by the additional e(low), so the increase of the experimental q_s observed for ^{106}Cd compared to the results of the Sr88 model space is not likely due to the major-shell truncation. Note the fp model space does

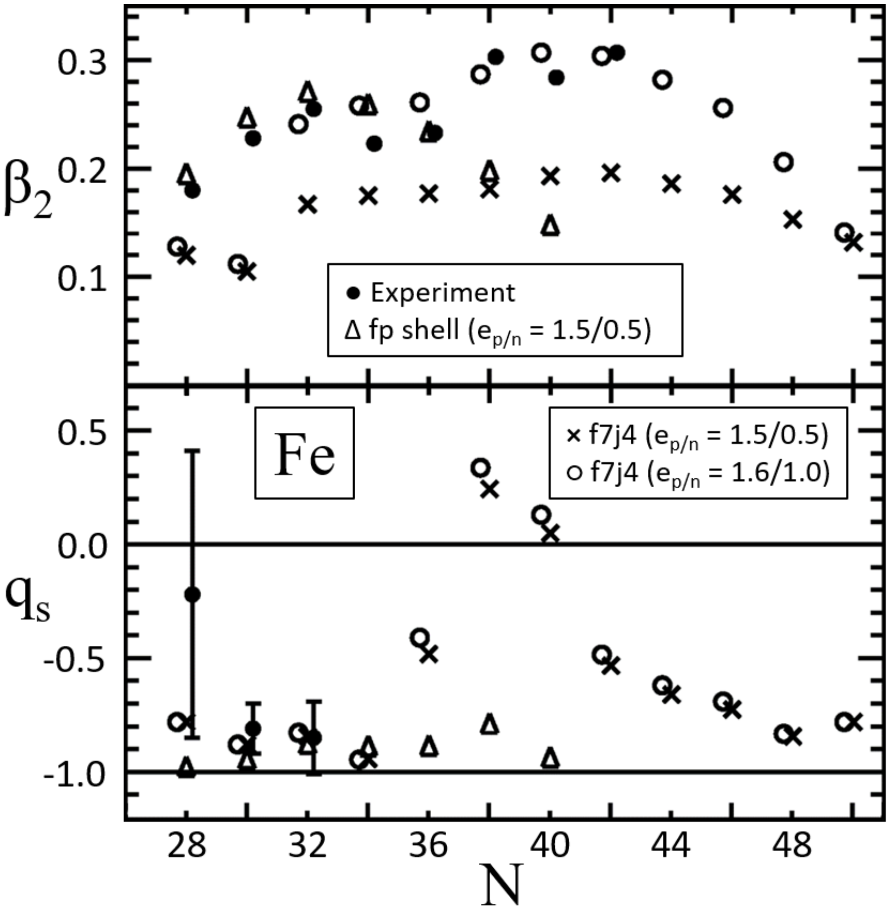

Figure 5.3: Calculated values of q_s (bottom) and quadrupole deformation β_2 (top) compared to experimental values for Fe isotopes. The data is taken from [164]. Figure adapted from [103].

not give an increasing q_s with increasing N as the neutron $0g_{9/2}$ orbit is not included in those calculations.

The $f7j4$ results for Fe reveal the reason for a change in q_s at large N. The q_s values for high-j configurations j^n are very simple. They are $q_s \approx +1$ for $n = 2$ and $q_s \approx -1$ for $n = -2$, with a nearly linear decrease in between. For both Fe and Cd, the protons are in a state with $n = -2$. Thus, the result for q_s as a function of N is determined by a constant $q_s \approx -1$ contribution from the protons combined with a varying q_s contribution from the neutrons which depends on the occupancy of the high-j $0g_{9/2}$ neutron orbital in Fe. In fact, the role of high-j configurations in determining nuclear shape in well-deformed nuclei is a much-explored phenomenon [165, 166, 167].

The analogy for Cd is that q_s should start to increase as the neutron $0h_{11/2}$ orbital starts to fill, and then decrease back to $q_s \approx -1$ as the $0h_{11/2}$ orbital becomes filled at $N = 82$. This anticipated impact of the neutron $0h_{11/2}$ orbital on the shape of Cd isotopes can indeed be seen in Fig. 5.2. The data for $N \geq 60$ show a smooth increase in q_s out to mid-shell, in line with the expectations set by the Fe calculations, though the effect is less pronounced in Cd.

Fig. 5.2 additionally includes shell model calculations from Schmidt *et. al.* [161]. The calculations from Ref [161] are also based on an ^{88}Sr core, but they made no truncation of the neutron $0h_{11/2}$ as was necessary for the calculations from this work. As can be seen, the calculations of Schmidt *et. al.* show an increase in q_s for all Cd isotopes and give good agreement with experiment at $N = 60$. The calculated q_s values from Ref [161] are larger than those from this work due to the location of the $0h_{11/2}$ single-particle energy. For ^{101}Sn the $0h_{11/2}$ orbital comes at an excitation energy of 6.76 MeV with our Sr88 interaction; it comes at 2.47 MeV with the interaction from [161]. Thus the admixture of the $0h_{11/2}$ single-particle configuration is larger in the wave-functions from [161] compared to the those from this work. The comparison of the calculations from Ref. [161] to those from this work, as well as the complementary calculation for the Fe isotopes presented here, strongly suggest the high-j $0h_{11/2}$ neutron orbital is critically important for determining the shape of neutron-rich Cd nuclei.

What is striking in Fig. 5.2 is the rapid increase in the experimental q_s with decreasing N starting at $N = 58$ compared to the calculations. This cannot be explained by the calculations presented in this work. To explore this discrepancy further, similar calculations were performed for $N = 58$ isotones (Fig. 5.2, right). The data show a clear increase of q_s with increasing Z. Again, the calculations presented in this work do not offer an explanation; the calculated q_s for the $N = 58$ isotones show the impact of the high-j proton configurations discussed earlier. The $Z = 44$ q_s calculation may be too high due to the employed model space being inappropriate for ruthenium; however, it is not likely that the experimental value would be reproduced even with an optimized model space.

These observations suggests several further investigations. Measurements of q_s in heavy Cd and Fe nuclei could confirm the similarity of the two isotopic chains pointed out in this work, and shell-model calculations which fully incorporate the neutron $0h_{11/2}$ for all heavy Cd isotopes could quantify the effect of this critical high-j orbital on the shape of Cd nuclei. Further, precise measurements of q_s in $^{100-104}$Cd, as well the $N = 58$ nucleus ^{108}Sn, could determine whether the trends observed in Fig. 5.2 continue. If so, it would represent a major deviation from the configuration-interaction based models presented here in a critical region of the nuclear chart near ^{100}Sn.

CHAPTER 6

SUMMARY AND OUTLOOK

This thesis focused on the experimental technique of barrier-energy Coulomb excitation. The analysis and results of a Coulomb excitation measurement of ^{106}Cd using the JANUS setup at ReA3 were presented. The experimental results agree well with both older Coulomb excitation data [149, 98] and more recent lifetime measurements [152, 143, 144] for several excited states. This lends confidence to the current results and strongly disfavors the discrepant results reported in Ref. [145]. Addressing this discrepancy was a primary motivation.

Large-scale shell-model calculations performed for comparison describe well the $B(E2)$ transition strengths in ^{106}Cd, but they fail to reproduce the quadrupole moments. An analysis of $E2$ rotational invariants extracted from both experiment and theory, including the particularly important contribution q_s, reveals a significant degree of triaxiality in ^{106}Cd which appears not to emerge from the present shell-model calculations. It was shown that this discrepancy cannot be reconciled within the Hamiltonians presently at hand, and that it cannot be fixed by changing the effective charges. A comparison with analogous calculations for the Fe isotopes, as well as with the similar calculations of Ref. [161], show that high-j neutron configurations cause the increase of q_s for Cd isotopes with $N \geq 60$. These comparisons also show that this effect cannot explain the current result for ^{106}Cd. The existing data for the light Cd isotopes and the $N = 58$ isotones with $Z \geq 44$ hint at a striking deviation from the presented shell-model calculations; this motivates similar measurements for more neutron-deficient Cd and Sn isotopes to explore the unexpected evolution of quadrupole moments in this critical region of the nuclear chart.

JANUS continues to be a powerful setup for nuclear structure studies of both stable and rare isotopes. Beyond the successful commissioning experiment [108, 100] and the work presented in this thesis [103], the nuclei ^{72,76}Se [102, 74] and ^{46}Ca [119] have been studied with the setup. In August to October of 2020, another successful campaign of Coulomb excitation experiments with JANUS at ReA3 was completed. Three separate experiments were performed which studied ^{80}Ge,

^{112,116,120}Sn, and ^{126,128}Xe. The analyses of these experiments are ongoing. The data analysis and preliminary results from the ^{80}Ge experiment is presented in the Appendix.

APPENDIX

APPENDIX

COULOMB EXCITATION OF GERMANIUM-80

A.1 Motivation

The stable to neutron-rich isotopes of germanium are a critical testing ground for nuclear models due to their detailed and rapidly changing structures. Near stability, the even-A $^{74-78}$Ge isotopes display triaxiality [168, 169, 170, 73, 171], while both shape coexistence [172] and triaxiality have been suggested for ^{72}Ge [72]. A transition from prolate to oblate deformation occurs at ^{70}Ge. Further, nuclei near the magic $N = 50$ isotone line, such as the very neutron-rich doubly magic nucleus ^{78}Ni [173, 174], have recently come into reach ab-initio-type models [175]. This makes experimentally determined indicators of nuclear structure crucial as these models attempt to extrapolate to the even more neutron-rich nuclei which will become available at facilities such as FRIB.

Two neutrons removed from $N = 50$, ^{80}Ge is important for a systematic understanding of neutron-rich nuclei in this region. Recent beyond-mean-field calculations [176], which compare well to the available data in the lighter Ge nuclei, have predicted a spherical configuration for magic $N = 50$ ^{82}Ge and a rapid onset of prolate deformation at both ^{80}Ge and ^{84}Ge. In order to test these recent predictions, and to further the experimental understanding of nuclear structure in a critical region of the nuclear chart, an inverse-kinematics sub-barrier Coulomb excitation experiment on ^{80}Ge was performed. The primary experimental goal is measure the ^{80}Ge $Q_s(2_1^+)$ and as such provide of one of the first benchmarks on nuclear shape in neutron rich Ge nuclei near $N = 50$. While the ^{80}Ge $B(E2; 0_1^+ \to 2_1^+)$ has been measured [177, 178], this experiment will provide a more precise value. The ^{80}Ge $B(E2)$ and $Q_s(2_1^+)$ are critical benchmarks for any theoretical model trying to extrapolate to neutron-rich nuclei such as ^{78}Ni and beyond.

A.2 Experimental Details

The experiment was performed at the NSCL ReA3 facility [101]. As ^{80}Ge is a rare-isotope, NSCL's scheme of projectile fragmentation and in-flight separation was required to create the RIB. A primary ^{82}Se beam was produced by the Advanced Room Temperature Ion Souce (ARTEMIS) [179] and accelerated by the K500 and K1200 coupled cyclotrons. The primary beam was impinged on a thick ^{9}Be production target to produce a "cocktail" secondary beam which consists of many different rare-isotopes. The ^{80}Ge nuclei were selected using the A1900 fragment separator [153] and delivered to a gas-cell which is used to stop and thermalize the high-energy beam. The ^{80}Ge nuclei were extracted from gas-cell, charge bred in an EBIT, and injected into the ReA3 accelerator chain to be delivered to the JANUS experimental setup.

The experiment consisted of only one setting. The ^{80}Ge nuclei were impinged at 3.52 MeV/u on a 1.59 mg/cm^2 ^{196}Pt target. This energy is 98% of the Coulomb barrier. The use of a ^{196}Pt target provided target excitations which, along with its well-known spectroscopic data, were used to define the normalization necessary to measure matrix elements in ^{80}Ge. As ^{196}Pt is a high-Z nucleus, this method provides sensitivity to both the quadrupole moment and transition strength of the 2_1^+ excited state in ^{80}Ge.

At the time of the experiment, it was discovered that the ^{80}Ge beam contained a roughly 7% contamination of stable ^{80}Kr, though the precise amount of contamination was observed to increase over the course of the experiment. This contamination originated from the gas-cell which is used to stop and thermalize the incoming rare-isotope beam, and the contaminant ^{80}Kr nuclei were accelerated to the same energy as the ^{80}Ge. Since the energies and masses of both nuclei were the same, it was not possible to discriminate between the two beam species using the silicon detectors.

This contamination must be accounted for, as the ^{80}Kr nuclei will Coulomb excite the ^{196}Pt target. The additional yield of ^{196}Pt γ-rays caused by impinging ^{80}Kr will incorrectly change the normalization extracted for the ^{80}Ge excitations unless this contribution can be removed. Because of this, a dedicated ^{80}Kr measurement was also performed in which a pure ^{80}Kr beam was impinged on the ^{196}Pt target under identical experimental settings. This setting provided a direct measure of

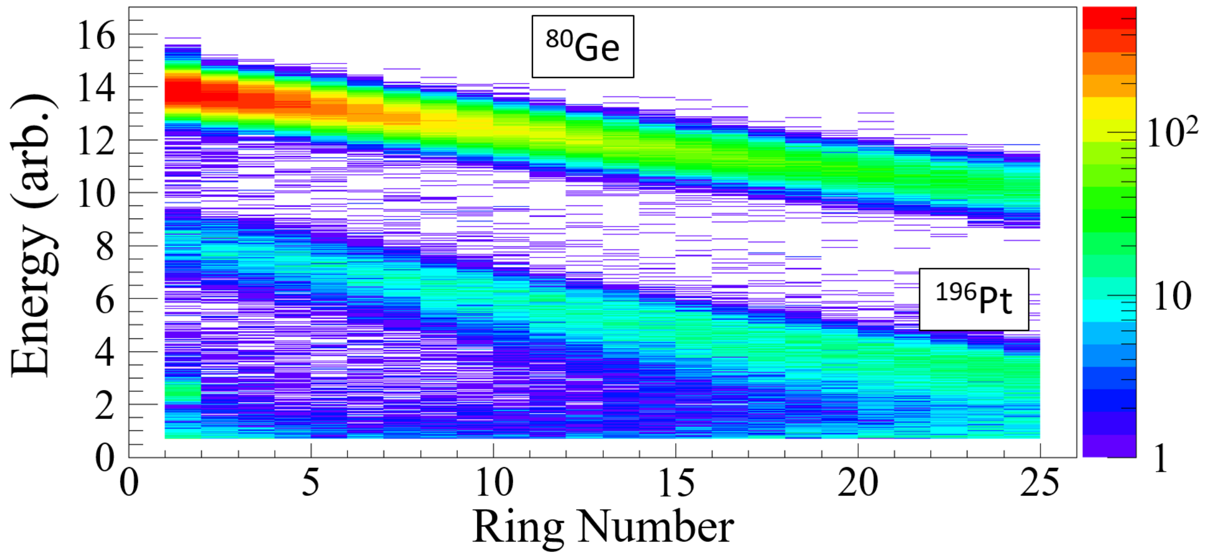

Figure A.1: Kinematic curve observed in the forward silicon detector. The scattered ^{80}Ge and recoiling ^{196}Pt are clear. It also clear there is no separation between the ^{80}Ge and the ^{80}Kr contamination.

the ^{196}Pt γ-ray yields produced by the impinging ^{80}Kr.

A.3 Analysis

The data analysis procedure is very similar to what was employed for the ^{106}Cd experiment. The kinematic curves collected over the entire experiment are shown in Fig. A.1. The separation between the scattered ^{80}Ge and recoiling ^{196}Pt is clear. However, from Fig. A.1 it is also clear that there is no separation between the ^{80}Ge and the ^{80}Kr contamination; the ^{80}Ge kinematic curve also contains the contaminant ^{80}Kr.

To increase the sensitivity the quadrupole moment, the data were further subdivided into angular ranges. The forward-scattered ^{80}Ge data were divided into three ranges: ^{80}Ge detected in rings 1 to 7, 8 to 14, and 15 to 24. The detected ^{196}Pt recoils were divided into two ranges: rings 1 to 13 and 14 to 24. The back-scattered ^{80}Ge were considered as a whole.

The Doppler-correction is again enabled by the segmentation of both detection systems and the well-know reaction kinematics. Because the kinematics of the scattered ^{80}Ge and ^{80}Kr nuclei are essentially identical, the γ-rays emitted by these two nuclei can be Doppler-corrected simultaneously.

To facilitate the data analysis of this experiment, and all other JANUS experiments, a GEANT4 simulation [180] of setup was developed [181]. Most importantly, the simulation assists in extracting γ-ray intensities by providing a realistic simulated response of the SeGA detectors which can be used to fit the experimental γ-ray spectra. By removing the full-energy peak component of the simulated γ rays, extracting peak areas amounts to taking a simple integral of the γ-ray spectrum which is above the background model. This is a simple and consistent method of extracting peak areas which is largely independent of any assumption about the shape of the Doppler-correct peaks.

Fitting the γ-ray spectra additionally enabled the ^{80}Kr contamination to be accounted for in a simple manner: the γ-ray spectra collected during the dedicated ^{80}Kr setting could be incorporated directly into the fits. By scaling the dedicated ^{80}Kr spectrum to the the amount of $2^+_1 \rightarrow 0^+_1$ transitions from ^{80}Kr collected during the experiment, the number of ^{196}Pt γ-rays caused by the impinging ^{80}Kr contamination can be determined in a direct and unambiguous manner. The γ-ray spectra collected during the experiment for each angle range, along with the simulated background response used to determine peak areas, are shown in Figs. A.2 to A.7. The orange curves in these figures are the ^{80}Kr γ-ray spectra measured during the dedicated setting, which are included in the fits.

As can be seen in Figs. A.2 to A.7, the contaminant ^{80}Kr nuclei contributed noticeably to the observed ^{196}Pt γ-ray yields. By using the γ-ray spectra collected during the dedicated ^{80}Kr setting, it was determined that on average 7% of the ^{196}Pt γ-ray yields were caused by impinging ^{80}Kr nuclei. The precise value depends on the angle range and is determined by the number of detected ^{80}Kr $2^+_1 \rightarrow 0^+_1$ γ-rays transitions as shown in the fits.

It is noted that some weak population of the 4^+_1 and 2^+_2 states in ^{80}Ge was also observed in the experiment. The transitions depopulating these states are shown if Fig. A.8 for detected ^{196}Pt recoils (all rings). A fit was not necessary for to extract peak areas from these transitions due to their low statistics and low background.

In order to transform the measured peak areas into γ-ray yields, the detection efficiency of

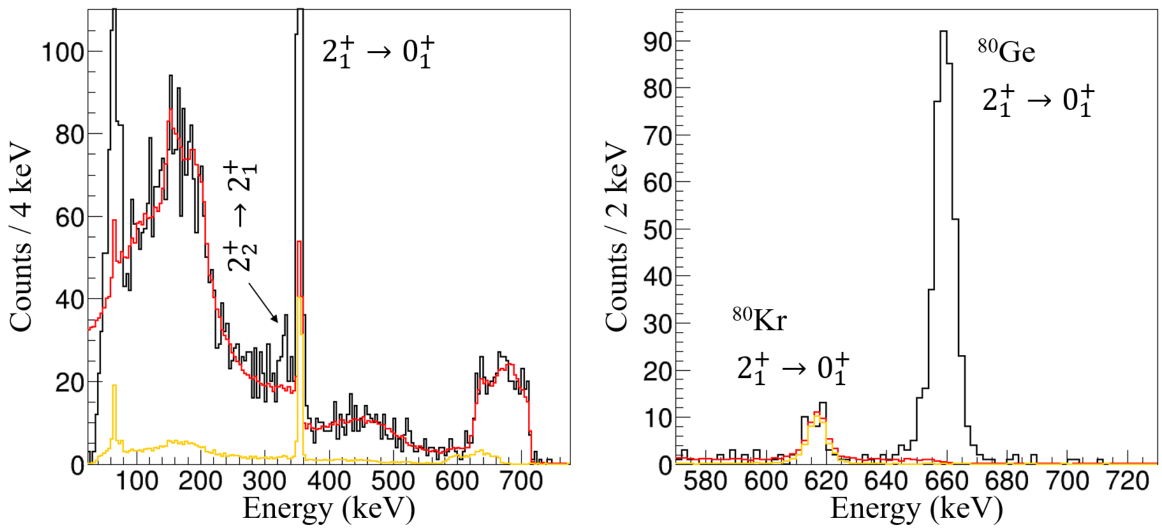

Figure A.2: The γ-ray spectrum collected in coincidence with ^{80}Ge scattered into rings 1 to 7 of the forward silicon detector. The left panel is Doppler-correct for ^{196}Pt, the right for ^{80}Ge. The red curves are a simulated response of the background combined with the measured contribution from ^{80}Kr. The orange curve shows the ^{80}Kr contribution.

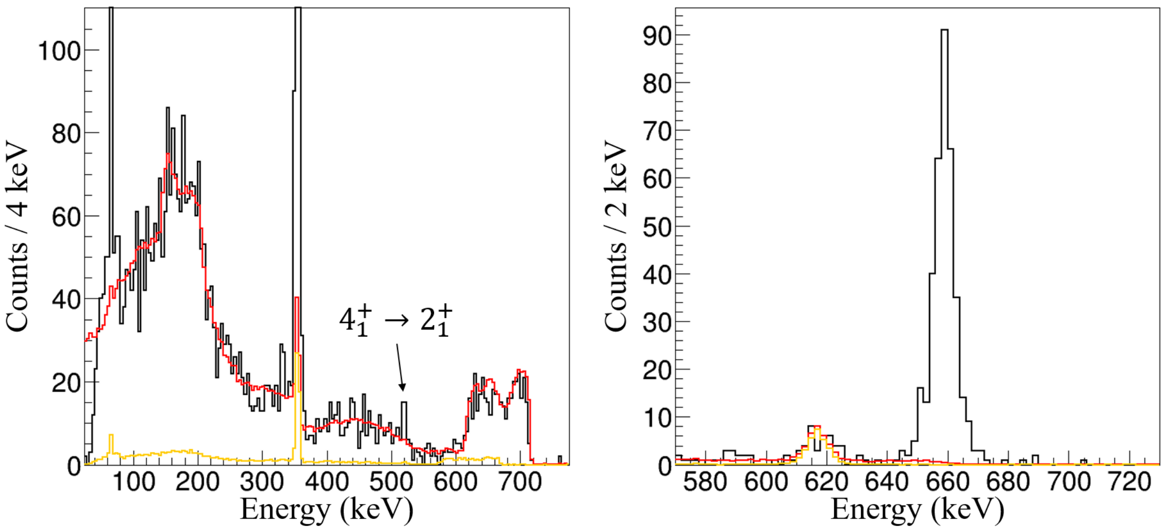

Figure A.3: The γ-ray spectrum collected in coincidence with ^{80}Ge scattered into rings 8 to 14 of the forward silicon detector. The left panel is Doppler-correct for ^{196}Pt, the right for ^{80}Ge. The red curves are a simulated response of the background combined with the measured contribution from ^{80}Kr. The orange curve shows the ^{80}Kr contribution.

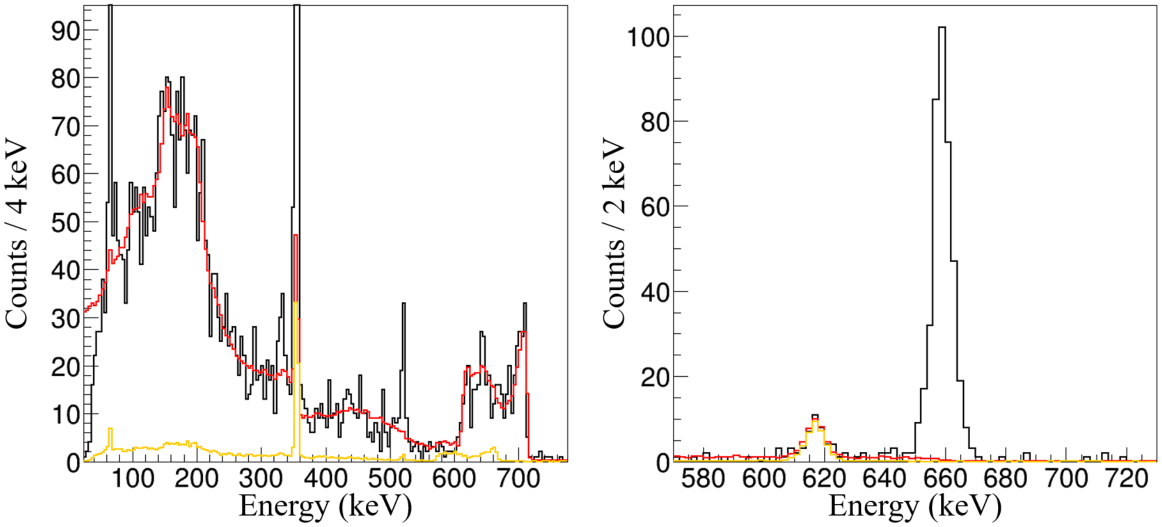

Figure A.4: The γ-ray spectrum collected in coincidence with ^{80}Ge scattered into rings 15 to 24 of the forward silicon detector. The left panel is Doppler-correct for ^{196}Pt, the right for ^{80}Ge. The red curves are a simulated response of the background combined with the measured contribution from ^{80}Kr. The orange curve shows the ^{80}Kr contribution.

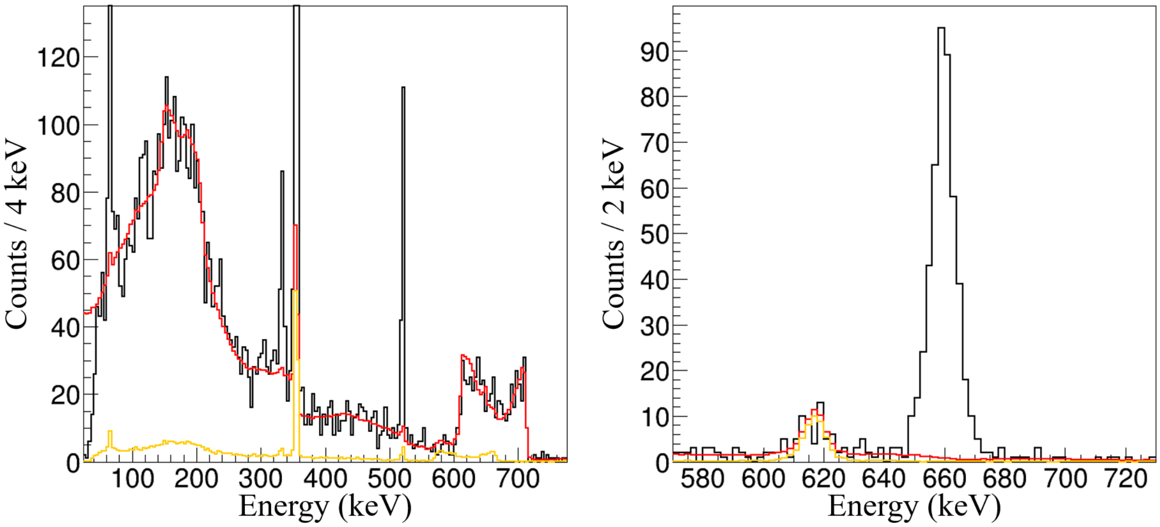

Figure A.5: The γ-ray spectrum collected in coincidence with ^{196}Pt in rings 14 to 24 of the forward silicon detector. The left panel is Doppler-correct for ^{196}Pt, the right for ^{80}Ge. The red curves are a simulated response of the background combined with the measured contribution from ^{80}Kr. The orange curve shows the ^{80}Kr contribution.

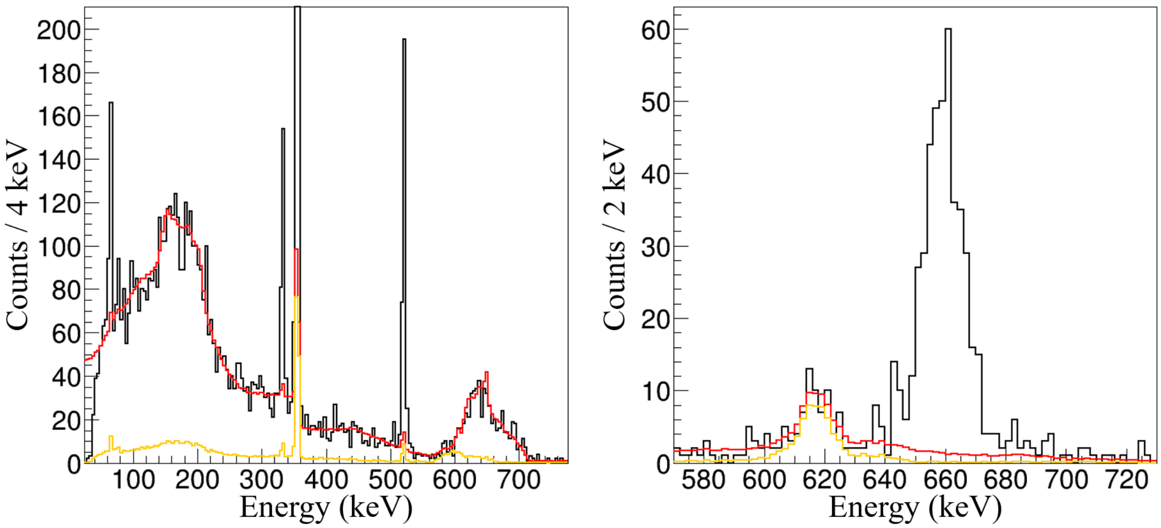

Figure A.6: The γ-ray spectrum collected in coincidence with ^{196}Pt in rings 1 to 13 of the forward silicon detector. The left panel is Doppler-correct for ^{196}Pt, the right for ^{80}Ge. The red curves are a simulated response of the background combined with the measured contribution from ^{80}Kr. The orange curve shows the ^{80}Kr contribution.

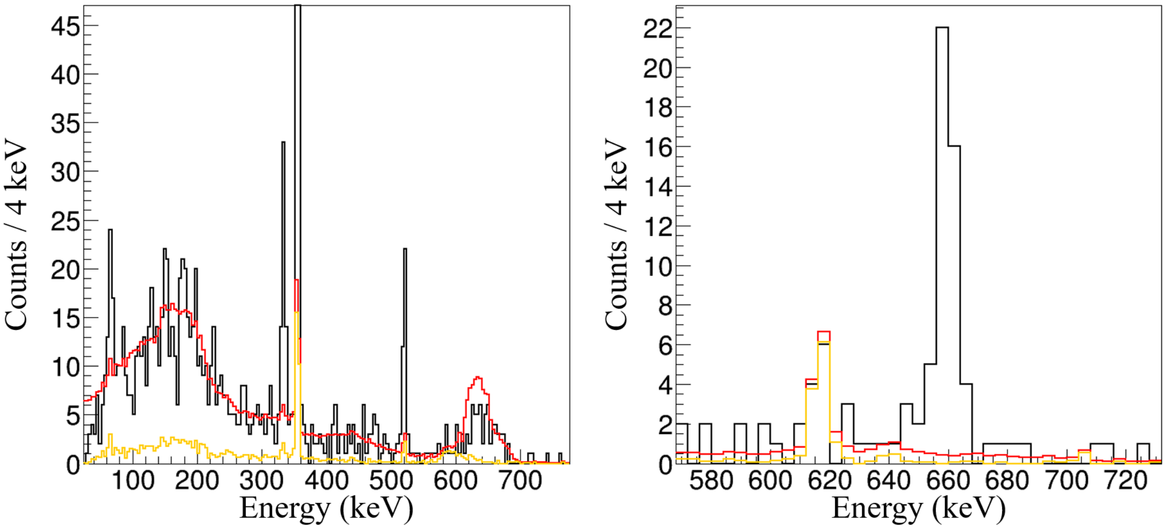

Figure A.7: The γ-ray spectrum collected in coincidence with back-scattered ^{80}Ge. The left panel is Doppler-correct for ^{196}Pt, the right for ^{80}Ge. The red curves are a simulated response of the background combined with the measured contribution from ^{80}Kr. The orange curve shows the ^{80}Kr contribution.

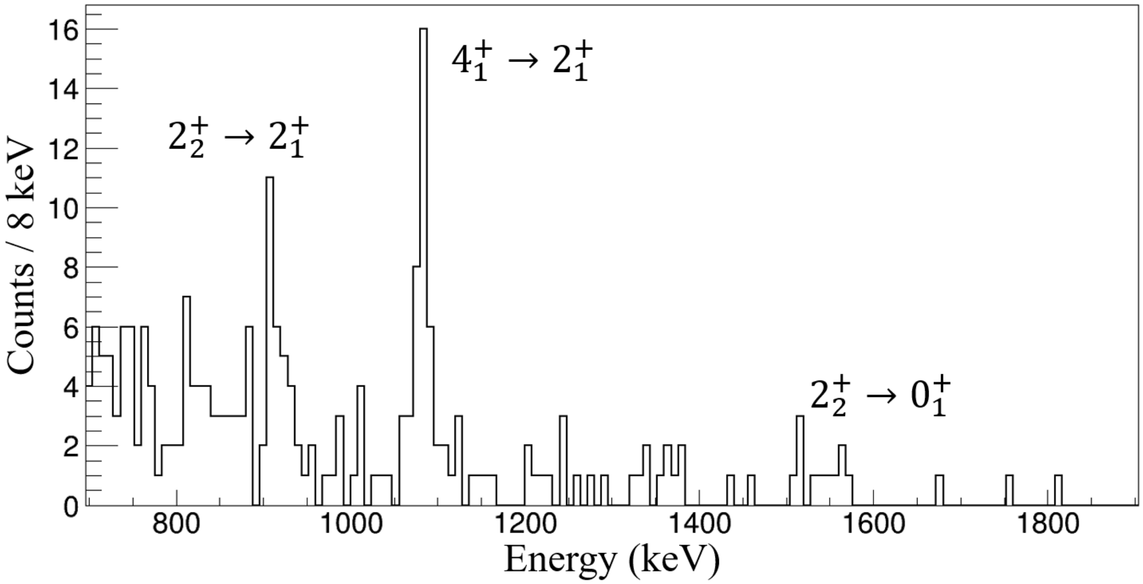

Figure A.8: The higher-energy portion of the γ-ray spectrum collected in coincidence with ^{196}Pt recoils (all rings). Due to the low statistics, a fit was not necessary.

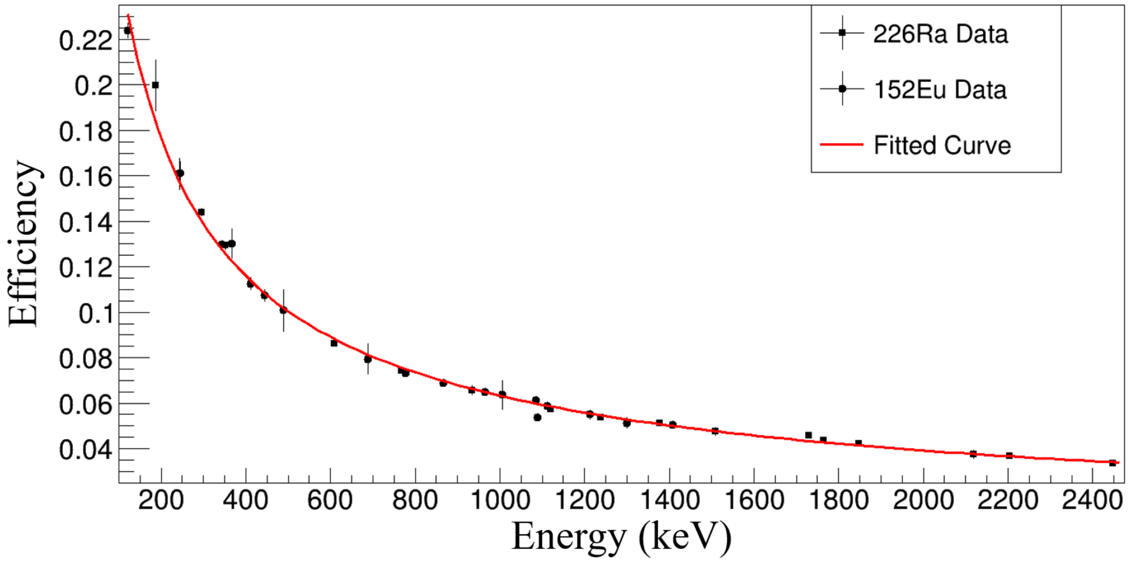

Figure A.9: The efficiency data collected for this experiment. The fitted efficiency curve used during analysis is shown.

SeGA was measured. The efficiency calibration was performed using two γ-ray sources: ^{152}Eu and ^{226}Ra. Only the ^{152}Eu source was used for the absolute efficiency calibration. The ^{226}Ra source was used for a relative efficiency calibration. The efficiency data collected from these two sources, as well as the fitted efficiency curve, is shown in Fig. A.9.

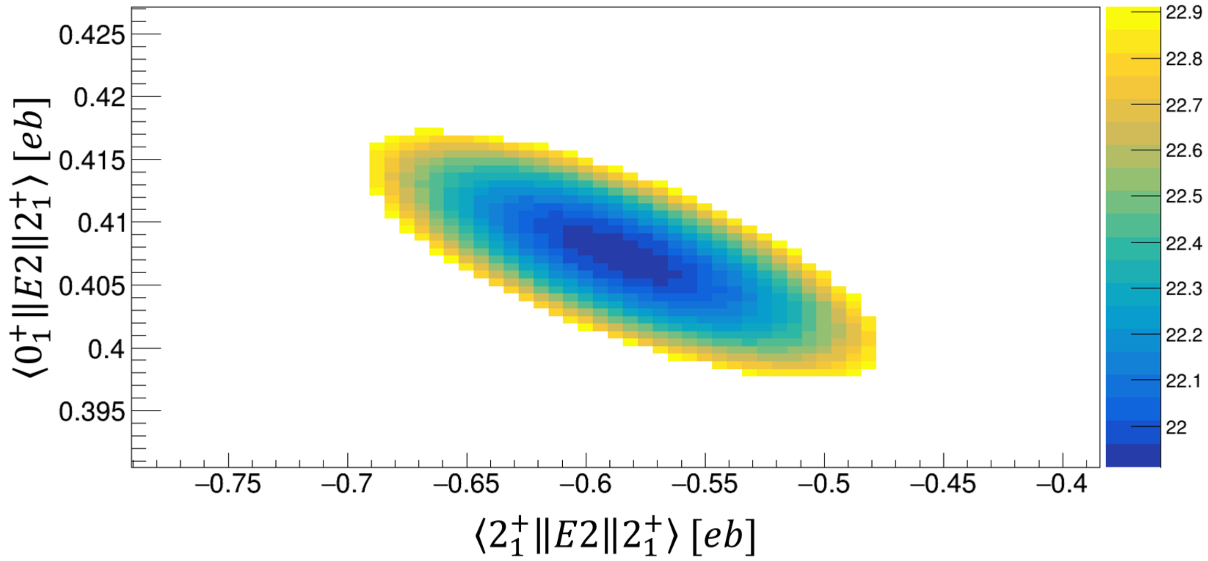

Figure A.10: The χ^2 surface with a 1σ restriction applied. Due to the high-Z of ^{196}Pt, significant sensitivity to both the transitional and diagonal matrix elements is achieved.

The detection efficiency of SeGA is well constrained for the γ-ray energies observed in this work, $300\,\text{keV} < E_\gamma < 1700\,\text{keV}$. During this experiment, SeGA provided an absolute γ-ray detection efficiency of 6.3% at 1000 keV, which is slightly lower than what was measured during the previous JANUS campaign. This is because SeGA was offset slightly from the target position, so the solid angle coverage of the array was reduced. Note that, as mentioned, only the relative energy dependence of the detection efficiency is important; the absolute efficiency in not strictly necessary.

A.4 Preliminary Results

The γ-ray yield data were analyzed with the GOSIA2 code. Just as in the GOSIA2 analysis of the ^{106}Cd experiment, the ^{80}Ge $\langle 0_1^+ || E2 || 2_1^+ \rangle$ and $\langle 2_1^+ || E2 || 2_1^+ \rangle$ matrix elements were manually scanned while all other matrix elements were fixed. At each pint in the scan, the GOSIA2 code was used to determine the agreement between the measured and calculated yields with respect to the normalization determined by the ^{196}Pt target excitations. The literature data used for ^{196}Pt is given in Table A.1, and the χ^2 surface from the GOSIA2 analysis is shown in Fig. A.10. No literature data was used for ^{80}Ge during the GOSIA2 analysis.

Table A.1: The literature data employed for ^{196}Pt during the GOSIA2 analysis. Data taken from NNDC/ENSDF [150].

State	τ (ps)	Transitions	BR	Matrix element	Value	Transition	δ
2_1^+	49.27(22)	$\frac{4_2^+\to4_1^+}{4_2^+\to2_2^+}$	0.17(5)	$\langle 2_1^+\vert\vert E2\vert\vert 2_1^+\rangle$	0.82(11)	$2_2^+ \to 2_1^+$	-5.2(5)
4_1^+	5.12(7)	$\frac{4_2^+\to2_1^+}{4_2^+\to2_2^+}$	0.17(2)	$\langle 4_1^+\vert\vert E2\vert\vert 4_1^+\rangle$	1.37(16)		
6_1^+	1.41(12)	$\frac{0_2^+\to2_2^+}{0_2^+\to2_1^+}$	0.39(4)	$\langle 6_1^+\vert\vert E2\vert\vert 6_1^+\rangle$	-0.3(4)		
8_1^+	0.61(6)	$\frac{3_1^+\to4_1^+}{3_1^+\to2_2^+}$	0.013(4)	$\langle 2_2^+\vert\vert E2\vert\vert 2_2^+\rangle$	-0.51(21)		
0_2^+	6.1(14)	$\frac{3_1^+\to2_1^+}{3_1^+\to2_2^+}$	0.044(10)				
2_2^+	48.8(10)						
4_2^+	3.8(8)						
6_2^+	1.1(3)						

The results of the χ^2 surface analysis are $\langle 0_1^+||E2||2_1^+\rangle = 0.408(10)$ eb and $\langle 2_1^+||E2||2_1^+\rangle = -0.59(11)$ eb; these determine both the transition strength and the quadrupole moment of ^{80}Ge. Matrix elements which couple to states beyond the 2_1^+ were determined with the GOSIA code by using the best-fit $\langle 0_1^+||E2||2_1^+\rangle$ matrix element as a constraint. Due to the weak population of the higher-lying states, only minimal sensitivity to the other matrix elements was observed and the joint GOSIA-GOSIA2 analysis rapidly converged.

A comparison of the current results for the $B(E2; 0_1^+ \to 2_1^+)$ and $Q_s(2_1^+)$ to the systematics along the Ge isotopic chain, including the previous $B(E2)$ measurements in ^{80}Ge, is shown in Fig. A.11. As can be seen, the current result for the ^{80}Ge $B(E2)$ is larger than both previous measurements. However, the trend still shows a smooth decrease from midshell at $A \approx 74$ out to the $N = 50$ closed shell at ^{82}Ge, in line with conventional shell-model arguments.

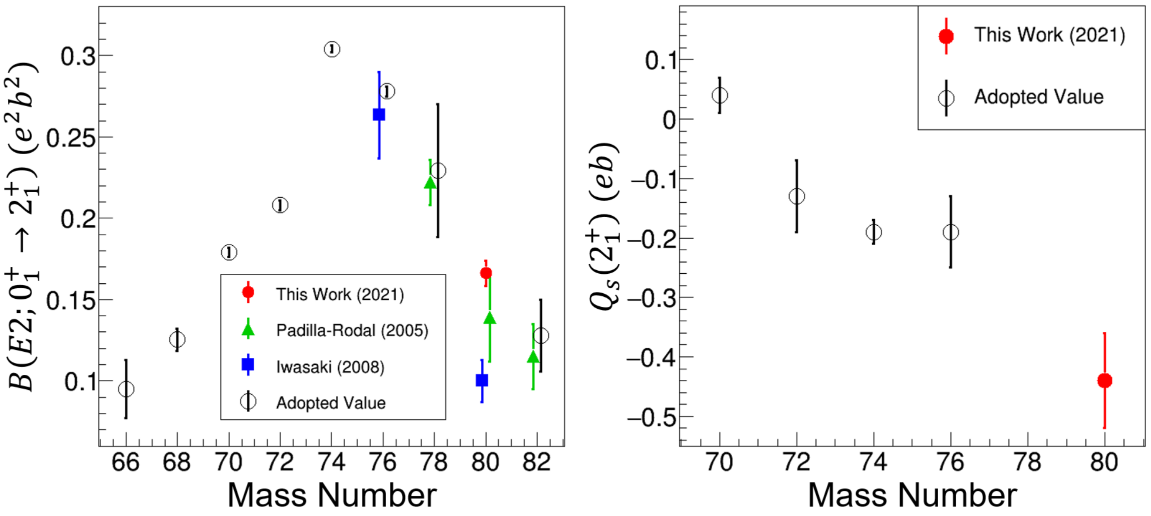

Figure A.11: The systematics of the $B(E2)$ (left) and $Q_s(2_1^+)$ (right) along the Ge isotopic chain with the results from this work in red. Literature data from: Adopted [150], Padilla-Rodal [177], and Iwasaki [178].

Table A.2: The experimental results for ^{80}Ge compared to shell model calculations. The quoted uncertainties are only statistical.

	Experiment	jj44b	JUN45
$B(E2;0_1^+ \rightarrow 2_1^+)$	0.166(8)	0.188	0.159
$Q_s(2_1^+)$	-0.44(8)	-0.301	-0.300
q_s	-1.21(23)	-0.766	-0.830

A.4.1 Shell Model Calculations

Shell model calculations were performed to understand the structure of ^{80}Ge using the NuShellX code [160]. The calculations were performed in the $jj44$ model space which consists of the ($0f_{7/2}$, $1p_{3/2}$, $1p_{1/2}$, $0g_{9/2}$) orbitals for both protons and neutrons, and effective charges of $e_p = 1.8$ and $e_n = 0.8$ were used. Two separate calculations were performed using the jj44b and JUN45 [182] interactions; these have been widely employed to study germanium nuclei [183, 184]. The comparison between the experimental and calculated results are shown in Table A.2.

As can be seen from Table A.2, the JUN45 interaction reproduces the experimental values most closely. Both interactions predict a quadrupole moment of -0.3 eb, but the jj44b interaction over-predicts the $B(E2)$ while the JUN45 interaction reproduces the $B(E2)$ value quite well. The experimentally determined spectroscopic quadrupole moment is almost 50% larger than the shell model prediction. As can be seen from the reduced quadrupole moment q_s, the experimental value is larger than the prediction for an axially-symmetric rigid rotor (though the error bar overlaps with the symmetric rotor value).

The magic $N = 50$ nucleus ^{82}Ge is predicted to be spherical [176] and thus have a very small quadrupole moment. As such the experimentally determined $Q_s(2_1^+)$ for ^{80}Ge indicates a rapid onset of essentially maximal prolate deformation just two neutrons removed from $N = 50$. As mentioned earlier, the lighter $^{72-76}$Ge isotopes have smaller quadrupole moments due to the triaxial nature of their deformation. The present experimental result is a first indication that ^{80}Ge does not exhibit significant triaxiality and instead points to rapid structural change in the heavy Ge isotopes. Measurement of the quadrupole moments in ^{78,82}Ge would be very beneficial to confirm and quantify this rapid evolution of shape.

The interpretation of the shell model results in comparison with the experimentally determined values is still ongoing, and as stated earlier, the quoted errors are purely statistical. Systematic effects are still being investigated. As such, the results quoted here should be considered preliminary.

BIBLIOGRAPHY

BIBLIOGRAPHY

[1] David J Griffiths. *Introduction to elementary particles; 2nd rev. version*. Wiley, New York, NY, 2008.

[2] V. G. J. Stoks, R. A. M. Klomp, C. P. F. Terheggen, and J. J. de Swart. Construction of high-quality NN potential models. *Physical Review C*, 49(6):2950–2962, 1994.

[3] R. Machleidt. High-precision, charge-dependent Bonn nucleon-nucleon potential. *Physical Review C*, 63(2):024001, 2001.

[4] R. Machleidt and H. Müther. Charge symmetry breaking of the nucleon-nucleon interaction: ρ-ω mixing versus nucleon mass splitting. *Physical Review C*, 63(3):034005, 2001.

[5] Sean Michael McDaniel. *A Study of Complementary Reactions: Single-Proton Knockout and Single-Proton Pickup*. PhD thesis, Michigan State University, East Lansing, Michigan, 2011.

[6] Hideki Yukawa. On the interaction of elementary particles I. *Proceedings of the Physico-Mathematical Society of Japan. 3rd Series*, 17:48–57, 1935.

[7] Brenden Robert Longfellow. *Coulomb excitation of neutron-rich sulfur isotopes*. PhD thesis, Michigan State University, East Lansing, Michigan, 2020.

[8] NSCL. Isotope science facility at michigan state university: Upgrade of the NSCL rare isotope research capabilities. MSU preprint MSUCL-1345, 2006.

[9] M. Thoennessen. Reaching the limits of nuclear stability. *Reports on Progress in Physics*, 67(7):1187–1232, 2004.

[10] Jochen Erler, Noah Birge, Markus Kortelainen, Witold Nazarewicz, Erik Olsen, Alexander M. Perhac, and Mario Stoitsov. The limits of the nuclear landscape. *Nature*, 486(7404):509–512, 2012.

[11] B. Alex Brown. Lecture notes in nuclear structure physics, 2021. National Superconducting Cyclotron Laboratory.

[12] C. F. von Weizsäcker. Zur theorie der kernmassen. *Zeitschrift für Physik*, 96(7):431–458, 1935.

[13] Steven Ragnar Stroberg. *Single-Particle Structure of Neutron-Rich Silicon Isotopes and the Breakdown of the* $N = 28$ *Shell Closure*. PhD thesis, Michigan State University, East Lansing, Michigan, 2014.

[14] G. Audi, M. Wang, A.H. Wapstra, F.G. Kondev, M. MacCormick, X. Xu, and B. Pfeiffer. The Ame2012 atomic mass evaluation. *Chinese Physics C*, 36(12):1603–2014, 2012.

[15] Maria Goeppert Mayer. On closed shells in nuclei. II. *Physical Review*, 75(12):1969–1970, 1949.

[16] Otto Haxel, J. Hans D. Jensen, and Hans E. Suess. On the "magic numbers" in nuclear structure. *Physical Review*, 75(11):1766–1766, 1949.

[17] K. A. Brueckner, C. A. Levinson, and H. M. Mahmoud. Two-body forces and nuclear saturation. I. central forces. *Physical Review*, 95(1):217–228, 1954.

[18] K. A. Brueckner. Nuclear saturation and two-body forces. II. tensor forces. *Physical Review*, 96(2):508–516, 1954.

[19] A. Bohr and B. R. Mottelson. *Nuclear Structure, Vol. I: Single Partilce Motion*. W. A. Benjamin, 1969.

[20] R. F. Casten. *Nuclear structure from a simple perspective*. Oxford University Press, 1990.

[21] Amos de Shalit and Igal Talmi. *Nuclear Shell Theory*. Academic Press, New York and London, 1963.

[22] D. R. Entem and R. Machleidt. Accurate charge-dependent nucleon-nucleon potential at fourth order of chiral perturbation theory. *Physical Review C*, 68(4):041001, 2003.

[23] B. A. Brown and B. H. Wildenthal. Status of the nuclear shell model. *Annual Review of Nuclear and Particle Science*, 38(1):29–66, 1988.

[24] B. A. Brown. The nuclear shell model towards the drip lines. *Progress in Particle and Nuclear Physics*, 47(2):517–599, 2001.

[25] A. Bohr. The coupling of nuclear surface oscillations to the motion of individual nucleons. *Mat. Fys. Medd. Dan. Vid. Selsk.*, 26(14), 1952.

[26] A. Bohr and B. Mottelson. Collective and individual-particle aspects of nuclear structure. *Mat. Fys. Medd. Dan. Vid. Selsk.*, 27(16), 1953.

[27] Brandon Alexander Elman. *Probing proton cross-shell excitations in ^{70}Ni using nucleon knockout reactions*. PhD thesis, Michigan State University, East Lansing, Michigan, 2019.

[28] David J. Griffiths. *Introduction to quantum mechanics*. Pearson Prentice Hall, Upper Saddle River, NJ, 2005.

[29] A. S. Davydov and G. F. Filippov. Rotational states in even atomic nuclei. *Nuclear Physics*, 8:237–249, 1958.

[30] R. F. Casten. Approaching nuclei through multiple perspectives and diverse models: Patterns, symmetries, interactions. *Frontiers of Physics*, 13(6):132104, 2018.

[31] James Rainwater. Nuclear energy level argument for a spheroidal nuclear model. *Physical Review*, 79(3):432–434, 1950.

[32] Sven Gösta Nilsson. Binding states of individual nucleons in strongly deformed nuclei. *Dan. Mat. Fys. Medd.*, 29(16), 1955.

[33] Aage Bohr and Ben Mottelson. Moments of inertia of rotating nuclei. *Dan. Mat. Fys. Medd.*, 30(1), 1955.

[34] J. M. Blatt and V. F. Weisskopf. *Theoretical Nuclear Physic*. Springer-Verlag, New York, 1979.

[35] B. Pritychenko, M. Birch, B. Singh, and M. Horoi. Tables of E2 transition probabilities from the first 2+ states in even–even nuclei. *Atomic Data and Nuclear Data Tables*, 107:1–139, 2016.

[36] H. J. Mang. Alpha decay. *Annual Review of Nuclear Science*, 14(1):1–26, 1964.

[37] Emil Jan Konopinski. Beta-decay. *Reviews of Modern Physics*, 15(4):209–245, 1943.

[38] Ian J. Thompson and Filomena M. Nunes. *Nuclear Reactions for Astrophysics: Principles, Calculation and Applications of Low-Energy Reactions*. Cambridge University Press, 2009.

[39] P.G. Hansen and J.A. Tostevin. Direct reactions with exotic nuclei. *Annual Review of Nuclear and Particle Science*, 53(1):219–261, 2003.

[40] U. Kneissl, H.H. Pitz, and A. Zilges. Investigation of nuclear structure by resonance fluorescence scattering. *Progress in Particle and Nuclear Physics*, 37:349–433, 1996.

[41] Douglas Cline. Nuclear shapes studied by Coulomb excitation. *Annual Review of Nuclear and Particle Science*, 36(1):683–716, 1986.

[42] E. Kwan, C. Andreoiu, R. Ashley, G. C. Ball, P. C. Bender, A. J. Boston, H. C. Boston, A. Chester, A. Close, D. Cline, D. S. Cross, R. Dunlop, A. Finley, A. Garnsworthy, A. B. Hayes, A. Laffoley, T. Nano, P. Voss, S. J. Williams, Z. M. Wang, T. E. Drake, G. Hackman, N. C. Summers, and C. Y. Wu. Precision measurements of the $B(E1)$ strengths in ^{11}Be. Technical Report alma991001635969706316, Lawrence Livermore National Laboratory (LLNL), Livermore, Ca, 2012.

[43] L. P. Gaffney, P. A. Butler, M. Scheck, A. B. Hayes, F. Wenander, M. Albers, B. Bastin, C. Bauer, A. Blazhev, S. Bönig, N. Bree, J. Cederkäll, T. Chupp, D. Cline, T. E. Cocolios, T. Davinson, H. De Witte, J. Diriken, T. Grahn, A. Herzan, M. Huyse, D. G. Jenkins, D. T. Joss, N. Kesteloot, J. Konki, M. Kowalczyk, Th. Kröll, E. Kwan, R. Lutter, K. Moschner, P. Napiorkowski, J. Pakarinen, M. Pfeiffer, D. Radeck, P. Reiter, K. Reynders, S. V. Rigby, L. M. Robledo, M. Rudigier, S. Sambi, M. Seidlitz, B. Siebeck, T. Stora, P. Thoele, P. Van Duppen, M. J. Vermeulen, M. von Schmid, D. Voulot, N. Warr, K. Wimmer, K. Wrzosek-Lipska, C. Y. Wu, and M. Zielinska. Studies of pear-shaped nuclei using accelerated radioactive beams. *Nature*, 497:199–204, 2013.

[44] B. Bucher, S. Zhu, C. Y. Wu, R. V. F. Janssens, D. Cline, A. B. Hayes, M. Albers, A. D. Ayangeakaa, P. A. Butler, C. M. Campbell, M. P. Carpenter, C. J. Chiara, J. A. Clark, H. L. Crawford, M. Cromaz, H. M. David, C. Dickerson, E. T. Gregor, J. Harker, C. R.

Hoffman, B. P. Kay, F. G. Kondev, A. Korichi, T. Lauritsen, A. O. Macchiavelli, R. C. Pardo, A. Richard, M. A. Riley, G. Savard, M. Scheck, D. Seweryniak, M. K. Smith, R. Vondrasek, and A. Wiens. Direct evidence of octupole deformation in neutron-rich ^{144}Ba. *Physical Review Letters*, 116(11):112503, 2016.

[45] A. Gade and B. M. Sherrill. NSCL and FRIB at Michigan State University: Nuclear science at the limits of stability. *Physica Scripta*, 91(5):053003, 2016.

[46] David J. Morrissey and Bradley M. Sherrill. Radioactive nuclear beam facilities based on projectile fragmentation. *Philosophical Transactions of the Royal Society A: Mathematical, Physical and Engineering Sciences*, 356(1744):1985–2006, 1998.

[47] D. Cline, H. S. Gertzman, H. E. Gove, P. M. S. Lesser, and J. J. Schwartz. The static quadrupole moment of the first excited state of ^{60}Ni. *Nuclear Physics A*, 133(2):445–464, 1969.

[48] P. M. S. Lesser, D. Cline, P. Goode, and R. N. Horoshko. Static electric quadrupole moments of the first excited states of ^{56}Fe and the even titanium nuclei. *Nuclear Physics A*, 190(3):597–634, 1972.

[49] P. B. Vold, D. Cline, P. Russo, J. K. Sprinkle, R. P. Scharenberg, and R. J. Mitchell. Quadrupole moment of the first excited 2+ state of ^{18}O. *Physical Review Letters*, 39(6):325–F328, 1977.

[50] T. Glasmacher. Coulomb excitation at intermediate energies. *Annual Review of Nuclear and Particle Science*, 48(1):1–31, 1998.

[51] T. Motobayashi, Y. Ikeda, Y. Ando, K. Ieki, M. Inoue, N. Iwasa, , T. Kikuchi, M. Kurokawa, S. Moriya, S. Ogawa, H. Murakami, S. Shimoura, Y. Yanagisawa, T. Nakamura, Y. Watanabe, M. Ishihara, T. Teranishi, H. Okuno, and R. F. Casten. Large deformation of the very neutron-rich nucleus ^{32}Mg from intermediate-energy Coulomb excitation. *Physics Letters B*, 346(1):9–14, 1995.

[52] B. Elman, A. Gade, D. Weisshaar, D. Barofsky, D. Bazin, P. C. Bender, M. Bowry, M. Hjorth-Jensen, K. W. Kemper, S. Lipschutz, E. Lunderberg, N. Sachmpazidi, N. Terpstra, W. B. Walters, A. Westerberg, S. J. Williams, and K. Wimmer. Quadrupole collectivity beyond $N = 50$ in neutron-rich Se and Kr isotopes. *Physical Review C*, 96(4):044332, 2017.

[53] B. Longfellow, D. Weisshaar, A. Gade, B. A. Brown, D. Bazin, K. W. Brown, B. Elman, J. Pereira, D. Rhodes, and M. Spieker. Shape changes in the $N = 28$ island of inversion: Collective structures built on configuration-coexisting states in ^{43}S. *Physical Review Letters*, 125(23):232501, 2020.

[54] B. Longfellow, D. Weisshaar, A. Gade, B. A. Brown, D. Bazin, K. W. Brown, B. Elman, J. Pereira, D. Rhodes, and M. Spieker. Quadrupole collectivity in the neutron-rich sulfur isotopes ^{38,40,42,44}S. *Physical Review C*, 103(5):054309, 2021.

[55] A. Gade, D. Bazin, C. M. Campbell, J. A. Church, D. C. Dinca, J. Enders, T. Glasmacher, Z. Hu, K. W. Kemper, W. F. Mueller, H. Olliver, B. C. Perry, L. A. Riley, B. T. Roeder, B. M. Sherrill, and J. R. Terry. Detailed experimental study on intermediate-energy Coulomb excitation of ^{46}Ar. *Physical. Review. C*, 68(1):014302, 2003.

[56] K. L. Yurkewicz, D. Bazin, B. A. Brown, C. M. Campbell, J. A. Church, D.-C. Dinca, A. Gade, T. Glasmacher, M. Honma, T. Mizusaki, W. F. Mueller, H. Olliver, T. Otsuka, L. A. Riley, and J. R. Terry. Intermediate-energy Coulomb excitation of ^{52}Fe. *Physical. Review. C*, 70(3):034301, 2004.

[57] C. Vaman, C. Andreoiu, D. Bazin, A. Becerril, B. A. Brown, C. M. Campbell, A. Chester, J. M. Cook, D. C. Dinca, A. Gade, D. Galaviz, T. Glasmacher, M. Hjorth-Jensen, M. Horoi, D. Miller, V. Moeller, W. F. Mueller, A. Schiller, K. Starosta, A. Stolz, J. R. Terry, A. Volya, V. Zelevinsky, and H. Zwahlen. $Z = 50$ shell gap near ^{100}Sn from intermediate-energy Coulomb excitations in even-mass $^{106-112}$Sn isotopes. *Physical Review Letters*, 99(16):162501, 2007.

[58] S. Ettenauer, H. Zwahlen, P. Adrich, D. Bazin, C. M. Campbell, J. M. Cook, A. D. Davies, D.-C. Dinca, A. Gade, T. Glasmacher, J.-L. Lecouey, W. F. Mueller, T. Otsuka, R. R. Reynolds, L. A. Riley, J. R. Terry, Y. Utsuno, and K. Yoneda. Intermediate-energy Coulomb excitation of ^{30}Na. *Physical Review C*, 78(1):017302, 2008.

[59] R. Winkler, A. Gade, T. Baugher, D. Bazin, B. A. Brown, T. Glasmacher, G. F. Grinyer, R. Meharchand, S. McDaniel, A. Ratkiewicz, and D. Weisshaar. Quadrupole collectivity beyond $N = 28$: intermediate-energy Coulomb excitation of ^{47,48}Ar. *Physical Review Letters*, 108(18):182501, 2012.

[60] T. Baugher, A. Gade, R. V. F. Janssens, S. M. Lenzi, D. Bazin, B. A. Brown, M. P. Carpenter, A. N. Deacon, S. J. Freeman, T. Glasmacher, G. F. Grinyer, F. G. Kondev, S. McDaniel, A. Poves, A. Ratkiewicz, E. A. McCutchan, D. K. Sharp, I. Stefanescu, K. A. Walsh, D. Weisshaar, and S. Zhu. Intermediate-energy Coulomb excitation of ^{58,60,62}Cr: The onset of collectivity toward $N = 40$. *Physical Review C*, 86(1):011305, 2012.

[61] I. Stefanescu, G. Georgiev, F. Ames, J. Äystö, D. L. Balabanski, G. Bollen, P. A. Butler, J. Cederkäll, N. Champault, T. Davinson, A. De Maesschalck, P. Delahaye, J. Eberth, D Fedorov, V. N. Fedosseev, L. M. Fraile, S. Franchoo, K. Gladnishki, D. Habs, K. Heyde, M. Huyse, O. Ivanov, J. Iwanicki, J. Jolie, B. Jonson, Th. Kröll, R. Krücken, O. Kester, U. Köster, A. Lagoyannis, L. Liljeby, G. Lo Bianco, B. A. Marsh, O. Niedermaier, T. Nilsson, M. Oinonen, G. Pascovici, P. Reiter, A. Saltarelli, H. Scheit, D. Schwalm, T. Sieber, N. Smirnova, J. Van De Walle, P. Van Duppen, S. Zemlyanoi, N. Warr, D. Weisshaar, and F. Wenander. Coulomb excitation of ^{68,70}Cu: First use of postaccelerated isomeric beams. *Physical Review Letters*, 98(12):122701, 2007.

[62] Aage Winther and Kurt Alder. Relativistic Coulomb excitation. *Nuclear Physics A*, 319(3):518–532, 1976.

[63] J. Dilling, R. Krücken, and G. Ball. ISAC overview. *Hyperfine Interactions*, 225(1):1–8, 2014.

[64] D. Voulot, F. Wenander, E. Piselli, R. Scrivens, M. Lindroos, H.B. Jeppesen, L.M. Fraile, S. Sturm, and P. Delahaye. Radioactive beams at REX–ISOLDE: present status and latest developments. *Nuclear Instruments and Methods in Physics Research Section B: Beam Interactions with Materials and Atoms*, 266(19):4103–4107, 2008.

[65] N. P. Heydenburg and G. M. Temmer. Coulomb excitation of energy levels in rhodium and silver. *Physical Review*, 95(3):861–863, 1954.

[66] G. M. Temmer and N. P. Heydenburg. Coulomb excitation of medium-weight nuclei. *Physical Review*, 104(4):967–980, 1956.

[67] P. H. Stelson and F. K. McGowan. Coulomb excitation of medium-weight even-even nuclei. *Physical Review*, 110(2):489–506, 1958.

[68] J. O. Newton and F. S. Stephens. Experimental observation of double coulomb excitation. *Physical Review Letters*, 1(2):63–65, 1958.

[69] M. A. Schumaker, D. Cline, G. Hackman, C. Pearson, C. E. Svensson, C. Y. Wu, A. Andreyev, R. A. E. Austin, G. C. Ball, D. Bandyopadhyay, J. A. Becker, A. J. Boston, H. C. Boston, L. Buchmann, R. Churchman, F. Cifarelli, R. J. Cooper, D. S. Cross, D. Dashdorj, G. A. Demand, M. R. Dimmock, T. E. Drake, P. Finlay, A. T. Gallant, P. E. Garrett, K. L. Green, A. N. Grint, G. F. Grinyer, L. J. Harkness, A. B. Hayes, R. Kanungo, A. F. Lisetskiy, K. G. Leach, G. Lee, R. Maharaj, J. P. Martin, F. Moisan, A. C. Morton, S. Mythili, L. Nelson, O. Newman, P. J. Nolan, J. N. Orce, E. Padilla-Rodal, A. A. Phillips, M. Porter-Peden, J. J. Ressler, R. Roy, C. Ruiz, F. Sarazin, D. P. Scraggs, J. C. Waddington, J. M. Wan, A. Whitbeck, S. J. Williams, and J. Wong. Coulomb excitation of radioactive ^{20,21}Na. *The European Physical Journal A*, 42(3):477, 2009.

[70] P. Ruotsalainen, J. Henderson, G. Hackman, G. H. Sargsyan, K. D. Launey, A. Saxena, P. C. Srivastava, S. R. Stroberg, T. Grahn, J. Pakarinen, G. C. Ball, R. Julin, P. T. Greenlees, J. Smallcombe, C. Andreoiu, N. Bernier, M. Bowry, M. Buckner, R. Caballero-Folch, A. Chester, S. Cruz, L. J. Evitts, R. Frederick, A. B. Garnsworthy, M. Holl, A. Kurkjian, D. Kisliuk, K. G. Leach, E. McGee, J. Measures, D. Mücher, J. Park, F. Sarazin, J. K. Smith, D. Southall, K. Starosta, C. E. Svensson, K. Whitmore, M. Williams, and C. Y. Wu. Isospin symmetry in $B(E2)$ values: Coulomb excitation study of ^{21}Mg. *Physical Review C*, 99(5):051301, 2019.

[71] K. Hadyńska-Klęk, P. J. Napiorkowski, M. Zielińska, J. Srebrny, A. Maj, F. Azaiez, J. J. Valiente Dobón, M. Kici ńska Habior, F. Nowacki, H. Naïdja, B. Bounthong, T. R. Rodríguez, G. de Angelis, T. Abraham, G. Anil Kumar, D. Bazzacco, M. Bellato, D. Bortolato, P. Bednarczyk, G. Benzoni, L. Berti, B. Birkenbach, B. Bruyneel, S. Brambilla, F. Camera, J. Chavas, B. Cederwall, L. Charles, M. Ciemała, P. Cocconi, P. Coleman-Smith, A. Colombo, A. Corsi, F. C. L. Crespi, D. M. Cullen, A. Czermak, P. Désesquelles, D. T. Doherty, B. Dulny, J. Eberth, E. Farnea, B. Fornal, S. Franchoo, A. Gadea, A. Giaz, A. Gottardo, X. Grave, J. Grębosz, A. Görgen, M. Gulmini, T. Habermann, H. Hess, R. Isocrate, J. Iwanicki, G. Jaworski, D. S. Judson, A. Jungclaus, N. Karkour, M. Kmiecik, D. Karpiński, M. Kisieliński, N. Kondratyev, A. Korichi, M. Komorowska, M. Kowalczyk, W. Korten,

M. Krzysiek, G. Lehaut, S. Leoni, J. Ljungvall, A. Lopez-Martens, S. Lunardi, G. Maron, K. Mazurek, R. Menegazzo, D. Mengoni, E. Merchán, W. Męczyński, C. Michelagnoli, J. Mierzejewski, B. Million, S. Myalski, D. R. Napoli, R. Nicolini, M. Niikura, A. Obertelli, S. F. Özmen, M. Palacz, L. Próchniak, A. Pullia, B. Quintana, G. Rampazzo, F. Recchia, N. Redon, P. Reiter, D. Rosso, K. Rusek, E. Sahin, M.-D. Salsac, P.-A. Söderström, I. Stefan, O. Stézowski, J. Styczeń, Ch. Theisen, N. Toniolo, C. A. Ur, V. Vandone, R. Wadsworth, B. Wasilewska, A. Wiens, J. L. Wood, K. Wrzosek-Lipska, and M. Zięblinski. Superdeformed and triaxial states in ^{42}Ca. *Physical Review Letters*, 117(6):062501, 2016.

[72] A.D. Ayangeakaa, R.V.F. Janssens, C.Y. Wu, J.M. Allmond, J.L. Wood, S. Zhu, M. Albers, S. Almaraz-Calderon, B. Bucher, M.P. Carpenter, C.J. Chiara, D. Cline, H.L. Crawford, H.M. David, J. Harker, A.B. Hayes, C.R. Hoffman, B.P. Kay, K. Kolos, A. Korichi, T. Lauritsen, A.O. Macchiavelli, A. Richard, D. Seweryniak, and A. Wiens. Shape coexistence and the role of axial asymmetry in ^{72}Ge. *Physics Letters B*, 754:254–259, 2016.

[73] A. D. Ayangeakaa, R. V. F. Janssens, S. Zhu, D. Little, J. Henderson, C. Y. Wu, D. J. Hartley, M. Albers, K. Auranen, B. Bucher, M. P. Carpenter, P. Chowdhury, D. Cline, H. L. Crawford, P. Fallon, A. M. Forney, A. Gade, A. B. Hayes, F. G. Kondev, Krishichayan, T. Lauritsen, J. Li, A. O. Macchiavelli, D. Rhodes, D. Seweryniak, S. M. Stolze, W. B. Walters, and J. Wu. Evidence for rigid triaxial deformation in ^{76}Ge from a model-independent analysis. *Physical Review Letters*, 123(10):102501, 2019.

[74] J. Henderson, C. Y. Wu, J. Ash, B. A. Brown, P. C. Bender, R. Elder, B. Elman, A. Gade, M. Grinder, H. Iwasaki, B. Longfellow, T. Mijatović, D. Rhodes, M. Spieker, and D. Weisshaar. Triaxiality in selenium-76. *Physical Review C*, 99(5):054313, 2019.

[75] K. Wrzosek-Lipska, L. Próchniak, M. Zielińska, J. Srebrny, K. Hadyńska-Klęk, J. Iwanicki, M. Kisieliński, M. Kowalczyk, P. J. Napiorkowski, D. Piętak, and T. Czosnyka. Electromagnetic properties of ^{100}Mo: Experimental results and theoretical description of quadrupole degrees of freedom. *Physical Review C*, 86(6):064305, 2012.

[76] T. Ahn, G. Rainovski, N. Pietralla, L. Coquard, T. Möller, A. Costin, R. V. F. Janssens, C. J. Lister, M. P. Carpenter, and S. Zhu. Identification of the $2^+_{1,\mathrm{ms}}$ mixed-symmetry state in ^{136}Ce. *Physical Review C*, 86(1):014303, 2012.

[77] C.Y. Wu, D. Cline, T. Czosnyka, A. Backlin, C. Baktash, R.M. Diamond, G.D. Dracoulis, L. Hasselgren, H. Kluge, B. Kotlinski, J.R. Leigh, J.O. Newton, W.R. Phillips, S.H. Sie, J. Srebrny, and F.S. Stephens. Quadrupole collectivity and shapes of Os-Pt nuclei. *Nuclear Physics A*, 607(2):178–234, 1996.

[78] B. Kotliński, D. Cline, A. Bäcklin, K.G. Helmer, A.E. Kavka, W.J. Kernan, E.G. Vogt, C.Y. Wu, R.M. Diamond, A.O. Macchiavelli, and M.A. Deleplanque. Coulomb excitation of ^{168}Er. *Nuclear Physics A*, 517(2):365–385, 1990.

[79] T. Czosnyka, D. Cline, L. Hasselgren, C.Y. Wu, R.M. Diamond, H. Kluge, C. Roulet, E.K. Hulet, R.W. Lougheed, and C. Baktash. E2 properties of the ground state band in ^{248}Cm. *Nuclear Physics A*, 458(1):123–136, 1986.

[80] Kurt Alder and Aage Winther. On the theory of multiple Coulomb excitation with heavy ions. *Mat. Fys. Medd . Dan. Vid. Selsk.*, 32(8), 1960.

[81] K. Alder, A. Bohr, T. Huus, B. Mottelson, and A. Winther. Study of nuclear structure by electromagnetic excitation with accelerated ions. *Reviews of Modern Physics*, 28(4):432–542, 1956.

[82] Kurt Alder and Aage Winther. *Electromagnetic Excitation, Theory of Coulomb Excitation with Heavy Ions*. North Holland Publishing Company, Amsterdam, 1975.

[83] T. Czosnyka, D. Cline, and C. Y. Wu. *Bulletin of the American Physical Society*, 28:745, 1983.

[84] K. Alder and A. Winther. *Coulomb Excitation: A Collection of Reprints*. Perspectives in Physics. A Series of Reprint Collections. Academic Publishing, New York, 1966.

[85] J. Henderson. Cygnus: A code for Coulomb excitation analysis in C++. https://github.com/jhenderson88/Cygnus, 2021.

[86] D. C. Kean. Measurement of quadrupole moments through Coulomb excitation. In B. A. Robson, editor, *Nuclear Interactions*, volume 92 of *Lecture Notes in Physics*, pages 80–94. Springer, Berlin, Heidelberg, 1976.

[87] M. Zielińska, L. P. Gaffney, K. Wrzosek-Lipska, E. Clément, T. Grahn, N. Kesteloot, P. Napiorkowski, J. Pakarinen, P. Van Duppen, and N. Warr. Analysis methods of safe Coulomb-excitation experiments with radioactive ion beams using the GOSIA code. *The European Physical Journal A*, 52(4):99, 2016.

[88] L. Hasselgren, C. Fahlander, F. Falk, L.O. Edvardson, J.E. Thun, B.S. Ghuman, and B. Skaali. Reorientation precession measurements on ^{108,110}Pd and the quadrupole moments of their first 2+ states. *Nuclear Physics A*, 264(2):341–364, 1976.

[89] Krishna Kumar. Intrinsic quadrupole moments and shapes of nuclear ground states and excited states. *Physical Review Letters*, 28(4):249–253, 1972.

[90] D. Cline, T. Czosnyka, A. Hayes, P. Napiorkowski, N. Warr, and C.Y. Wu. GOSIA user manual for simulation and analysis of Coulomb excitation experiments. *Gosia Steering Committee*, 18:19–60, 2012.

[91] J. Henderson. Convergence of electric quadrupole rotational invariants from the nuclear shell model. *Physical Review C*, 102(5):054306, 2020.

[92] J. Srebrny, T. Czosnyka, Ch. Droste, S.G. Rohoziński, L. Próchniak, K. Zajac, K. Pomorski, D. Cline, C.Y. Wu, A. Bäcklin, L. Hasselgren, R.M. Diamond, D. Habs, H.J. Körner, F.S. Stephens, C. Baktash, and R.P. Kostecki. Experimental and theoretical investigations of quadrupole collective degrees of freedom in ^{104}Ru. *Nuclear Physics A*, 766:25–51, 2006.

[93] A. J. Ferguson. *Angular Correlation Methods in Gamma-Ray Spectroscopy*. North Holland Publishing Company, Amsterdam, 1965.

[94] H. Frauenfelder and R. Steffen. In K. Siegban, editor, *Alpha-, Beta and Gamma Spectroscopy*, volume 2, page 997. North Holland Publishing Company, 1965.

[95] R. Brenn, H. Spehl, A. Weckherlin, H. A. Doubt, and G. van Middelkoop. Nuclear deorientation for heavy ions recoiling in vacuum and low pressure gas. *Zeitschrift für Physik A Hadrons and Nuclei*, 281(3):219–227, 1977.

[96] F. Bosch and H Spehl. Asymptotic attenuation coefficients in random perturbations of angular correlations. *Zeitschrift für Physik A Hadrons and Nuclei*, 280(4):329–339, 1977.

[97] Alexander Edgar Kavka. *Coulomb excitation: analytical methods and experimental results on even selenium nuclei.* PhD thesis, Uppsala University, Uppsala, Sweden, 1989.

[98] M. T. Esat, D. C. Kean, R. H. Spear, and A. M. Baxter. Mass dependence of the static quadrupole moments of the first 2^+ states in the cadmium isotopes. *Nuclear Physics A*, 274(1-2):237–252, 1976.

[99] Z. Berant, R. A. Eisenstein, Y. Horowitz, U. Smilansky, P. N. Tandon, J. S. Greenberg, A. M. Kleinfeld, and H. G. Maggi. The reorientation effect in ^{110}Cd and ^{114}Cd. *Nuclear Physics A*, 196(2):312–336, 1972.

[100] E. Lunderberg, J. Belarge, P. C. Bender, B. Bucher, D. Cline, B. Elman, A Gade, S. N. Liddick, C. Prokop, D. Weisshaar, and C. Y. Wu. JANUS - a setup for low-energy Coulomb excitation at ReA3. *Nuclear Instrumentation and Methods in Physics Research, A*, 885(1):30–37, 2018.

[101] A. C. C. Villari, D. Alt, G. Bollen, D. B. Crisp, M. Ikegami, S. W. Krause, A. Lapierre, S. M. Lidia, D. J. Morrissey, S. Nash, R. J. Rencsok, R. Ringle, S. Schwarz, R. Shane, C. Sumithrarachchi, S.J. Williams, and Qiang Zhao. Proceedings of the international particle accelerator conference (IPAC'16). page 1287, 2016.

[102] J. Henderson, C. Y. Wu, J. Ash, P. C. Bender, B. Elman, A. Gade, M. Grinder, H. Iwasaki, E. Kwan, B. Longfellow, T. Mijatović, D. Rhodes, M. Spieker, and D. Weisshaar. Localizing the shape transition in neutron-deficient selenium. *Physical Review Letters*, 121(8):082502, 2018.

[103] D. Rhodes, B. A. Brown, J. Henderson, A. Gade, J. Ash, P. C. Bender, R. Elder, B. Elman, M. Grinder, M. Hjorth-Jensen, H. Iwasaki, B. Longfellow, T. Mijatovic, M. Spieker, D. Weisshaar, and C. Y. Wu. Exploring the role of high-j configurations in collective observables through the Coulomb excitation of ^{106}Cd. *Physical Review C*, 103(5):L051301, 2021.

[104] W. F. Mueller, J. A. Church, T. Glasmacher, D. Gutknecht, G. Hackman, P. G. Hansen, Z. Hu, K. L. Miller, and P. Quirin. Thirty-two-fold segmented germanium detectors to identify γ-rays from intermediate-energy exotic beams. *Nuclear Instrumentation and Methods in Physics Research, A: Accelerators, Spectrometers, Detectors and Associated Equipment,*, 466(3):492–498, 2001.

[105] Jack Henderson. Nuclear collectivity: From first principles to $0\nu2\beta$ decay, March 2018. Florida State University – Nuclear Physics Seminar.

[106] Glenn F. Knoll. *Radiation detection and measurement; 4th ed.* John Wiley & Sons, Inc, 2010.

[107] William R. Leo. *Techniques for nuclear and particle physics experiments: how-to approach; 2nd ed.* Springer, Berlin, 1994.

[108] Eric Michael Lunderberg. *Subbarrier Coulomb Excitation at ReA3 - Commissioning of the SeGA-JANUS Experimental setup*. PhD thesis, Michigan State University, East Lansing, Michigan, 2017.

[109] J. B. Marion and S. T. Thornton. *Classical dynamics of particles and systems; 5th ed.* Saunders College Publishing, Fort Worth, Texas, 1995.

[110] Herbert Goldstein, Charles Poole, and John Safko. *Classical Mechanics*. Addison Wesley, Reading, Massachusetts, 2002.

[111] M. J. Berger, J. H. Hubbell, S. M. Seltzer, J. Chang, J. S. Coursey, R. Sukumar, D. S. Zucker, and K. Olsen. Xcom: Photon cross section database (version 1.5). *National Institute of Standards and Technology, Gaithersburg, MD.*, 2010.

[112] O. Klein and Y. Nishina. Uber die streuung yon strahlung durch freie elektronen nach der neuen relativistischen quantendynamik yon dirac. *Zeitschrift für Physik*, 52(11-12):853–868, 1929.

[113] Travis Baugher. *Neutron-Rich Chromium and Manganese Isotopes and the Role of the Neutron* $0g_{9/2}$ *and* $1d_{5/2}$ *Orbitals in the Region below* ^{68}*Ni*. PhD thesis, Michigan State University, East Lansing, Michigan, 2013.

[114] S. Paschalis, I.Y. Lee, A.O. Macchiavelli, C.M. Campbell, M. Cromaz, S. Gros, J. Pavan, J. Qian, R.M. Clark, H.L. Crawford, D. Doering, P. Fallon, C. Lionberger, T. Loew, M. Petri, T. Stezelberger, S. Zimmermann, D.C. Radford, K. Lagergren, D. Weisshaar, R. Winkler, T. Glasmacher, J.T. Anderson, and C.W. Beausang. The performance of the gamma-ray energy tracking in-beam nuclear array GRETINA. *Nuclear Instruments and Methods in Physics Research Section A: Accelerators, Spectrometers, Detectors and Associated Equipment*, 709:44–55, 2013.

[115] D. Weisshaar, D. Bazin, P.C. Bender, C.M. Campbell, F. Recchia, V. Bader, T. Baugher, J. Belarge, M.P. Carpenter, H.L. Crawford, M. Cromaz, B. Elman, P. Fallon, A. Forney, A. Gade, J. Harker, N. Kobayashi, C. Langer, T. Lauritsen, I.Y. Lee, A. Lemasson, B. Longfellow, E. Lunderberg, A.O. Macchiavelli, K. Miki, S. Momiyama, S. Noji, D.C. Radford, M. Scott, J. Sethi, S.R. Stroberg, C. Sullivan, R. Titus, A. Wiens, S. Williams, K. Wimmer, and S. Zhu. The performance of the γ-ray tracking array GRETINA for γ-ray spectroscopy with fast beams of rare isotopes. *Nuclear Instruments and Methods in Physics Research Section A: Accelerators, Spectrometers, Detectors and Associated Equipment*, 847:187–198, 2017.

[116] C.J. Prokop, S.N. Liddick, B.L. Abromeit, A.T. Chemey, N.R. Larson, S. Suchyta, and J.R. Tompkins. Digital data acquisition system implementation at the National Superconducting Cyclotron Laboratory. *Nuclear Instruments and Methods in Physics Research Section A: Accelerators, Spectrometers, Detectors and Associated Equipment*, 741:163–168, 2014.

[117] XIA LLC, Hayward, CA. *Pixie-16 User Manual; v. 3.03*, 2018.

[118] NSCL data acquisition documentation. `http://docs.nscl.msu.edu/daq/newsite/home.php`. Accessed: 2021-06-24.

[119] J. Ash, H. Iwasaki, T. Mijatović, T. Budner, R. Elder, B. Elman, M. Friedman, A. Gade, M. Grinder, J. Henderson, B. Longfellow, A. Revel, D. Rhodes, M. Spieker, Y. Utsuno, D. Weisshaar, and C. Y. Wu. Cross-shell excitations in ^{46}Ca studied with fusion reactions induced by a reaccelerated rare isotope beam. *Physical Review C*, 103(5):L051302, 2021.

[120] V. M. Bader, A. Gade, D. Weisshaar, B. A. Brown, T. Baugher, D. Bazin, J. S. Berryman, A. Ekström, M. Hjorth-Jensen, S. R. Stroberg, W. B. Walters, K. Wimmer, and R. Winkler. Quadrupole collectivity in neutron-deficient Sn nuclei: ^{104}Sn and the role of proton excitations. *Physical Review C*, 88(5):051301, 2013.

[121] Vincent Maximilian Bader. *Quadrupole collectivity in neutron-deficient Sn nuclei:* ^{104}*Sn*. PhD thesis, Michigan State University, East Lansing, Michigan, 2014.

[122] D. Rosiak, M. Seidlitz, P. Reiter, H. Naïdja, Y. Tsunoda, T. Togashi, F. Nowacki, T. Otsuka, G. Colò, K. Arnswald, T. Berry, A. Blazhev, M. J. G. Borge, J. Cederkäll, D. M. Cox, H. De Witte, L. P. Gaffney, C. Henrich, R. Hirsch, M. Huyse, A. Illana, K. Johnston, L. Kaya, Th. Kröll, M. L. Lozano Benito, J. Ojala, J. Pakarinen, M. Queiser, G. Rainovski, J. A. Rodriguez, B. Siebeck, E. Siesling, J. Snäll, P. Van Duppen, A. Vogt, M. von Schmid, N. Warr, F. Wenander, and K. O. Zell. Enhanced quadrupole and octupole strength in doubly magic ^{132}Sn. *Physical Review Letters*, 121(25):252501, 2018.

[123] M. Siciliano, J.J. Valiente-Dobón, A. Goasduff, F. Nowacki, A.P. Zuker, D. Bazzacco, A. Lopez-Martens, E. Clément, G. Benzoni, T. Braunroth, F.C.L. Crespi, N. Cieplicka-Oryńczak, M. Doncel, S. Ertürk, G. de France, C. Fransen, A. Gadea, G. Georgiev, A. Goldkuhle, U. Jakobsson, G. Jaworski, P.R. John, I. Kuti, A. Lemasson, T. Marchi, D. Mengoni, C. Michelagnoli, T. Mijatović, C. Müller-Gatermann, D.R. Napoli, J. Nyberg, M. Palacz, R.M. Pérez-Vidal, B. Sayği, D. Sohler, S. Szilner, D. Testov, M. Zielińska, D. Barrientos, B. Birkenbach, H.C. Boston, A.J. Boston, B. Cederwall, J. Collado, D.M. Cullen, P. Désesquelles, C. Domingo-Pardo, J. Dudouet, J. Eberth, F.J. Egea-Canet, V. González, L.J. Harkness-Brennan, H. Hess, D.S. Judson, A. Jungclaus, W. Korten, M. Labiche, A. Lefevre, S. Leoni, H. Li, A. Maj, R. Menegazzo, B. Million, A. Pullia, F. Recchia, P. Reiter, M.D. Salsac, E. Sanchis, O. Stezowski, and Ch. Theisen. Pairing-quadrupole interplay in the neutron-deficient tin nuclei: First lifetime measurements of low-lying states in ^{106,108}Sn. *Physics Letters B*, 806:135474, 2020.

[124] N.-G. Jonsson, A. Bäcklin, J. Kantele, R. Julin, M. Luontama, and A. Passoja. Collective states in even Sn nuclei. *Nuclear Physics A*, 371(2):333–348, 1981.

[125] D. C. Radford, C. Baktash, J. R. Beene, B. Fuentes, A. Galindo-Uribarri, J. Gomez del Campo, C. J. Gross, M. L. Halbert, Y. Larochelle, T. A. Lewis, J. F. Liang, J. Mas, P. E. Mueller, E. Padilla, D. Shapira, D. W. Stracener, R. L. Varner, C.-H. Yu, C. J. Barton,

M. A. Caprio, D. J. Hartley, and N. V. Zamfir. Nuclear structure studies with heavy neutron-rich RIBS at the HRIBF. *Nuclear Physics A*, 746:83–89, 2004. Proceedings of the Sixth International Conference on Radioactive Nuclear Beams (RNB6).

[126] D. C. Radford, C. Baktash, C. J. Barton, J. Batchelder, J. R. Beene, C. R. Bingham, M. A. Caprio, M. Danchev, B. Fuentes, A. Galindo-Uribarri, J. Gomez del Campo, C. J. Gross, M. L. Halbert, D. J. Hartley, P. Hausladen, J. K. Hwang, W. Krolas, Y. Larochelle, J. F. Liang, P. E. Mueller, E. Padilla, J. Pavan, A. Piechaczek, D. Shapira, D. W. Stracener, R. L. Varner, A. Woehr, C.-H. Yu, and N. V. Zamfir. Coulomb excitation and transfer reactions with rare neutron-rich isotopes. *Nuclear Physics A*, 752:264–272, 2005. Proceedings of the 22nd International Nuclear Physics Conference (Part 2).

[127] A. Banu, J. Gerl, C. Fahlander, M. Górska, H. Grawe, T. R. Saito, H.-J. Wollersheim, E. Caurier, T. Engeland, A. Gniady, M. Hjorth-Jensen, F. Nowacki, T. Beck, F. Becker, P. Bednarczyk, M. A. Bentley, A. Bürger, F. Cristancho, G. de Angelis, Zs. Dombrádi, P. Doornenbal, H. Geissel, J. Grebosz, G. Hammond, M. Hellström, J. Jolie, I. Kojouharov, N. Kurz, R. Lozeva, S. Mandal, N. Mărginean, S. Muralithar, J. Nyberg, J. Pochodzalla, W. Prokopowicz, P. Reiter, D. Rudolph, C. Rusu, N. Saito, H. Schaffner, D. Sohler, H. Weick, C. Wheldon, and M. Winkler. ^{108}Sn studied with intermediate-energy Coulomb excitation. *Physical Review C*, 72(6):061305, 2005.

[128] J. Cederkäll, A. Ekström, C. Fahlander, A. M. Hurst, M. Hjorth-Jensen, F. Ames, A. Banu, P. A. Butler, T. Davinson, U. Datta Pramanik, J. Eberth, S. Franchoo, G. Georgiev, M. Górska, D. Habs, M. Huyse, O. Ivanov, J. Iwanicki, O. Kester, U. Köster, B. A. Marsh, O. Niedermaier, T. Nilsson, P. Reiter, H. Scheit, D. Schwalm, T. Sieber, G. Sletten, I. Stefanescu, J. Van de Walle, P. Van Duppen, N. Warr, D. Weisshaar, and F. Wenander. Sub-barrier Coulomb excitation of ^{110}Sn and its implications for the ^{100}Sn shell closure. *Physical Review Letters*, 98(17):172501, 2007.

[129] J. N. Orce, S. N. Choudry, B. Crider, E. Elhami, S. Mukhopadhyay, M. Scheck, M. T. McEllistrem, and S. W. Yates. $2_1^+ \to 0_1^+$ transition strengths in Sn nuclei. *Physical Review C*, 76(2):021302, 2007.

[130] P. Doornenbal, P. Reiter, H. Grawe, H. J. Wollersheim, P. Bednarczyk, L. Caceres, J. Cederkäll, A. Ekström, J. Gerl, M. Górska, A. Jhingan, I. Kojouharov, R. Kumar, W. Prokopowicz, H. Schaffner, and R. P. Singh. Enhanced strength of the $2_1^+ \to 0_{\text{g.s.}}^+$ transition in ^{114}Sn studied via Coulomb excitation in inverse kinematics. *Physical Review C*, 78(3):031303, 2008.

[131] A. Ekström, J. Cederkäll, C. Fahlander, M. Hjorth-Jensen, F. Ames, P. A. Butler, T. Davinson, J. Eberth, F. Fincke, A. Görgen, M. Górska, D. Habs, A. M. Hurst, M. Huyse, O. Ivanov, J. Iwanicki, O. Kester, U. Köster, B. A. Marsh, J. Mierzejewski, P. Reiter, H. Scheit, D. Schwalm, S. Siem, G. Sletten, I. Stefanescu, G. M. Tveten, J. Van de Walle, P. Van Duppen, D. Voulot, N. Warr, D. Weisshaar, F. Wenander, and M. Zielińska. $0_{\text{gs}}^+ \to 2_1^+$ transition strengths in ^{106}Sn and ^{108}Sn. *Physical Review Letters*, 101(1):012502, 2008.

[132] R. Kumar, P. Doornenbal, A. Jhingan, R. K. Bhowmik, S. Muralithar, S. Appannababu, R. Garg, J. Gerl, M. Górska, J. Kaur, I. Kojouharov, S. Mandal, S. Mukherjee, D. Siwal, A. Sharma, Pushpendra P. Singh, R. P. Singh, and H. J. Wollersheim. Enhanced $0^+_{\mathrm{g.s.}} \to 2^+_1$ $E2$ transition strength in ^{112}Sn. *Physical Review C*, 81(2):024306, 2010.

[133] J. M. Allmond, D. C. Radford, C. Baktash, J. C. Batchelder, A. Galindo-Uribarri, C. J. Gross, P. A. Hausladen, K. Lagergren, Y. Larochelle, E. Padilla-Rodal, and C.-H. Yu. Coulomb excitation of ^{124,126,128}Sn. *Physical Review C*, 84(6):061303, 2011.

[134] A. Jungclaus, J. Walker, J. Leske, K.-H. Speidel, A.E. Stuchbery, M. East, P. Boutachkov, J. Cederkäll, P. Doornenbal, J.L. Egido, A. Ekström, J. Gerl, R. Gernhäuser, N. Goel, M. Górska, I. Kojouharov, P. Maier-Komor, V. Modamio, F. Naqvi, N. Pietralla, S. Pietri, W. Prokopowicz, H. Schaffner, R. Schwengner, and H.-J. Wollersheim. Evidence for reduced collectivity around the neutron mid-shell in the stable even-mass Sn isotopes from new lifetime measurements. *Physics Letters B*, 695(1):110–114, 2011.

[135] G. J. Kumbartzki, N. Benczer-Koller, D. A. Torres, B. Manning, P. D. O'Malley, Y. Y. Sharon, L. Zamick, C. J. Gross, D. C. Radford, S. J. Q. Robinson, J. M. Allmond, A. E. Stuchbery, K.-H. Speidel, N. J. Stone, and C. R. Bingham. Transient field g factor and mean-life measurements with a rare isotope beam of ^{126}Sn. *Physical Review C*, 86(3):034319, 2012.

[136] G. Guastalla, D. D. DiJulio, M. Górska, J. Cederkäll, P. Boutachkov, P. Golubev, S. Pietri, H. Grawe, F. Nowacki, K. Sieja, A. Algora, F. Ameil, T. Arici, A. Atac, M. A. Bentley, A. Blazhev, D. Bloor, S. Brambilla, N. Braun, F. Camera, Zs. Dombrádi, C. Domingo Pardo, A. Estrade, F. Farinon, J. Gerl, N. Goel, J. Grębosz, T. Habermann, R. Hoischen, K. Jansson, J. Jolie, A. Jungclaus, I. Kojouharov, R. Knoebel, R. Kumar, J. Kurcewicz, N. Kurz, N. Lalović, E. Merchan, K. Moschner, F. Naqvi, B. S. Nara Singh, J. Nyberg, C. Nociforo, A. Obertelli, M. Pfützner, N. Pietralla, Z. Podolyák, A. Prochazka, D. Ralet, P. Reiter, D. Rudolph, H. Schaffner, F. Schirru, L. Scruton, D. Sohler, T. Swaleh, J. Taprogge, Zs. Vajta, R. Wadsworth, N. Warr, H. Weick, A. Wendt, O. Wieland, J. S. Winfield, and H. J. Wollersheim. Coulomb excitation of ^{104}Sn and the strength of the ^{100}Sn shell closure. *Physical Review Letters*, 110(17):172501, 2013.

[137] P. Doornenbal, S. Takeuchi, N. Aoi, M. Matsushita, A. Obertelli, D. Steppenbeck, H. Wang, L. Audirac, H. Baba, P. Bednarczyk, S. Boissinot, M. Ciemala, A. Corsi, T. Furumoto, T. Isobe, A. Jungclaus, V. Lapoux, J. Lee, K. Matsui, T. Motobayashi, D. Nishimura, S. Ota, E. C. Pollacco, H. Sakurai, C. Santamaria, Y. Shiga, D. Sohler, and R. Taniuchi. Intermediate-energy Coulomb excitation of ^{104}Sn: Moderate $E2$ strength decrease approaching ^{100}Sn. *Physical Review C*, 90(6):061302, 2014.

[138] J. M. Allmond, A. E. Stuchbery, A. Galindo-Uribarri, E. Padilla-Rodal, D. C. Radford, J. C. Batchelder, C. R. Bingham, M. E. Howard, J. F. Liang, B. Manning, S. D. Pain, N. J. Stone, R. L. Varner, and C.-H. Yu. Investigation into the semimagic nature of the tin isotopes through electromagnetic moments. *Physical Review C*, 92(4):041303, 2015.

[139] G. J. Kumbartzki, N. Benczer-Koller, K.-H. Speidel, D. A. Torres, J. M. Allmond, P. Fallon, I. Abramovic, L. A. Bernstein, J. E. Bevins, H. L. Crawford, Z. E. Guevara, G. Gürdal, A. M. Hurst, L. Kirsch, T. A. Laplace, A. Lo, E. F. Matthews, I. Mayers, L. W. Phair, F. Ramirez, S. J. Q. Robinson, Y. Y. Sharon, and A. Wiens. $Z = 50$ core stability in ^{110}Sn from magnetic-moment and lifetime measurements. *Physical Review C*, 93(4):044316, 2016.

[140] R. Kumar, M. Saxena, P. Doornenbal, A. Jhingan, A. Banerjee, R. K. Bhowmik, S. Dutt, R. Garg, C. Joshi, V. Mishra, P. J. Napiorkowski, S. Prajapati, P.-A. Söderström, N. Kumar, and H.-J. Wollersheim. No evidence of reduced collectivity in Coulomb-excited Sn isotopes. *Physical Review C*, 96(5):054318, 2017.

[141] M. Spieker, P. Petkov, E. Litvinova, C. Müller-Gatermann, S. G. Pickstone, S. Prill, P. Scholz, and A. Zilges. Shape coexistence and collective low-spin states in ^{112,114}Sn studied with the $(p, p'\gamma)$ doppler-shift attenuation coincidence technique. *Physical Review C*, 97(5):054319, 2018.

[142] D. Rosiak, M. Seidlitz, P. Reiter, H. Naïdja, Y. Tsunoda, T. Togashi, F. Nowacki, T. Otsuka, G. Colò, K. Arnswald, T. Berry, A. Blazhev, M. J. G. Borge, J. Cederkäll, D. M. Cox, H. De Witte, L. P. Gaffney, C. Henrich, R. Hirsch, M. Huyse, A. Illana, K. Johnston, L. Kaya, Th. Kröll, M. L. Lozano Benito, J. Ojala, J. Pakarinen, M. Queiser, G. Rainovski, J. A. Rodriguez, B. Siebeck, E. Siesling, J. Snäll, P. Van Duppen, A. Vogt, M. von Schmid, N. Warr, F. Wenander, and K. O. Zell. Enhanced quadrupole and octupole strength in doubly magic ^{132}Sn. *Physical Review Letters*, 121(25):252501, 2018.

[143] M. Siciliano. Study of quadrupole correlations in the neutron-deficient Snand Cd region via lifetime measurements. *Il Nuovo Cimento C*, 40(2):84, 2017.

[144] M. Siciliano, J. J. Valiente-Dobón, A. Goasduff, T. R. Rodríguez, D. Bazzacco, G. Benzoni, T. Braunroth, N. Cieplicka-Oryńczak, E. Clément, F. C. L. Crespi, G. de France, M. Doncel, S. Ertürk, C. Fransen, A. Gadea, G. Georgiev, A. Goldkuhle, U. Jakobsson, G. Jaworski, P. R. John, I. Kuti, A. Lemasson, H. Li, A. Lopez-Martens, T. Marchi, D. Mengoni, C. Michelagnoli, T. Mijatović, C. Müller-Gatermann, D. R. Napoli, J. Nyberg, M. Palacz, R. M. Pérez-Vidal, B. Sayği, D. Sohler, S. Szilner, and D. Testov. Lifetime measurements in the even-even $^{102-108}$Cd isotopes. https://arxiv.org/abs/2101.08711, 2021.

[145] N. Benczer-Koller, G. J. Kumbartzki, K.-H. Speidel, D. A. Torres, S. J. Q. Robinson, Y. Y. Sharon, J. M. Allmond, P. Fallon, I. Abramovic, L. A. Bernstein, J. E. Bevins, H. L. Crawford, Z. E. Guevara, A. M. Hurst, L. Kirsch, T. A. Laplace, A. Lo, E. F. Matthews, I. Mayers, L. W. Phair, F. Ramirez, and A. Wiens. Magnetic moment and lifetime measurements of Coulomb-excited states in ^{106}Cd. *Physical Review C*, 94(3):034303, 2016.

[146] S. Ilieva, M. Thürauf, Th. Kröll, R. Krücken, T. Behrens, V. Bildstein, A. Blazhev, S. Bönig, P. A. Butler, J. Cederkäll, T. Davinson, P. Delahaye, J. Diriken, A. Ekström, F. Finke, L. M. Fraile, S. Franchoo, Ch. Fransen, G. Georgiev, R. Gernhäuser, D. Habs, H. Hess, A. M. Hurst, M. Huyse, O. Ivanov, J. Iwanicki, P. Kent, O. Kester, U. Köster, R. Lutter, M. Mahgoub, D. Martin, P. Mayet, P. Maierbeck, T. Morgan, O. Niedermeier, M. Pantea, P. Reiter, T. R. Rodríguez, Th. Rolke, H. Scheit, A. Scherillo, D. Schwalm, M. Seidlitz, T. Sieber, G. S.

Simpson, I. Stefanescu, S. Thiel, P. G. Thirolf, J. Van de Walle, P. Van Duppen, D. Voulot, N. Warr, W. Weinzierl, D. Weisshaar, F. Wenander, A. Wiens, and S. Winkler. Coulomb excitation of neutron-rich Cd isotopes. *Physical Review C*, 89(1):014313, 2014.

[147] A. Ekström, J. Cederkäll, D. D. DiJulio, C. Fahlander, M. Hjorth-Jensen, A. Blazhev, B. Bruyneel, P. A. Butler, T. Davinson, J. Eberth, C. Fransen, K. Geibel, H. Hess, O. Ivanov, J. Iwanicki, O. Kester, J. Kownacki, U. Köster, B. A. Marsh, P. Reiter, M. Scheck, B. Siebeck, S. Siem, I. Stefanescu, H. K. Toft, G. M. Tveten, J. Van de Walle, D. Voulot, N. Warr, D. Weisshaar, F. Wenander, K. Wrzosek, and M. Zielińska. Electric quadrupole moments of the 2_1^+ states in ^{100,102,104}Cd. *Phys. Rev. C*, 80(5):054302, 2009.

[148] N. Boelaert, A. Dewald, C. Fransen, J. Jolie, A. Linnemann, B. Melon, O. Möller, N. Smirnova, and K. Heyde. Low-spin electromagnetic transition probabilities in ^{102,104}Cd. *Physical Review C*, 75(5):054311, 2007.

[149] W. T. Milner, F. K. McGowan, P. H. Stelson, R. L. Robinson, and R. O. Sayer. Coulomb excitation of the even-A cadmium nuclei. *Nuclear Physics A*, 129(3):687–696, 1969.

[150] BNL evaluated nuclear structure data file (ENSDF). https://www.nndc.bnl.gov, 2021.

[151] A. P. Zuker. Quadrupole dominance in the light Sn and in the Cd isotopes. *Physical Review C*, 103(2):024322, 2021.

[152] Jian Zhong, Ying-Jun Ma, Xiao-Guang Wu, Bao-Ji Zhu, Cong-Bo Li, Guang-Sheng Li, Yun Zheng, Qi-Ming Chen, Chuang-Ye He, Li-Tao Deng, Wen-Kui Zhou, Ke-Yan Ma, Dong Yang, Hao Guo, Jia-Qi Wang, Xian Guang, Ji Sun, Hui-Bin Sun, Shi-Peng Hu, Lin Gan, Hai-Ge Zhao, Qi Luo, and Zheng-Xin Wu. Lifetime measurement for the 2_1^+ state in ^{106}Cd. *Chinese Physics C*, 44(9):094001, 2020.

[153] D. J. Morrissey, B. M. Sherrill, M. Steiner, A. Stolz, and I. Wiedenhoever. Commissioning the A1900 projectile fragment separator. *Nuclear Instruments and Methods in Physics Research Section B: Beam Interactions with Materials and Atoms*, 204:90–96, 2003. 14th International Conference on Electromagnetic Isotope Separators and Techniques Related to their Applications.

[154] A. Lapierre, G. Bollen, D. Crisp, S. W. Krause, L. E. Linhardt, K. Lund, S. Nash, R. Rencsok, R. Ringle, S. Schwarz, M. Steiner, C. Sumithrarachchi, T. Summers, A. C. C. Villari, S. J. Williams, and Q. Zhao. First two operational years of the electron-beam ion trap charge breeder at the National Superconducting Cyclotron Laboratory. *Physical Review Accelerators and Beams*, 21(5):053401, 2018.

[155] James F. Ziegler, M.D. Ziegler, and J.P. Biersack. SRIM – the stopping and range of ions in matter (2010). *Nuclear Instruments and Methods in Physics Research Section B: Beam Interactions with Materials and Atoms*, 268(11):1818–1823, 2010. 19th International Conference on Ion Beam Analysis.

[156] S. A. Berendakov, L. I. Govor, A. M. Demidov, and I. V. Mikhailov. Gamma-rays from the ^{106}Cd(n, n'γ) reaction. Technical Report INDC(CCP)299/G,P26, 1988. https://www-nds.iaea.org/publications/indc/indc-ccp-0299.pdf.

[157] Z. W. Grabowski and R. L. Robinson. Properties of the $2'$ and $2''$ states in ^{106,112,114}Cd. *Nuclear Physics A*, 206(3):633–640, 1973.

[158] M. P. Fewell, R. H Spear, G. K. Adam, and M. T. Esat. Determination of $B(E3; 0_1^+ \to 3_1^-)$ values for the stable isotopes of cadmium. *Australian Journal of Physics*, 38(4):555–562, 1985.

[159] A. Dewald, O. Möller, and P. Petkov. Developing the recoil distance Doppler-shift technique towards a versatile tool for lifetime measurements of excited nuclear states. *Progress in Particle and Nuclear Physics*, 67(3):786–839, 2012.

[160] B. A. Brown and W. D. M. Rae. The shell-model code NuShellX@MSU. *Nuclear Data Sheets*, 120:115–118, 2014.

[161] T. Schmidt, K. L. G. Heyde, A. Blazhev, and J. Jolie. Shell-model-based deformation analysis of light cadmium isotopes. *Physical Review C*, 96(1):014302, 2017.

[162] W. A. Richter, S. Mkhize, and B. Alex Brown. sd-shell observables for the USDA and USDB Hamiltonians. *Physical Review C*, 78(6):064302, 2008.

[163] M. Honma, T. Otsuka, B. A. Brown, and T. Mizusaki. New effective interaction for pf-shell nuclei and its implications for the stability of the $N = Z = 28$ closed core. *Physical Review C*, 69(3):034335, 2004.

[164] Y.Y. Sharon, N. Benczer-Koller, G.J. Kumbartzki, L. Zamick, and R.F. Casten. Systematics of the ratio of electric quadrupole moments $Q(2_1^+)$ to the square root of the reduced transition probabilities $B(E2; 0_1^+ \to 2_1^+)$ in even–even nuclei. *Nuclear Physics A*, 980:131–142, 2018.

[165] S. Frauendorf and F.R. May. Triaxial shapes of rotating nuclei with neutron numbers 88, 89, 90. *Physics Letters B*, 125(4):245–250, 1983.

[166] Ikuko Hamamoto and Ben Mottelson. On the intrinsic spectra of rotating nuclei with tri-axial shape. *Physics Letters B*, 127(5):281–285, 1983.

[167] Ikuko Hamamoto. A comment on the analysis of nuclei with triaxial shape. *Physics Letters B*, 143(1):31–35, 1984.

[168] J.J. Sun, Z. Shi, X.Q. Li, H. Hua, C. Xu, Q.B. Chen, S.Q. Zhang, C.Y. Song, J. Meng, X.G. Wu, S.P. Hu, H.Q. Zhang, W.Y. Liang, F.R. Xu, Z.H. Li, G.S. Li, C.Y. He, Y. Zheng, Y.L. Ye, D.X. Jiang, Y.Y. Cheng, C. He, R. Han, Z.H. Li, C.B. Li, H.W. Li, J.L. Wang, J.J. Liu, Y.H. Wu, P.W. Luo, S.H. Yao, B.B. Yu, X.P. Cao, and H.B. Sun. Spectroscopy of 74Ge: from soft to rigid triaxiality. *Physics Letters B*, 734:308–313, 2014.

[169] S. Mukhopadhyay, B. P. Crider, B. A. Brown, S. F. Ashley, A. Chakraborty, A. Kumar, M. T. McEllistrem, E. E. Peters, F. M. Prados-Estévez, and S. W. Yates. Nuclear structure of ^{76}Ge from inelastic neutron scattering measurements and shell model calculations. *Physical Review C*, 95(1):014327, 2017.

[170] Y. Toh, C. J. Chiara, E. A. McCutchan, W. B. Walters, R. V. F. Janssens, M. P. Carpenter, S. Zhu, R. Broda, B. Fornal, B. P. Kay, F. G. Kondev, W. Królas, T. Lauritsen, C. J. Lister, T. Pawłat, D. Seweryniak, I. Stefanescu, N. J. Stone, J. Wrzesiński, K. Higashiyama, and N. Yoshinaga. Evidence for rigid triaxial deformation at low energy in ^{76}Ge. *Physical Review C*, 87(4):041304, 2013.

[171] A. M. Forney, W. B. Walters, C. J. Chiara, R. V. F. Janssens, A. D. Ayangeakaa, J. Sethi, J. Harker, M. Alcorta, M. P. Carpenter, G. Gürdal, C. R. Hoffman, B. P. Kay, F. G. Kondev, T. Lauritsen, C. J. Lister, E. A. McCutchan, A. M. Rogers, D. Seweryniak, I. Stefanescu, and S. Zhu. Novel $\Delta J = 1$ sequence in ^{78}Ge: Possible evidence for triaxiality. *Physical Review Letters*, 120(21):212501, 2018.

[172] Kris Heyde and John L. Wood. Shape coexistence in atomic nuclei. *Reviews of Modern Physics*, 83(4):1467–1521, 2011.

[173] F. Nowacki, A. Poves, E. Caurier, and B. Bounthong. Shape coexistence in ^{78}Ni as the portal to the fifth island of inversion. *Physical Review Letters*, 117(27):272501, 2016.

[174] R. Taniuchi, C. Santamaria, P. Doornenbal, A. Obertelli, K. Yoneda, G. Authelet, H. Baba, D. Calvet, F. Château, A. Corsi, A. Delbart, J.-M. Gheller, A. Gillibert, J. D. Holt, T. Isobe, V. Lapoux, M. Matsushita, J. Menéndez, S. Momiyama, T. Motobayashi, M. Niikura, F. Nowacki, K. Ogata, H. Otsu, T. Otsuka, C. Péron, S. Péru, A. Peyaud, E. C. Pollacco, A. Poves, J.-Y. Roussé, H. Sakurai, A. Schwenk, Y. Shiga, J. Simonis, S. R. Stroberg, S. Takeuchi, Y. Tsunoda, T. Uesaka, H. Wang, F. Browne, L. X. Chung, Z. Dombradi, S. Franchoo, F. Giacoppo, A. Gottardo, K. Hadyńska-Klęk, Z. Korkulu, S. Koyama, Y. Kubota, J. Lee, M. Lettmann, C. Louchart, R. Lozeva, K. Matsui, T. Miyazaki, S. Nishimura, L. Olivier, S. Ota, Z. Patel, E. Şahin, C. Shand, P.-A. Söderström, I. Stefan, D. Steppenbeck, T. Sumikama, D. Suzuki, Z. Vajta, V. Werner, J. Wu, and Z. Y. Xu. ^{78}Ni revealed as a doubly magic stronghold against nuclear deformation. *Nature*, 569(7754):53–58, 2019.

[175] G. Hagen, G. R. Jansen, and T. Papenbrock. Structure of ^{78}Ni from first-principles computations. *Physical Review Letters*, 117(17):172501, 2016.

[176] K. Nomura, R. Rodríguez-Guzmán, and L. M. Robledo. Structural evolution in germanium and selenium nuclei within the mapped interacting boson model based on the Gogny energy density functional. *Physical Review C*, 95(6):064310, 2017.

[177] E. Padilla-Rodal, A. Galindo-Uribarri, C. Baktash, J. C. Batchelder, J. R. Beene, R. Bijker, B. A. Brown, O. Castaños, B. Fuentes, J. Gomez del Campo, P. A. Hausladen, Y. Larochelle, A. F. Lisetskiy, P. E. Mueller, D. C. Radford, D. W. Stracener, J. P. Urrego, R. L. Varner, and C.-H. Yu. $B(E2)\uparrow$ measurements for radioactive neutron-rich Ge isotopes: Reaching the $N = 50$ closed shell. *Physical Review Letters*, 94(12):122501, 2005.

[178] H. Iwasaki, S. Michimasa, M. Niikura, M. Tamaki, N. Aoi, H. Sakurai, S. Shimoura, S. Takeuchi, S. Ota, M. Honma, T. K. Onishi, E. Takeshita, H. J. Ong, H. Baba, Z. Elekes, T. Fukuchi, Y. Ichikawa, M. Ishihara, N. Iwasa, S. Kanno, R. Kanungo, S. Kawai, T. Kubo, K. Kurita, T. Motobayashi, A. Saito, Y. Satou, H. Suzuki, M. K. Suzuki, Y. Togano, and

Y. Yanagisawa. Persistence of the $N = 50$ shell closure in the neutron-rich isotope ^{80}Ge. *Physical Review C*, 78(2):021304, 2008.

[179] G. Machicoane, D. Cole, J. Ottarson, J. Stetson, and P. Zavodszky. ARTEMIS-B: a room-temperature test electron cyclotron resonance ion source for the National Superconducting Cyclotron Laboratory at Michigan State University. *Review of Scientific Instruments*, 77(3):03A322, 2006.

[180] S. Agostinelli, J. Allison, K. Amako, J. Apostolakis, H. Araujo, P. Arce, M. Asai, D. Axen, S. Banerjee, G. Barrand, F. Behner, L. Bellagamba, J. Boudreau, L. Broglia, A. Brunengo, H. Burkhardt, S. Chauvie, J. Chuma, R. Chytracek, G. Cooperman, G. Cosmo, P. Degtyarenko, A. Dell'Acqua, G. Depaola, D. Dietrich, R. Enami, A. Feliciello, C. Ferguson, H. Fesefeldt, G. Folger, F. Foppiano, A. Forti, S. Garelli, S. Giani, R. Giannitrapani, D. Gibin, J.J. Gómez Cadenas, I. González, G. Gracia Abril, G. Greeniaus, W. Greiner, V. Grichine, A. Grossheim, S. Guatelli, P. Gumplinger, R. Hamatsu, K. Hashimoto, H. Hasui, A. Heikkinen, A. Howard, V. Ivanchenko, A. Johnson, F.W. Jones, J. Kallenbach, N. Kanaya, M. Kawabata, Y. Kawabata, M. Kawaguti, S. Kelner, P. Kent, A. Kimura, T. Kodama, R. Kokoulin, M. Kossov, H. Kurashige, E. Lamanna, T. Lampén, V. Lara, V. Lefebure, F. Lei, M. Liendl, W. Lockman, F. Longo, S. Magni, M. Maire, E. Medernach, K. Minamimoto, P. Mora de Freitas, Y. Morita, K. Murakami, M. Nagamatu, R. Nartallo, P. Nieminen, T. Nishimura, K. Ohtsubo, M. Okamura, S. O'Neale, Y. Oohata, K. Paech, J. Perl, A. Pfeiffer, M.G. Pia, F. Ranjard, A. Rybin, S. Sadilov, E. Di Salvo, G. Santin, T. Sasaki, N. Savvas, Y. Sawada, S. Scherer, S. Sei, V. Sirotenko, D. Smith, N. Starkov, H. Stoecker, J. Sulkimo, M. Takahata, S. Tanaka, E. Tcherniaev, E. Safai Tehrani, M. Tropeano, P. Truscott, H. Uno, L. Urban, P. Urban, M. Verderi, A. Walkden, W. Wander, H. Weber, J.P. Wellisch, T. Wenaus, D.C. Williams, D. Wright, T. Yamada, H. Yoshida, and D. Zschiesche. Geant4—a simulation toolkit. *Nuclear Instruments and Methods in Physics Research Section A: Accelerators, Spectrometers, Detectors and Associated Equipment*, 506(3):250–303, 2003.

[181] D. Rhodes. JANUS: A GEANT4 simulation of low-energy Coulomb excitation experiments with SeGA-JANUS. https://github.com/danielmrhodes/JANUS, 2021.

[182] M. Honma, T. Otsuka, T. Mizusaki, and M. Hjorth-Jensen. New effective interaction for f_5pg_9-shell nuclei. *Physical Review C*, 80(6):064323, 2009.

[183] S. J. Q. Robinson, L. Zamick, and Y. Y. Sharon. Comparison of shell model results for some properties of even-even Ge isotopes. *Physical Review C*, 83(2):027302, 2011.

[184] J. G. Hirsch and P. C. Srivastava. Shell model description of Ge isotopes. *Journal of Physics: Conference Series*, 387:012020, 2012.